



# **NAVAL POSTGRADUATE SCHOOL**

**MONTEREY, CALIFORNIA**

**EFFECTS OF FLUID-STRUCTURE INTERACTION ON  
DYNAMIC RESPONSE OF COMPOSITE STRUCTURES:  
EXPERIMENTAL AND NUMERICAL STUDIES**

by

Young W. Kwon

August 1, 2013

**Approved for public release; distribution is unlimited**

Prepared for: Office of Naval Research, Solid Mechanics Program (ONR 332)

One Liberty Center (Suite 1425), 875 North Randolph Street, Arlington, VA 22203-1995

THIS PAGE INTENTIONALLY LEFT BLANK

<b>REPORT DOCUMENTATION PAGE</b>				Form Approved OMB No. 0704-0188	
Public reporting burden for this collection of information is estimated to average 1 hour per response, including the time for reviewing instructions, searching existing data sources, gathering and maintaining the data needed, and completing and reviewing this collection of information. Send comments regarding this burden estimate or any other aspect of this collection of information, including suggestions for reducing this burden to Department of Defense, Washington Headquarters Services, Directorate for Information Operations and Reports (0704-0188), 1215 Jefferson Davis Highway, Suite 1204, Arlington, VA 22202-4302. Respondents should be aware that notwithstanding any other provision of law, no person shall be subject to any penalty for failing to comply with a collection of information if it does not display a currently valid OMB control number. <b>PLEASE DO NOT RETURN YOUR FORM TO THE ABOVE ADDRESS.</b>					
<b>1. REPORT DATE (DD-MM-YYYY)</b> 1 August 2013		<b>2. REPORT TYPE</b> Project Report		<b>3. DATES COVERED (From-To)</b> Jan. 2009 – Dec. 2012	
<b>4. TITLE AND SUBTITLE</b> Effects of Fluid-Structure Interaction on Dynamic Responses of Composite Structures: Experimental and Numerical Studies				<b>5a. CONTRACT NUMBER</b> N0001410WX20281	
				<b>5b. GRANT NUMBER</b>	
				<b>5c. PROGRAM ELEMENT NUMBER</b>	
<b>6. AUTHOR(S)</b> Young W. Kwon				<b>5d. PROJECT NUMBER</b>	
				<b>5e. TASK NUMBER</b>	
				<b>5f. WORK UNIT NUMBER</b>	
<b>7. PERFORMING ORGANIZATION NAME(S) AND ADDRESS(ES) AND ADDRESS(ES)</b> Dept. of Mechanical and Aerospace Engineering Naval Postgraduate School, 700 Dyer Rd. Monterey, CA 93943-5000				<b>8. PERFORMING ORGANIZATION REPORT NUMBER</b> NPS-MAE-13-002	
<b>9. SPONSORING / MONITORING AGENCY NAME(S) AND ADDRESS(ES)</b> Yapa D. S. Rajapakse Program Manager, Solid Mechanics Office of Naval Research (ONR 332) One Liberty Center (Suite 1425) 875 North Randolph Street Arlington, VA 22203-1995				<b>10. SPONSOR/MONITOR'S ACRONYM(S)</b>	
				<b>11. SPONSOR/MONITOR'S REPORT NUMBER(S)</b>	
<b>12. DISTRIBUTION / AVAILABILITY STATEMENT</b> Approved for public release; distribution is unlimited					
<b>13. SUPPLEMENTARY NOTES</b> The views expressed in this report are those of the author and do not reflect the official policy or position of the Department of Defense or the U.S. Government.					
<b>14. ABSTRACT</b> The technical objectives of the study were to understand and predict the effects of fluid-structure interaction on the dynamic responses and failures of polymer composite structures used for naval applications. More specifically, they were to compare dynamical responses, and failure mechanisms and modes of composite structures in water and air to enhance the understanding of the effects of fluid-structure interaction on marine composite structural behaviors; and to identify the major factors of fluid-structure interaction that affect composite structures					
<b>15. SUBJECT TERMS</b> Composite patch, aluminum structure, crack repair					
<b>16. SECURITY CLASSIFICATION OF:</b>			<b>17. LIMITATION OF ABSTRACT</b> Unlimited	<b>18. NUMBER OF PAGES</b>	<b>19a. NAME OF RESPONSIBLE PERSON</b>
<b>a. REPORT</b> Unclassified	<b>b. ABSTRACT</b> Unclassified	<b>c. THIS PAGE</b> Unclassified			<b>19b. TELEPHONE NUMBER (include area code)</b>

Standard Form 298 (Rev. 8-98)  
Prescribed by ANSI Std. Z39.18

THIS PAGE INTENTIONALLY LEFT BLANK

**NAVAL POSTGRADUATE SCHOOL  
Monterey, California 93943-5000**

Jan. E. Tighe  
Interim President

Douglas Hensler  
Provost

The report entitled “Effects of Fluid-Structure Interaction on Dynamic Responses of Composite Structures: Experimental and Numerical Studies” was prepared for “Office of Naval Research - Solid Mechanics Program (ONR 332) and funded by “Office of Naval Research – Solid Mechanics Program (ONR 332)”.

**Further distribution of all or part of this report is authorized.**

**This report was prepared by:**

---

Young W. Kwon  
Distinguished Professor of MAE

**Reviewed by:**

---

Knox T. Millsaps  
Chair, MAE Department

**Released by:**

---

Jeffrey D. Paduan  
Dean of Research

THIS PAGE INTENTIONALLY LEFT BLANK

## **Table of Contents**

Executive Summary

1. Introduction
2. Technical Objective
3. Technical Approach
4. Major Findings and Results
5. Impact on Naval Technology
6. Acknowledgement
7. List of Publications

Appendix: Collection of Journal Papers

THIS PAGE INTENTIONALLY LEFT BLANK



## **Executive Summary**

The project titled “*Effects of Fluid-Structure Interaction on Dynamic Responses of Composite Structures: Experimental and Numerical Studies*” was undertaken by Prof. Young W. Kwon at Naval Postgraduate School during the years of 2010-2012 under the sponsorship by Office of Naval Research Solid Mechanics Program managed by Dr. Yapa D. S. Rajapakse. The project award number is 000141-0W-R2-0-061. The original project was for two years but it was extended for one more year without any extra cost.

Polymer composite materials have been used increasingly for naval structures, both for surface and submersible vessels. These materials are much lighter than conventional metals with comparable strength and stiffness. Additionally, composite materials can eliminate the maintenance cost associated with corrosion. As a result, ships made of composite materials can save energy and maintenance costs compared to conventional metal ships in addition to other tactical advantages.

Most naval structures are in continuous contact with a water medium. As a result, proper understanding of fluid-structure interaction is important for a reliable design and analysis of those structures. In particular, because polymer composite structures are much lighter than steel structures, the Fluid-Structure Interaction (FSI) is more critical for the former structures.

The objective of this study was to investigate the effect of water on transient dynamic responses of polymer-based composite structures which are in contact with water. To this end, a special impact testing machine was developed and installed in an anechoic water tank at a laboratory of Naval Postgraduate School. Square shapes of composite plates were clamped and they were impacted on the top side using the free fall impact mechanism.

In order to assess the effect of FSI with composite structures, a series of tests were conducted in four different cases of impact environments. The first case has a clamped composite plate impacted in air. There is no water contact with the plate. This is called dry impact. The second case has a composite plate submerged in water. As a result, both sides of the plate are in contact with water. This test is called water-backed wet impact. The third one has a composite plate whose impacted side is wet while the opposite side is dry. It is called air-backed wet impact. This represents a situation of an impact loading on

outside of a ship hull such as rocks, mammals, drifting ice, water slamming, etc. The last case has the opposite of the third case. That is, the impact side is dry. This case is called water-backed dry impact. This condition occurs when a mechanical impact occurs from inside a ship hull like machinery vibration. When a composite is in contact with water on either or both side(s), it is just called wet impact from now on.

Both laminated and sandwich composite plates were tested under the different environments as described above using the same impact energy, i.e., the same impact mass and drop height; and their dynamic responses and damage initiation and growth were compared to examine the FSI effect on composite structures.

Because of the hydrodynamic mass effect of the surrounding water, the impact on composite plates resulted in much greater impact forces for wet impact compared to dry impact under the same impact energy. The wet impact resulted in greater strains and stresses in the plates yielding pre-mature failure of the structures. Hence, the damage and failure occurs at a lower impact energy level under wet impact. On the other hand, three different wet impact conditions did not produce a major difference among them. Furthermore, the effect of fluid-structure interaction was not uniform over the composite plate. Comparing strain responses between the dry and wet impact shows significant variation from location to location over the plate.

The experimental results suggest that the fluid-structure interaction must be included in the design and analysis of composite structures in order to avoid failure in the structures in contact with water. Otherwise, unexpected pre-mature failure can happen with them.

Computational models were also developed to study the FSI effect on composite structures using the newly developed solid-like plate/shell element which has only displacement degrees of freedom but not rotational degrees of freedom like a 3-D solid element. As a result, coupling of the fluid and solid media is easy with the element. The fluid domain was modeled using the Cellular Automata technique which is computationally very efficient. Additionally, a preliminary study was conducted to understand as well as predict the effect of non-uniform varying strain rates on material behaviors and failure. During most of practical dynamic loading, the applied strain rate changes as a function of time. As a result, it is important to investigate the varying strain

rate effect on materials. As a starting point, an aluminum material was selected instead of composite materials because the latter has too many variables beyond control. The study showed that the varying strain rate affects the material behavior significantly. For example, the stress-strain curve including failure strength and strain depends on the history of the applied strain rates. Some simple failure criteria were proposed based on the experimental study. However, more extensive research is needed in this topic.

THIS PAGE INTENTIONALLY LEFT BLANK

## **1. Introduction**

Polymer composites have been used increasingly for marine structures including surface and submersible ships. These materials are much lighter than steels with comparable strength and stiffness. Additionally, composite materials can eliminate the maintenance cost associated with corrosion. As a result, ships made of composite materials can save energy and maintenance costs compared to conventional metal ships. Recently, composite materials have been also used for repairing damage such as cracks and corrosion occurring in aluminum super-structures of ships.

Composite materials, especially carbon fiber composites, have been very popular for Air Force and aerospace industry applications since weight is very critical in the design of aero-structures. However, the density of the water is approximately 1000 times greater than that of air. Furthermore, the densities of the composite materials are comparable to that of water. Therefore, the interaction between the polymer composite structure and water cannot be neglected. Because most of marine structures are in contact with water, it is essential to understand and predict the Fluid-Structure Interaction Effect (FSI) on composite structures under transient dynamic loading.

## **2. Technical Objective**

The technical objectives of the study were to understand and predict the effects of fluid-structure interaction on the dynamic responses and failures of polymer composite structures used for naval applications. More specifically, they were to compare dynamical responses, and failure mechanisms and modes of composite structures in water and air to enhance the understanding of the effects of fluid-structure interaction on marine composite structural behaviors; and to identify the major factors of fluid-structure interaction that affect composite structures

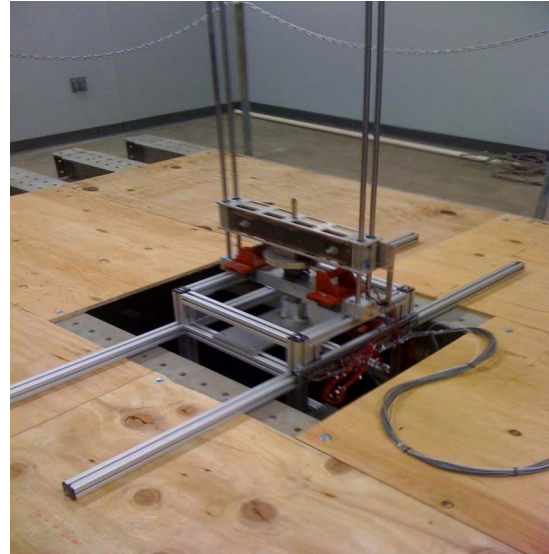
## **3. Technical Approach**

During this research period, mostly experimental studies have been conducted to achieve the objectives. Some numerical work has been conducted but more extensive modeling and simulation work is planned to be reported for the next phase of research.

In order to assess the fluid-structure interaction effect on a composite structure, it is necessary to compare its dynamic response in water to that in air under the same conditions. To this end, an impact testing machine was designed and fabricated as shown in Fig. 1. The figure shows the same impact testing equipment in air as well as in the anechoic water tank. Some key aspects of the impact machine are the following. First of all, the equipment is portable so that it can be moved in and out of anechoic water tank for either dry or wet testing. The impact loading is provided outside the water in order to avoid water disturbance caused by the large moving object entering into water. Therefore, an intermediate member is introduced between the impactor and a composite plate. The member is located just a small distance above the composite plate. As the top of the member is stricken by the impactor, its bottom side hit the composite plate. However, the movement of the member is so small that its perturbation on water is minimal to provide a fair comparison between dry and wet impact cases.



(a) Impact testing machine in air



(b) Impact machine in anechoic water tank

Figure 1. Impact testing equipment

Four impact environments were considered during the study. The first case was a dry impact in air. There is no water contact in this case. This is the air-backed dry impact, or simply dry impact. The second and third cases had impacts while submerged in water.

Both cases had the top surfaces of test plates, where impacted, in contact with water, but the bottom surfaces were different. The second case had a dry bottom surface, i.e., no water contact, which is called the air-backed wet impact. The third case had a wet bottom surface, i.e., in contact with water, called the water-backed wet impact. The second and third loading conditions represented impact on the ship hulls from the water side, which may be floating ice and sea animal impact on ship hulls. The three cases mentioned above are shown in Fig. 2(a) through (c). For the last case, the impact side is dry while the opposite side is wet, which is called the water-back dry impact as sketched in Fig. 2(d). This case is to simulate an impact from the inside of a composite hull such as ship-board equipments and sailors. If a composite is in contact with water on one side or both sides, it is called wet impact here.

Strain gages were attached to every composite plate so that the impact force and strain history were measured during each impact testing. Besides, the plates were inspected for any visual damage before and after impact. Most of the damages were delamination on the tension side of the plate as well as some penetration of impactor on the impact side, which mostly occurred for a balsa-core sandwich plate with thin skin layers.

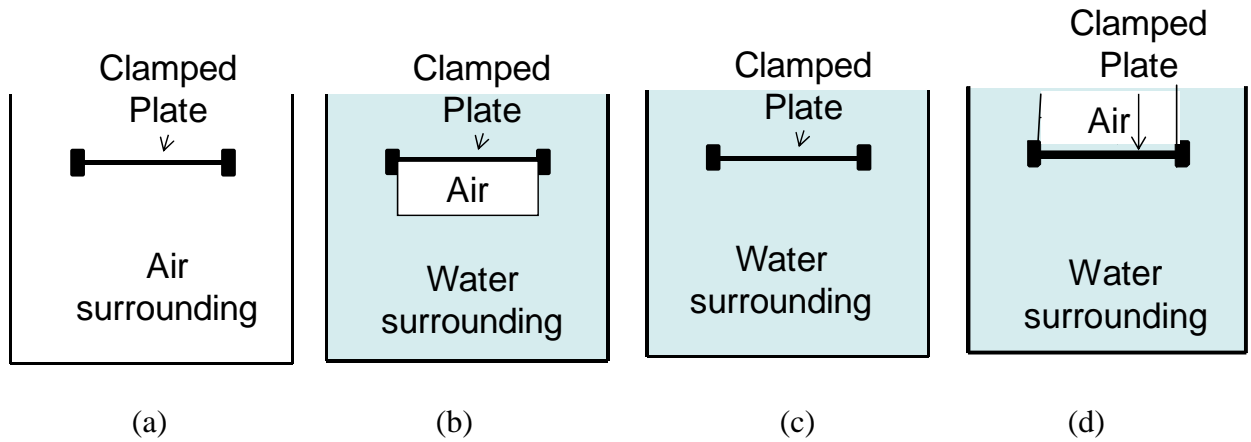


Figure 2. Comparison of different impact conditions with impact on the top side of composite plate: (a) air-backed dry impact (or simply dry impact), (b) air-backed wet impact, (c) water-backed wet impact, (d) water-backed dry impact

#### 4. Major Findings and Results

Since detailed results and discussions have been reported in publications listed in Section 6 and Appendix includes all the journal papers, only the major findings are summarized here.

- The wet impact resulted in a much greater impact force than the dry impact under the same impact energy, i.e., the same impact mass and drop height. Figure 3 shows comparisons between dry and wet impacts. The water-backed air impact also showed a similar comparison to the dry impact. The hydrodynamic mass is added to the composite mass under water. Then, the larger mass moves slowly under than same impact load, which results in a great contact force between the impactor and the composite plate. However, this difference occurs only before damage occurs in the plate.
- The higher impact force due to wet environment also yielded greater strains. However, the FSI effect is non-uniform over the plate. Some locations have a larger effect than others. This was observed in the strain responses. Comparing strains at two different locations as shown in Figures 4 and 5 shows that the FSI effect is greater for the location in Figure 5. The strain gage locations are provided in Figure 6.
- The greater impact force under wet impact resulted in damage initiation earlier than dry impact. Figure 7 plots the delamination size as a function of the impact height while the impact mass remains constant. The figure compares the damage size between the dry and wet impact. Figure 8 compares the damage between dry and wet impacts under the same impact energy level.
- Once damage occurs earlier for the wet impact, the damage reduces the stiffness of the composite plate under wet impact. This causes reduction in contact force for wet impact than dry impact. Figure 9 compares the forces as damage progresses.



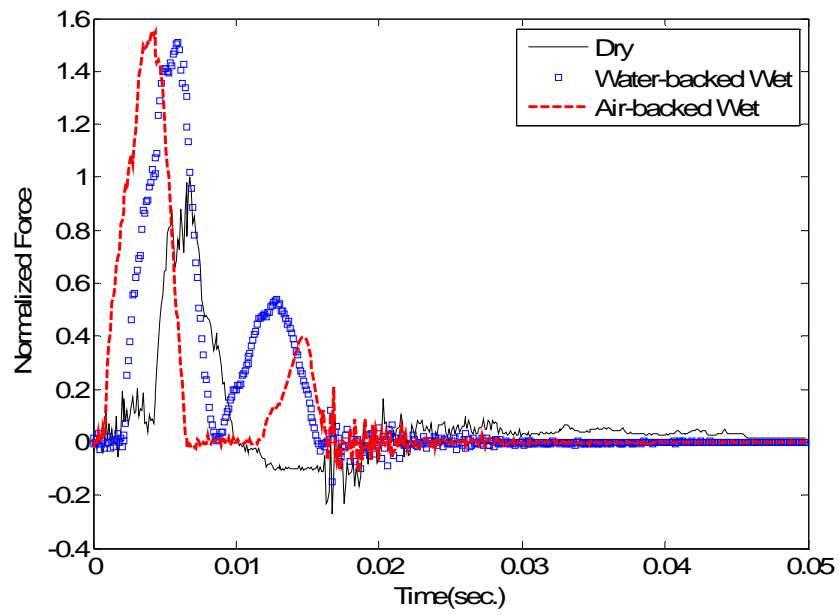


Figure 3. Comparison of impact forces among dry, water-backed and air-backed wet impact cases

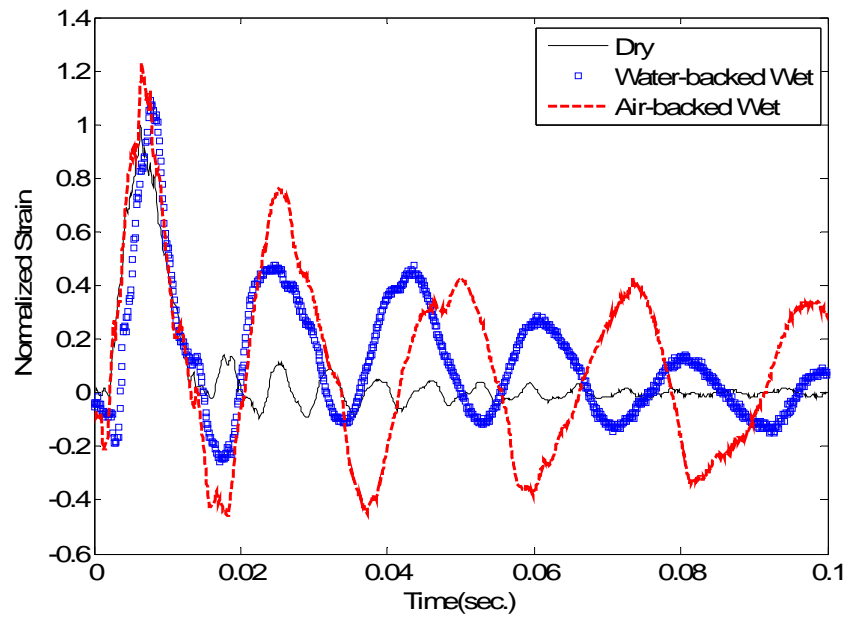


Figure 4. Comparison of strains at position #2 among dry, water-backed and air-backed wet impact cases

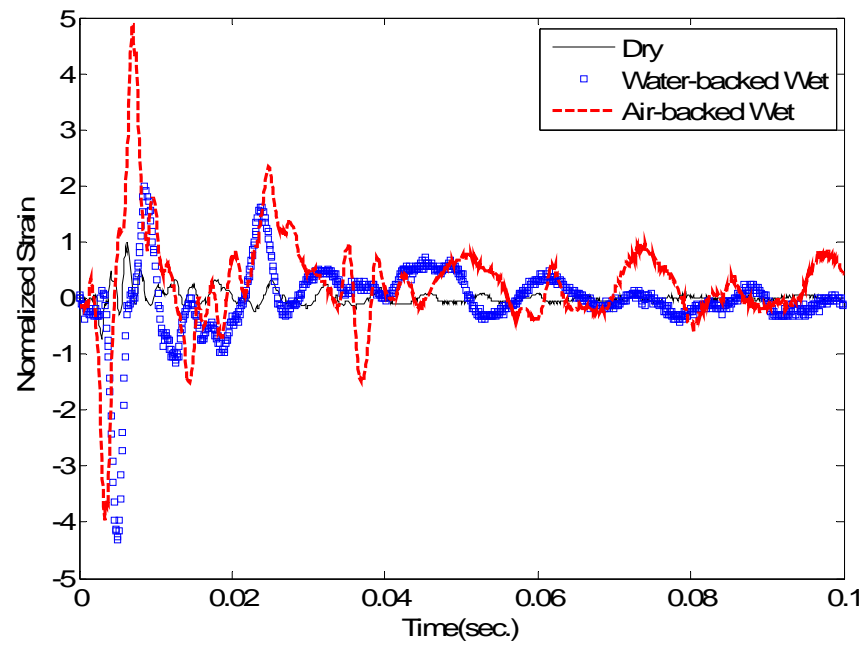


Figure 5. Comparison of  $x$ -strains at position #4 among dry, water-backed and air-backed wet impact cases

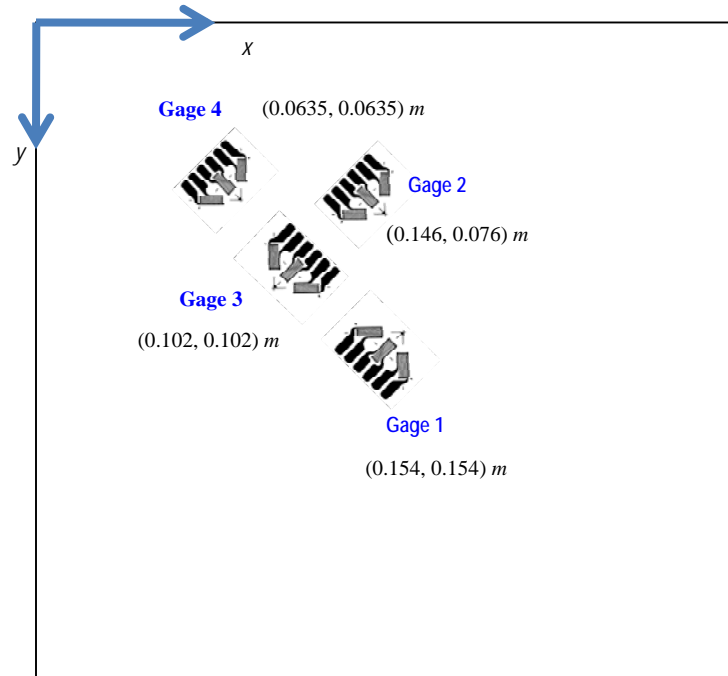


Figure 6. Strain Gage layout on composite samples.

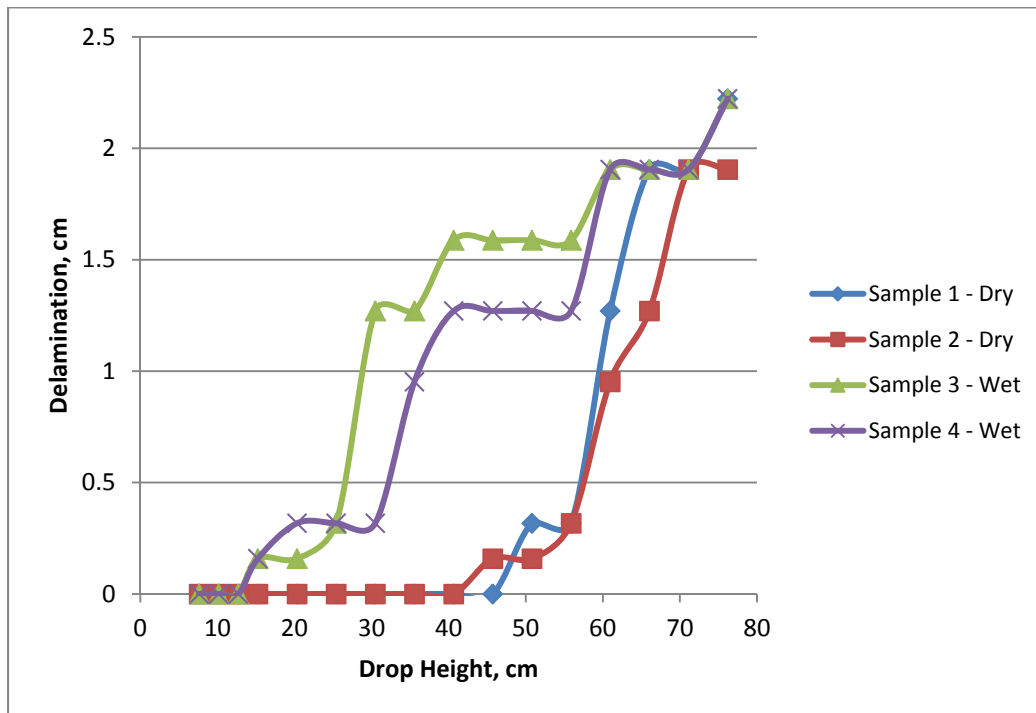


Figure 7. Damage size as a function of drop height for both wet and dry samples.



(a) Without FSI (air)



(b) With FSI (water-backed)

Figure 8. Comparison of delamination damage of sandwich plates with and without FSI under the same impact condition

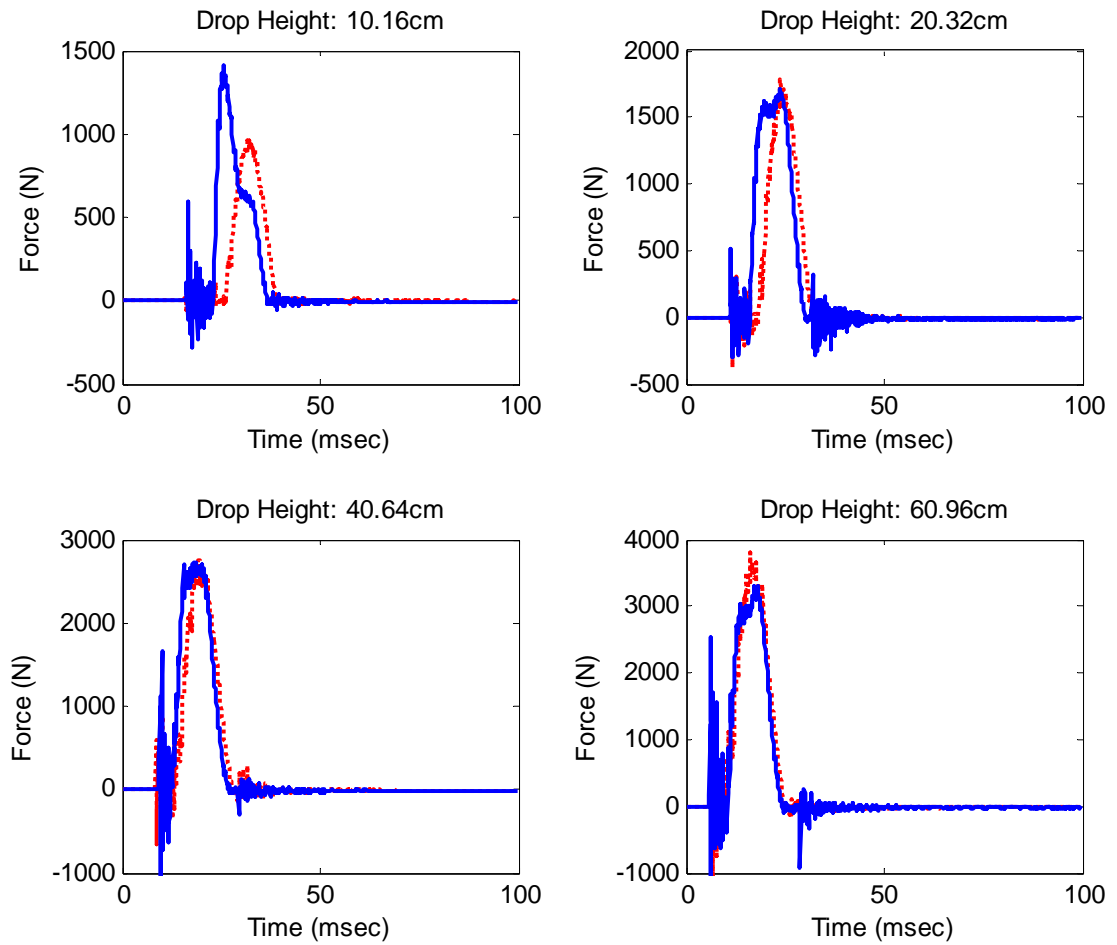


Figure 9. Comparison of impact force-time histories with progressive impact with damage. (solid line - water-backed wet impact; broken line - dry impact)

- The effect of varying strain rates is important on material behavior. Figure 10 shows the stress-strain curves between uniform strain rates and non-uniform strain rates. As the strain rate changes from one rate to another rate, the stress-strain curve does not follow the stress-strain curve of the second rate. The stress-strain curves as well as fracture strength and strain depend on the history of the applied strain rates.

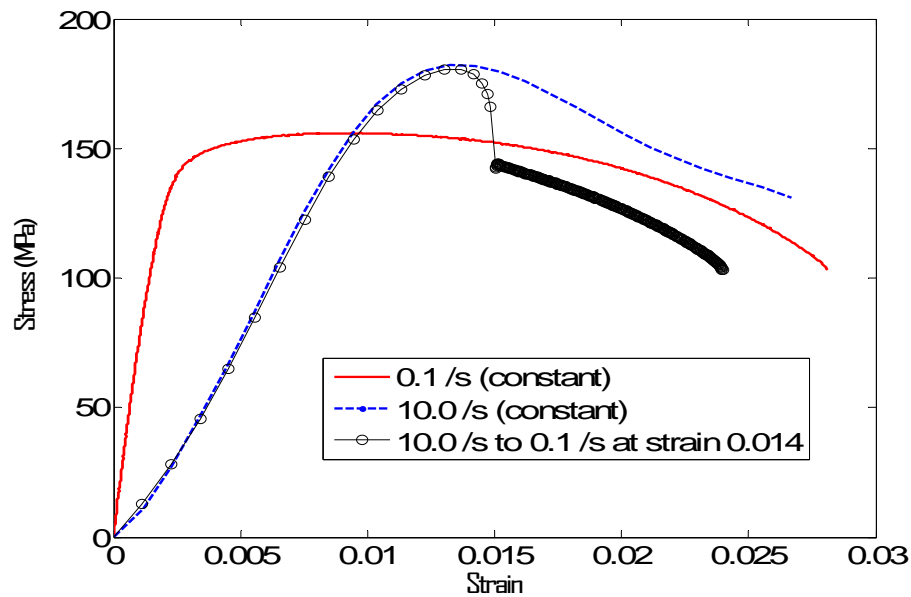


Figure 10. Comparison of stress-strain curves between uniform and non-uniform strain rates

## 5. Impact on Naval Technology

Most naval structures are in contact with a water medium. As a result, proper understanding of fluid-structure interaction is important for a reliable design and analysis of those structures. In particular, because composite structures are lighter and more flexible than steel structures, the fluid-structure interaction is more critical for the former structures.

Multiple U.S. Naval officers participated in the project as a part of their thesis research. The education and experience they received through the project is important for

them as ship commanders, ship-building supervisors, and/or program managers throughout their careers. As an example, one of the naval officers from this research program became a supervisor for building the composite superstructure for DDG 1000.

## **6. Acknowledgement**

The project titled “*Effects of Fluid-Structure Interaction on Dynamic Responses of Composite Structures: Experimental and Numerical Studies*” was undertaken by Prof. Young W. Kwon at Naval Postgraduate School during the years of 2009-2013 under the sponsorship by Office of Naval Research Solid Mechanics Program managed by Dr. Yapa D. S. Rajapakse. The project award number is 000141-0W-R2-0-061. The support is greatly appreciated.

## **7. List of Publications**

### Journal Papers:

- J1) Y. W. Kwon, A. C. Owens, A. S. Kwon, and J. M. Didoszak, “Experimental Study of Impact on Composite Plates with Fluid-Structure Interaction”, Int. Journal of Multiphysics, Vol. 4, No. 3, 2010, pp. 259-271.
- J2) Y. W. Kwon, M. A. Violette, R. D. McCrillis, and J. M. Didoszak, “Transient Dynamic Response and Failure of Sandwich Composite Structures under Impact Loading with Fluid Structure Interaction”, Applied Composite Materials. (DOI: 10.1007/s10443-012-9249-8)
- J3) Y. W. Kwon and R.P. Conner, “Low Velocity Impact on Polymer Composite Plates in Contact with Water”, International Journal of Multiphysics, Vol. 6, No. 3, 2012, pp. 179-197.
- J4) Y. W. Kwon, “Study of Fluid Effects on Dynamics of Composite Structures”, ASME Journal of Pressure Vessel Technology, Vol. 133, June 2011, 031301-6.
- J5) Y. W. Kwon, “Analysis of Laminated and Sandwich Composite Structures Using Solid-Like Shell Elements”, Applied Composite Materials, Vol. 20, 2013, pp. 355-373. (DOI: 10.1007/s10443-012-9273-8)

- J6) L. E. Craugh and Y. W. Kwon, “Coupled Finite Element and Cellular Automata Methods for Analysis of Composite Structures with Fluid-Structure Interaction”, *Composite Structures*, Vol. 102, August 2013, pp. 124-137.
- J7) Y. W. Kwon and K. S. Tan, “Failure of Ductile Materials Subject to Varying Strain Rates”, *ASME Journal of Pressure Vessel Technology*, Vol. 133, February 2011, 011402-1:6.
- J8) Y. W. Kwon, Y. Esmaeili, and C. M. Park, “Stress-Strain Behavior of an Aluminum Alloy under Transient Strain rates”, *ASME Journal of Pressure Vessel Technology*, Vol. 133, August 2011, 044501-1.

Book Chapter:

- B1) Y. W. Kwon and A. C. Owens, “Dynamic Responses of Composite Structures with Fluid-Structure Interaction”, *Advances in Composite Materials*, IN-TECH publisher, 2011.

Edited Volume:

- V1) Y. W. Kwon and Y. D. S. Rajapakse, *Marine Application of Composite Structures and Materials*, *International Journal of Multiphysics*, Vol. 6, No. 3, 2012.

Conference Papers:

- C1) K. S. Tan and Y. W. Kwon, “Failure Criterion for Varying Strain Rate Loading”, (PVP2010-25149) 2010 ASME Pressure Vessel and Piping Conference, Bellevue, Washington, July 2010.
- C2) A. C. Owens, J. M. Didoszak, A. S. Kwon, and Y. W. Kwon, “Underwater Impact of Composite Structures”, (PVP2010-25065) 2010 ASME Pressure Vessel and Piping Conference, Bellevue, Washington, July 2010.
- C3) Y. W. Kwon, “Lattice Boltzmann Method for Fluid-Structure Interaction”, 19<sup>th</sup> Discrete Simulation of Fluid Dynamics (DFDS 2010), Rome, Italy, July, 2010.

- C4) Y. W. Kwon and S. Blair, “Dynamic Behavior of Composite Structures with Fluid-Structure Interaction”, 25<sup>th</sup> American Society Composite Conference, Dayton, Ohio, Sept. 20-22, 2010.
- C5) Y. W. Kwon, “Dynamic Response and Failure of Composite Structure with Fluid-Structure Interaction”, ONR Review Meeting, Maryland, September, 2010.
- C6) Y. W. Kwon, “Impact on Composite and Sandwich Structures Undergoing Fluid Structure Interaction”, Second High resolution Non-Invasive Damage Diagnostics and Predictive Modeling Workshop, Oxfordshire, UK, March 8-10, 2011.
- C7) Y. W. Kwon and R. D. McCrillis, “Dynamic Response and Failure of Composite and Sandwich Structures under Fluid Structure Interaction”, The 18<sup>th</sup> International Conference on Composite Materials, Jeju Island, Korea, August 21-26, 2011.
- C8) Y. W. Kwon, “Dynamic Response and Failure of Sandwich Composite Structure under Impact with Fluid-Structure Interaction”, ONR Review Meeting, Maryland, September, 2011.
- C9) Y. K. Boey and Y. W. Kwon, “Progressive Damage And Failure Strength of Notched Woven Fabric Composites Under Axial Loading With Varying Strain Rates”, Mechanics of Nano, Micro and Macro Composite Structures, Torino, Italy, June 18-20, 2012.
- C10) Y. W. Kwon, M. A. Violette, and R. D. McCrillis, “Effect of Fluid Structure Interaction on Composite Structures under Impact Loading”, 15<sup>th</sup> European Conference on Composite Materials, Venice, Italy, June 24-28, 2012.



## **INITIAL DISTRIBUTION LIST**

1. Defense Technical Information Center  
Ft. Belvoir, Virginia
2. Dudley Knox Library  
Naval Postgraduate School  
Monterey, California
3. Research Sponsored Programs Office, Code 41  
Naval Postgraduate School  
Monterey, CA 93943
4. Young W. Kwon  
Naval Postgraduate School  
Monterey, CA 93943
5. Yapa Rajapakse  
Solid Mechanics Program (ONR 332)  
Office of Naval Research  
Arlington, Virginia
6. Erik A. Rasmussen  
Naval Surface Warfare Center Carderock Division  
West Bethesda, Maryland
7. Douglas C. Loup  
Naval Surface Warfare Center Carderock Division  
West Bethesda, Maryland

THIS PAGE INTENTIONALLY LEFT BLANK

### **Appendix: Collection of Journal Papers**

The published journal papers resulting from this project are attached as separate PDF files. Each paper is named according to the paper list in Section 7.

.

# Experimental Study of Impact on Composite Plates with Fluid-Structure Interaction

by

**Young W. Kwon, Angela C. Owens, Aric S. Kwon,  
Jarema M. Didoszak**

reprinted from

## **THE INTERNATIONAL JOURNAL OF MULTIPHYSICS**

**2010: VOLUME 4 NUMBER 3**

**MULTI-SCIENCE PUBLISHING**

# Experimental Study of Impact on Composite Plates with Fluid-Structure Interaction

**Young W. Kwon, Angela C. Owens, Aric S. Kwon,  
Jarema M. Didoszak**

Department of Mechanical & Aerospace Engineering  
Naval Postgraduate School  
Monterey, California 93943

## **ABSTRACT**

The transient dynamic response of composite structures under water is affected by Fluid Structure Interaction (FSI), which results in an added mass effect as well as damping. Because the density of composites is comparable to that of water, the added mass effect becomes even more critical to the transient dynamic response of composites in water. In this study, an experimental testing set-up was designed and fabricated, and testing was conducted to investigate FSI effects on composite laminate plates immersed in fluid and subjected to impact loading. Square composite laminates made of carbon fiber weave and vinyl ester resin were subjected to impact loading using a specially developed vertical drop-weight testing machine. The composite samples were fitted with gages to provide time-history on strains and impact forces generated during impact. Impact tests were performed on four-side clamped laminate plates in air-backed wet, water-backed wet, and dry environments. The results showed non-uniform effects on transient responses of wet composites with FSI. Generally, wet impacts on composite plates increased both transient impact forces and strains significantly compared to dry impacts under the same impact mass and velocity condition. The findings of this study will provide a better understanding for use of composite materials in underwater structural applications where impact loading is expected.

**Keywords:** impact, composites, fluid-structure interaction

## **1. INTRODUCTION**

The growing use of composites in ship masts, superstructures, deck grates, piping, ducting, rudders, propellers, stacks, and various submarine structures requires extensive modeling and testing to help designers, builders and operators better understand composite response [1]. These materials are subjected to a wide spectrum of loads during manufacturing and service life. Dynamic loadings, in particular, impact type events, represent a serious design concern for use of composites since composite structures are more susceptible to impact damage than similar metallic structures which are more ductile in nature and can typically absorb large amounts of energy without failure [2]. Furthermore, the damage in composites from impact can go undetected even when the mechanical properties may be drastically reduced from an impact. For these reasons, numerous experimental and analytical studies have been conducted to study the dynamic response of composites subjected to impact loading. A review article [3] surveyed over 300 papers and provided a comprehensive view

of the state of knowledge in this area. According to ref. [3], most of the current research effort has been focused on low velocity impact damage, specifically, the damage predictions and the evaluation and prediction of residual properties of damaged laminates. All of the research completed thus far has focused on damage in composites under impact loading in dry environments to support development of composites in aircraft structures.

As far as dynamic response of structures under water is concerned, a great deal of analytical and experimental studies have been conducted on the effect of fluid force on the natural frequencies, damping ratios and mode shapes of vibrating structures in contact with fluid. This is commonly known as the Fluid Structure Interaction (FSI) problem. FSI investigations have supported many problems in submarine signaling, offshore oil structure stability, and ship structure vibrations. Through these studies, many numerical and analytical methods have been developed in order to predict the added mass and the resulting changes in natural frequency of a structure in contact with fluid. It has been determined and widely proven that the effect of fluid surrounding a structure decreases the natural frequency of a structure due to the increase in total kinetic energy of the vibrating structure and fluid from the addition of kinetic energy of the fluid. This effect can be interpreted as an added mass to the vibrating structure in the analysis of the dynamic response. Essentially as the structure vibrates, its mass is increased by the mass of the vibrating fluid with which it is in contact, consequently decreasing its natural frequency. Studies of fluid structure interaction and the added mass effect, also known as virtual mass effect, hydrodynamic mass, and hydroelastic vibration of structures, started with Lamb [4] in 1920 who calculated the first bending mode of a submerged circular plate. In response to a problem of submarine signaling, Lamb investigated the vibrations of a thin elastic circular plate in contact with water. In his investigation he discovered that the natural frequencies for structures in contact with fluid are lower than the frequencies in air, based on the assumption that the modes shapes are virtually the same in water as in a vacuum. The resonant frequency was determined using Rayleigh's method. Powell and Roberts [5] experimentally verified Lamb's theoretical results. Lindholm et al. [6], Volcy et al. [7], Fu and Price [8] did extensive experimental study on the response of cantilever plates under various orientations, boundary conditions, geometrical shapes and levels of submergence. The above studies were mainly focused on the fundamental mode of a circular plate. Kwak and Kim [9] investigated the problem of axisymmetric vibration of circular plates. They, by employing Hankel transformation, solved the mixed boundary problem and calculated the Nondimensionalized Added Virtual Mass Incremental (NAVMI) factors for higher modes of clamped, simply supported and free plates. The NAVMI factor is the ratio of kinetic energy of water and the kinetic energy of the plate based on the assumption that the mode shape does not change under the influence of water. They also determined that for plates in contact with water on both sides, the NAVMI factor is twice the value of a plate in contact on only one side. Kwak [10] calculated the added virtual mass of rectangular plates with simply supported and clamped boundary conditions vibrating in contact with water. The Green function was used to solve the boundary value problem of the water domain. This method was combined with the Rayleigh-Ritz method. Haddara and Cao [11] presented analytical and experimental studies of the dynamic response of submerged rectangular plates. An approximate expression to calculate the modal added mass for flat rectangular plates was developed and compared to experimental results. Those FSI studies considered natural frequencies of free vibrations of wet structures.

The objective of this paper is to investigate the FSI effects on the transient dynamic responses of composite plates submerged in water and subjected to impact loading. Because

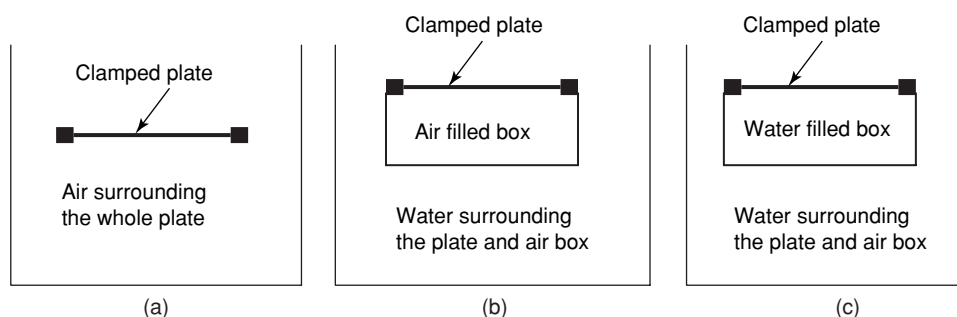


Figure 1. Three different impact conditions with composite plates held in place: (a) dry impact, (b) air-backed wet impact, (c) water-backed wet impact.

the density of the composites is close to that of the density of water, the added mass effect of the water is expected to be even more critical to the transient dynamic response of composites in water. Damage in composite plates was avoided in order to focus on their transient dynamic response with FSI.

The composites were made of carbon fiber woven fabric and vinyl ester resin using the Vacuum Assisted Resin Transfer Molding (VARTM) technique. The impact testing was conducted with a specifically developed vertical drop weight testing apparatus, and the composite samples were fitted with gages to provide real-time information on strain levels and impact forces generated during impact. The transient response of the sample included forces and strains as a function of time. Many tests were performed to verify repeatability. Phases of research included testing the samples in various environmental surroundings: dry environment for the baseline, water-backed wet, and air-backed wet environments as sketched in Fig. 1. These impact environments are described in more detail later. The dry case was completed as the baseline for comparison with the other cases in order to identify the change in response of the composite from the surrounding fluid.

## 2. COMPOSITE SPECIMENS AND TESTING EQUIPMENT

### 2.1 FABRICATION OF COMPOSITE SPECIMENS

Three carbon fiber laminate samples were constructed for this study. Each sample was fabricated from TORAY T700CF carbon fiber bidirectional weave and DERAKANE 510-A vinyl-ester matrix resin. Each plate was fabricated through the VARTM process, which consists of pulling resin through layers of carbon fibers using a vacuum. The plates consisted of eight plies oriented [0/90/0/90] at 2.38 mm nominal thickness with dimensions of  $457 \times 457$  mm. The DERAKANE resin was mixed with three hardeners, Methyl Ethyl Ketone Peroxide (MEKP), Cobalt Napthenate (CoNAP), and N- Dimethylaniline (DMA) to achieve a nominal 60 minute curing time. The hardeners were added solely to achieve proper gel time and do not affect composite strength. All resin components were mixed based on a percent weight for a nominal cure time per manufacturer's directions at a temperature of less than 70°F. The DERAKANE 510-A was measured by volume and the MEKP, CoNAP, and DMA were measured by weight. The VARTM apparatus consists of a glass surface, resin reservoir, vacuum pump, gauge board, and resin trap as shown in Fig. 2. The glass working surface is made of a sheet of 12 mm thick tempered glass for hardness, durability, and thermodynamic properties, as well as to promote the proper seal for the vacuum bag. The pump provides the vacuum necessary to draw the resin from the resin reservoir through the composite sample,



Figure 2. Fabrication of samples using the VARTM process.

and ensures a vacuum seal to prevent air from entering the composite sample. The gage board measures and regulates the vacuum pressure in the sample. The purpose of the resin trap is to allow air from the sample to pass freely through the gage board to the vacuum pump while simultaneously preventing the resin from contaminating these sensitive components by providing collection reservoir. After a satisfactory vacuum was established and all air leaks in the vacuum bag assembly were eliminated, inlet tubing is inserted into the resin reservoir allowing the resin to flow through the composite sample.

## 2.2 IMPACT TESTING APPARATUS

Impact tests were conducted using a specially designed drop weight instrumented testing system, as shown in Fig. 3. This instrumented apparatus consisted of a drop weight impactor, a load transducer, strain gages, high speed data analyzer, and an air box. The sample supporting fixture at the bottom of the drop tower was made of aluminum and facilitated square clamped conditions with a clear span of  $305 \times 305$  mm. The composite plates were then clamped to the impactor frame using c-clamps to represent clamped boundary conditions. The transient response measurement of the sample included force and strains as a function of time.

The drop weight impactor consisted of a drop weight and an impact rod. The drop weight was supported by 4 steel guide rods, and the impact rod was supported by an aluminum frame base and a linear spring of spring constant 7508 N/m. The dimensions of the guide rods were 1.219 m high with a 6.35 mm diameter, and the dimensions of the base frame were 1.168 m high  $\times$  0.457 m wide  $\times$  0.457 m deep. The aluminum framing pieces and fasteners were designed and assembled for this research. The falling weight was guided by four small linear bearings. The impact rod was guided with two plain brushing aluminum linear bearings of 38.1 mm diameter enclosed in a casing for support. The top of the impact rod stayed above the water surface so that the drop weight would not go into the water as it hit the impact rod on its top. This fact is important not to disturb water during the impact testing



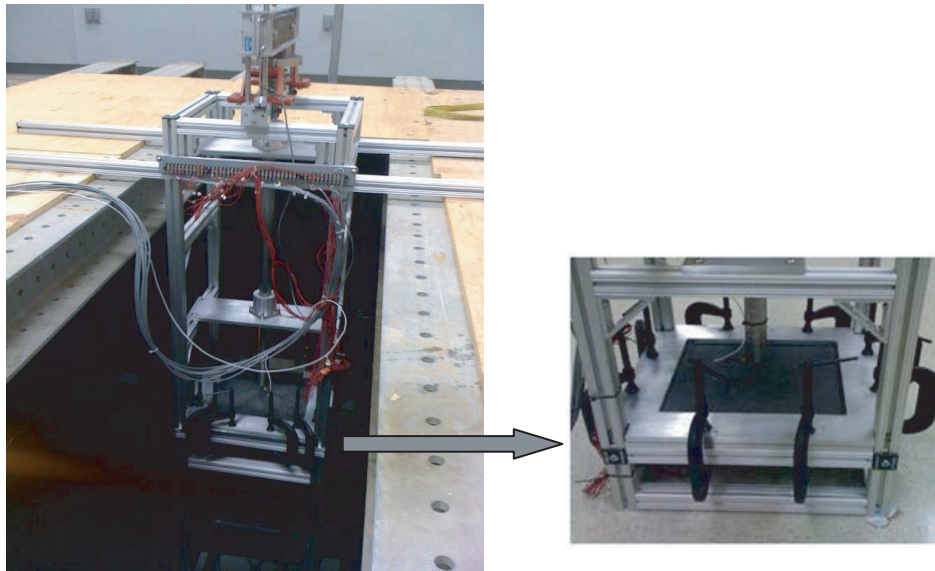


Figure 3. Drop weight instrumented testing system in anechoic water tank.

so that a composite plate interacts with still water. The other end of the impact rod, which struck a composite plate during impact, was initially very close to the specimen surface inside the water such that the disturbance of water due to the impact rod was negligible. Therefore, FSI occurred only resulting from dynamic motion of composite plates.

A trigger at the base of the falling weight was used to initiate data collection. The drop weight was kept constant at 12.0 kg. The impact rod was made of steel and had a mass of 12.7 kg. Impact energy could be varied by changing the drop height. The maximum height was 1.06 m, which could produce approximately 4.6 m/s initial velocity upon impact. The impact location was at the center of the composite sample. The selection of impact mass and height was made not to cause any damage to the composite plates so that the transient dynamic response of the plates could be focused in the study. The damage study will be conducted later and presented in a separate paper.

The load cell used was an ICP® force sensor manufactured by PCB Piezotronics, Inc. which converts force into a measurable electrical output. The load transducer was mounted on the end of the impactor rod. The gage had an impact diameter of 15.88 mm. In the case of wet testing, the gages and cable connection were coated. The strain gages were three-element 45° single-plane rosettes, model CEA-00-250UR-350, by Vishay Micro-Measurements. There were four rosette strain gages bonded to each composite sample. The gages were bonded to the underside of the laminate samples, opposite side of impact, and bonded for waterproofing. Figure 4 illustrates the orientation, location and designated x-y axis. Gage location #1 was directly at the center on the underside of the sample opposite to the impact location. Gages #3 and #4 were placed along a diagonal line of the composite plate with Gage #4 at the quarter distance of the diagonal length. Gage #2 was located close to the vertical symmetric line of the plate.

Data acquisition was carried out using an acquisition system specifically developed for this project, that consisted of a Pentium™ 4, 2.4 GHz, 512-MB RAM system, National Instruments™ simultaneous sampling multifunction DAQ, and five Vishay™ 2120 multi-channel strain signal conditioners. The system had 16 bit analog-to-digital conversion resolution and was capable of reading a total of 16 channels at a throughput rate of up to

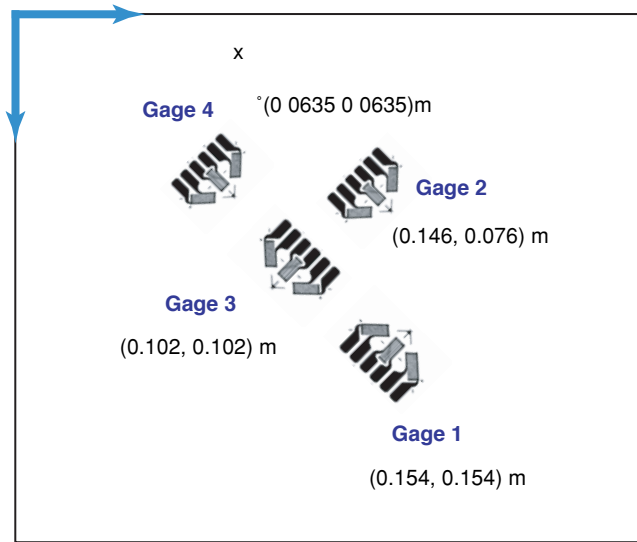


Figure 4. Strain gage rosette locations opposite the side of impact. (The plate size is  $0.305 \text{ m} \times 0.3045 \text{ m}$ ).

250 kS/s per channel, which was appropriate for the rate of testing used in this study. The data-acquisition process was controlled using the NI-DAQmx driver software and LabVIEW™ interactive data-logging software that was specifically formatted for this research. A trigger located at the top of the impact rod was used to initiate data acquisition. Strain readings from four signal conditioners were multiplexed in order to accommodate all strain gages within the available number of channels. Errors due to instrumentation noise did not appear to cause problems in the data capture so no filtering was used.

An air box was constructed to facilitate testing for air-backed wet environments. The box was made of 12.7 mm thick plexi-glass with dimensions 330 mm wide  $\times$  330 mm long  $\times$  127 mm deep. This box was then secured to the bottom aluminum support plate for the composite sample using 8 c-clamps of dimensions 76 mm jaw  $\times$  60 mm throat, and sealed with putty tape to prevent water leakage. The box completely covered the sample so that the bottom side of the plate was not exposed to water. A 19 mm diameter hole was cut out from the side to feed the wiring from the strain gages to the data analyzer, which was filled with putty to prevent water leakage during testing.

An anechoic water tank used for underwater surroundings testing was measured 2.75 m wide  $\times$  2.75 m long  $\times$  2.75 m deep. The anechoic tank was used to minimize the influence of the wave reflection from the boundary walls. The tank was filled with fresh water. A standing platform was constructed across the top of the tank made with aluminum I-beams and plywood, leaving a  $0.635 \text{ m} \times 0.914 \text{ m}$  square opening for suspension of the drop weight impactor.

### 3. IMPACT TESTING

Three different impact cases were studied in order to examine the effects of FSI on composite structures under dynamic loading. These cases were shown in Fig. 1. First, the dry impact was conducted as the baseline. For the dry impact test, the composite plates were impacted without having any contact with the water. This is shown in Fig. 1(a). Subsequent wet impact tests were undertaken for the same composite plates. In order to avoid any moisture effect on the composite materials, the wet impact testing was performed as soon as the composite

plates were submerged into the anechoic water tank. Furthermore, once the wet impact testing was completed, dry impact of the plate was conducted immediately following the wet impact. The responses of the dry impact tests before and after the wet impact testing were compared. Their results were consistent. By doing so, it could be verified that the composite plates did not absorb any moisture to affect their material properties.

Two different wet impact conditions were considered. The first case has an air-containing rigid box attached to the bottom of the composite plates. The box was completely sealed so that no water penetrated into the box when the composite plate with the attached box was submerged into the water of the anechoic water tank. Then, impact loading was applied to the composite plate submerged in water. This is called the air-backed wet impact and is shown in Fig. 1(b). The air-backed composite plate is only in contact with water at the top side where the impact occurs. The other wet impact case was very similar to the previous one except that the air-box was no longer sealed so that water filled the box when the plate and the box were submerged into the water tank. This is sketched in Fig. 1(c) and called the water-backed wet impact. The water-backed plate is exposed to water on both sides in this case. The same impact conditions, i.e. the same drop weight and height, were applied to the three impact loading cases. The wet impact responses were compared to the dry impact data in order to evaluate the FSI effects.

#### 4. EXPERIMENTAL RESULTS AND DISCUSSION

Impact testing was conducted for both dry and wet composite plates. The mass of the free falling object was 12 Kg which was dropped from the height 1.07 m. In order to confirm the repeatability of the impact test data, every test condition was repeated several times for the same composite plate. The measured force and strain data were very close one another. This fact confirmed not only repeatability but also no damage in the specimen. If damage occurred and accumulated in the composite plate, repeated testing would show different results with the damage. Figure 5 compares the two force data curves under the same dry impact condition. Other force data, which

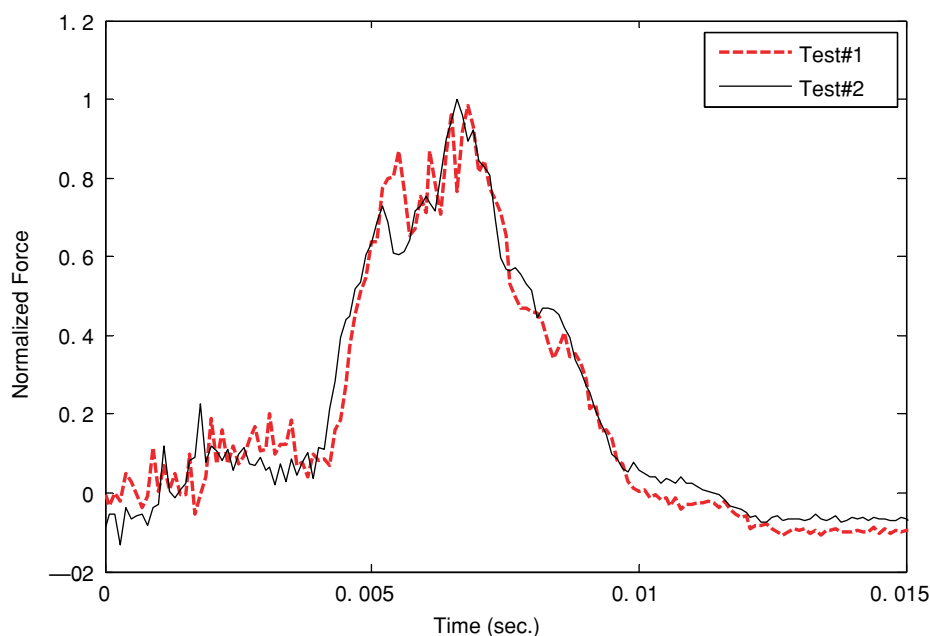


Figure 5. Comparison of dry impact forces under the same impact condition.

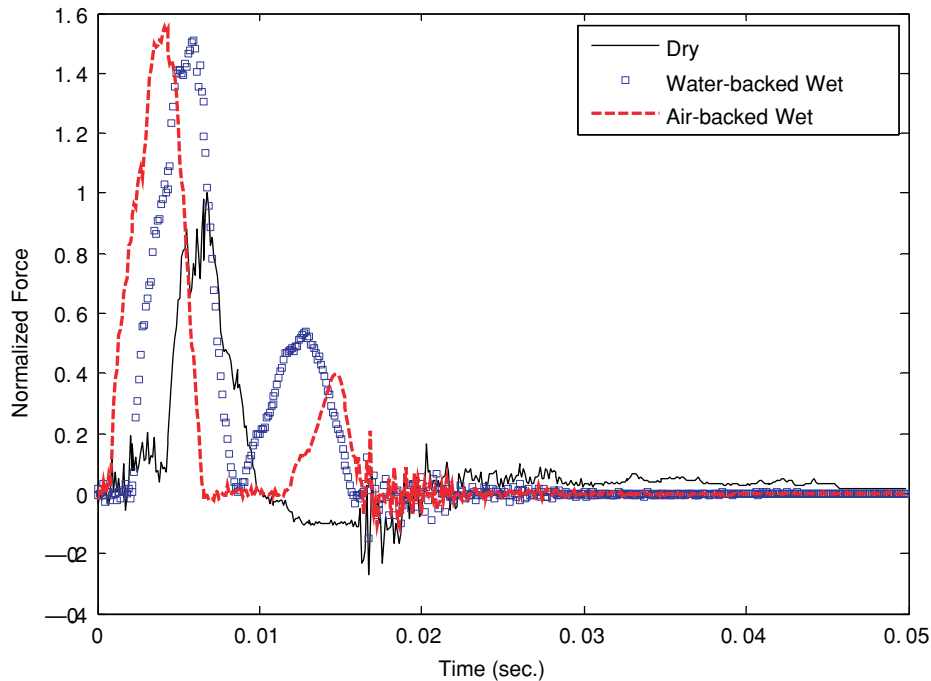


Figure 6. Comparison of impact forces among dry, water-backed and air-backed wet impact cases.

were not plotted here to avoid crowding, are very close to the graphs shown in the figure. In all figures unless otherwise mentioned, the force or strain plots were normalized in terms of the dry impact data so that the effects of FSI could be better represented in the plots.

The impact force is compared in Fig. 6 for the dry impact as well as the water-backed and air-backed wet impact cases. As shown in this figure, the air-backed and water-backed wet impacts yielded 55% and 50% greater impact force than the dry case, respectively. The larger wet impact forces were caused by the hydrodynamic added mass effect. Because the density of the composite plate is only 60% greater than that of water, the plate with the added mass moves with a much slower velocity. As the plate moves more slowly, the contact force between the impactor and the plate becomes larger, which is recorded to the force gage. In order to support this argument, a series of finite element analyses were conducted. In the numerical study, the same composite plate was subjected to an impact loading condition with the same impactor mass and velocity as in the air experiment. However, the impact rod and the spring were not considered in the model in order to simplify the numerical model. The peak impact force was obtained from the analysis. Then, the mass density of the composite plate was increased uniformly over the plate by 50% or 100%, respectively, while all other conditions including the plate stiffness and impact condition remained the same. The increase of the mass density was to represent the added mass effect with wet impact. The real added mass would be non-uniform over the plate. However, since the actual distribution was not known a priori, a uniform distribution of added mass was considered in the finite element analysis. The analyses showed that as the composite mass increased by 50% or 100%, the peak impact force increased to 20% or 30% when compared to that with the original mass. Because the wet structure certainly does not have a uniform added mass effect, the actual

increase of the peak force in the experiment was different from the finite element analysis results. However, the analyses support the experimental results qualitatively as stated previously.

Both wet impact forces have steep monotonic increases to their peak values just after the impactor hit the plates while the dry impact force shows an initial low plateau before it moves steeply to its peak value. Because the impactor was not held after the initial impact, it rebounded and landed again. As a result, both wet impacts showed secondary peak forces. However, the dry impact did not have the secondary contact. In particular, the air-backed wet impact case gave a quite a delay between the initial and secondary impact forces while the water-backed wet impact case showed the secondary force occurring just after the initial one.

The reason that the air impact test did not produce the secondary impact was due to the spring in the impact test machine. The spring supports the impact rod, which will hit the composite plate, a small distance above the plate initially before the impact loading. As the impact weight drops and hits the impact rod, the latter moves down with compression of the spring to hit the composite plate. For the air impact case, the initial impact force was lower than that for wet impact cases. Therefore, the rebounding and landing force from the air impact was not large enough to overcome the spring force so that the rod could not hit the plate again.

Because strain gage location #1 lies directly underneath the impact site of the composite plate, the strains contain many higher frequency components compared to strains at other locations. A comparison of Fig. 6 to Fig. 7 shows that the peak values of impact forces and strains at position #1 occur simultaneously. Strains under wet impacts are more than double the dry impact strain at location #1. This ratio of peak strains between the wet and dry impacts is even greater than that of the impact forces.

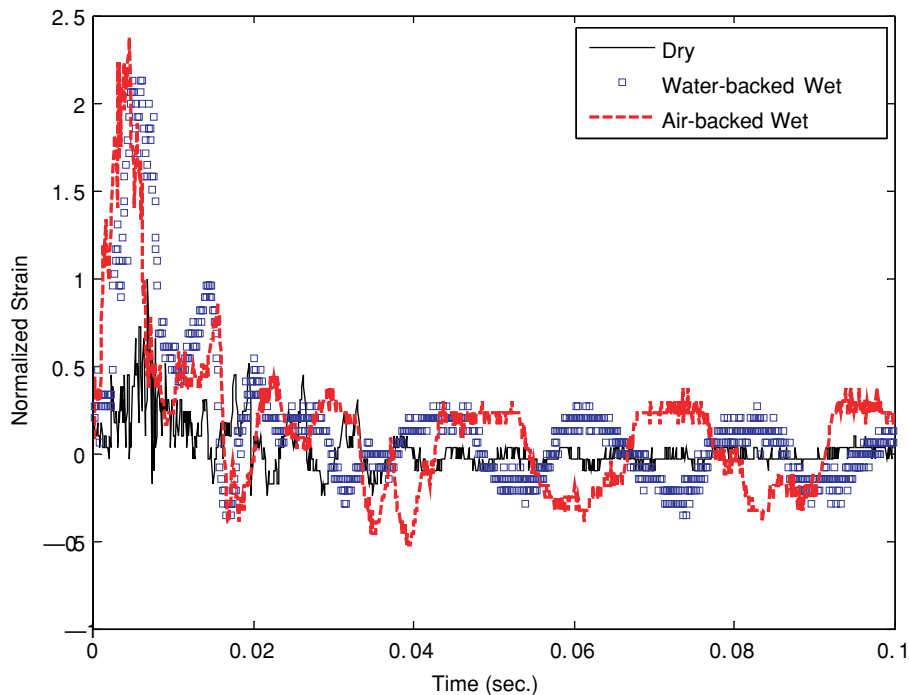
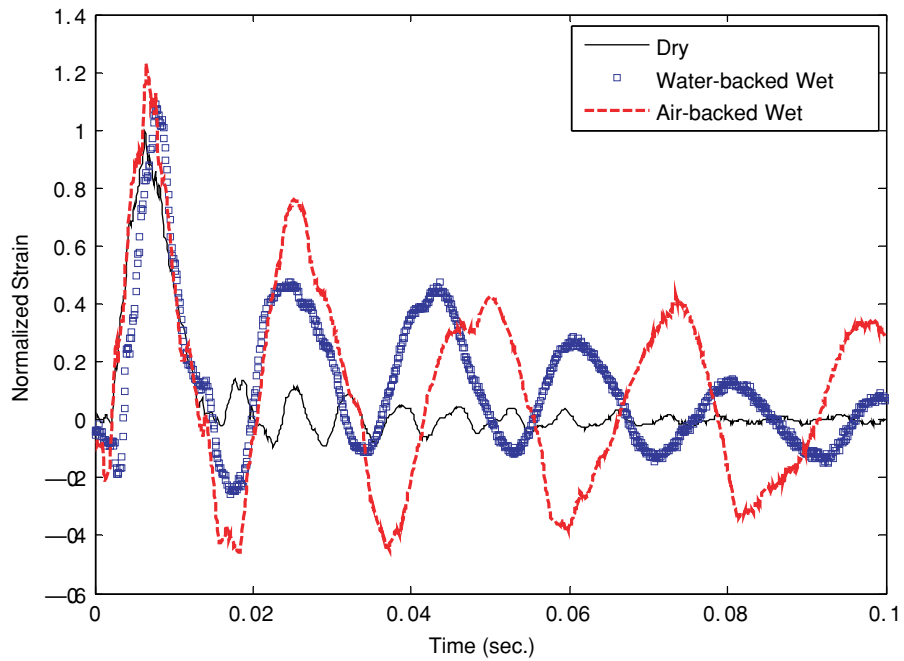
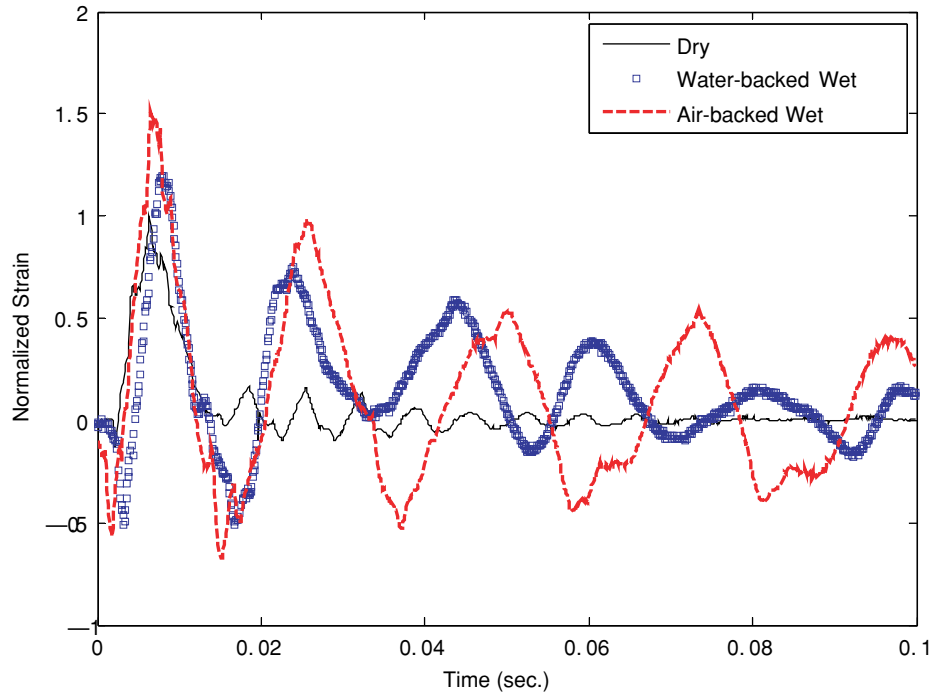


Figure 7. Comparison of strains along x-axis at position #1 among dry, water-backed and air-backed wet impact cases.



(a) Strain along x-axis



(b) Strain along y-axis

Figure 8. Comparison of strains at position #2 among dry, water-backed and air-backed wet impact cases.

The differences between the wet and dry impact strains were smaller at gage location #2 than those at location #1. The strains under the air-backed wet impact were 20% and 50% greater than the dry impact strains along the  $x$ -axis and  $y$ -axis, respectively, as shown in Fig. 8. On the other hand, the water-backed impact resulted in 10% and 20% greater strains in the  $x$ -axis and  $y$ -axis, respectively, than the dry impact. The gage location #2 is closer to the clamped boundary in the  $y$ -axis direction. Thus, this suggests that the clamped boundary resulted in a greater FSI effect on the composite plate. Both wet impact strains showed initial compressive strains before much larger tensile strains. Furthermore, these strain measurements show a clear difference among the response frequencies due to the added mass effect. Comparing the wet impact responses to the dry impact response, the response frequencies under the wet impacts are less than a half of the dry impact response frequency. Such a drastic reduction is caused by the light composite structure which is only about 1.6 times as heavy as the water in terms of density. The response frequency is higher for the water-backed wet impact case than for the air-backed wet impact case by approximately 20%. This is an interesting result because the water-backed wet structure was expected to have a greater added mass effect with a lower response frequency. However, as was expected, the decay of the strain peak values was greater for the water-backed wet impact case than the air-backed case. For example, the average damping ratio was 0.053, 0.062, and 0.11 for the dry, air-backed, and water-backed impact cases, respectively. This means the damping effect is greatest for the water-backed case.

Calculation of the Added Virtual Mass Incremental Factor (AVMIF),  $\beta$  from Eq. (1) given below, yields approximately 6.5 and 11.5 for the water-backed and air-backed wet composite plates, respectively.

$$\frac{\omega_w}{\omega_d} = \frac{1}{\sqrt{1+\beta}} \quad (1)$$

where  $\omega$  is the frequency and subscripts  $w$  and  $d$  denote the wet and dry cases, respectively. AVMIF represents the ratio of the kinetic energy of the water to that of the composite plate. The AVMIF for steel submerged in water ranges from 1.4 to 2.4 depending on the boundary conditions [8, 11]. Comparison of AVMIF between the composite and steel shows clearly a much larger effect of FSI on the composite than steel.

As seen in Fig. 9, the strain gage readings at gage location #3 have similar response characteristics as observed in the gage at location #2. Both air-backed and water-backed wet impacts resulted in 30% greater strains in  $x$ -axis than the dry impact. Because the gage location #3 is on the diagonal direction, strains in the  $y$ -axis were very close to those in the  $x$ -axis.

The effect of FSI is very significant for the strain gage reading at location #4, as shown in Fig. 10, and the strain readings were much less harmonic with more constraint effects from the clamped boundaries of the plate. First of all, both wet impact cases resulted in very large initial compressive strains compared to the dry impact case. The initial compressive strains were due to the clamped boundary conditions. After following the initial large compression, the air-backed wet impact case shows another large tensile strain while the water-backed case has a modest magnitude of tensile strain. The water on the backside of the water-backed composite plate seems to prevent further tensile strain at this gage location. The magnitudes of the strains at the gage location #4 are 4 to 5 times higher for the wet impact cases.



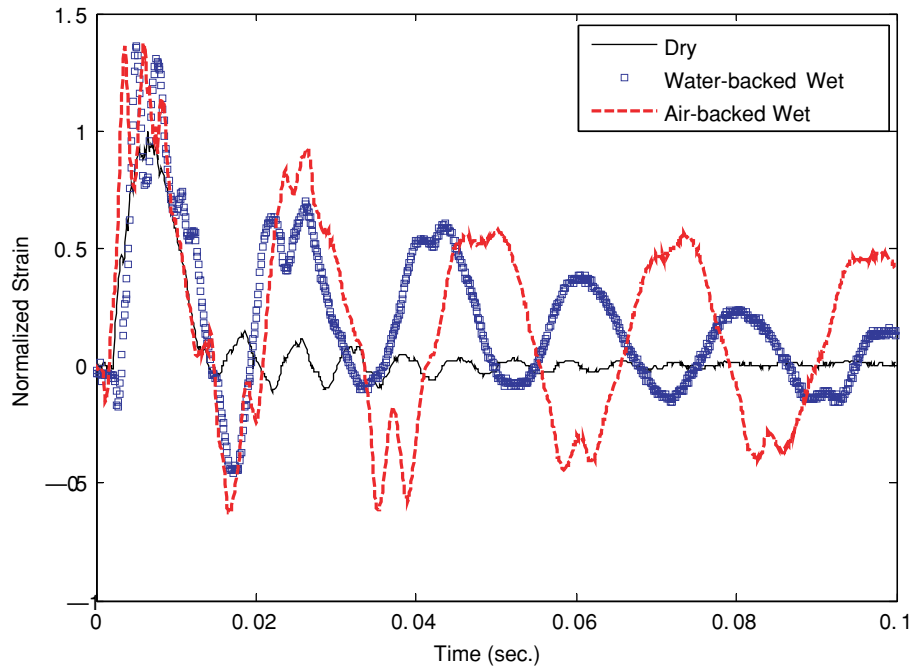


Figure 9. Comparison of x-strains at position #3 among dry, water-backed and air-backed wet impact cases

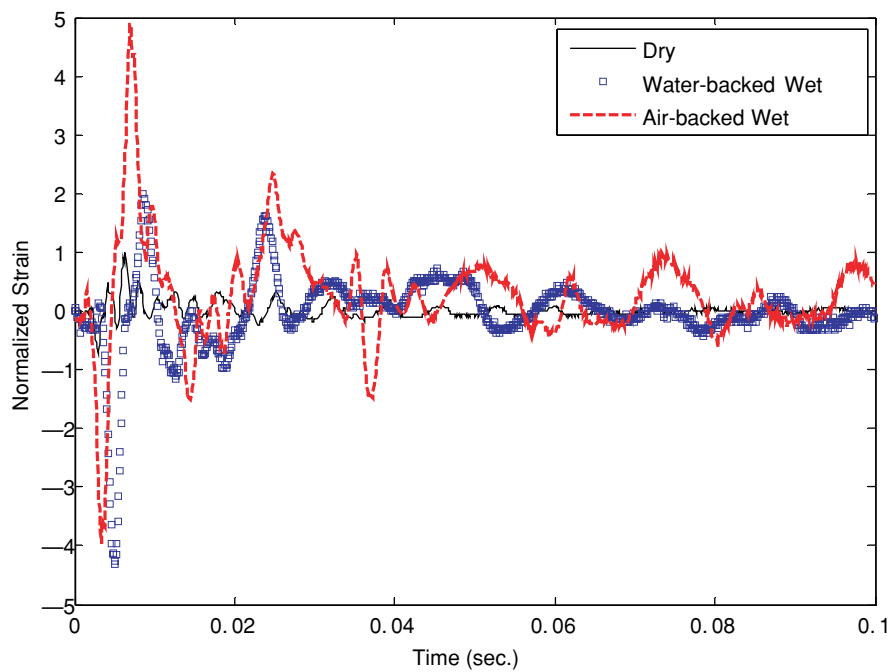


Figure 10. Comparison of x-strains at position #4 among dry, water-backed and air-backed wet impact cases.



## 5. CONCLUSIONS

An experimental set-up was designed and fabricated for impact testing on composite plates submerged in water. In order to investigate the transient dynamic response of composite plates with FSI effects under impact loading; three impact conditions, dry, air-backed wet, and water-backed wet impact conditions were considered, respectively. In order to focus on the FSI effects on the transient dynamic responses, impact loading was controlled not to cause any damage to the composite plates. Since the composite material has a very comparable density to water, the FSI effects were very significant on the impact force and transient responses of the plates. Due to the added mass effect of water, the impact force was much greater for the wet impact cases than in the dry impact. Similarly, wet impact produced much greater transient strains on the composite plates. As a result, the wet impact was more detrimental to the structure than the dry impact. However, the increase of magnitude of transient strain responses resulting from the FSI with wet impacts varied significantly depending on the location of the composite plate because the added mass effect was not uniform over the plate. The location near to the clamped boundary corner had generally a greater FSI effect on the transient strain response. This suggests that very careful evaluation is necessary for design and analysis of composite structures for underwater application subjected to transient dynamic loading. Finally, comparison of AVMIF between the composite and steel shows approximately 3 to 5 time greater values for composites than steel, which indicates a much greater effect of FSI on the composite than steel.

## ACKNOWLEDGEMENT

This work was conducted through a grant from the ONR Solid Mechanics Program. Dr. Yapa Rajapakse was the program manager.

## REFERENCES

- [1] A.P. Mouritz, E. Gellert, P. Burchill, K. Challis, Review of Advanced Composite Structures for Naval Ships and Submarines, *Composite Structures* 53 (2001) 21–41.
- [2] Z. Aslan, R. Karakuzu, B. Okutan, The Response of Laminated Composite Plates Under Low-Velocity Impact Loading, *Composites Structures* 59 (2003) 119–127.
- [3] S. Abrate, Impact on Laminated Composites; Recent Advances, *Applied Mechanics Reviews* 47 (11) (1994) 517–544.
- [4] H. Lamb, On the vibrations of an elastic plate in contact with water, *Proceeding of the Royal Society (London)* A 98 (1921) 205–216.
- [5] J.H. Powell, J.H.T. Roberts, On the frequency of vibration of circular diaphragms, *Proceeding of the Royal Society (London)* 35 (1923) 170–182.
- [6] U.S. Lindholm, D.D. Kana, W.H. Chu, et al., Elastic vibration characteristics of cantilever plates in water, *Journal Ship Research* 9 (1) (1965) 11–22.
- [7] G.C. Volcy, P. Morel, M. Bureau, et al, Some studies and research related to the hydro-elasticity of steel work, *Proceedings of the 122<sup>nd</sup> Euromech Colloquium on numerical analysis of the dynamics of ship structures*, (1979) 403–406.
- [8] Y. Fu, W.G. Price, Interactions between a partially or totally immersed vibrating cantilever plate and the surrounding fluid, *Journal of Sound and Vibration* 118 (3) (1987) 495–513.
- [9] M. K. Kwak, K.C. Kim, Axisymmetric vibration of circular plates in contact with fluid, *Journal of Sound and Vibration* 146 (1991) 381–389.
- [10] M. K. Kwak, Hydroelastic vibration of rectangular plates, *Journal of Applied Mechanics* 63 (1996) 110–115.
- [11] M.R. Haddara, S. Cao, A study of the dynamic response of submerged rectangular flat plates, *Marine Structures* 9 (1996) 913–933.



# *Transient Dynamic Response and Failure of Sandwich Composite Structures under Impact Loading with Fluid Structure Interaction*

**Y. W. Kwon, M. A. Violette,  
R. D. McCrillis & J. M. Didoszak**

## **Applied Composite Materials**

An International Journal for the Science  
and Application of Composite Materials

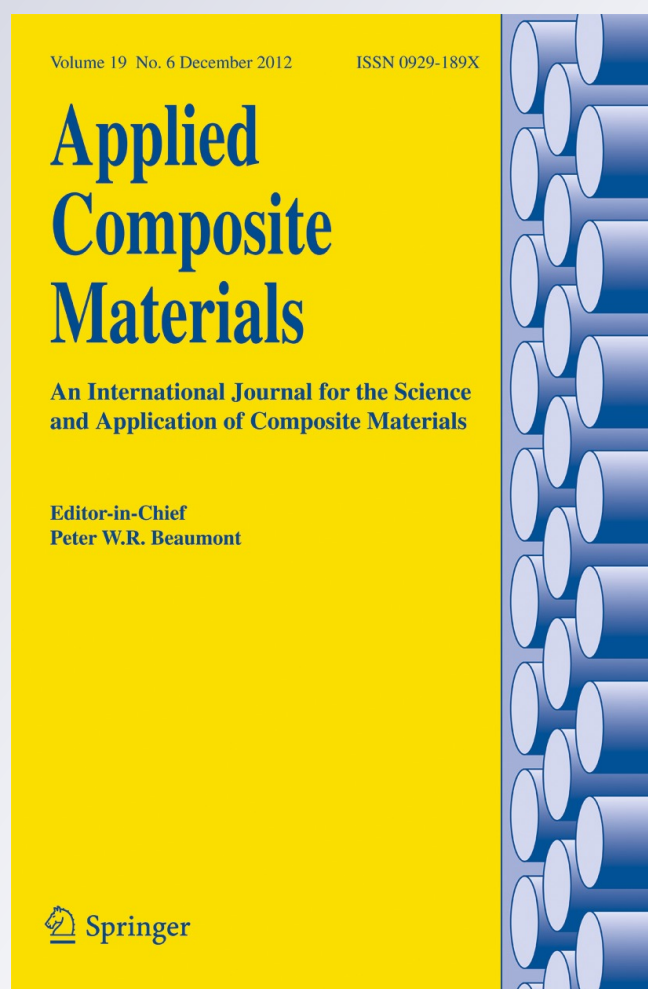
ISSN 0929-189X

Volume 19

Number 6

Appl Compos Mater (2012) 19:921-940

DOI 10.1007/s10443-012-9249-8



**Your article is protected by copyright and all rights are held exclusively by Springer Science+Business Media B.V. (outside the USA). This e-offprint is for personal use only and shall not be self-archived in electronic repositories. If you wish to self-archive your work, please use the accepted author's version for posting to your own website or your institution's repository. You may further deposit the accepted author's version on a funder's repository at a funder's request, provided it is not made publicly available until 12 months after publication.**

# Transient Dynamic Response and Failure of Sandwich Composite Structures under Impact Loading with Fluid Structure Interaction

Y. W. Kwon · M. A. Violette · R. D. McCrillis ·  
J. M. Didoszak

Received: 18 October 2011 / Accepted: 18 January 2012 / Published online: 8 February 2012  
© Springer Science+Business Media B.V. (outside the USA) 2012

**Abstract** The objective of this study is to examine the Fluid Structure Interaction (FSI) effect on transient dynamic response and failure of sandwich composite structures under impact loading. The primary sandwich composite used in this study consisted of a 6.35 mm balsa core and a multi-ply symmetrical plain weave 6 oz E-glass skin. Both clamped sandwich composite plates and beams were studied using a uniquely designed vertical drop-weight testing machine. There were three impact conditions on which these experiments focused. The first of these conditions was completely dry (or air surrounded) testing. The second condition was completely water submerged. The final condition was also a water submerged test with air support at the backside of the plates. The tests were conducted sequentially, progressing from a low to high drop height to determine the onset and spread of damage to the sandwich composite when impacted with the test machine. The study showed the FSI effect on sandwich composite structures is very critical such that impact force, strain response, and damage size are generally much greater with FSI under the same impact condition. As a result, damage initiates at much lower impact energy conditions with the effect of FSI. Neglecting to account for FSI effects on sandwich composite structures results in very non-conservative analysis and design. Additionally, it was observed that the damage location changed for sandwich composite beams with the effect of FSI.

**Keywords** Fluid–structure interaction · Sandwich composites · Damage · Impact

## 1 Introduction

The use of composite materials in fabrication is traced as far back as ancient Egyptian times in their use of straw and bricks or more recently with the introduction of steel bar reinforced concrete in the 1850's. The sought after goal in either of these applications is increased strength properties of a structure without the customary weight penalty. In the post industrial

---

Y. W. Kwon (✉) · M. A. Violette · R. D. McCrillis · J. M. Didoszak  
Department of Mechanical & Aerospace Engineering, Naval Postgraduate School, Monterey, CA 93943,  
USA  
e-mail: ywkwon@nps.edu

revolution era, the modern era of composite use began around World War II. Since that time the research and use of composite materials grew rather modestly until a rapid rise in the 1990's and into the early 2000's [1].

The aerospace industry, in particular, has been very aggressive in its use of composites in its most critical applications when compared to other industries. NASA's Jet Propulsion Laboratory at the California Institute of Technology lists structural laminate composites as one of their preferred practices for the recently retired Space Shuttle program. Among the chief reasons for the use of composites is the high strength to weight ratio [2].

The maritime defense industry is seeking to follow the aerospace example and has been using composites in naval construction since the post-World War II era. Previously, the use of composites was primarily limited to component structures or smaller patrol craft. However the last decade has significantly changed the paradigm such that the marine industry has started to build military ships using all-composite construction as demonstrated in European military ships reaching up to 90 m in length [1]. The U.S. Navy has recently been making significant strides in the use of composites in critical combat hardware as well. The first major example aboard a U.S. Navy combatant was the Advanced Enclosed Mast used aboard the *USS Arthur W. Radford (DD 968)* [3]. The *Radford* mast was fully enclosed and constructed entirely of composites. This innovative proof of concept subsequently led to the design currently used in the LPD-17 *San Antonio* class amphibious docking ships [4]. Looking ahead and building on the successes of *Radford* and the LPD 17 class, the Navy has begun construction on the next-generation destroyer: the DDG-1000 *Zumwalt* class. The *Zumwalt* class will include a seven-story superstructure composed almost entirely of composite materials, manufactured using the resin transfer technique primarily with carbon fiber/vinyl ester skins and balsa wood and/or foam cores, thus creating a "sandwich" composite.

What is the advantage of using products like wood in a ship's construction? The idea of using balsa wood is more advanced than the construction of the Navy's only other in service wooden ship, the now ceremonial, *USS Constitution*. The balsa wood core takes advantage of favorable strength to weight ratios gaining its strength from the reinforcing carbon fiber skins. In addition to the strength to weight advantages, the sandwich composite provides an ability to simplify tooling in construction, reduce corrosion, and reduces the ship's radar cross section [4]. The reduced radar cross section makes the ship significantly stealthier, while the other composite attributes allow for increased range and payload. The maintenance costs are also likely to be reduced over the lifecycle as a result of reduced manufacturing costs and required preventive and corrective maintenance requirements, which in turn decrease the number of crewmembers needed to maintain the ship. Advances have also been made in rudder construction using the same composite technology that may help reduce cavitation, resulting in reduced stresses on the ship's rudders [5].

One of the concerns in the design of composite structures is impact failure. Impact damage is a serious design concern because composite structures are more susceptible to impact damage than similar metallic structures. Not only are they typically not as hard, but they also lack the ductility that allows metallic structures to absorb large amounts of energy without failure [6]. In addition, the damage in composites from impact can go undetected, even when the mechanical properties may be drastically reduced by impact damage. For these reasons, numerous experimental and analytical studies have been conducted to examine the dynamic response of composites subjected to impact loading. As a result, there has been extensive research investigating damage initiation and growth as well as various damage modes occurring in laminated and sandwich composite structures under impact loading. Because of vast number of publications on the topic, there was no attempt to review and list them all here. A select group of these are listed in Refs. [6–10]. The predominance of

the research has been focused on low velocity impact damage, and concentrates on damage prediction and evaluation of residual properties of damaged laminates. The aforementioned research primarily considered composites under low velocity impact in dry surroundings, mainly to support development of composites for aircraft structures. However, recently some new work has started looking at fully coupled fluid–structure interaction with composites under low velocity impact [11–13].

A previous study [11, 13] showed, from both experimental and numerical results, that the impact force resulting from the same impact loading condition was much larger when the carbon-fiber composite plate was under the water than in air. The test was conducted without causing damage to the composite plate so that the dynamic response without failure could be compared between the submerged and dry structures. The greater impact force on the submerged plate was determined to be due to an added mass effect, since the carbon-fiber composite plate was only slightly denser than the water. For a sandwich composite structure, the core material is less dense than water, suggesting that added mass would have an even more profound effect on the dynamic response.

Because composites are being used more and more frequently in underwater structures such as in submarine sails, sonar domes, rudders, and even propellers, as well as hull skin and structure, there is a need to understand composite characteristics in order to successfully design such structures [14]. This is especially true in sandwich composites which have been used increasingly because of their tactical and structural benefits for naval ships. Therefore, the objective of this study was to examine the transient dynamic response and progressive failure of sandwich composite structures under impact loading while the structures interacted with the surrounding water. This study considered dry impact (i.e. structure surrounded by air) and wet impact (i.e. structure surrounded by water) and compared their responses. For the wet impact cases, both air-backed and water-backed structures were examined as shown in Fig. 1.

The following section describes the preparation of the sandwich composite samples and the experimental technique. Results for both sandwich plates and beams are presented. A discussion of the results and conclusions follow.

## 2 Sandwich Composite Preparation and Testing

### 2.1 Material Selection and Properties

The skin material for this study was 5.8 oz/square yard non-biased plain weave E-glass cloth. All plies were laid in  $0^\circ$  and  $90^\circ$  directions, respectively, so that 50% of the fibers were

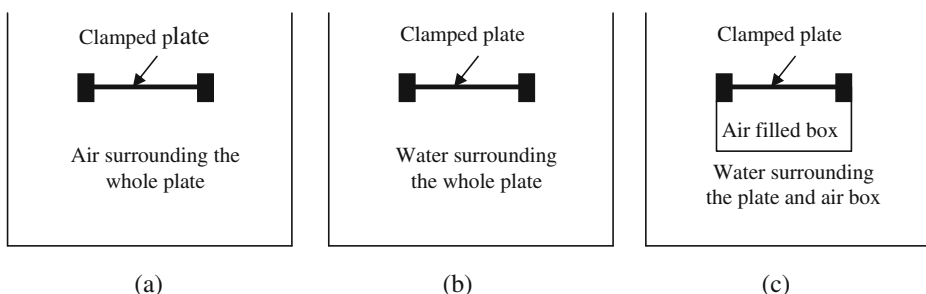


**Fig. 1** Three different impact conditions: **a** dry impact, **b** water-backed wet impact, **c** air-backed wet-impact



oriented along the length of the coupon with the other 50% oriented across the coupon. E-glass was selected because it is translucent, making damage analysis easier.

The selected core material is ProBalsa Plus, an industrial core material from DIAB with a density of  $155 \text{ kg/m}^3$  [15]. ProBalsa Plus is micro sanded and treated with a special coating to reduce resin absorption. End grain balsa core material is composed of square sections of cross cut balsa glued together much like a butcher block as shown in Fig. 2. With the grain oriented vertically, the cellular structure of the balsa wood is often characterized as micro honeycomb structure. This structure has very good properties in both compression and shear. Furthermore, because it is a naturally occurring, rapidly renewable resource, it is relatively inexpensive. This ideal core material is very popular in the maritime industry, and in fact is used in many naval applications.

## 2.2 Fabrication of Test Coupons

The sandwich composite test panels were constructed to match, as closely as possible, the industry standard used in current marine construction. The test panels were constructed using a Vacuum Assisted Resin Transfer Molding (VARTM) process. Each sandwich composite consists of a 6.35 mm end grain balsa core with each skin consisting of five layers of E-glass woven fabrics. The material and chemical requirements necessary to mimic standard maritime construction techniques consisted of Derakane 510A vinyl ester resin, Methyl Ethyl Ketone Peroxide (MEKP), Cobalt Naphthenate (CoNap), Ndimthylaniline (DMA), and 5.8 oz/square yard plain weave E-glass cloth. Derakane 510A was used as the base matrix resin throughout the project. MEKP, CoNap, and DMA were used as hardening and accelerating agents, with amounts varied to achieve the desired gel time of 45 min. Normal ambient temperature in the lab remained between  $17^\circ \text{C}$  and  $20^\circ \text{C}$ . To achieve a gel time of approximately 45 min, the ratios in Table 1 were followed.

Once the proper procedure for composite construction was identified, the procedure was standardized to ensure each test sample was constructed in the same fashion. Coupons were cut with a high quality laminate blade on a table. The plate samples had a test section of  $30.48 \text{ cm} \times 30.48 \text{ cm}$ . Each plate sample was cut much larger than the test section so that all edges of the plate could be properly clamped. The beam coupons used for impact testing were  $45.72 \text{ cm} \times 2.54 \text{ cm}$  for a  $30.48 \text{ cm}$  test span. All sides of every coupon where core is exposed were waxed with mold release wax to inhibit water intrusion into the core when the

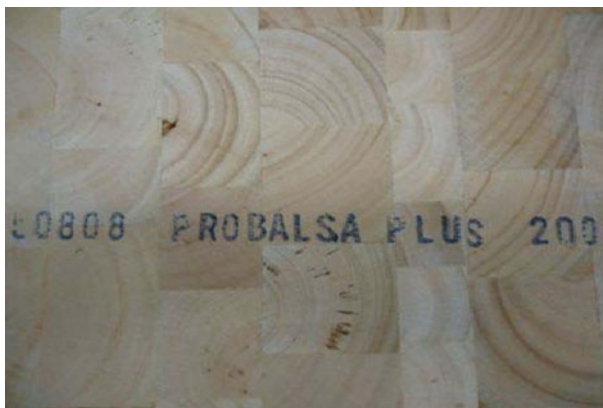


**Fig. 2** Balsa core layer made like a “butcher block”



**Table 1** Resin matrix composition by volume

Component	Amount
DERAKANE 510-A	1000 mL
Methyl Ethyl Ketone Peroxide (MEKP)	12.5 mL
Cobalt Napthenate (CoNAP)	3.0 mL
N, N- Dimethylaniline (DMA)	0.5 mL

coupons were submerged in water. For the sandwich plates 45° strain gage rosettes were attached at the opposite side of the impact location as shown in Fig. 3.

### 2.3 Testing Equipment

Impact tests were conducted using a specially designed drop weight testing system, described in Ref. [11, 13] and as seen in Fig. 4. It consisted of a drop weight impactor, load transducer, strain gages, high speed data analyzer. The machine was adjusted slightly to decrease the gap between the force gage and the specimen in order to achieve greater throw and ensure specimen failure. A force gage with an axial connector was also fitted to the machine to prevent connector damage in the event that the force gage penetrated the specimen. Because the force gage was attached to the impactor, the gage was in direct contact with the composite specimens during impact. The force gage has a cylindrical shape with a diameter of 12.7 mm. C-clamps were used to facilitate clamped boundary conditions in both the plate and beam specimens. Transient response of the sample included force and strain as a function of time.

During testing, the impact tower was lowered into an anechoic water tank that was filled with water, so that the submerged samples were below the free surface. Then, impact was applied to the specimen. This is called wet impact. For the wet impact, two cases were

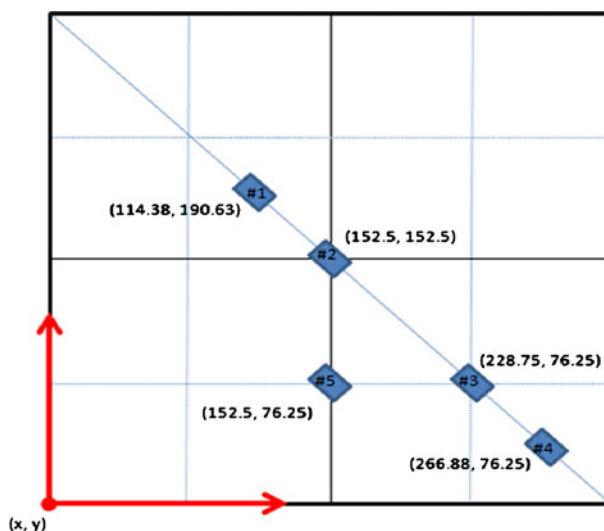


**Fig. 3** Strain gage locations on the opposite side of the impact. (The unit for the coordinate values is mm. Each strain gage is a 45° rosette)

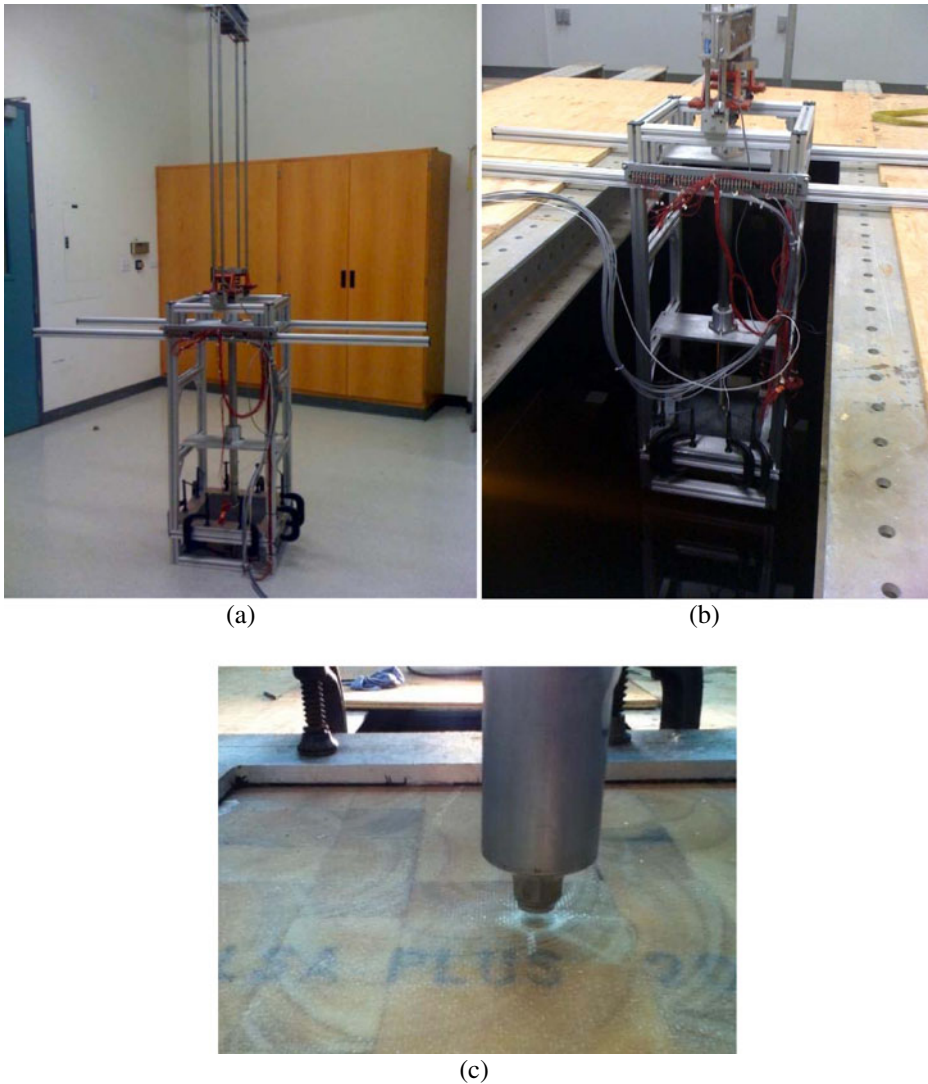


**Fig. 4** Picture **a** shows impact machine on floor, picture **b** shows the same impact machine lowered into an anechoic water tank, and picture **c** shows the impactor head

considered as sketched in Fig. 1. One version of the wet test plates had an air-filled bucket attached to the bottom. This was called the air-backed wet impact. The other wet test samples were exposed to water on both the top and bottom sides of the plates. These were called water-backed wet impact. Dry testing took place with the tower in the same position, but with the water drained out of the tank. This is called dry impact.

The load cell was an ICP<sup>®</sup> force sensor manufactured by PCB Piezotronics, Inc. The load transducer was mounted on the end of the impactor rod. The gage had a diameter of 1.6 cm. In order to increase longevity in an aqueous environment, both the gage and cable connection were coated with M-Coat A bond. Additional waterproofing was provided by a thin latex sleeve fitted over the end of the impacting rod.

Data acquisition was carried out using a specifically developed acquisition system that consisted of a Pentium™ 4, 2.4 GHz, 512-MB RAM system, National Instruments™ simultaneous sampling multifunction DAQ, and five Vishay™ 2120 multi-channel strain signal conditioners. The system had a 16 bit analog-to-digital conversion resolution and was capable of reading a total of 16 channels at a throughput rate of up to 250 kS/s per channel. Data was recorded at 10,000 Hz for 100 milliseconds each time the trigger was activated. The data-acquisition process was controlled using NI-DAQmx driver software and Lab-VIEW™ interactive data-logging. A trigger located on the drop weight was used to initiate data acquisition.

### 3 Results of Sandwich Plates

#### 3.1 Results Without Damage

First of all, in order to compare transient dynamic response of a sandwich composite plate without damage under three different impact conditions (dry, air-backed wet, and water-backed wet impacts), the same sandwich composite plate was tested for all three conditions. By doing so, a fair comparison could be made without worrying about a variation of the test sample from one to another. Low impact energy was used to avoid any damage. The impact height was 7.62 cm and the impact mass was 6.7 Kg, which is equivalent to the initial impact energy 5.01 J. Using the same impact mass, the initial impact energy is proportional to the impact height. As a result, most of the results from now on are discussed in terms of the impact height.

Because E-glass skin layers are translucent, the sandwich plate was examined visually for any damage after each impact test. For consistency, the plate was tested multiple times for the same impact condition. If there was damage, the response would be different from one test to another. However, the test results were quite the same.

Figure 5 compares the impact force-time history of the sandwich plate without damage under three different impact conditions. Because the data acquisition system was activated before the initiation of impact, the impact force and strain response did not start at time zero in all plots. As shown in Fig. 5, there is a distinct difference in the impact force response

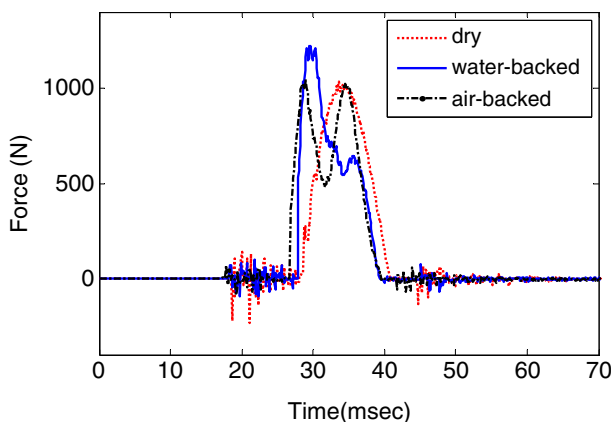


**Fig. 5** Comparison of impact force-time histories among three impact cases without damage

under the three different impact conditions. The dry impact resulted in a half sine shape with a single peak while both wet impacts yielded double peaks. The water-backed wet impact has the largest first peak followed by the relatively smaller second peak while the air-backed wet impact has equal magnitudes of double peaks. In terms of the magnitude of the maximum peak forces, the water-backed wet impact has the largest value while the other two have similar magnitude. Comparing the present results with those obtained for the carbon-fiber laminated composite plate [10, 13], they show consistent findings. Both the wet impact cases yielded double peaks in the impact forces while dry impact resulted in only a single peak. Since the carbon-fiber laminated composite is much stronger than the present E-glass/balsa sandwich composite, much greater impact energy could be applied to the carbon fiber plate without causing any damage while the impact energy level was varied. The results indicated that the larger the applied impact energy, the greater the difference in the peak forces between dry and wet impacts.

The reason why the wet impact resulted in a greater impact force is the hydrodynamic mass, also called added mass, resulting from the FSI between the sandwich composite plate and the surrounding water. The added mass effect makes the sandwich plate moves slower in water than in air. As the plate moves slowly, the contact force between the force gage and the plate becomes larger. Comparing the added mass effect on the present sandwich plate to the carbon-fiber composite, the effect was greater for the sandwich plate because the density of the sandwich plate is lower than that of the carbon-fiber composite. As a result, the sandwich plate had a greater ratio of peak force between wet and dry impacts than the carbon fiber plate even though the former was subjected to lower impact energy. On the other hand, wet impact is considered to result in a change of vibrational modes when compared to that for the dry impact. The strain gage measurements partially illustrate that. This will be further explained in a future study.

The strain-time history was measured at the gage location as shown in Fig. 3. The strain gage rosettes were attached to the sandwich plate surface opposite to the impact side. The strains along the y-axis at gage locations #1 through #4 have similar characteristics as those along the x-axis, even though their magnitudes are different. The reason for the difference is the non-isotropic core balsa material as shown in Fig. 2. As a result, only x-strains are discussed here.

Figure 6 shows the comparison of three strain-history plots at the center of the sandwich plate along the x-axis shown in Fig. 3. The strain gage is located along the line of impact

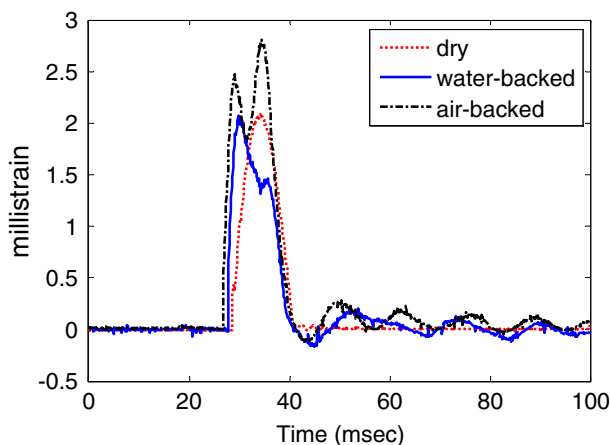


**Fig. 6** Comparison of impact strain-time histories among three impact cases without damage at the gage location #2 of Fig. 3 along the x-axis

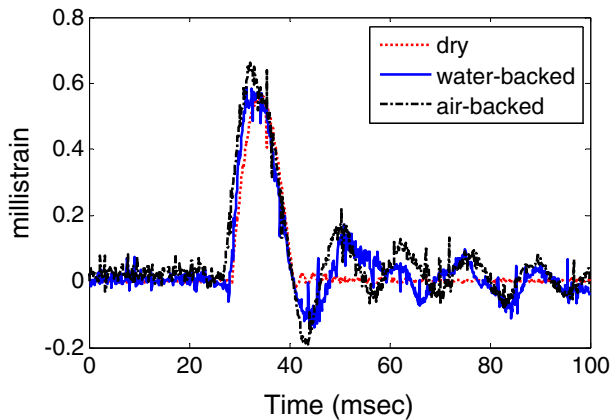


**Fig. 7** Comparison of impact strain-time histories among three impact cases without damage at the gage location #1 of Fig. 3 along the x-axis

force and on the opposite side of the impact. As a result, the shapes of strain-time histories are very similar to the force-time history as seen in Fig. 5. Wet impact resulted in double peaks while dry impact yielded only a single peak. However, one thing to be noted is that the air-backed wet impact shows the largest peak strain even though the impact force is largest for the water-backed wet impact. It seems to be related to the change of vibrational mode shape of the sandwich plate as influenced by the surrounding water and/or air media.

Strain responses at gage location #1 are close among the three impact tests while the air-backed water impact resulted in a slightly greater strain than the others as shown in Fig. 7. This suggests that the FSI effect is minimal at this location. However, Fig. 7 shows the change of vibrational frequency with FSI. Figures 8 and 9 show the strain-time histories at gage locations #3 and #4 of Fig. 3, respectively. These figures clearly indicate the strains under wet impact are much greater than those under dry impact. Among these, the water-backed wet impact yielded the largest strain at the gage location #4.

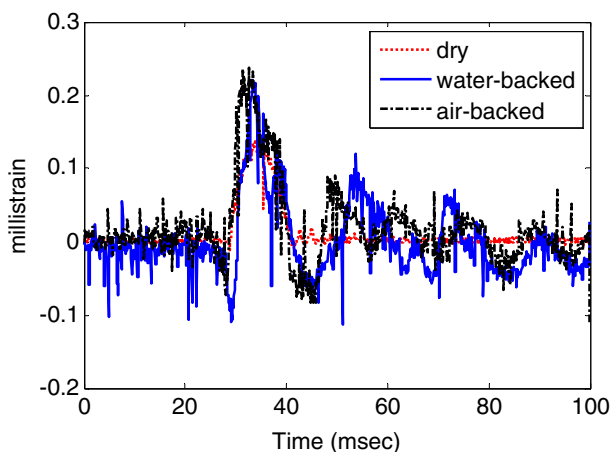


**Fig. 8** Comparison of impact strain-time histories among three impact cases without damage at the gage location #3 of Fig. 3 along the x-axis

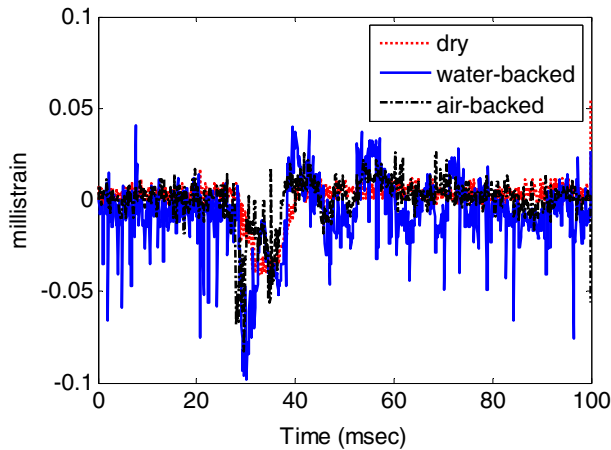


**Fig. 9** Comparison of impact strain-time histories among three impact cases without damage at the gage location #4 of Fig. 3 along the x-axis

The largest difference between the wet and dry impact is shown at the gage location #5 as shown in Fig. 10. Both wet impacts gave multiple times greater strains than did the dry impact at this location. The water-backed wet impact has the largest strain among all. Both wet impacts show large initial compressive strains followed by lesser magnitude tensile strains while the dry impact shows a much smaller initial compression followed by negligible tension. Figures 7 and 8 also exhibit such a sign change in the strain response associated with FSI. The initial compressive strains are considered to be influenced by the clamped boundary edges. Those results suggest that the vibrational mode shapes under wet impacts are different from that under dry impact. Otherwise, dry and wet impact would result in similar shapes of strain responses while only differing in terms of magnitude and frequency.

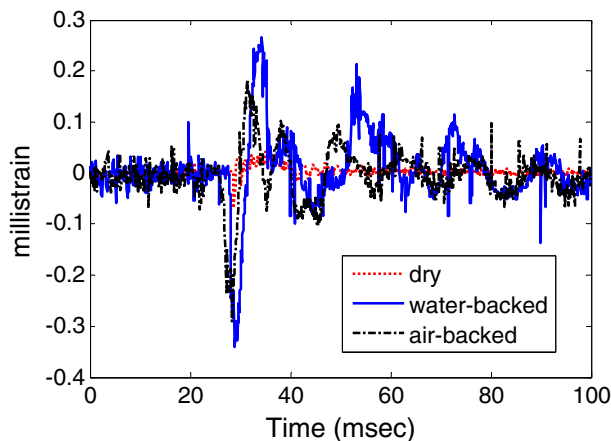


**Fig. 10** Comparison of impact strain-time histories among three impact cases without damage at the gage location #5 of Fig. 3 along the x-axis

**Table 2** Comparison of impact height and peak impact force at the onset of initial delamination

Sample No.	Impact height (cm)	Impact velocity (m/s)	Impact Force (N)
Dry Impact #1	25.4	2.23	1866
Dry Impact #2	20.3	2.00	1614
Dry Impact #3	20.3	2.00	2336
Average Dry Impact	22.0	2.08	1939
Water-backed Impact #1	20.3	2.00	1279
Water-backed Impact #2	15.2	1.73	1473
Water-backed Impact #3	15.2	1.73	1557
Average Water-backed Impact	16.9	1.82	1436

### 3.2 Results with Damage

For the progressive damage tests, the same sandwich composite sample cannot be used to compare the results from different impact conditions with the same impact energy. As a result,



(a) Dry Impact



(b) Water-backed Wet Impact

**Fig. 11** Comparison of delamination size between air and water-backed wet impact with the impact height 35.6 cm

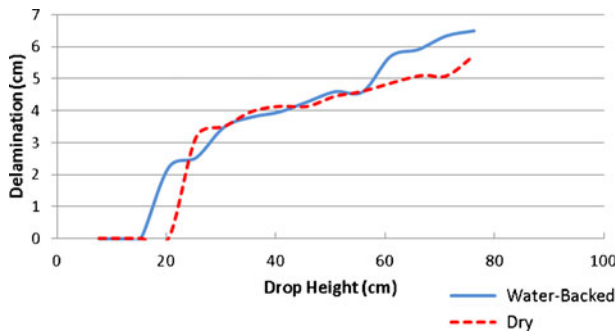


**Fig. 12** Comparison of delamination size vs. impact drop height between dry and water-backed wet impact

an individual composite sample was used for each impact test condition. Because of the potential for some variations in the composite material properties, especially in the balsa core, from sample to sample, multiple tests were conducted under each impact condition. Table 2 summarizes the drop heights and the peak impact forces at the onset of initial damage using the 6.7 Kg impact mass. The impact velocity was computed from the impact height using the conservation of energy and is listed in the table.

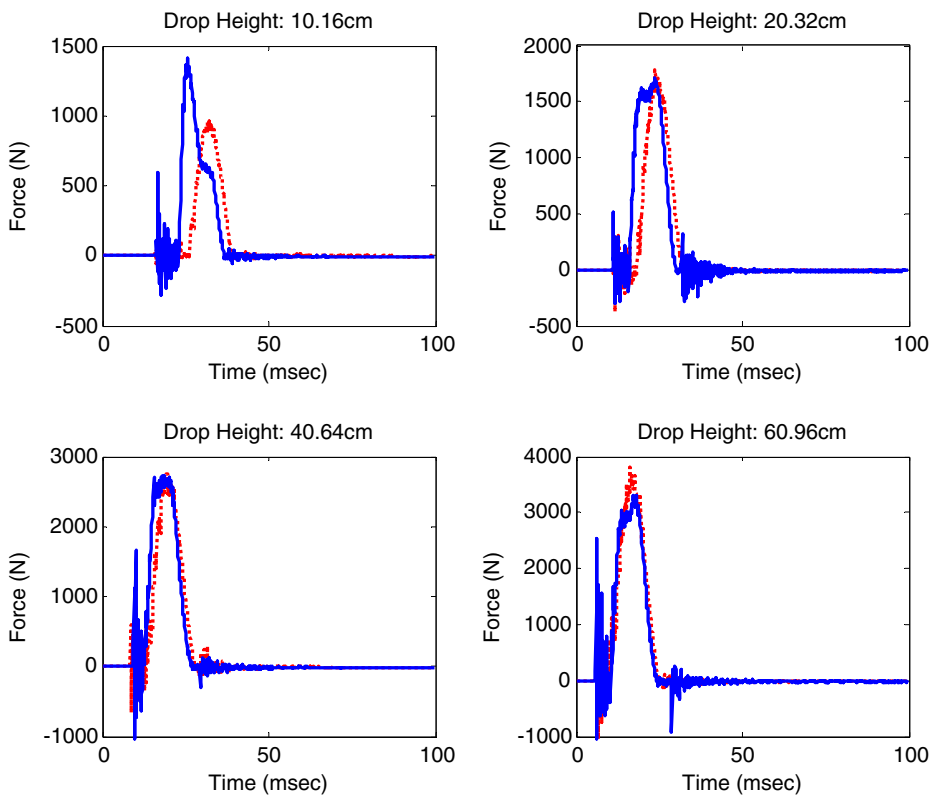


**Fig. 13** Comparison of impact force-time histories with progressive impact with damage. (solid line - water-backed wet impact; broken line - dry impact)



The onset of damage was the delamination between the core and the skin opposite to the impact side. Because the air-backed wet impact case had an enclosure with air to the delamination side, the delamination could not be inspected properly. As a result, the comparison was only made between the air and water-backed wet impact. Table 2 shows that water-backed wet impact consistently resulted in damage initiation at a lower impact height with a lower peak impact force. This indicates that water-backed wet impact is more detrimental to damage than the air impact. Considering the FSI in a sandwich composite structure in contact with water is essential for reliable design and analysis of the structure.

Both dry and wet impacts were applied to each respective sample with a discrete increment of the impact height beyond the onset of damage. Figure 11 compares the delamination sizes between the dry and water-backed wet impact cases with 35.6 cm impact height. The figure clearly exhibits the water-backed wet impact results in greater damage under the same impact energy than the dry impact. The skin layers were quasi-isotropic while the balsa core was anisotropic. The delamination shapes of most of other specimens were approximately circular but not as circular as that shown in Fig. 11. As the delamination grew, the shape generally deviated more from the circular shape.

Another set of sandwich plates were also tested, and the delamination sizes were measured along with progressive impact height. The result is plotted in Fig. 12 and the following observation can be made. First and foremost, the initiation of delamination occurs at a lower impact height for water-backed wet impact as stated previously. This means the

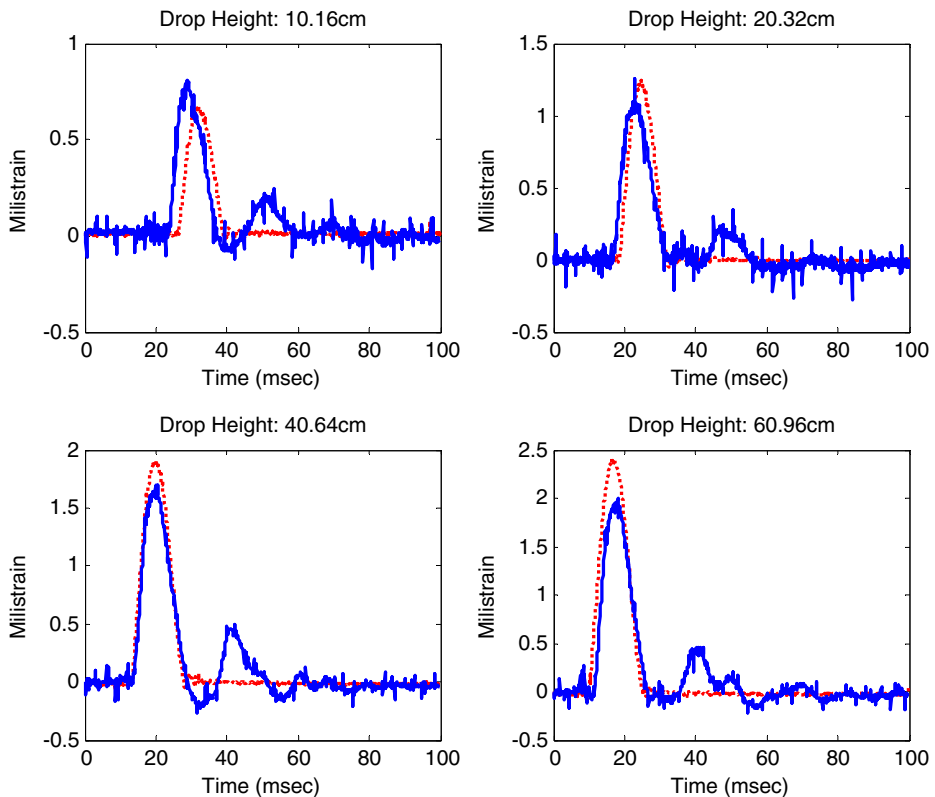


**Fig. 14** Comparison of x-strain-time histories with progressive impact with damage at gage location #1 of Fig. 3. (solid line - water-backed wet impact; broken line - dry impact)

damage is much greater for the water-backed wet impact than for the air impact at the same impact drop height, as demonstrated in Fig. 11 from another set of samples. The damaged sandwich plate submerged in water yields a lower impact force than the less damaged plate in air because the greater damaged section loses more stiffness. This, in turn, results in a larger delamination for the air impact. That is why the delamination size for air impact becomes slightly greater or almost equal to that for water-backed wet impact as shown in Fig. 12 for the drop heights approximately in the range 25 cm to 60 cm. As the impact height moves beyond about 65 cm, the delamination size becomes larger for the water-backed wet impact under the same drop height because both dry and wet plates have almost the same damage state so that their states of stiffness were more or less similar. Figure 13 shows the progressive comparison of impact forces between the two impact conditions. At a drop height of 10.16 cm, the wet impact case has a larger impact force. However, as the drop height increases to 60.96 cm, the dry impact yields a greater impact force as explained above. Even though there is delamination between the core and the bottom skin layer, it is not large enough to make a noticeable change in the stiffness of the sandwich plate. As a result, there is no distinct instability point on the force-time history indicating the onset and growth of the delamination crack.

For the damage tests, strain gage location #3 was omitted in all test plates in order to check delamination initiation and growth at the center of the plates. As a result, four strain gage sets were attached for each sample, i.e. locations #1, #3, and #4 in Fig. 3. Figures 14,

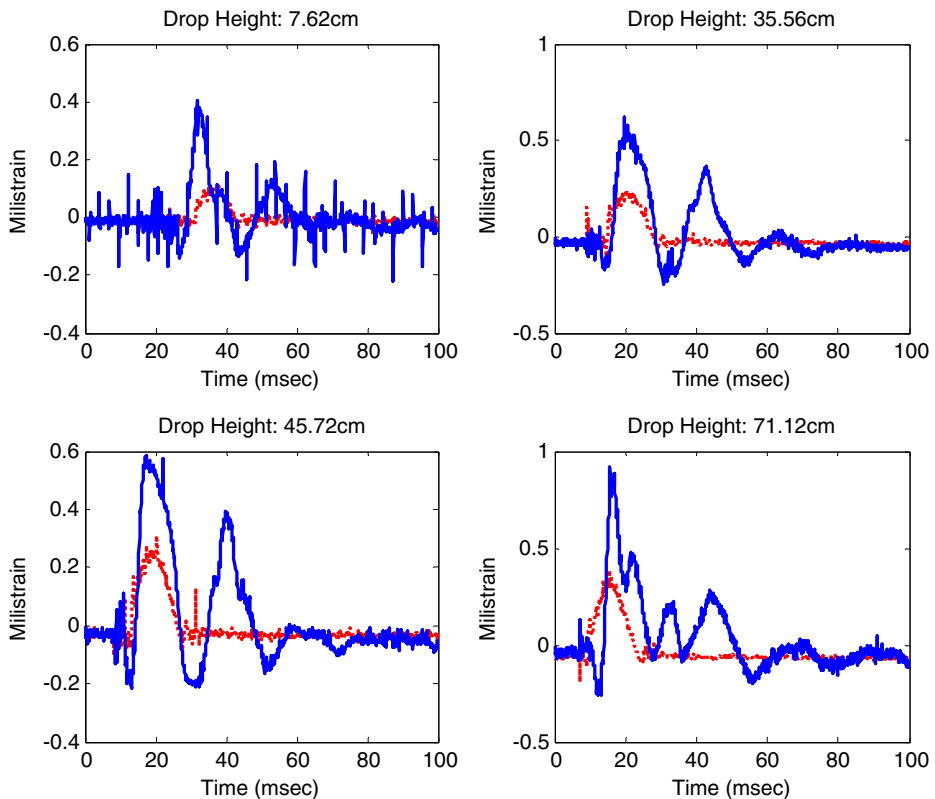


**Fig. 15** Comparison of x-strain-time histories with progressive impact with damage at gage location #3 of Fig. 3. (solid line - water-backed wet impact; broken line - dry impact)

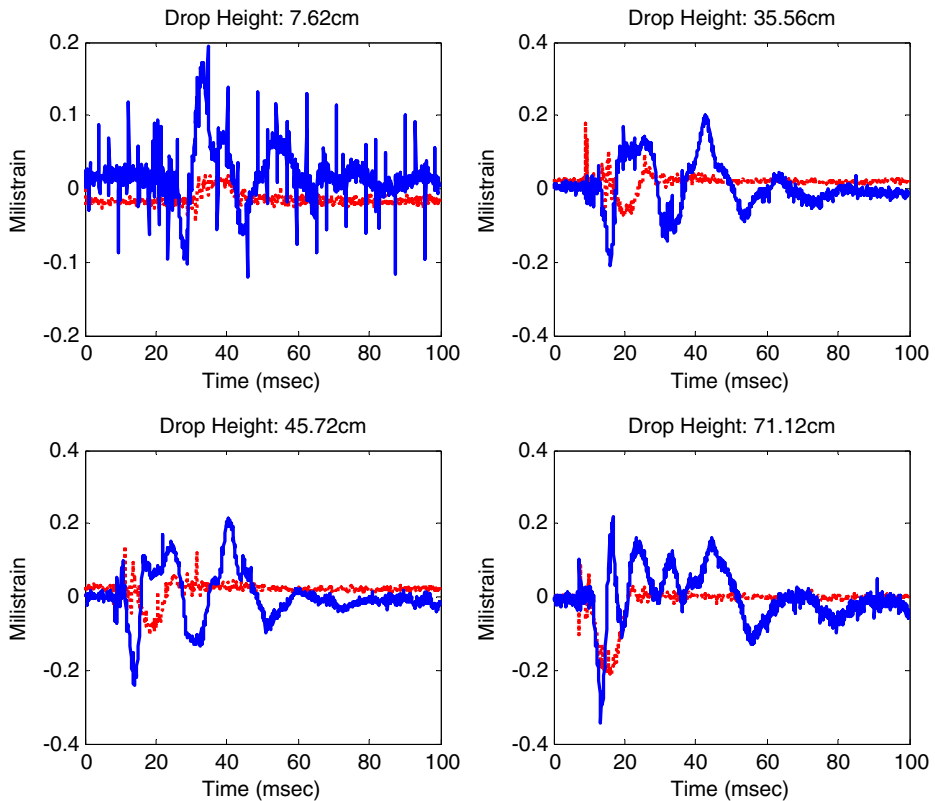


**Fig. 16** Comparison of x-strain-time histories with progressive impact with damage at gage location #4 of Fig. 3. (solid line - water-backed wet impact; broken line - dry impact)

15 and 16 are the plots of x-strain comparisons with progressive drop heights at every gage location. The strain at location #5 is similar to that at location #3 in terms of characteristic behavior. As a result, it was not included in the plot.

**Table 3** Peak Impact Forces Resulting from Progressive Impact Testing

Impact Test Specimen		Drop Height (cm)						Failure Site
		35.56	40.64	45.72	55.88	60.96	66.04	
		Impact Velocity (m/s)						
		2.64	2.82	3.00	3.31	3.46	3.60	
Force (N)	Wet Test #1	805	869	885*	—	—	—	Mid-span
	Wet Test #2	916	1030	1090*	—	—	—	Mid-span
	Avg. Wet test	861	950	988				
	Dry Test #1	720	767	792	912	1032*		Boundary
	Dry Test #2	829	892	905	934	990	1010*	Boundary
	Avg. Dry Test	774	830	849	923	1011	1010	

\* indicates first failure of the sample

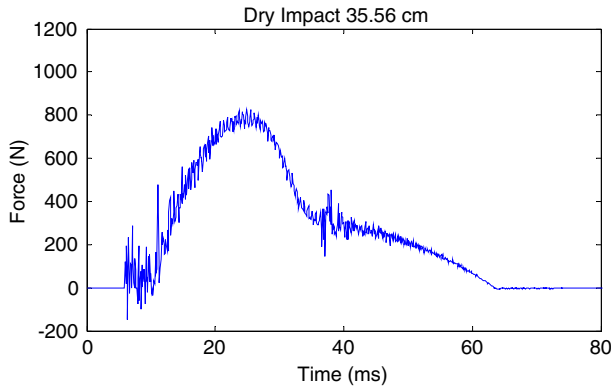


**Fig. 17** Dry sandwich beam without failure

At the gage location #1, the strain-time history follows a similar trend to the force-time history. That is, the water-backed wet impact has a larger strain at the drop height of 10.16 cm while the dry impact has a greater magnitude for higher impact drop heights as shown in Fig. 14. This is because gage location #1 is close to the delamination site and the response was affected by the damage. On the other hand, strain response at other gage locations shown in Figures 15 through 16 exhibits much greater strain magnitudes for the wet impact consistently for all drop heights even though the general behavior indicates the strain magnitude ratio of the wet to dry impact decreases along with the increase of the drop height. Additionally, strains under wet impact at gage locations #3 through #4 show more major peaks and valleys as the drop height increases with more damage. This may suggest that the vibration mode shape is altered for the bottom skin layer with the spread of delamination. More study is needed for a better understanding of the vibrational behavior.

#### 4 Results of Sandwich Beams

Water-backed wet and dry impact tests were conducted for multiple sandwich beams, respectively. First wet impact was applied to a sandwich beam clamped at both ends starting

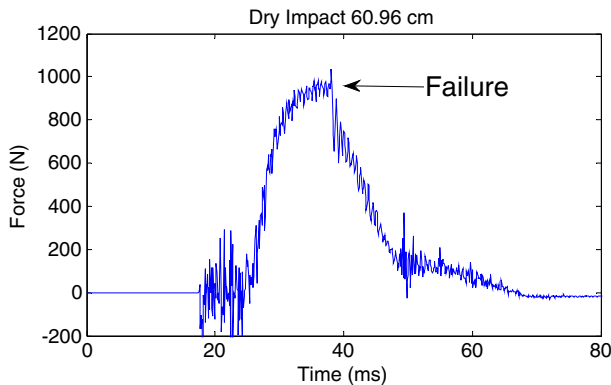


**Fig. 18** Dry sandwich beam with failure

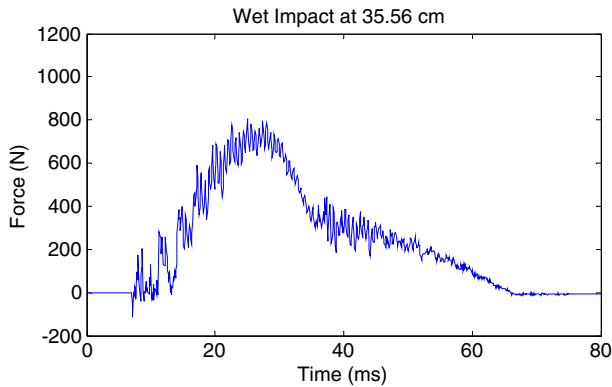


**Fig. 19** Wet sandwich beam without failure

from a drop height at 35.56 cm for two impacts, and then increased by 5.08 cm for two more impacts, continuing in this pattern until the sample failed. Failure was determined by a significant loss of impact force on the second impact at the same height, visual damage, or an obvious failure on the force/time plot. The same kind of progressive impact testing was also conducted for another set of dry sandwich beams. All results showed that the first failure occurred when the drop height was increased from one level to another. In other words, failure did not occur at the second impact at the same drop height. As a result, the summary of progressive impact tests, as shown in Table 3, includes the average value of two impacts at the same drop height for each test sample before failure.

The test results showed that impact on the sandwich beam submerged in water had a significant effect on both failure loads and modes of failure. The dry samples failed at the clamped boundary with no damage at the mid-span where impacted. On the other hand, the submerged samples failed at the mid-span. In other words, the failure location was shifted because of the hydrodynamic mass effect.

Comparing the peak impact forces between the dry and wet impacts before any failure, the wet impact produces higher forces than the dry impact at the same drop height, as experienced in the plate samples. Table 3 compares the average peak impact forces between the dry and submerged sandwich beams at the same drop heights. The wet impact forces are

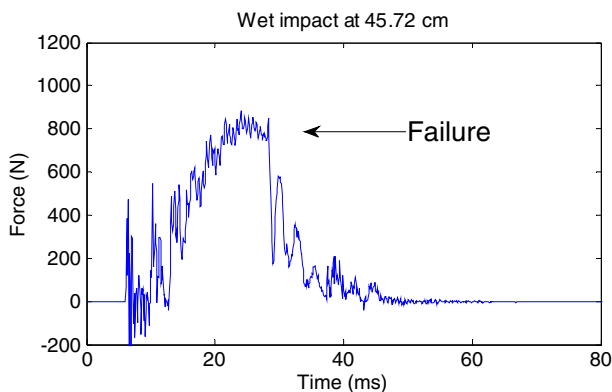


**Fig. 20** Wet sandwich beam with failure



**Fig. 21** Typical failure under dry impact at the boundary edge

about 13% greater than the dry impact forces for the same height drops. Furthermore, as the drop height increases, the ratio of the wet to dry impact forces becomes greater. Eventually, failure occurred at a lower drop height for the wet impact. This indicates that wet impact is more detrimental to sandwich composites than dry impact as demonstrated by plate specimens.

At failure, the forces were close between the dry and wet impact tests. The average failure force was 1021 N for the dry impact and 988 N for the wet impact, respectively, with approximately a 3% difference. On the other hand, the wet failure load has a greater variation than the dry failure load. This is expected because wet impact involves FSI so there are more variables affecting the response of the composite structure.

Figure 17 shows the impact force-time history at the center of a dry sandwich beam without failure while Fig. 18 is the same for a dry specimen with failure. Likewise, Figs. 19 and 20 are the force-time histories for the wet impact specimen. As expected, failure in both the dry and wet sandwich beams shows a steep drop in force which is more significant for the wet impact than for the dry impact. A possible reason for this is the difference in failure location. Because the wet impact results in failure at the impact site, i.e. at the mid-span, the impact force drops more significantly. Another difference is that the dry impact failure resulted in a steep drop of force at its peak value while the wet impact yielded a sharp decrease in force slightly after reaching the peak value. Figures 21 and 22 are images of the failed sandwich beams under dry and wet impact, respectively.

The next sequence of testing was determined based on the progressive impact test data. Each specimen was impacted only once at a drop height which would induce failure. For the dry impact, the chosen single drop height was 66.04 cm which was the height resulting in failure from the progressive impact testing. On the other hand, the selected single drop heights for the wet impacts were 45.72 cm and 66.04 cm, respectively. The first height was determined from the failure in the progressive drop test while the second height was chosen



**Fig. 22** Typical failure under wet impact at the impact site

**Table 4** Failure impact forces from single impact testing

Impact Type	Drop Height (cm)	Impact Velocity (m/s)	Force (N)
Wet Impact	45.72	3.00	974
Wet Impact	66.04	3.60	1006
Dry Impact	66.04	3.60	1032

to compare the wet impact to the dry impact at the same drop height inducing failure for both cases. Several specimens were tested for both dry and wet impacts, respectively, and the results are tabulated in Table 4.

The failure forces were found to be similar in both the progressive and single impact tests when Tables 3 and 4 are compared. This fact supports that the progressive impact did not yield any premature damage before failure. Failure forces for submerged specimens at two different drop heights were also very similar. Furthermore, the dry impact resulted in a slightly greater failure force than the wet impact. The failure locations for dry and wet impacts are summarized in Table 5. Five out of seven samples failed at the mid-span for the wet-impact while five out of six beams failed at the boundary for the dry impact. This data supports the point that the failure location was changed due to the FSI not because of the variation of the core material.

Wet impact damage was primarily observed at the center span with some damage occurring at the edges of the beam in a few samples. The failure mode was skin compression adjacent to the point of impact on the top skin. The submerged beam specimens showed neither localized delamination nor core failure except for one sample. There was no evidence of water intrusion at any point. For the dry impact, failure was dominated by skin failure on the bottom side of the clamped boundary. Some of the specimens also showed core shear failure with delamination at the failed boundary.

## 5 Conclusions

The effect of FSI was studied on the transient dynamic response as well as damage initiation and growth of sandwich plates and beams constructed with E-glass skin layers and balsa core. To achieve the objective, dry and wet impact tests were conducted using the same impact energy which was increased gradually, and their results were compared by measuring impact force-time history as well as strain-time responses. The results demonstrated that the added mass effect of FSI plays a significant role in the response of the sandwich composite structure, both in terms of transient dynamic response and damage.

For each series of tests, the damage occurred at a lower drop height for the wet impact because of the added mass effect. In addition to the earlier onset of damage, the delamination

**Table 5** No. of Sandwich Samples Failed at Different Locations

	No. of Failed Samples	
	@ Mid-span	@ Clamped Boundary
Wet Impact	5 samples	2 samples
Dry Impact	1 sample	5 samples

patterns were generally larger at the same drop height for the water-backed samples when compared to the dry impact baseline. The wet impact also affected the damage location. The clamped sandwich beams subjected to impact at the center failed at the center for the wet impact while it failed at the boundary for the dry impact.

The dynamic response showed a clear trend that the water-backed impact produced larger strains in almost every location. The dynamic responses of the plates indicated the FSI effect altered not only their vibrational frequencies but also modal shapes. This fact will be further examined in a future study using a full field deformation measurement technique. Including FSI effect for sandwich composite structures in contact with water is essential for the structural design and analysis. Failure to do so will result in a non-conservative analysis.

## References

1. Vinson, J.R., Sierakowski, R.L.: The behavior of structures composed of composite materials. Kluwer Academic Publishers, Secaucus (2002)
2. NASA Preferred Reliability Practices: Structural Laminate Composites for Space Applications, Practice No. PD-ED-1217, NASA Jet Propulsion Laboratory California Institute of Technology 4800 Oak Grove Dr. Pasadena, CA USA, Dec 2009, <http://engineer.jpl.nasa.gov/practices/1217.pdf> Accessed August 24, 2010.
3. Business Development in the New Navy, Ball Aerospace & Technologies Corp, Boulder, CO USA, Aug 2003 [http://www.nps.edu/academics/institutes/meyer/docs/SI4000/Seminar\\_topics\\_04/Navy\\_Marketing\\_Brief\\_Ball\\_Aerospace.pdf](http://www.nps.edu/academics/institutes/meyer/docs/SI4000/Seminar_topics_04/Navy_Marketing_Brief_Ball_Aerospace.pdf) Accessed August 24, 2010.
4. LeGault, M.R.: DDG-1000 Zumwalt: stealth warship. Compos. Tech. (2010)
5. Griffiths, B.: Rudder gets new twist with composites. Compos. Tech. (2006)
6. Aslan, Z., Karakuzu, R., Okutan, B.: The response of laminated composite plates under low-velocity impact loading. Compos Struct **59**, 119–127 (2003)
7. Kwon, Y.W., Wojcik, G.W.: Impact study of sandwich composite structures with delamination. J Compos Mater **32**(5), 407–430 (1998)
8. Abrate, S.: *Impact engineering of composite structures*. Cambridge, (CISM Courses and Lectures, Vol. 526), printed in Italy, Springer, 2011.
9. Baucom, J.N., Zikry, M.A.: Low velocity impact damage progression in woven E-glass composite systems. Compos Appl Sci Manuf **36**(5), 658–664 (2005)
10. Mines, R.A.W., Worrall, C.M., Gibson, A.G.: Low velocity perforation behaviour of polymer composite sandwich panels. Int J Impact Eng **21**(10), 855–879 (1998)
11. Kwon, Y.W., Owens, A.C., Kwon, A.S., Didoszak, J.M.: Experimental Study of Impact on Composite Plates with Fluid–structure Interaction. Int J Multiphys **4**(3), 259–271 (2010)
12. Kwon, Y.W.: Study of fluid effects on dynamics of composite structures. ASME J Pres Ves Tech **133**, 031301–031306 (2011)
13. Kwon, Y.W., Owens, A.C.: Dynamic responses of composite structures with fluid–structure interaction. Adv. Compos. Mater. IN-TECH publisher, (2011)
14. Mouritz, A.P., Gellert, E., Burchill, P., Challis, K.: Review of advanced composite structures for naval ships and submarines. Compos Struct **53**, 21–41 (2001)
15. DIAB Sandwich Handbook: Sandwich Concept, DIAB AB, box 201, S-312 22, Laholm, Sweden, Sept 2003, [http://www.diabgroup.com/europe/literature/e\\_pdf\\_files/man\\_pdf/sandwich\\_hb.pdf](http://www.diabgroup.com/europe/literature/e_pdf_files/man_pdf/sandwich_hb.pdf) Accessed August 23, 2010.



Low velocity impact on polymer composite plates in  
contact with water

by

**Y. W. Kwon and R. P. Conner**

reprinted from

**THE INTERNATIONAL JOURNAL OF  
MULTIPHYSICS**

**2012: VOLUME 6 NUMBER 3**

**MULTI-SCIENCE PUBLISHING**

# Low velocity impact on polymer composite plates in contact with water

**Y. W. Kwon and R. P. Conner**

Dept. of Mechanical & Aerospace Engineering,  
Naval Postgraduate School, Monterey,  
California, USA

## **ABSTRACT**

In this study, composite materials were tested in two different environments to determine the role of Fluid Structure Interaction with composites under a low velocity impact. This was done using a low velocity impact machine and polymer composite plates. The composite is made of laminated symmetrical plain weave E-glass fabrics. The test area of the composite plates is 30.5 cm by 30.5 cm with clamped boundary conditions. The testing was done using a drop weight system to impact the center of the test area. One testing was performed with composite plates in air, called dry impact. The other testing was conducted while composite plates were submerged in water, called wet impact. A Plexiglas box in conjunction with the impact machine was used to keep the top of the composite sample dry while it was submerged in an anechoic water tank, so called water-backed air impact. Output from the tests was recorded using strain gauges and a force impact sensor. The results show that an added mass effect from the water plays a large role in the Fluid Structure Interaction with composites due to the similar densities of water and the composites. The wet impact results in a larger impact force and damage than the dry impact under the same impact condition, i.e., the same impact mass and drop height.

## **1. INTRODUCTION**

Composites are becoming more and more important in today's world. They have been popular in the aircraft industry for many years, and are currently attempting to make their way into the maritime industry as well. The application of these composites to the marine military environment is very appealing because of the high corrosion resistance offered by the composite. Another main reason for the use of composites is the very high strength to weight ratio. Similar composites have already made their way into the military marine environment. The U.S. Navy's DDG-1000 Zumwalt class destroyer has a superstructure made almost completely of composite materials. The use of composites on naval ships is gaining ground because they allow for lighter, faster, and corrosion free ships [1]. Other marine military applications include the use of composites to build ship's rudders. Composite rudders can be shaped and built from a mold which allows for a much lower cost than a steel rudder of the same design, while having similar strength properties [2]. The U.S. Navy has also looked into composite applications to rudders, propellers, stairwells, handrails, valves,

and armors [3]. The downside to using composite materials for ship building and shipboard applications is the cost of construction and the cost of training for construction. It is estimated that ships made of composites can cost up to 20% more than a ship made of steel. However, the higher construction cost can be compensated by the lower maintenance and operation cost. It has been estimated that the cost of corrosion and corrosion related maintenance cost the U.S. Navy approximately \$22 billion annually [4].

Fluid Structure Interaction (FSI) is very important in the application of composites to the marine environment. There is no FSI issue with using composites on parts of the ship that are above the water line because they are not in contact with water. However, a problem does arise when the composite is used in a place where a fluid such as water can interact with the composite. Especially, polymer composites have densities similar to that of water, as opposed to steel which has a much greater density than the water density. The similar magnitudes of densities play a larger role in FSI. The low velocity impact in water can be critical to the transient dynamic response of the composite. The added mass effect of the water causes a large amount of stress and strain on the composite that it would not encounter in air. This causes the composite to fail in water more rapidly. This problem is much less likely to occur in steel because there is much less of an added mass effect of the water because the density of steel is so large compared to water.

The objective of this study is to further the previous study of FSI and its effects on composite materials. Recently, experiments have been conducted to study the FSI on their respective composite samples [5–6]. In the research, FSI was studied under three different testing conditions. The first testing was a dry impact in air. There is no water contact in this case. This is the air-backed dry impact, or simply dry impact. The second and third cases had impacts while submerged in water. Both cases had the top surfaces of test plates, where impacted, in contact with water, but the bottom surfaces were different. The second case had a dry bottom surface, i.e., no water contact, which is called the air-backed wet impact. The third case had a wet bottom surface, i.e., in contact with water, called the water-backed wet impact. The second and third loading conditions represented impact on the ship hulls from the water side, which may be floating ice and sea animal impact on ship hulls. The three cases mentioned above are shown in Fig. 1(a) through (c). On the other hand, this study will continue that research for different loading condition such that the impact side is dry while the opposite side is wet, which is called the water-back dry impact as sketched in Fig. 1(d). This case is to simulate an impact from the inside of a composite hull such as ship-board equipments and sailors. In this paper, the two impacts are simply called dry and wet impacts, respectively.

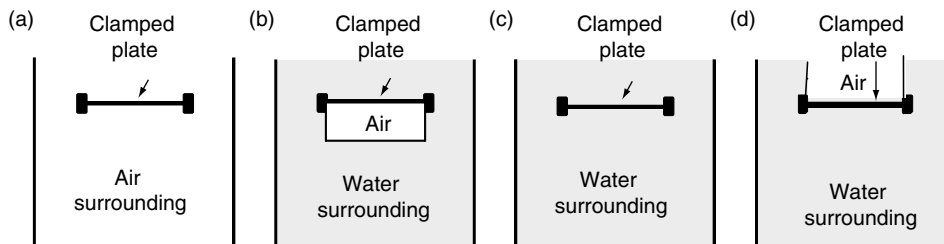


Figure 1 Comparison of different impact conditions with impact on the top side of composite plate: (a) air-backed dry impact (or simply dry impact), (b) air-backed wet impact, (c) water-backed wet impact, (d) water-backed dry impact.

## 2. EXPERIMENTAL METHODS

### 2.1. MATERIALS

There are two main materials used to form the composite and there are many other materials used as tools to accomplish the production. The two most important materials for the composite composition are the resin and the E-Glass woven fabrics. This section discusses about the material properties of the resin and the E-glass woven fabrics, as well as the other materials required to complete the process and how they are used.

The composite was made using a woven fiberglass cloth known as a 6 ounce E-Glass as shown Fig. 2. These types of woven fiberglass cloths are very common for marine composite construction and repair. The woven cloth was chosen for its uniformity and because of the fact that it is lightweight and is very common in small boat building. If this E-Glass is paired with the correct resin, it can maintain a high corrosion resistance and provide a water proof layer [7].

The resin chosen for this composite fabrication was a Vinyl Ester Resin known as Derakane 510A. As stated above, a smart choice of resin could improve the qualities of a composite material. This particular resin improves corrosion resistance and also has certain fire retardant properties which make it perfect for shipboard use as well as other marine applications. The method used for hardening of the resin is known as clear casting. Clear casting is accomplished by allowing the resin to cure at room temperature for 24 hours and then another 2 hours at a temperature of 120 degrees Celsius. The strength properties of the resin for clear casting are shown in Table 1 [8].

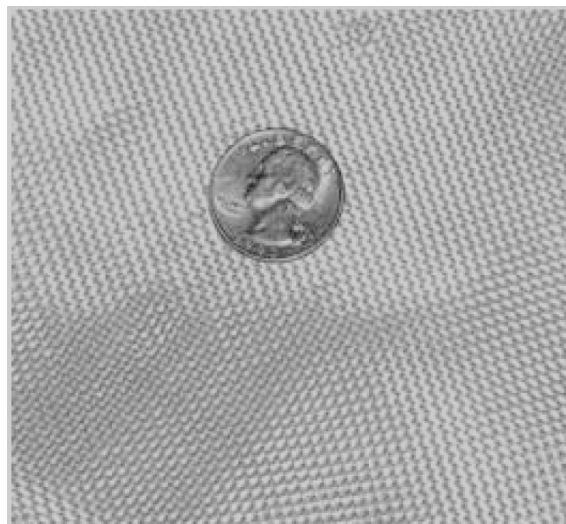


Figure 2 6 ounce E-Glass weave.

Table 1 Strength properties for clear casting of vinyl ester resin [8].

<b>Property of Clear Casting at 25°C (75°F)</b>	<b>Value (SI)</b>	<b>Value (US)</b>
Tensile Strength	86 MPa	12,300 psi
Tensile Modulus	3400 MPa	490 kpsi
Flexural Strength	150 MPa	21,700 psi
Flexural Modulus	3600 MPa	520 si

There are three main hardening agents used for the fabrication process of the composite sample. Two of them are always required and the third is only required if a faster cure time is desired. The first hardening agent is the Methyl Ethyl Ketone Peroxide (MEKP). The second is Cobalt Naphthenate 6%, and the third is Dimethylaniline (DMA). MEKP is a basic catalyst which is usually added to polyester and vinyl resins. The addition of the MEKP causes a chemical reaction and heat generation which begins the hardening process in the resin. The second hardening agent is a deep blue purple liquid known as Cobalt Naphthenate 6%. Since this is a cobalt solution, its main role in the process is as an oil drying agent, but it also adds some waterproofing to the composite material as well. It is used as a crosslinking catalyst during the hardening process of the fabrication and this particular catalyst is an oxidation dryer with the strongest drying activity. The Naphthenic acid is added to make the cobalt more oil soluble. Dimethylaniline is the third hardening agent used in the process. The DMA serves as a promoter to the curing of the resin during the fabrication of the composite. This hardening agent is used for a more rapid curing process of the resin and is only used when fast curing times are desired.

## 2.2. COMPOSITE CONSTRUCTION METHOD

The process used to fabricate the composite samples used in this research is known as Vacuum Assisted Resin Transfer Molding (VARTM). VARTM is a very common method used in low pressure composite molding production. This is done by constructing an air tight vacuum around the materials used to make the composite. A vacuum pump is used to expel all the air from the preform assembly of the composite. Once there is an air tight seal, the resin is pulled through the preform of e-glass weave from the bottom to the top. A distribution medium is used to accelerate the processing time of the VARTM and it also ensures total coverage of the preform [9].

There are many different materials needed to complete the VARTM process. A list of all the materials used is shown below; E-Glass, Vinyl Ester Resin, Airtech Resinflow 75 Distribution Medium, Teflon, Peel Ply, Stretchlon 200 1.5 Vacuum Bag Film, AT-200Y Sealant Tape, Plastic Tubing, and Resin Trap.

The distribution medium is a green mesh fabric that is used to evenly distribute the resin throughout the whole preform. The Teflon is used to prevent the resin from adhering to the glass which is used at the base of the set up. Peel ply is a nylon material that is placed between the distribution media and the E-glass weave for easy release after curing. The vacuum bag is made from a Polyolefin material and is used to cover the preform and adhere to the sealant tape to achieve a vacuum around the preform. The sealant tape is to hold down the vacuum bag. The plastic tubing is used to transfer the resin through the preform from the resin reservoir to the resin trap. Finally, the resin trap is used to collect any waste resin during the VARTM process.

The resin preparation is the most important part of the process. An incorrect mixture of resin and hardening agents will make the difference between a good sample and one that is not usable. The first step to the resin preparation is to pour the desired amount of resin into your resin bucket. For the composite samples made for this research, one liter of the resin was sufficient for the process. Once the desired amount of resin is in the bucket, it is important to measure out the exact amounts of hardening agents needed for the desired curing time. Table 2 shows the amount of each hardening agent needed for the desired cure time at the room temperature. The values given are in parts per hundred resin molding compound (phr).

Table 2 Typical Gel Times using MEKP, DMA, and Cobalt [8].

<b>Gel Times at 25°C (75°F)</b>	<b>MEKP (phr)</b>	<b>Cobalt (phr)</b>	<b>DMA (phr)</b>
15 +/- 5 minutes	2.00	0.30	0.05
30 +/- 10 minutes	1.25	0.30	—
50 +/- 15 minutes	1.00	0.20	—

It is important to note that the gel times of this mixture will vary based on the surrounding environment. This is why it is so difficult and important to come up with a mixture that works well and stick to that mixture. The gel times for approximately 50 minutes was used in this research. Furthermore, 1 drop of DMA from a 3 mL syringe was used as well. It was found that using a 30 minute gel time mixture made it difficult for the resin transfer process to completely cover the preform. When using the 50 minute gel time, sometimes the resin was unable to set and the vacuum began to pull resin from the preform after the transfer was stopped. The DMA was added to help the resin set faster into the preform.

Another important part of the mixture process is how to actually mix the components. It was discovered during the first couple trials that the MEKP and Cobalt react to one another if they are added at the same time. To fix this problem, the MEKP was added first and thoroughly stirred into the resin before the Cobalt was added. In addition, once all the required components are added to the resin, it is important to keep mixing it on and off for approximately 15 minutes to allow for a proper mixture. Once the air bubbles stop forming in the mixture, it is ready to go.

### 2.3. POST FABRICATION METHODS AND REQUIREMENTS

The curing process is relatively simple, but it takes some time. After the resin transfer is complete, the tube used on the resin side of the preform is clamped to keep the vacuum seal intact. Now the vacuum must stay on for 8 hours during the initial cure period. Then the composite must cure another 24 hours with the vacuum off. Both of these cure processes take place at room temperature. The last step in the cure process is to cure the composite for another 6 hours at an elevated temperature of 70°C.

Once the curing is complete, the samples will need to be cut down in size. The overall size of the composite must be able to fit into the impact machine, but there is no correct exact size. The only important part of the sizing is the 30.48 cm by 30.48 cm test area. To keep the test area consistent, a grid of 7.62 cm by 7.62 cm squares were drawn onto the sample. This allowed for a consistent placement of the strain gages on each composite sample.

The strain gages were an important part of this research. They gave great insight into the mechanics of what is actually occurring during the testing of each sample. They showed a quantitative difference between each of the testing environments which allowed for a better analysis of the results. The strain gage rosette measures the strain in the composite during the testing. The strain is measured in three different directions per strain gage. The measurement of strain in three different directions is important because they allow us to determine strains in any orientation.

This strain gages used for this research were from Vishay Precision Group. Each square composite sample had four strain gages placed throughout the surface of the sample. Figure 3 shows the strain gage rosette configuration. Figure 4 shows the arrangement of strain gages used for the square composites.

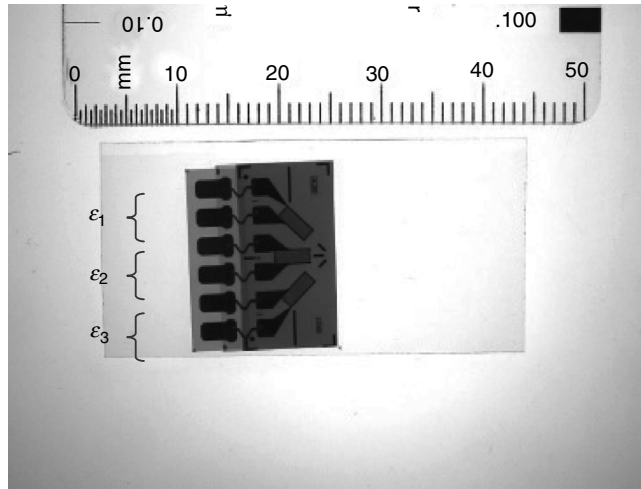


Figure 3 Square strain gage rosette showing  $\epsilon_1$ ,  $\epsilon_2$ ,  $\epsilon_3$ .

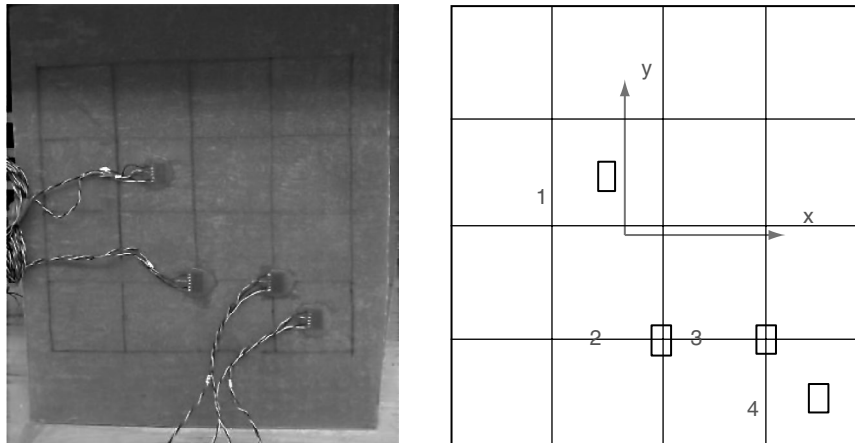


Figure 4 Strain Gage layout on composite samples.

#### 2.4. TEST EQUIPMENT

The only piece of test equipment used in this research was a drop weight test machine designed and used in previous research [10]. The impact machine was used for testing composites used in this research. The impact machine is a simple drop weight system that allows the user to drop a desired amount of weight from a desired height. Figure 5 shows the apparatus. The test machine gets lowered into the anechoic water tank during testing to give the best stability possible. Both dry and wet impact tests are done in the tank. For the dry testing, water is drained from the tank while water is retained for the wet impact testing.

The drop weight apparatus has two main components. The first is a trigger that starts the data acquisition process at the same height for each drop. The second component is at the tip of the impactor itself. The impactor has a built in force sensor and for each drop the force data is acquired using a specifically designed LabVIEW program. The LabVIEW program



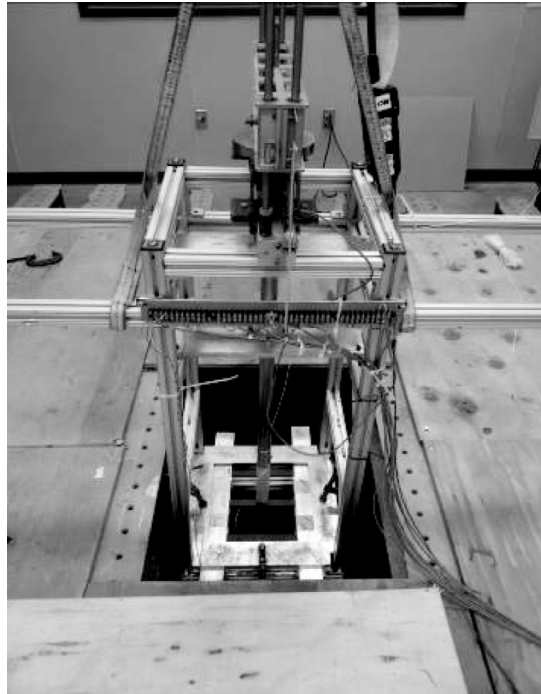


Figure 5 Impact test machine.

recorded 1000 samples of data over a 100 millisecond period of time. This was consistent throughout the testing of both composite samples.

## 2.5. TEST METHODS

A primary goal of this study was to determine the amount of force that initially caused damage to the composite sample. This allowed for the data before and after the damage to be analyzed and compared/contrasted. The damage was attempted to be detected visually after each drop. The initial damage is considered to be at the time the first delamination of the composite is visible. This testing gives great insight into when damage can be expected to occur and how that damage will affect the composite after more impacts are experienced.

The first test done was the dry impact test. This was done to use as a baseline test so that the differences in damage, force, and strain data could be compared between the two test environments. This test was repeated 3 times to show consistency in the data being obtained and determine its reliability. The results from the dry testing are shown in the next section.

The next test was done in the water environment. A Plexiglas box was fabricated to fit over the top of the composite sample in order to keep the top of it dry while being lowered into the water filled tank. The goal of this testing was to determine the FSI with the composite during impact testing with a water backed, dry top test environment throughout a set of different drop heights. For this testing, it was chosen to use the larger weight of 10.8 kg. The weights were dropped from a starting height of 7.62 cm (3 in) and ended with a drop height of 76.20 cm (30 in). These drop heights were chosen because it is known that from 7.62 cm (3 in) no damage will incur and at 76.20 cm (30 in) the impact sensor approaches the maximum force recording levels [6]. All of the drop heights are shown in Table 3.



Table 3 Drop heights used in the tests.

Drop Number	Height (in)	Height (cm)
1	3	7.62
2	4	10.16
3	5	12.7
4	6	15.24
5	8	20.32
6	10	25.4
7	12	30.48
8	14	35.56
9	16	40.64
10	18	45.72
11	20	50.8
12	22	55.88
13	24	60.96
14	26	66.04
15	28	71.12
16	30	76.20

### 3. RESULTS AND DISCUSSION

In order to determine the FSI effects on damage initiation and growth as well as their resulting dynamic responses of composite structures, an important aspect of this study is keeping track of the damage incurred by the composite so that we can determine when the composite fails and how this failure affects the composite's response to further impacts. The damage done to the composites can be hard to detect. Composite materials have distinct modes of failure depending on materials used to construct the composite. In laminated composites, delamination of the back side of the composite, where it is in tension after impact, is the most common place for the damage to occur. The most common causes of delamination are tensile and compressive fatigue loading and impact loading [11]. In recent literature there are many great reviews of published papers on the failure modes, and damage identification and significance which can be used as general references [12–15]. Small areas of delamination are capable of reducing the compression strength of composite materials by 50 percent. For this reason, after each impact on the composite sample, the backside was examined for any evidence of damage. All damages observed during this testing were delamination of the composites as expected.

For all the samples tested, measurement was conducted to track the visible damage of delamination in the samples. Delamination occurred at a significantly lower drop height during the submerged testing versus the dry testing. Figure 6 shows an example of the delamination occurring at the underside of the impact zone.

After a total of six tests, three in water and three in air, the data proved to be consistent from one sample to another. Figure 7 shows the consistency of the data for two of the samples tested under the same impact condition.

There is plenty of information available from the force data that is collected during the testing. First, the impact force experienced in a water submerged environment is higher than the force in a dry environment for the same drop height before damage occurs. Figure 8 shows that the wet impact force for a 15.24 cm drop height has approximately a 350 N higher

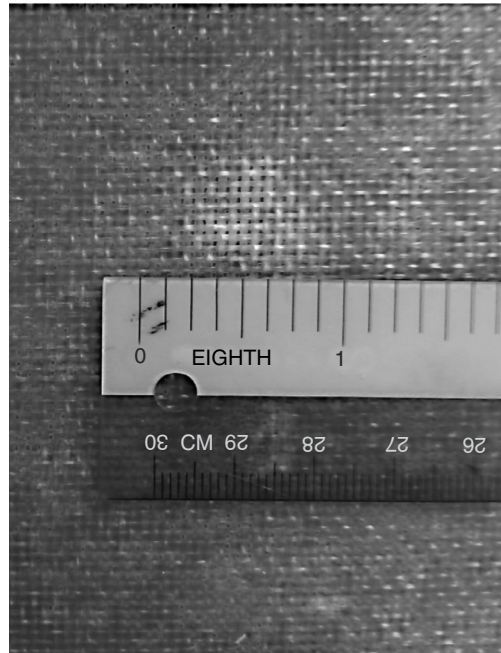


Figure 6 Close up of delamination under impact zone of wet sample.

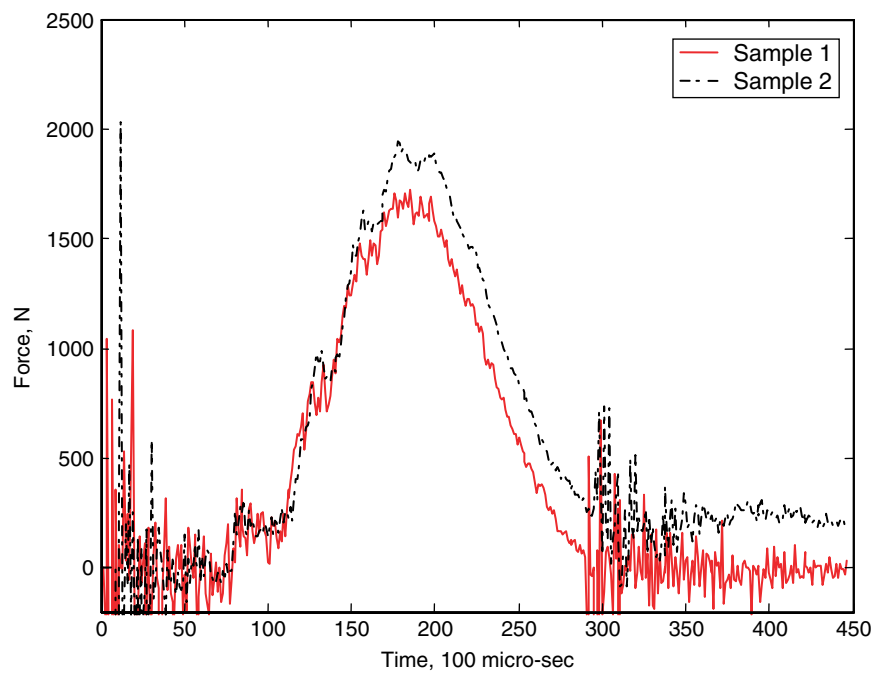


Figure 7 Force comparison between two samples with 30.48 cm drop height dry testing.

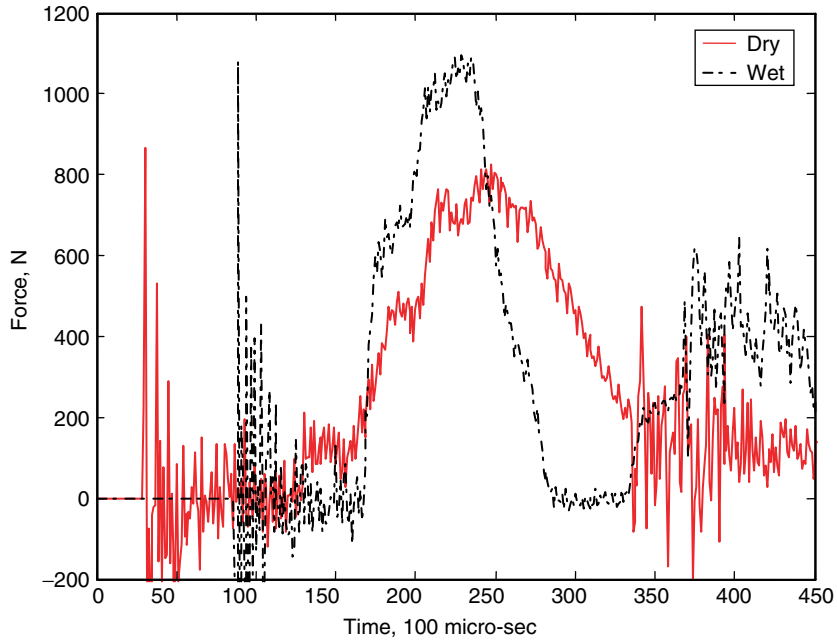


Figure 8 Impact force comparison between wet and dry testing with drop height of 15.24 cm.

than the dry impact force. At this drop height, the wet impact began to initiate delamination at the underside of the sample while there was no sign of delamination for the dry impact.

The fact that this drop height is the first sign of delamination is significant, because after this point, the impact force for the wet samples will no longer be greater than the dry impact force. As the drop heights increase, the dry impact force becomes greater than the wet impact force. This is because the damage induced from the wet impact results in a reduced stiffness of the structure, eventually leading to reduction in the impact force. This fact that the change in impact force occurs after damage is significant because even if no visible damage is detectable, the force data can be analyzed to determine if any internal damage has occurred to the composite sample.

In every case, the damage occurred earlier in the wet sample versus the dry sample. In all cases for the wet impact test, a drop height of 15.24 cm resulted in initial damages. However, in all cases for the dry impact test, initial damages occurred between drop heights of 55.88 cm and 71.12 cm. Thus, the dry impact produced damages at approximately four to five times greater impact heights than the wet impact. In other words, the FSI induced damage at much lower impact height or impact energy since the same impact mass was used for both dry and wet tests. Figure 9 shows the delamination damage size as a function of drop height for both the wet and dry samples. The plot shows that delamination under the wet impact grew in a step-like function rather than a continuous function as the impact height increased. A similar but less distinct behavior can be also observed for the delamination growth under dry impact.

Figure 10 compares impact forces at 20.32 cm, just after damage occurred in the wet sample but no damage for the dry sample. Their impact force magnitudes are almost identical. The damaged sample experienced a loss of stiffness and therefore the impact force decreased. Since these low drop heights have caused damage in the wet samples but not for the dry samples, the impact force for the dry samples becomes larger than the wet samples until

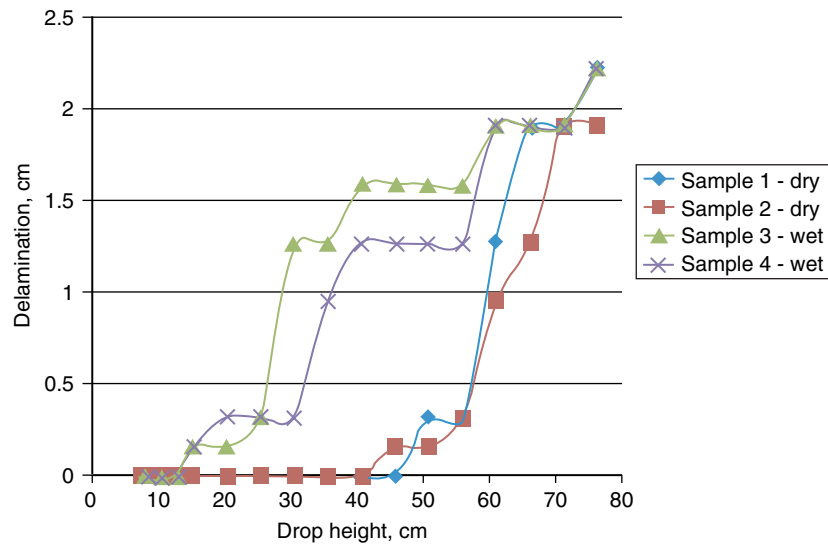


Figure 9 Damage size as a function of drop height for both wet and dry samples.

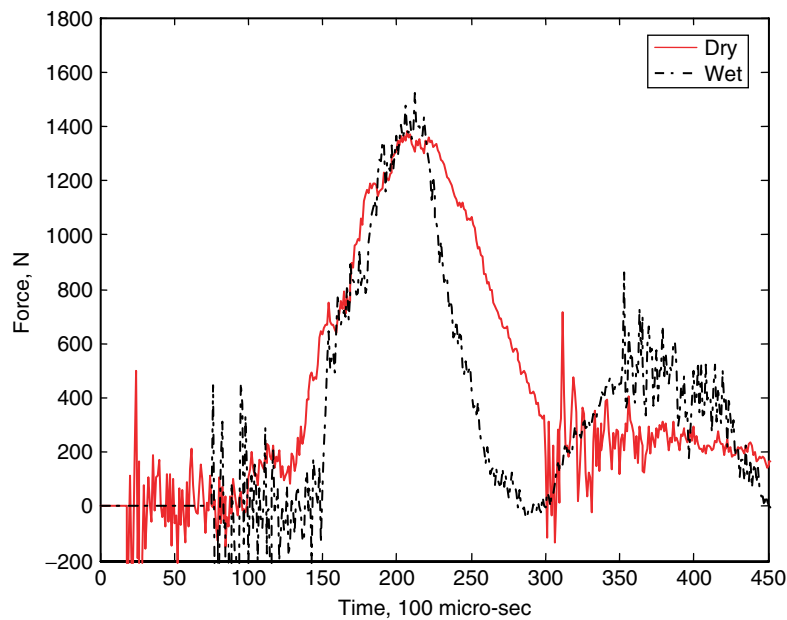


Figure 10 Impact force comparison showing same impact force due to damage in wet sample with a drop height of 20.32 cm.

damage is incurred for the dry samples. Figure 11 shows how the dry impact force is now much larger than the wet impact force because the dry samples still do not have any damage.

During the testing of the dry samples, visual damage was not noticed until about the 66.04 cm drop heights. Hence, if the wet vs. dry impact forces are compared at that drop height, it is expected to see the impact forces to be similar again because they have both

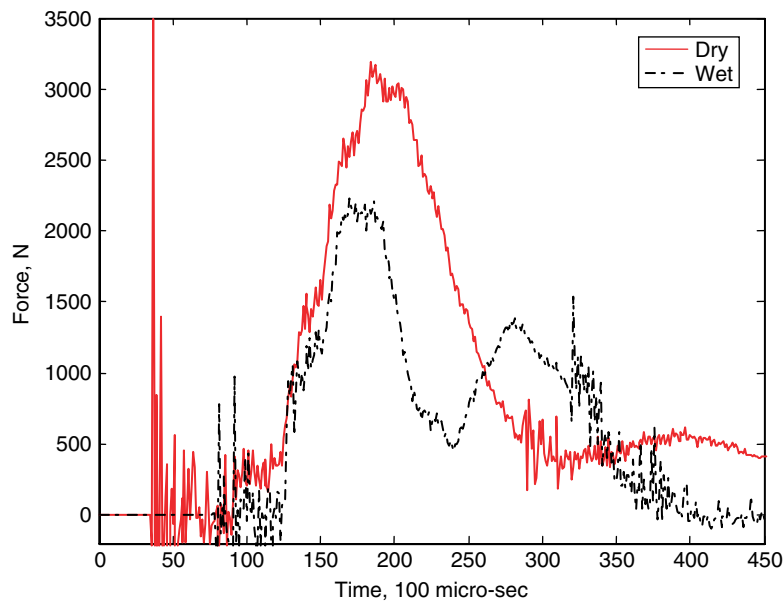


Figure 11 Impact force comparison showing the dry force larger than the wet force at 50.80 cm drop height.

sustained damage. Figure 12 shows the comparison at a drop height of 71.12 cm and the results are what is expected. At that impact height, the delamination size was almost the same between the dry and wet impacts as shown in Fig. 9, which shows the average delamination

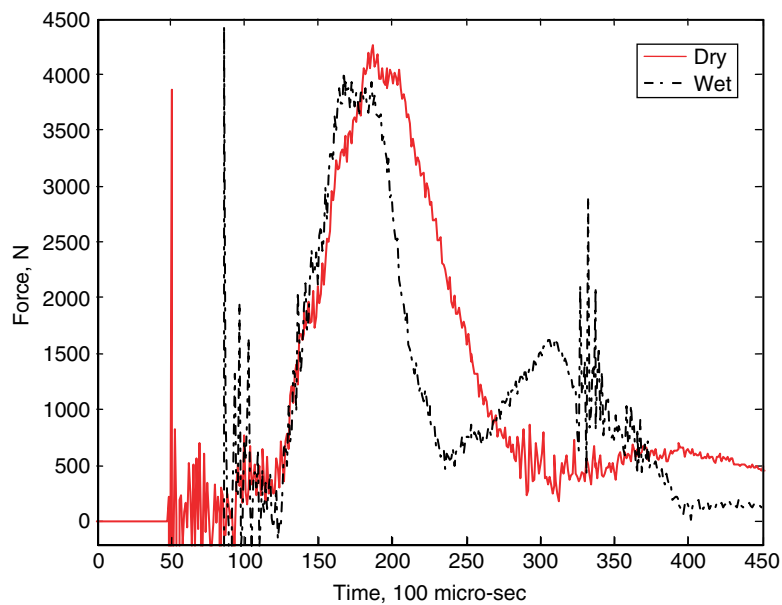


Figure 12 Impact force comparison showing impact force magnitudes becoming similar again due to damage sustained in both samples for drop height of 71.12 cm.

growth slope (i.e. change of damage size divided by the change of the impact height) is higher for the dry impact than the wet impact even though the former started the damage initiation at a larger impact height.

The strain data gathered can help determine what is occurring locally in each sample and it gives a great insight into the fluid structure interaction occurring at each impact height. Being able to compare the dry versus wet strain data at the exact same drop height and weight combination is very important in determining how the fluid structure interaction deforms each composite sample. It is expected that the deformation in the wet samples would be higher at each strain gage throughout the sample than that of its dry counterpart. Strain data for the x and y directions were recorded at the four different strain gages on each sample as shown in Fig. 4.

Figures 13 through 17 show the strain results for all four strain gages along the x- or y-direction at the 15.24 cm drop height. If the strains in the x- and y-axis are similar, only one strain component is plotted. As can be seen at each strain gage, the strain magnitude of the wet composite sample is greater than that of the dry sample in all locations. This is because the wet impact produced a greater impact force than the dry impact before damage occurs. The differences in strain responses between the wet and dry impacts vary from the strain gage location to location. While the difference in strain magnitude as well as its shape in the strain-time history is smaller at strain gage #1 (i.e., near the center of the composite plate), it is much larger at the gage #4 (i.e., near the clamped boundary edges). This result suggests that the FSI effect is not uniform over the clamped plate and is more significant near the clamped boundary. The latter fact can be further confirmed by comparing the x- and y-strain at the gage location #2 (i.e., Fig. 14 vs. Fig. 15). The y-strain is much more different at that location because that component is more affected by the clamped boundary.

Once the damage occurs only for the wet sample, the impact force at the same impact height is greater for the dry impact, which can result in a larger strain for the dry impact. On the other hand, the wet sample has a reduced stiffness with the damage, which can

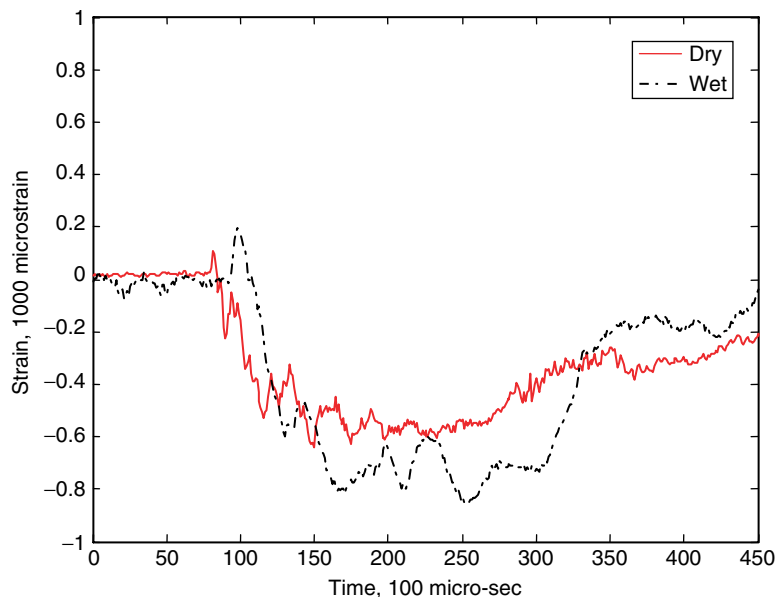


Figure 13 Strain along x-direction at strain gage #1 with impact height 15.24 cm.

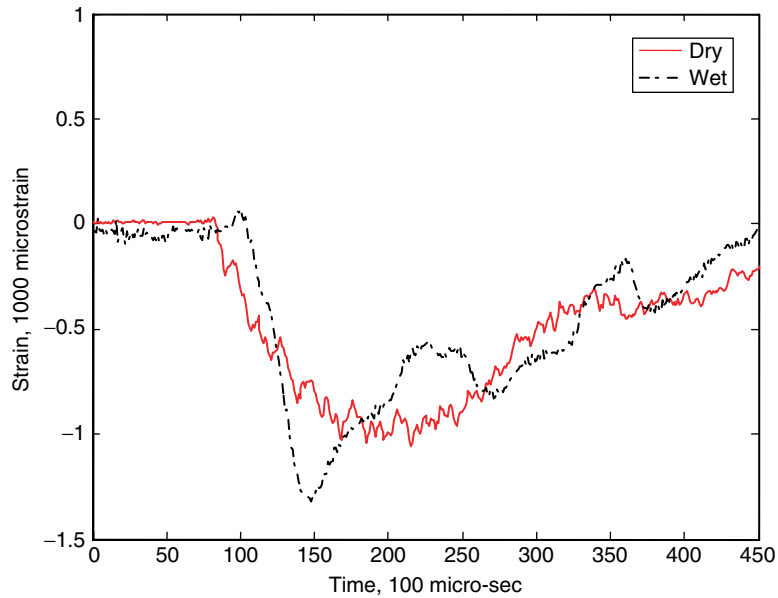


Figure 14 Strain along x-direction at strain gage #2 with impact height 15.24 cm.

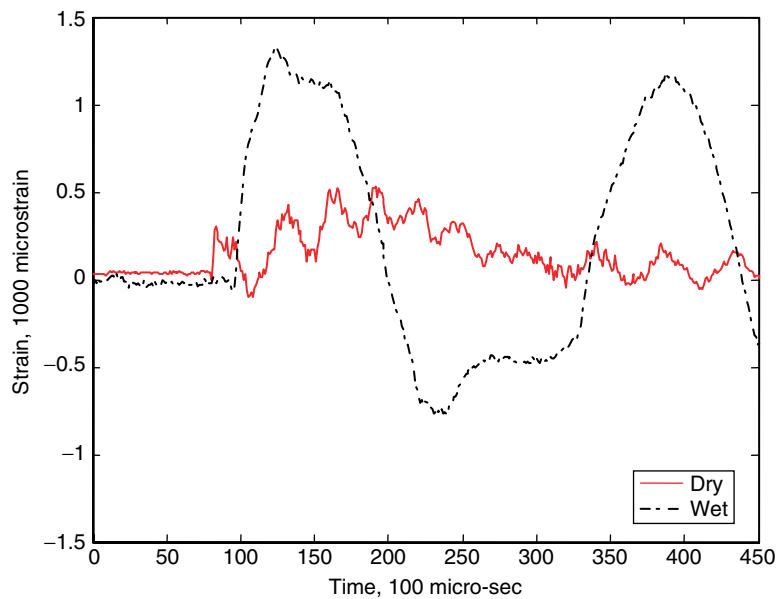


Figure 15 Strain along y-direction at strain gage #2 with impact height of 15.24 cm.

result in a larger strain for the wet impact. As a result, the two facts act against each other. However, the reduced stiffness effect with the wet impact is larger on the strain response than the larger impact force with the dry impact. Hence, the wet impact results in always

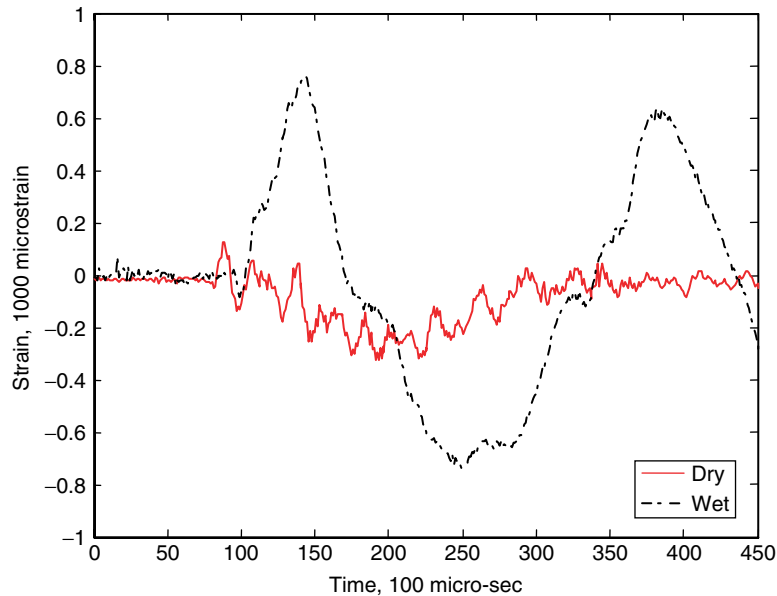


Figure 16 Strain along x-direction at strain gage #3 with impact height 15.24 cm.

larger strains regardless there is damage or not. Besides, the strain-time history plots change in terms of their frequencies and shapes along with damage. Figures 18 through 22 show the strain plots after both wet and dry impact has a similar size of damage at the drop height of 76.20 cm. These figures can be compared to Figs. 13 through 17,

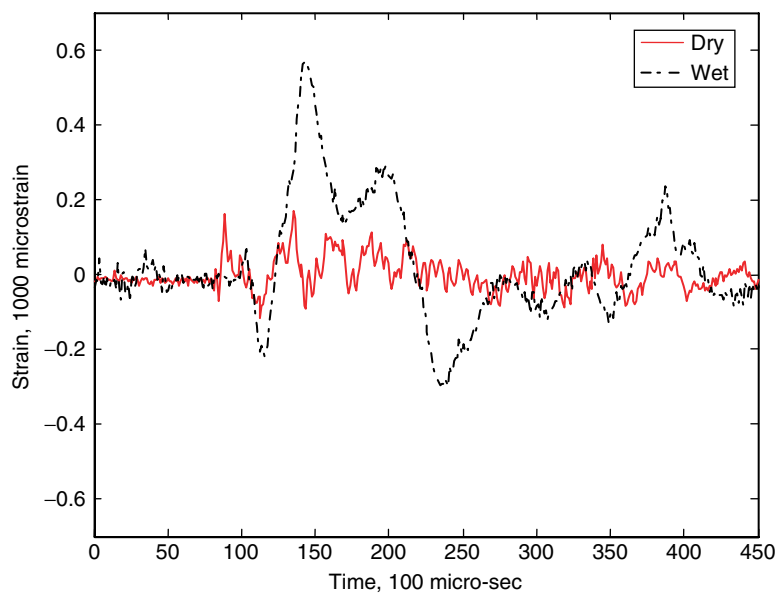


Figure 17 Strain along y-direction at strain gage #4 impact height 15.24 cm.



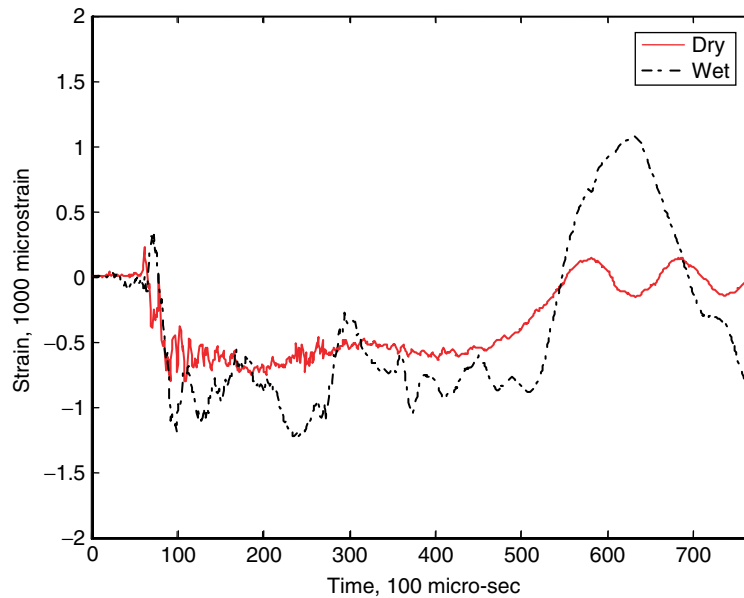


Figure 18 Strain along x-direction at strain gage #1 with impact height of 76.20 cm.

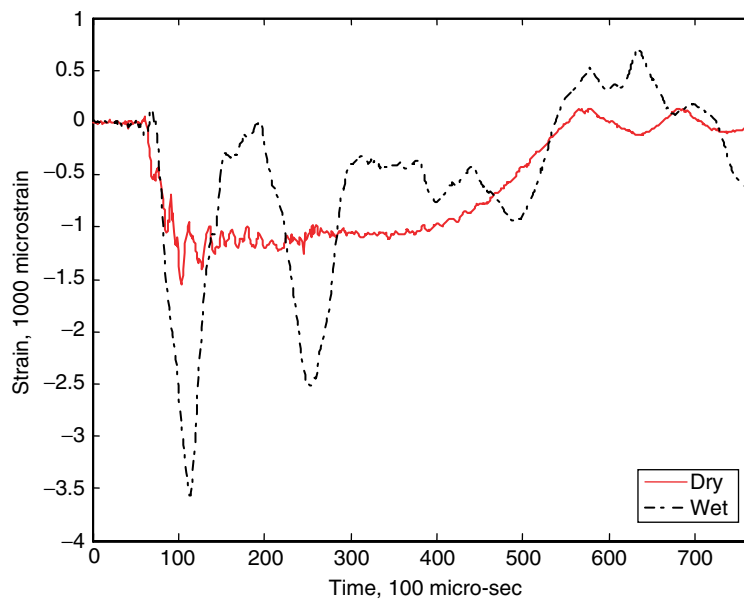


Figure 19 Strain along x-direction at strain gage #2 with impact height of 76.20 cm.

respectively. At the gage location #1, the strain responses of both wet and dry impacts do not change much between the two impact heights except for the magnitude as compared in Figs. 13 and 18. The gage #2 shows a big difference between the dry and wet responses as the impact height increases. The strain with wet impact is much greater than the dry

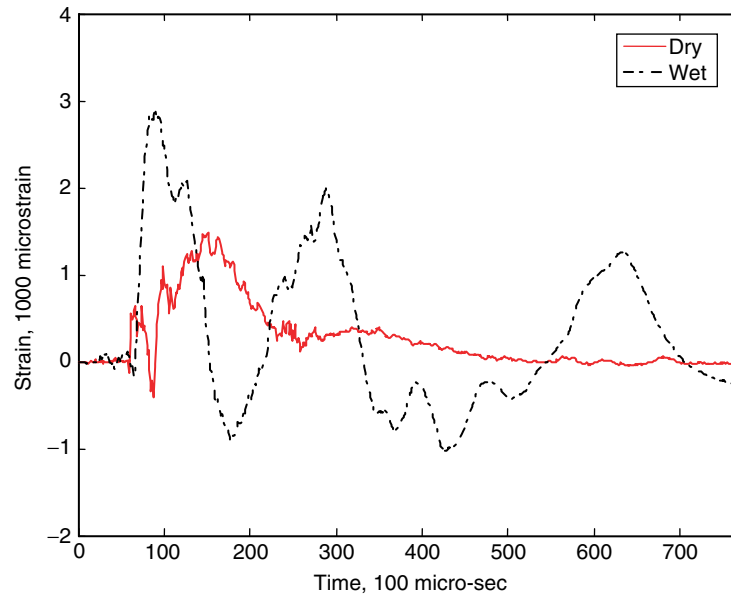


Figure 20 Strain along y-direction at strain gage #2 with impact height of 76.20 cm.

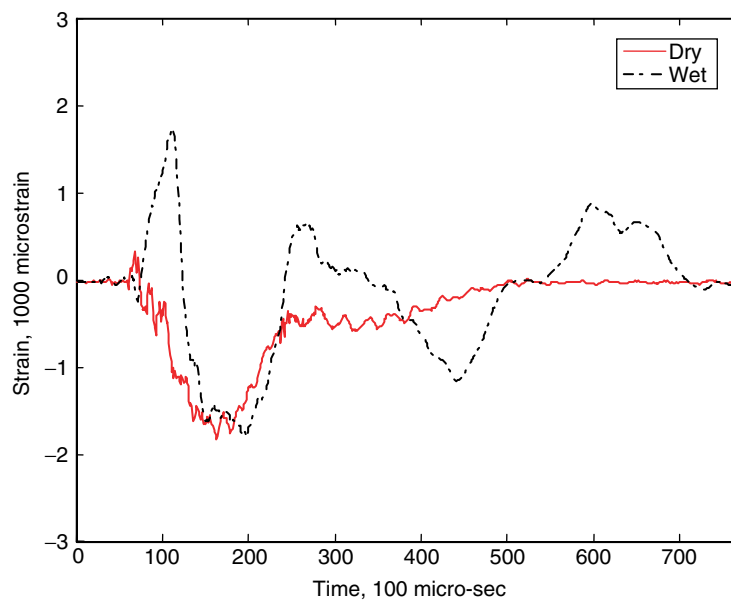


Figure 21 Strain along x-direction at strain gage #3 with impact height of 76.20 cm.

impact at the drop height of 76.20 cm. On the other hand, the magnitude of the compressive strains becomes similar between the wet and dry impacts at the impact height of 76.20 cm. The change in the strain responses between the two different drop heights is the severest at the gage location #4 as shown in Figs. 17 and 22.

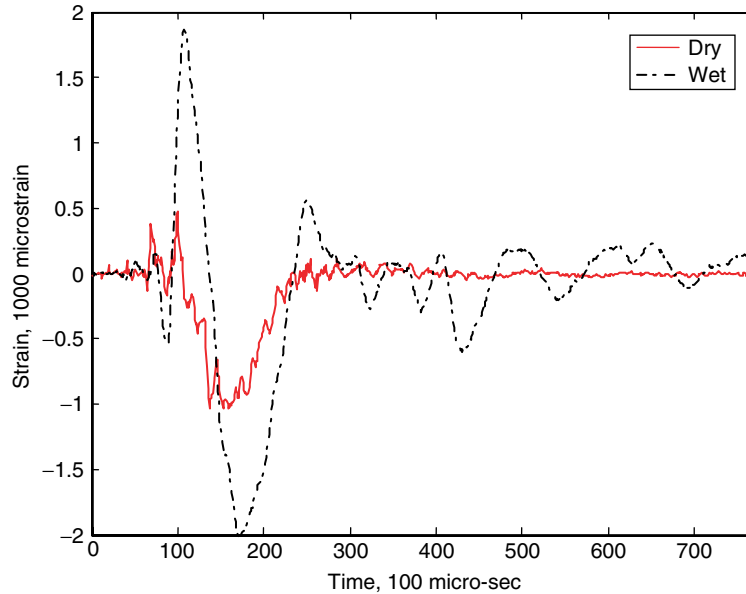


Figure 22 Strain along y-direction at strain gage #4 with impact height of 76.20 cm.

#### 4. CONCLUSION

This study was undertaken to pursue a better understanding of FSI effects on composite materials made from a woven fabric E-glass cloth. In order to investigate the dynamic response of the composite materials with FSI effects under impact loading, two impact conditions were considered. The conditions were dry impact and water-backed dry impact.

Since the composite materials have a very similar density to water, the FSI effects are very significant on the impact force and dynamic response of the plates. Due to the added mass effect of the water, the wet impact force is larger than the dry impact force before any damage occurs in both cases. As a result, the wet impact is more detrimental to the composite material than the dry impact. It is possible to show a quantitative explanation of the added mass effect by calculating Added Mass Factor. This can be seen in the analysis done by Ref. [5]. However, it was found that the added mass effect was not uniform over the whole surface of the plate. This was discovered through the comparison of strain gage responses between the dry and wet impacts at different locations. A location near to the clamped boundary shows a larger FSI effect.

In summary, the experimental results show that the dynamic response in a water environment is significantly different than in a dry environment. The impact force experience in water is larger than the force experience in air which leads to an earlier onset of damage. The strain deformations clearly show that a water environment will produce larger strains than an air environment. Neglecting the FSI effect in composite structures in contact with water would result in the non-conservative design and analysis leading to a pre-mature failure.

#### ACKNOWLEDGEMENT

This work was supported by the Solid Mechanics Program of Office Naval Research. The Program Manager is Dr. Yapa Rajapakse.

## REFERENCES

- [1] Composite Technology, (2010, January 18). *DDG-1000 Zumwalt: Stealth Warship*. [Online]. Available: <http://www.compositesworld.com/articles/ddg-1000-zumwalt-stealth-warship>.
- [2] B. Griffiths, (2006, August 1). *Rudder Gets New Twist With Composites* [Online]. Available: <http://www.compositesworld.com/articles/rudder-gets-new-twist-with-composites>.
- [3] R. Tiron, (2004, July 1). *Navy Gradually Embracing Composite Materials in Ships*. [Online]. Available: [http://www.nationaldefensemagazine.org/archive/2004/July/Pages/Navy\\_gradually\\_3506.aspx](http://www.nationaldefensemagazine.org/archive/2004/July/Pages/Navy_gradually_3506.aspx)
- [4] E.F. Herzberg, "The Annual Cost of Corrosion for DOD," LMI, McLean, VA, Tech. Rep. SKT50T1, Apr. 2006.
- [5] Y. W. Kwon, M. A. Violette, R. D. McCrillis, and J. M. Didoszak, "Transient Dynamic Response and Failure of Sandwich Composite Structures under Impact Loading with Fluid Structure Interaction", *Applied Composite Materials*. (DOI: 10.1007/s10443-012-9249-8).
- [6] Y. W. Kwon and M. A. Violette, "Damage Initiation and Growth in Laminated Polymer Composite Plates with Fluid-Structure Interaction under Impact Loading", *International Journal of Multiphysics*, Vol. 6, No.1, 2012.
- [7] US Composite, (2011). *Fiberglass Cloths* [Online]. Available: <http://uscomposites.com/cloth.html>
- [8] Ashland Inc, (2012). *Derakane epoxy vinyl ester resin* [Online]. Available: <http://www.ashland.com/products/derakane-epoxy-vinyl-ester-resin>
- [9] X. Song, "Vacuum Assisted Resin Transfer Molding (VARTM): Model Development and Verification," Ph.D. dissertation, Dept. Mech. Eng., Virginia Tech Univ., Blacksburg, VA, 2003.
- [10] Y.W. Kwon, A.C. Owens, A.S. Kwon, and J.M. Didoszak, "Experimental Study of Impact on Composite Plates with Fluid-Structure Interaction." *The International Journal of Multiphysics*, Volume 4 Number 3, 2010.
- [11] W.J. Cantwell and J. Morton, "The significance of damage and defects and their detection in composite materials: a review," *The Journal of Strain Analysis for Eng. Design*, doi:10.1243/03093247V271029, Jan. 1992.
- [12] T.W. Shyr and Y.H. Pan, "Impact resistance and damage characteristics of composite laminates," *Composite Struc.* 62, 193–203, 2003.
- [13] W.J. Cantwell and J. Morton, "The impact resistance of composite materials: a review," *Composites* 22(5), 347–362, 1991.
- [14] S. Abrate, "Impact on laminated composite materials: recent advances," *Appl. Mech. Rev.* 47(11), 517–544, 1994.
- [15] M. W. Richardson and M.J. Wiseheart, "Review of low-velocity impact properties of composite materials," *Composites* 27A, 1123–1131, 1996.



# Study of Fluid Effects on Dynamics of Composite Structures

**Y. W. Kwon**

Department of Mechanical and Aerospace  
Engineering,  
Naval Postgraduate School,  
Monterey, CA 93943

*This study investigated the effect of fluid-structure interaction on dynamic responses of submerged composite structures subjected to a mechanical impact loading. The research was focused on finding various parameters that affected the transient dynamic responses of the submerged composite structures. To this end, coupled fluid-structure interaction analyses of composite structures surrounded by a water medium were conducted numerically for various parametric studies and their results were compared with those of dry (i.e., in air) structures in order to understand the role of each parameter under study. Furthermore, modified dry structural models were developed to represent the dynamic responses of the same structures under water with a reasonable accuracy. Those models would be beneficial to predict the structural behaviors under water without an expensive computational or experimental cost. [DOI: 10.1115/1.4002377]*

**Keywords:** composite structures, fluid-structure interaction, transient analysis

## 1 Introduction

Composite materials have been used increasingly for structural applications because of their benefits especially their light weight and high strength. For instance, current surface ship and submarine construction is progressing toward the use of composite structures to reduce the weight and bulk of various structures contained on these vessels. When composite structures are submerged under water, their dynamic responses are significantly affected by the surrounding fluid medium. This is because of fluid-structure interaction (FSI). Especially because composite structures are much lighter than metallic structures, the effect of FSI is expected to be greater.

The effect of FSI has been studied intensively for metallic structures especially for underwater explosive loading. Some of those studies are listed in Refs. [1–6]. Some of them were experimental studies while others were numerical works. On the other hand, a limited number of studies have been undertaken to study FSI in composite structures subjected to underwater explosion [7–13].

Structural response subjected to shock loading is one of the FSI phenomena. As a result, this study investigated the effects of surrounding fluid on dynamic responses of composite structures subjected to a mechanical impact loading. The research was focused on finding major parameters that affected the transient dynamic responses of the submerged structures. For this purpose, coupled fluid-structure interaction analyses of composite structures under water were conducted numerically for various parametric studies and their results were compared with those of dry structures in order to understand the role of each parameter under study. In addition, modified dry structural models were developed to represent the dynamic response of the same structure under water with a reasonable accuracy. Those modified dry structural models would be very beneficial for predicting the submerged structural behaviors without using an expensive coupled fluid-structural analysis. Furthermore, in most cases, a structural dynamic experiment would be difficult to undertake under water; then, the equivalent modified dry structures might be utilized instead.

The next section describes the analysis models followed by the numerical results and discussion. Conclusions are provided at the end.

## 2 Analysis Models

For the finite element analysis, the software called DYTRAN [14] was utilized. In the analysis, composite structures were modeled using 3D solid elements unless stated otherwise. For example, composite axial bars, beams, and plates were modeled using 3D solid elements. Multiple solid elements were used along the thickness direction of those structures in order to represent multiple layers of laminated composites and their bending responses. This was computationally expensive because the 3D solid mesh should be fine enough to represent properly how these structures behave. However, such a model had an advantage of expressing the composite material characteristics fully as well as the FSI with the surrounding water medium. The water medium was modeled for a very large domain in order to simulate the infinite medium. The nonreflecting boundary conditions were imposed on the outer surfaces of the fluid medium. Furthermore, since the composite structure was located at the center of the large fluid medium and the dynamic analysis time was relatively short, the effect of any wave reflected from the fluid boundary due to the imperfect nonreflecting boundary condition was assumed negligible. The fluid mesh was much greater than the structural mesh because the fluid domain was much larger than the structural size and the program could handle the mismatch of fluid and structural meshes. A typical composite plate had about 6400 3D Lagrangian solid elements while the water medium had approximately 100,000 3D Eulerian fluid elements. These numbers of solid and fluid elements were selected based on a mesh sensitivity study to achieve a balance between the accuracy and the computational time.

## 3 Results and Discussion

Composite materials considered in this study were constructed of E-glass fiber and vinyl-ester resin. The fiber architecture was a plain woven cloth. The composite has an inplane elastic modulus of 17 GPa, transverse elastic modulus of 7.9 GPa, inplane shear modulus of 6.6 GPa, transverse shear modulus of 2.9 GPa, inplane Poisson's ratio of 0.3, transverse Poisson's ratio of 0.24, and density of 2020 kg/m<sup>3</sup>. For a dry structure (i.e., in air), there was no

Contributed by the Pressure Vessel and Piping Division of ASME for publication in the JOURNAL OF PRESSURE VESSEL TECHNOLOGY. Manuscript received March 19, 2009; final manuscript received August 11, 2010; published online March 29, 2011. Assoc. Editor: Shawn Kenny.

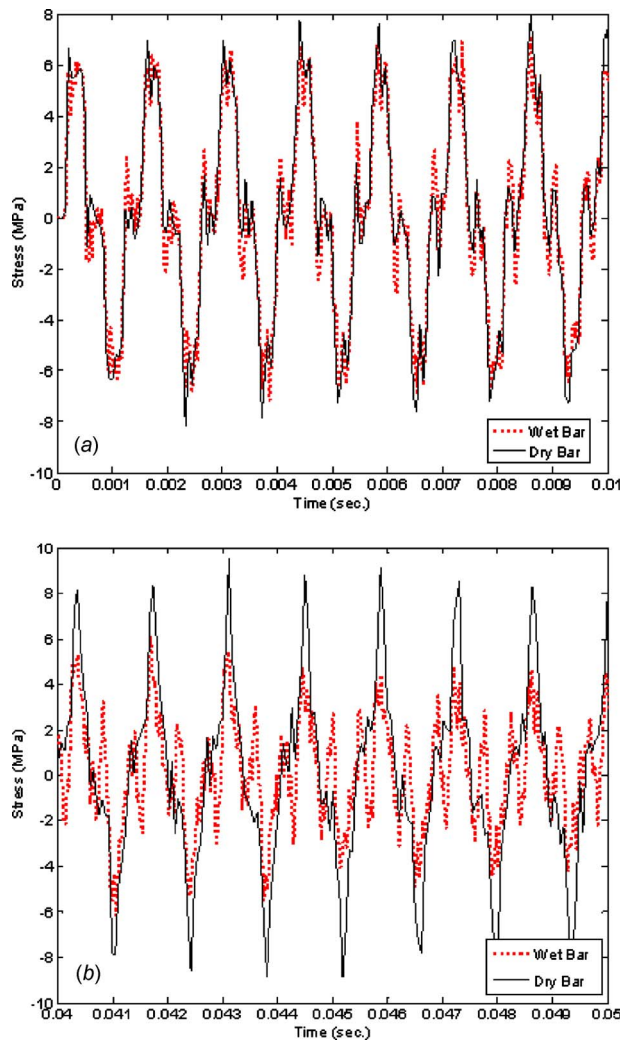


**Fig. 1 Comparison of stresses in the middle of a 3D composite axial bar with free vibration between being in air and being in water: (a) early time response and (b) later time response**

specific modeling of the air medium. On the other hand, the water was modeled with a density of  $1000 \text{ kg/m}^3$  and bulk modulus of  $2.2 \text{ GPa}$ . Water viscosity was neglected.

The first example cases were axial bars of a square cross-section of  $0.1 \times 0.1 \text{ m}^2$  and  $1 \text{ m}$  long. One axial bar was made of an E-glass/vinyl-ester composite while the other one was made of steel. Each bar was placed in air (making it a dry structure) and water (making it a wet structure), respectively. The dry structure did not include the surrounding air medium explicitly because it was negligible. On the other hand, the wet structure included a very large size of the surrounding water medium in order to simulate an infinite fluid domain. For each case, the axial bar had an initial velocity of unity along the longitudinal direction while one end was fixed and the other end was free. Longitudinal vibrations of the bars were compared between being in air and being in water. Figure 1 compares the axial stress at the center of the bar when it vibrated in air and under water, respectively. In order to show the difference in the responses inside the two different media more clearly, the figure separates the early and later time responses. As shown in the figure, longitudinal vibration of the composite bar in the water was damped out as time went along because of the FSI effect. On the other hand, Fig. 2 shows the comparison of longitudinal vibrations of a steel bar between being in air and being in water. Comparing the steel bar to the composite bar of the same dimension (i.e., Figs. 1 and 2), the composite bar

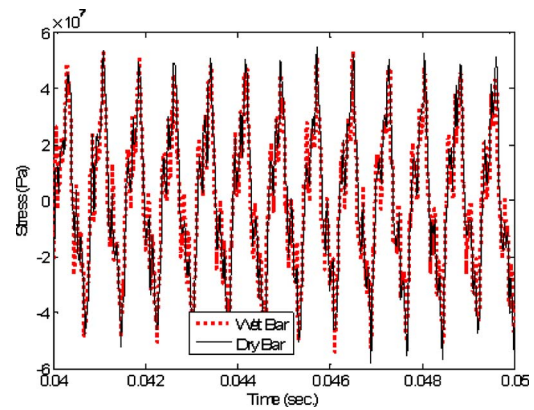


**Fig. 2 Comparison of stresses in the middle of a 3D steel axial bar with free vibration between being in air and being in water**

shows a much greater FSI effect because composite density is much lower than the steel density and is more comparable to the water density. That is, the surrounding water medium dissipated the energy from the composite bar much faster than from the steel bar.

In order to better understand the fluid damping, a simple 1D axial model was considered. The model was an axial member whose left end was fixed and whose right end was attached to an elastic bar, which represented a fluid medium in a simplistic sense. The axial bar had an elastic modulus of  $20 \text{ GPa}$  and density of  $2000 \text{ kg/m}^3$ . It was  $10 \text{ m}$  long with a cross-section of  $0.1 \times 0.1 \text{ m}^2$ . On the other hand, the attached elastic medium, which will be called a pseudofluid medium from now on, had an elastic modulus of  $6 \text{ GPa}$  and density of  $1000 \text{ kg/m}^3$ . The pseudofluid medium was very long so as to represent an infinitely long medium. A constant compressive pressure loading of  $10 \text{ kPa}$  was applied to the right end of the axial bar as a step function until the end of response. Because of the pseudofluid medium attached to the axial member, the axial member dissipates energy as illustrated in Fig. 3. The tip displacement at the right end of the axial member is plotted in Fig. 3. The frequency of the response was about  $60 \text{ Hz}$  and the damping factor  $\zeta$  was approximately  $0.054$ . If there were no pseudofluid medium, the natural frequency would be  $79 \text{ Hz}$ . Therefore, the pseudofluid medium decreased the frequency and increased the damping ratio significantly.

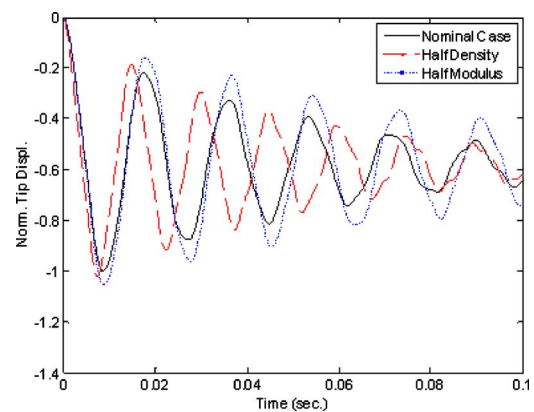


**Fig. 3 Comparison of normalized displacements of the right end of the 1D axial member whose left end was fixed while the right end was under a constant compressive loading and attached to an infinite pseudofluid medium; the density and modulus of pseudofluid medium were varied to determine their effects on the structural member vibration**



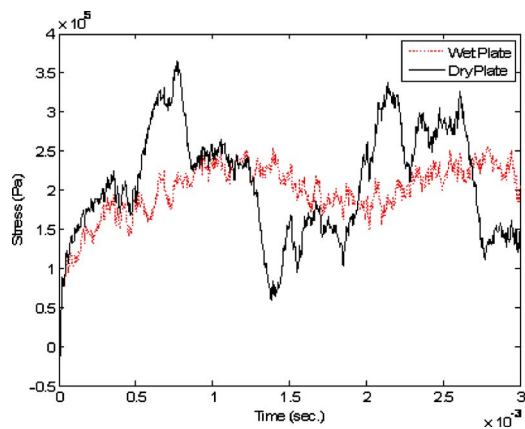


**Fig. 4 Comparison of bending stresses at the center of a square E-glass composite plate under a constant center force while the plate was in air or under water**

The material property of the pseudofluid was varied to determine its effect on the structural vibration. As its density was halved, the frequency increased to 71 Hz while the damping factor decreased to 0.048. On the other hand, as the modulus of the pseudofluid decreased by half, the vibrational frequency of the bar decreased slightly to 58 Hz and the damping factor decreased to 0.037. Examining these results indicated that a lower pseudofluid density or modulus decreased the damping factor. On the other hand, lowering the pseudofluid density increased the frequency of the solid bar while lowering its modulus decreased its frequency.

The next example studied dynamic responses of an E-glass composite plate. The plate was a square plate 0.4 m long and 0.02 m thick. The plate was subjected to a constant force of 100 N at the center in the downward direction. Figure 4 plots the bending stresses at the opposite side of the force when the plate is in air or under water. As expected, water affected the dynamic response of the composite plate significantly. The peak bending stresses were reduced by almost 30% and the plate's major frequency was decreased.

As a parametric study, the density of the composite plate was increased four times while all other properties remained the same as before. Dynamic responses of the heavier composite plate are also compared between being in air and being under water, as seen in Fig. 5. Comparing Figs. 4 and 5 clearly illustrates the effect of the structural density. As the structural density becomes much greater than the fluid density, the FSI effect becomes much

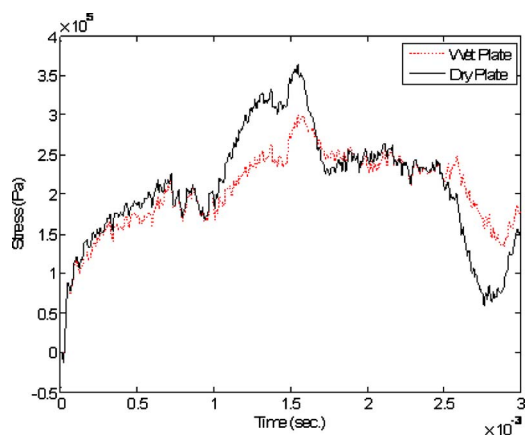


**Fig. 5 Comparison of bending stresses at the center of a square E-glass composite plate under a constant center force while the plate was in air or under water as the density of the plate increased four times as a parametric study**

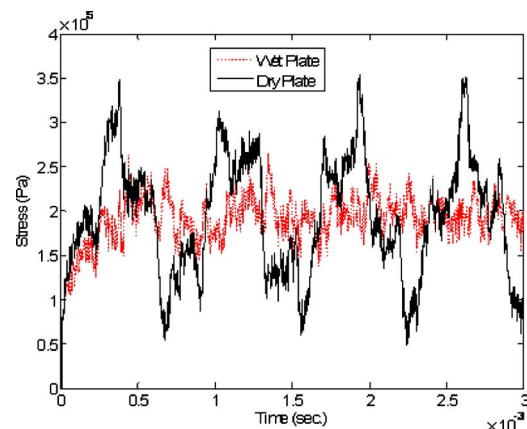


**Fig. 6 Comparison of bending stresses at the center of a square E-glass composite plate under a constant center force while the plate was in air or under water as the inplane elastic modulus of the plate increased four times as a parametric study**

smaller. On the other hand, an increase of the inplane elastic modulus of the composite plate by fourfold still shows a significant effect of FSI as sketched in Fig. 6. Comparing the effects of density and elastic modulus of the composite structure on FSI, FSI was more sensitive to density. In other words, the bending stress varied more significantly with the structural density while both density and modulus affected the frequency of the bending stress as expected. The density decreased the frequency while the modulus increased the frequency.

The next study investigated the FSI effect on a thinner composite plate. In this case, the composite plate had half the thickness of the previous plate. In other words, the ratio of plate length to thickness was 40. The thinner plate was more flexible and the water effect was more significant for the more flexible plate. Comparing Fig. 7 with Fig. 4, it can be observed that the two plates have different frequencies of dynamic responses due to change of stiffness and mass. However, the difference between the dry and wet responses until the first peak is greater for the thinner composite plate as shown in Fig. 7. Thus, the geometry of the structure also affected the FSI significantly.

The subsequent studies were intended to develop modified dry structure models, which would be equivalent to the submerged structural models (i.e., wet models) with a reasonable accuracy. If such an equivalent model were successfully developed, it would reduce the computational and experimental costs significantly. The first case for this study was a 1D axial bar model, as dis-

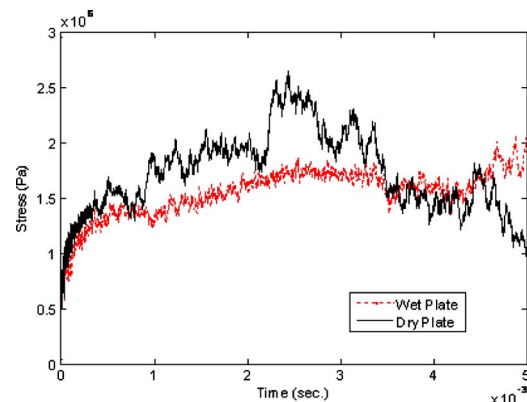


**Fig. 7 Comparison of bending stresses at the center of the bottom surface of a thinner composite plate ( $L/t=40$ ) in air (dry) and under water (wet) conditions**



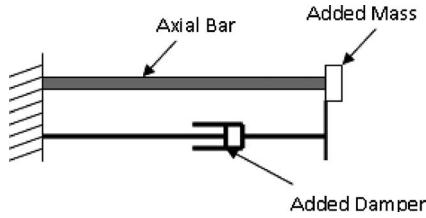


**Fig. 8 Modified dry axial member model that substitutes the axial member submerged under water with FSI**

cussed previously, whose result is shown in Fig. 3. In that analysis, the pseudofluid influenced the structural behavior in terms of both frequency and damping when compared with the response of the same dry structure. As a result, the dry structure (i.e., 1D axial member) was modified by an added mass and added damper at the free end of the axial member, which was in contact with the pseudofluid, as sketched in Fig. 8. The next step was to determine proper values for the added mass and damper. Some reasoning as well as some trial and error suggested the following values for the added mass and damper:

$$m_a = \rho_f V_s = \rho_f A_s L_s \quad (1)$$

$$c_a = z_f(z_s - z_f)/(z_s + z_f) \quad (2)$$

in which  $m_a$  and  $c_a$ , respectively, indicated added mass and damper resulting from the pseudofluid,  $\rho_f$  is the fluid density,  $V_s$  is the volume of the structural member,  $A_s$  is the cross-sectional area of the axial member,  $L_s$  is its length, and subscripts  $s$  and  $f$  denote the structure and pseudofluid, respectively. In addition, the impedance  $z$  can be computed from

$$z_i = A_s \sqrt{\rho_i E_i} \quad (3)$$

in which  $E$  is the elastic modulus and subscript  $i$  is either  $s$  or  $f$ , respectively. As the above equations were used to estimate the added mass and damper, and those were attached to the free end of an axial member, the response of the modified dry axial member was compared with the same member with pseudofluid as described previously. Figure 9 shows the comparison between the two responses. The frequencies between the two models agreed well and the damping effect was reasonably well represented by the modified dry structure.

The next study considered an axial member of dimensions  $1 \times 0.2 \times 0.2$  m<sup>3</sup> submerged in water, which was modeled using 3D solid elements in order to model the wet surface area of the member properly for FSI. The solid member had an elastic modulus of

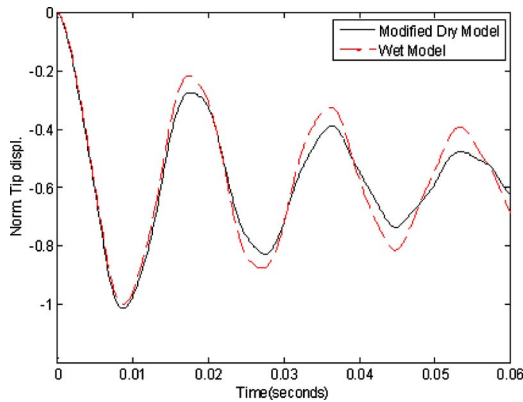


**Fig. 9 Comparison of tip displacements of 1D axial members between the modified dry member with added mass and damper (modified dry model) and the same axial member in contact with pseudofluid (wet model)**

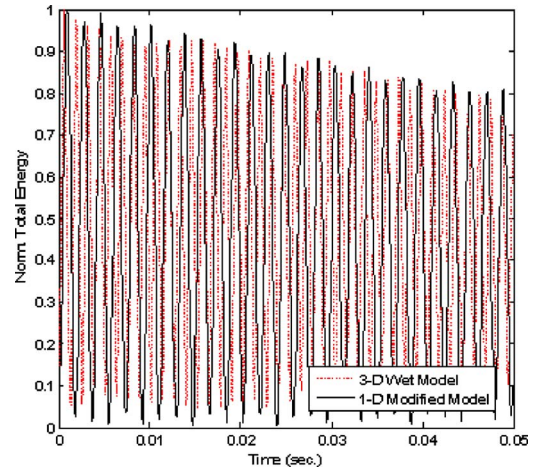


**Fig. 10 Comparison of total energy variations of axial members between 3D wet model and modified 1D model with added mass and damper; the axial member had a cross-sectional area of  $0.2 \times 0.2$  m<sup>2</sup>**

20 GPa and mass density of 2000 kg/m<sup>3</sup>. In order to make the 3D axial model as close as possible to a 1D axial member, the value of Poisson's ratio was set to zero. The axial member was fixed at the left end while the right end was subjected to a constant normal force. The axial member was embedded in a much larger fluid medium whose density was 1000 kg/m<sup>3</sup> with a bulk modulus of 2 GPa. In order to see the energy dissipation of the axial member through FSI as a function of time, the total energy of the axial member is plotted in Fig. 10. The energy dissipation becomes clear in the figure. Furthermore, the 3D wet axial bar model was represented by an equivalent 1D axial member with added mass and damping as sketched in Fig. 8. The same added mass as Eq. (1) was applied to the right end node, which was supposed to be in interaction with fluid. The added damper was computed from

$$\tilde{c}_a = \alpha \tilde{z}_f A_s (z_s - \tilde{z}_f)/(z_s + \tilde{z}_f) \quad (4)$$

where  $\alpha$  is a constant coefficient to be determined and fluid impedance  $\tilde{z}_f$  is computed from

$$\tilde{z}_f = \sqrt{\rho_f \kappa_f} \quad (5)$$

and  $\kappa_f$  is the fluid bulk modulus. As the added mass and damper were added to the 1D axial member with the same force applied to the 3D model, its total energy is also plotted in Fig. 10. The total energy of the 1D model was different from that of the 3D model as expected. However, the energy dissipation rate was almost the same between the 3D wet model and the 1D modified model. Therefore, the energy loss of the structure due to FSI was well represented by the modified 1D model with an added mass and damper. For this calculation as well as the following axial bar simulations,  $\alpha$  was selected as 0.5.

As a parametric study, the cross-section of the axial member was reduced four times (i.e.,  $0.1 \times 0.1$  m<sup>2</sup> versus  $0.2 \times 0.2$  m<sup>2</sup>). That is, the major interaction surface area between the fluid and the structure was reduced. As expected, the energy dissipation from the structure to the surrounding water was significantly decreased as shown in Fig. 11. Furthermore, the density of the reduced cross-sectional bar was decreased by a half. Then, the energy dissipation increased due to the smaller structural density as shown in Fig. 12. Again, the 3D wet model and the 1D equivalent model agreed well for the energy dissipation rate. On the other hand, the elastic modulus had minimum effect on the energy dissipation.

Another 1D equivalent model was examined for a beam bending structure. For this study, a beam 0.4 m long with a  $0.02 \times 0.02$  m<sup>2</sup> cross-sectional area was considered. The same mate-

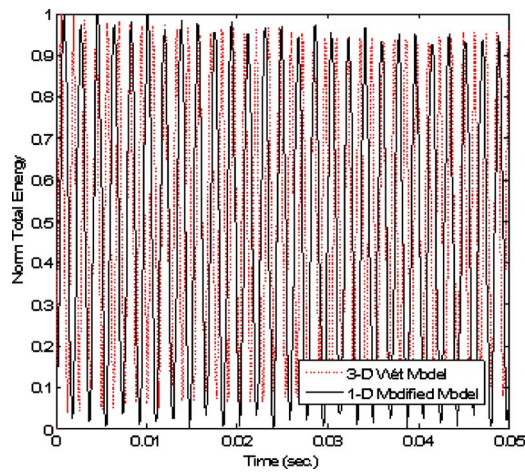


Fig. 11 Comparison of total energy variations of axial members between 3D wet model and modified 1D model with added mass and damper; the axial member had a cross-sectional area of  $0.1 \times 0.1 \text{ m}^2$

rial properties as the previous axial bar were used. The beam was fixed at both ends and a transient force was applied at the center of the beam. The force varied linearly from 100 N initially to zero at the time of 0.01 s. After this time, there was no external force applied to the beam. For the wet 3D beam model, 3D solid elements were used again with a large surrounding water medium. On the other hand, for an equivalent 1D beam model, the added mass and damping were attached to every beam node as sketched in Fig. 13. Because the diagonal mass matrix was used for the beam structure, the added mass was also included in the diagonal terms of the mass matrix. For the  $i$ th beam element with two nodes, the added mass was computed as

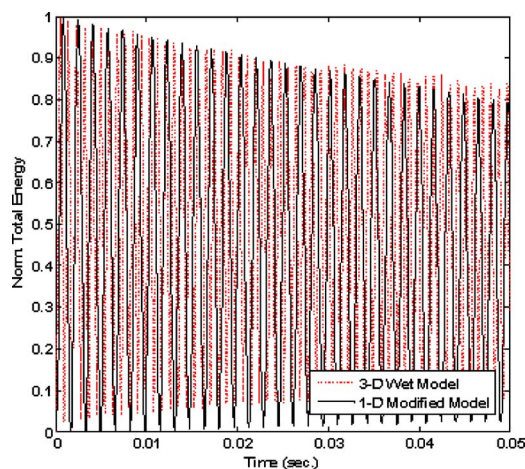


Fig. 12 Comparison of total energy variations of axial members between 3D wet model and modified 1D model with added mass and damper; the axial member had a cross-sectional area of  $0.1 \times 0.1 \text{ m}^2$ , and its density was also reduced by a half

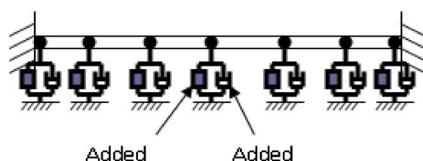


Fig. 13 Modified dry beam model that represents the beam structure submerged under water with FSI

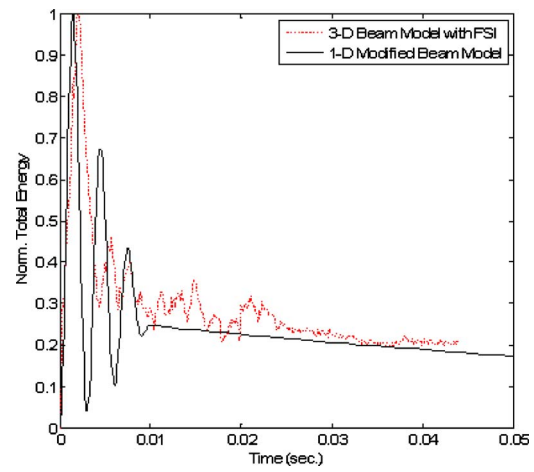


Fig. 14 Comparison of total energy variations of beam members between 3D wet model and modified 1D model with added mass and damper

$$m_a^i = \rho_f V^i / 2 \quad (6)$$

and its value was added to both nodes of the element. Here, superscript  $i$  denotes the  $i$ th element and  $V$  is the volume of the beam element. The added damper was also applied to each node as a diagonal component of the damping matrix and its value was calculated from the same equation as Eq. (4). However,  $A_s$  in the equation is the cross-sectional area of the beam element such that  $A_s = 2w_s^i l_s^i$ , where  $w_s^i$  is the width of the  $i$ th beam element and  $l_s^i$  is the length of the element. The constant “2” was applied because the beam interacts with water on both the top and bottom sides. In addition,  $\alpha = 0.75$  was selected. The total energy variation as a function of time is plotted in Fig. 14. As seen in the figure, the total energy fluctuation decreases significantly after the external force becomes zero after 0.01 s. The energy decrease due to FSI is clearly shown in the figure. Both wet 3D and equivalent 1D models indicate the energy dissipation very closely.

Finally, so as to further understand the FSI effect, the hydrodynamic mass was estimated and added to the dry plate. Then, the dynamic response of the dry composite plate with hydrodynamic mass, or added mass, was compared with that under water and in air. The added mass effect is not considered to be uniform throughout the plate surface. However, for simplicity as the first approximation, a uniform added mass of  $\pi \rho_f L^3 / 4$  was applied to the composite plate. Here,  $\rho_f$  is the water density and  $L$  is the length of a square plate. Figures 15 and 16 plot the bending

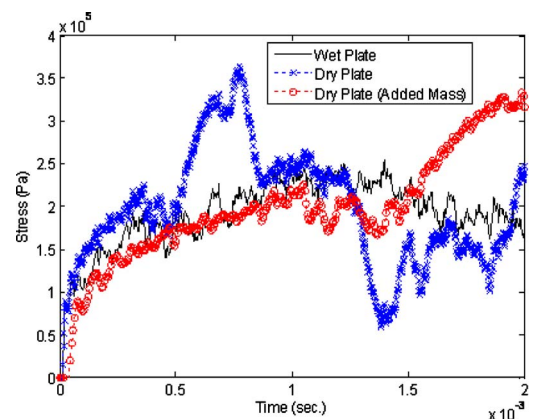
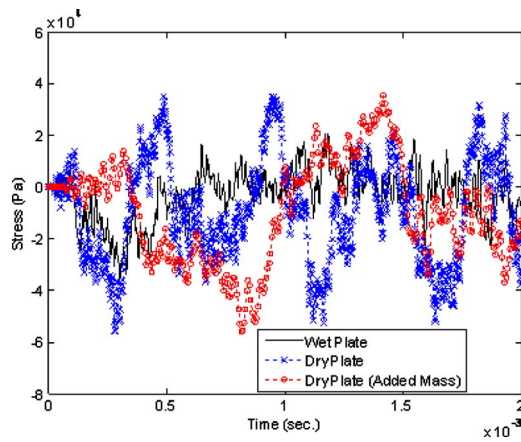


Fig. 15 Comparison of bending stresses at the center point of the bottom surface of a composite plate in air (dry), under water (wet), and in air with added mass



**Fig. 16 Comparison of bending stresses at the quarter point along the diagonal line of the bottom surface of a composite plate in air (dry), under water (wet), and in air with added mass**

stresses in the composite plate under a constant center force. Figure 15 compares the stress at the plate center for three cases, namely, in air, under water, and in air with added mass. Figure 16 compares the same three cases at the quarter point along the diagonal line of the plate. As shown in Fig. 15, the dry plate response with the added mass matches that of the wet plate for an early time. This indicates that the added mass represented the FSI effect well up to that time line. This is because the center point of the plate has the least constraint from the clamped boundaries. However, as time went on, the damping effect was not properly represented by the added mass only. On the other hand, because the quarter point is more constrained from the fixed edges, the uniform added mass did not represent the FSI effect properly. The effects of added mass and damping on the composite plates and shells will be studied further in subsequent research.

#### 4 Conclusions

This study investigated the effect of water on the dynamic response of submerged composite structures. Because composite structures were very light and only about twice as heavy as the water for E-glass composites, the effect of FSI was very significant. The FSI completely changed the structural dynamic behaviors such as frequencies, damping, and magnitudes. This would change also the failure of composite structures under water, which is under ongoing study.

By comparing the wet structural response to the dry structural response, it could be observed that a change of density of a struc-

ture played a more important role on FSI than elastic modulus. Furthermore, the interaction area between the fluid and structure was also significant for FSI.

Modified dry structural models for axial bar and beam structures were developed to represent the structural behavior under water by adding properly estimated mass and damping terms. The former models provided reasonable accuracies in terms of energy dissipation through the surrounding water medium. These models can save expensive computational or experimental costs to predict the wet structural behavior. Modified dry models for composite plates and shells representing such wet structures would be developed in subsequent research.

#### Acknowledgment

The work presented here was supported and funded by ONR. The Program Manager is Dr. Yapa D.S. Rajapakse.

#### References

- [1] Kwon, Y. W., and Fox, P. K., 1993, "Underwater Shock Response of a Cylinder Subjected to a Side on Explosion," *Comput. Struct.*, **48**(4), pp. 637–646.
- [2] Kwon, Y. K., Bergensen, J. K., and Shin, Y. S., 1994, "Effect of Surface Coatings on Cylinders Exposed to Underwater Shock," *Shock Vib.*, **1**(3), pp. 637–646.
- [3] Malone, P. E., and Shin, Y. S., 2000, "Sensitivity Analysis of Coupled Fluid Volume to Ship Shock Simulation," *Proceedings of 71st Shock and Vibration Symposium*, Crystal City, VA, Nov. 6–9.
- [4] Shin, Y. S., 2004, "Ship Shock Modeling and Simulation for Far-Field Underwater Explosion," *Comput. Struct.*, **82**(23–26), pp. 2211–2219.
- [5] Shin, Y. S., and Park, S. Y., 1999, "Ship Shock Trial Simulation of USS John Paul Jones (DDG 53) Using LS-DYNA/USA: Three Dimensional Analysis" *70th Shock and Vibration Symposium Proceedings*, Vol. 1.
- [6] Shin, Y. S., and Schneider, N. A., 2003, "Ship Shock Trial Simulation of USS Winston S. Churchill (DDG81): Modeling and Simulation Strategy and Surrounding Fluid Volume Effects," *74th Shock and Vibration Symposium*, San Diego, CA, Oct. 27–31.
- [7] Rasmussen, E. A., 1992, "Underwater Shock Testing and Analysis of Composite Cylinders," *Shock and Vibration Symposium*.
- [8] Rousseau, M. P., Kwon, Y. W., and Shin, Y. S., 1993, "Modeling the Effects of Shock on an Underwater Composite Cylinder," *64th Shock and Vibration Symposium*, Ft. Walton Beach, FL.
- [9] Mouritz, A. P., 1995, "The Damage to Stitched GRP Laminated by Underwater Explosion Shock Loading," *Compos. Sci. Technol.*, **55**, pp. 365–374.
- [10] Mouritz, A. P., 1996, "The Effect of Underwater Explosion Shock Loading of the Flexural Properties of GRP Laminates," *Int. J. Impact Eng.*, **18**(2), pp. 129–139.
- [11] McCoy, W., and Sun, C. T., 1997, "Fluid-Structure Interaction Analysis of a Thick-Section Composite Cylinder Subjected to Underwater Blast Loading," *Compos. Struct.*, **37**(1), pp. 45–55.
- [12] Gong, S. W., and Lam, K. Y., 1998, "Transient Response of Stiffened Composite Submersible Hull Subjected to Underwater Explosive Shock," *Compos. Struct.*, **41**(1), pp. 27–37.
- [13] Lam, K. Y., Zong, Z., and Wang, Q. X., 2003, "Dynamic Response of a Laminated Pipeline on the Seabed Subjected to Underwater Shock," *Composites, Part B*, **34**, pp. 59–66.
- [14] 2008, *DYTRAN 2008 r1 User's Guide*, MSC Software Corporation, Santa Ana, CA.



# *Analysis of Laminated and Sandwich Composite Structures Using Solid-like Shell Elements*

**Y. W. Kwon**

## **Applied Composite Materials**

An International Journal for the Science  
and Application of Composite Materials

ISSN 0929-189X  
Volume 20  
Number 4

Appl Compos Mater (2013) 20:355-373  
DOI 10.1007/s10443-012-9273-8



**Your article is protected by copyright and all rights are held exclusively by Springer Science+Business Media B.V. (outside the USA). This e-offprint is for personal use only and shall not be self-archived in electronic repositories. If you wish to self-archive your article, please use the accepted manuscript version for posting on your own website. You may further deposit the accepted manuscript version in any repository, provided it is only made publicly available 12 months after official publication or later and provided acknowledgement is given to the original source of publication and a link is inserted to the published article on Springer's website. The link must be accompanied by the following text: "The final publication is available at [link.springer.com](http://link.springer.com)".**

# Analysis of Laminated and Sandwich Composite Structures Using Solid-like Shell Elements

Y. W. Kwon

Published online: 17 June 2012

© Springer Science+Business Media B.V. (outside the USA) 2012

**Abstract** A new solid-like shell element was formulated which is suitable for analysis of laminated and sandwich composite structures. Then, a multiscale analysis technique was implemented to the shell element formulation so that micro-level stresses and strains (i.e. stresses and strains in reinforcing fibers and the binding matrix) in those structures can be computed. The shell element has three displacement degrees of freedom per node like a 3-D solid element. Therefore, the shell elements can be stacked easily on top of one another like 3-D solid elements in order to represent multiple layers through the thickness of laminated and sandwich structures. The effect of a thin resin or adhesive layer in laminated and sandwich composite structures was investigated on both static and the dynamic responses of the structures using the developed shell elements. The study showed an apparent effect of the resin/adhesive layer even though it is very thin. As a result, the present shell element can be used effectively to include those thin layers in finite element analysis models of laminated and sandwich composite structures.

**Keywords** Solid-like shell element · Laminated and sandwich composite · Adhesive layer · Resin layer · Multiscale analysis

## 1 Introduction

Plates and shells support transverse loads effectively through fiber directional stresses. As a result, the finite element analysis method has been applied to the design and analysis of plates and shell structures. Initially, plate/shell finite elements were developed based on their classical theories [1–3]. However, the rigorous relationship between the transverse displacement and slopes was not easy to be satisfied at the interfaces of the finite elements. As a result, the relationship was relaxed by introducing the transverse shear energy as included in the Resissner-Mindlin theory [4, 5]. One of

---

Y. W. Kwon (✉)

Department of Mechanical & Aerospace Engineering, Naval Postgraduate School, Monterey,  
CA 93943, USA  
e-mail: ywkwon@nps.edu

the drawbacks of the latter formulation was so called “shear locking”. As the plate/shell thickness becomes smaller, the shear energy begins to dominate over the bending energy, which should be the opposite in physics. In order to overcome the problem, many different techniques have been developed and proposed [6, 7]. Furthermore, the shell element formulations were started from the 3-D solid geometry by reducing the thickness dimension and assuming the inplane displacements vary linearly through the thickness direction [8–11]. This was achieved by introducing the inplane displacements at a reference plate/shell plane (mostly at the midplane along the thickness) and rotations (or called slopes) of the reference plane. Naturally, the plate/shell elements have both displacements and rotations as nodal degrees of freedom.

Having rotational degrees of freedom makes it inconvenient to stack plate/shell elements on top of one another so as to maintain deformation continuity from one element to another when stacked together. Hence, most laminated and sandwich structures have been modeled using a single plate/shell element through the thickness. Properly smeared material properties were applied to the single layer element. Using a single element through the thickness certainly reduces the total degrees of freedom in the finite element model. The overall stiffness behavior such as global deformation of such composite structures can be well predicted using the smeared properties with a single layer model. However, strength and failure depends on local characteristics. Therefore, the smearing technique with a single layer of plate/shell elements will miss such critical local information which is important to predict fracture of the structure.

There have been some efforts to develop plate/shell elements with displacement degrees of freedom without rotational degrees of freedom. References [12, 13] developed plate elements for a flat structure. These elements were not straightforward for extension into a curved structure. Some shell elements with displacement only degrees of freedom were developed [14–16]. One shell element has seven degrees of freedom per node [14] while another element used assumed strain methods [15].

The objective of this study is to develop a simple solid-like plate/shell element which is geometrically identical to a 3-D solid element in terms of node locations and nodal degrees of freedom. As a result, the plate/shell elements can be stacked easily like 3-D solid elements, and the former elements are fully compatible with 3-D solid elements without introducing any special or additional condition between the two types of elements.

The next section shows the formulation of the new solid-like plate/shell finite element. After that, the multiscale analysis technique is presented for a woven fabric composite structure. A set of examples are presented first to check the accuracy of the developed plate/shell elements. Then, another set of examples are examined to investigate the microscale stresses in sandwich structures made of woven fabric skin layers. In those examples, multiple layers of plate/shell elements are used across the structural thickness. Finally, conclusions are provided at the end.

## 2 Shell Element Formulation

### 2.1 Displacement Interpolations

The shell element has the same geometric feature as a 3-D solid element except that the shell element has a much smaller dimension along the thickness direction compared to inplane dimensions. As a result, it is assumed to have a negligible normal strain in the thickness

direction. Because the present shell element has three displacement degrees of freedom like 3-D solid elements, three displacements can be expressed as

$$u = u(x, y, z) \quad (1)$$

$$v = v(x, y, z) \quad (2)$$

$$w = w(x, y) \quad (3)$$

where  $u$ ,  $v$ , and  $w$  are two inplane displacements and the transverse displacement of the shell element in terms of its local coordinate system  $(x, y, z)$ , respectively. The local axes  $x$  and  $y$  lie on the inplane of the shell element while  $z$  is the local transverse axis (i.e. in the thickness orientation of the shell element) as sketched in Fig. 1. The global reference coordinate system is also shown in the figure.

The interpolations for displacements inside the shell element in terms of nodal displacements can be written as

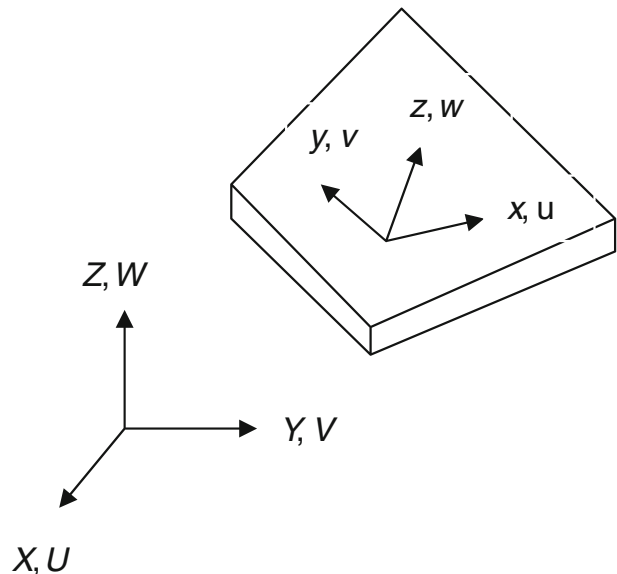
$$u(x, y, z) = \sum_{i=1}^{n_1} \sum_{j=1}^{n_2} N_i(\xi, \eta) H_j(\zeta) u_{ij} \quad (4)$$

$$v(x, y, z) = \sum_{i=1}^{n_1} \sum_{j=1}^{n_2} N_i(\xi, \eta) H_j(\zeta) v_{ij} \quad (5)$$

$$w(x, y, z) = \sum_{i=1}^{n_1} \sum_{j=1}^{n_2} N_i(\xi, \eta) H_j(\zeta) w_{ij} \quad (6)$$

in which  $N_i(\xi, \eta)$  is the 2-D shape function for the inplane interpolation while  $H_j(\zeta)$  is the 1-D shape function for the transverse interpolation. Here,  $(\xi, \eta, \zeta)$  is the natural coordinate system

**Fig. 1** Shell element in terms of its local and global coordinate systems





associated with the isoparametric shape functions  $N_i$  and  $H_j$ . Because the transverse normal strain is neglected, two nodes are enough to represent the inplane displacement along the thickness of the shell element, i.e.  $n_2=2$  in Eqs. (4) through (6). On the other hand, the number of nodes in the inplane directions may be selected depending on the need of higher order shell elements. However, for simplicity, bilinear shape functions are selected in the present formulation with  $n_1=4$ . The resultant shell element is shown in Fig. 2 in terms of the natural coordinate system. As a result, the shell element is identical to the eight-node solid element in terms of the nodal degrees of freedom. This means that the present shell element can be connected to regular 3-D elements naturally without any special operation.

## 2.2 Stresses and Strains

The strain components are divided into two groups, inplane strains and transverse shear strains. The inplane strains in terms of the shell local coordinate system are expressed as

$$\{\varepsilon_{inpl}\} = \begin{Bmatrix} \varepsilon_x \\ \varepsilon_y \\ \gamma_{xy} \end{Bmatrix} = \begin{bmatrix} \frac{\partial}{\partial x} & 0 & 0 \\ 0 & \frac{\partial}{\partial y} & 0 \\ \frac{\partial}{\partial y} & \frac{\partial}{\partial x} & 0 \end{bmatrix} \begin{Bmatrix} u \\ v \\ w \end{Bmatrix} \quad (7)$$

while the transverse shear strains are given by

$$\{\varepsilon_{tranv}\} = \begin{Bmatrix} \gamma_{xz} \\ \gamma_{yz} \end{Bmatrix} = \begin{bmatrix} \frac{\partial}{\partial z} & 0 & \frac{\partial}{\partial x} \\ 0 & \frac{\partial}{\partial z} & \frac{\partial}{\partial y} \end{bmatrix} \begin{Bmatrix} u \\ v \\ w \end{Bmatrix} \quad (8)$$

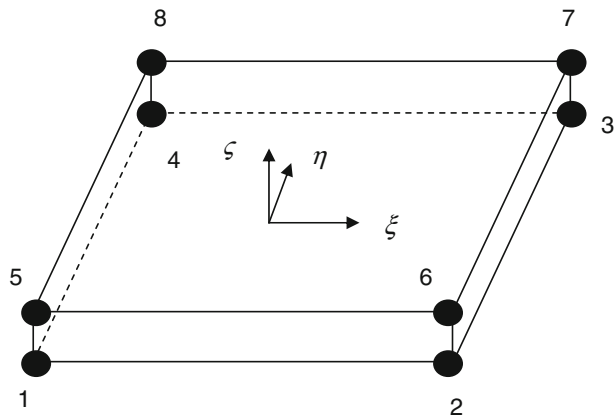
As noted previously, the transverse normal strain was neglected. Substitution of Eqs. (4) through (6) into Eq. (7) yields the expression for the inplane strains in terms of nodal displacements.

$$\{\varepsilon_{inpl}\} = [B_b]\{d\} \quad (9)$$

where

$$[B_b] = [B_{b1} \quad B_{b2}] \quad (10)$$

**Fig. 2** Shell element in terms of natural coordinate system



$$[B_{bi}] = \begin{bmatrix} H_i \frac{\partial N_1}{\partial x} & 0 & 0 & H_i \frac{\partial N_2}{\partial x} & 0 & 0 & H_i \frac{\partial N_3}{\partial x} & 0 & 0 & H_i \frac{\partial N_4}{\partial x} & 0 & 0 \\ 0 & H_i \frac{\partial N_1}{\partial y} & 0 & 0 & H_i \frac{\partial N_2}{\partial y} & 0 & 0 & H_i \frac{\partial N_3}{\partial y} & 0 & 0 & H_i \frac{\partial N_4}{\partial y} & 0 \\ H_i \frac{\partial N_1}{\partial y} & H_i \frac{\partial N_1}{\partial x} & 0 & H_i \frac{\partial N_2}{\partial y} & H_i \frac{\partial N_2}{\partial x} & 0 & H_i \frac{\partial N_3}{\partial y} & H_i \frac{\partial N_3}{\partial x} & 0 & H_i \frac{\partial N_4}{\partial y} & H_i \frac{\partial N_4}{\partial x} & 0 \end{bmatrix} \quad (11)$$

$$\{d_{local}\}^T = \{d_1 \quad d_2 \quad d_3 \quad d_4 \quad d_5 \quad d_6 \quad d_7 \quad d_8\} \quad (12)$$

$$\{d_i\} = \{u_i \quad v_i \quad w_i\} \quad (13)$$

The sequence in node numbers in Eq. (12) is shown in Fig. 2. Likewise the substitution of Eqs. (4) through (6) into (8) gives the transverse shear strains in terms of the nodal displacements.

$$\{\varepsilon_{trans}\} = [B_s]\{d\} \quad (14)$$

where

$$[B_s] = [B_{s1} \quad B_{s2}] \quad (15)$$

$$[B_{si}] = \begin{bmatrix} N_i \frac{\partial H_1}{\partial z} & 0 & H_i \frac{\partial N_1}{\partial x} & N_i \frac{\partial H_1}{\partial z} & 0 & H_i \frac{\partial N_2}{\partial x} & N_i \frac{\partial H_1}{\partial z} & 0 & H_i \frac{\partial N_3}{\partial x} & N_i \frac{\partial H_1}{\partial z} & 0 & H_i \frac{\partial N_4}{\partial x} \\ 0 & N_i \frac{\partial H_1}{\partial z} & H_i \frac{\partial N_1}{\partial y} & 0 & N_i \frac{\partial H_1}{\partial z} & H_i \frac{\partial N_2}{\partial y} & 0 & N_i \frac{\partial H_1}{\partial z} & H_i \frac{\partial N_3}{\partial y} & 0 & N_i \frac{\partial H_1}{\partial z} & H_i \frac{\partial N_4}{\partial y} \end{bmatrix} \quad (16)$$

The inplane stresses and transverse shear stresses are expressed using proper constitutive equations. For an orthotropic material, the constitutive expression for the inplane stresses and strains is

$$[D_b] = \begin{bmatrix} D_{11} & D_{12} & 0 \\ D_{12} & D_{22} & 0 \\ 0 & 0 & D_{33} \end{bmatrix} \quad (17)$$

where

$$D_{11} = \frac{E_1}{1 - \nu_{12}\nu_{21}} \quad (18)$$

$$D_{12} = \frac{E_2 \nu_{21}}{1 - \nu_{12}\nu_{21}} \quad (19)$$

$$D_{22} = \frac{E_2}{1 - \nu_{12}\nu_{21}} \quad (20)$$

$$D_{33} = G_{12} \quad (21)$$

Here,  $E_i$  and  $\nu_{ij}$  are the elastic modulus and Poisson's ratio, while  $G_{ij}$  is the shear modulus of the inplane directions. Similarly, the constitutive matrix for the transverse shear stresses and strains is expressed as

$$[D_s] = \begin{bmatrix} G_{13} & 0 \\ 0 & G_{23} \end{bmatrix} \quad (22)$$

### 2.3 Element Stiffness Matrix

The element stiffness matrix with respect to the shell local coordinate system can be written as

$$[K_{local}] = \int_{\Omega^e} [B_b]^T [D_b] [B_b] d\Omega + \int_{\Omega^e} [B_s]^T [D_s] [B_s] d\Omega + \sum_{i=1}^4 \alpha_i (w_i - w_{i+4})^2 \quad (23)$$

The first term is from the bending energy and the second term is from the transverse shear energy. In order to prevent transverse shear locking, the second term is integrated using the reduced integration order. Because the transverse normal strain is neglected, the penalty method is applied to the transverse displacements as shown in the third term.

The final step is to apply the coordinate transformation from the local axes to the global axes so that every element stiffness matrix can be assembled properly. Let  $(l_1, m_1, n_1)$  be the direction cosines between  $x$ - and  $X$ -axis,  $(l_2, m_2, n_2)$  be the direction cosines between  $y$ - and  $Y$ -axis, and  $(l_3, m_3, n_3)$  be the direction cosines between  $z$ - and  $Z$ -axis.

The compatibility of displacement between the two coordinate systems requires

$$\begin{Bmatrix} \frac{u^i + u^{i+4}}{2} \\ \frac{v^i + v^{i+4}}{2} \\ \frac{w^i + w^{i+4}}{2} \end{Bmatrix} = \begin{bmatrix} l_1 & m_1 & n_1 \\ l_2 & m_2 & n_2 \\ l_3 & m_3 & n_3 \end{bmatrix} \begin{Bmatrix} \frac{U^i + U^{i+4}}{2} \\ \frac{V^i + V^{i+4}}{2} \\ \frac{W^i + W^{i+4}}{2} \end{Bmatrix} \quad (24)$$

and

$$\begin{Bmatrix} u^{i+4} - u^i \\ v^{i+4} - v^i \\ w^{i+4} - w^i \end{Bmatrix} = \begin{Bmatrix} U^{i+4} - U^i \\ V^{i+4} - V^i \\ W^{i+4} - W^i \end{Bmatrix} \quad (25)$$

where the superscript 'i' denotes the node from 1 to 4 in Fig. 2. Solving the two set of equations results in

$$\begin{Bmatrix} u^i \\ v^i \\ w^i \\ u^{i+4} \\ v^{i+4} \\ w^{i+4} \end{Bmatrix} = \frac{1}{2} \begin{bmatrix} l_1 + 1 & m_1 & n_1 & l_1 - 1 & m_1 & n_1 \\ l_2 & m_2 + 1 & n_2 & l_2 & m_2 - 1 & n_2 \\ l_3 & m_3 & n_3 + 1 & l_3 & m_3 & n_3 - 1 \\ l_1 - 1 & m_1 & n_1 & l_1 + 1 & m_1 & n_1 \\ l_2 & m_2 - 1 & n_2 & l_2 & m_2 + 1 & n_2 \\ l_3 & m_3 & n_3 - 1 & l_3 & m_3 & n_3 + 1 \end{bmatrix} \begin{Bmatrix} U^i \\ V^i \\ W^i \\ U^{i+4} \\ V^{i+4} \\ W^{i+4} \end{Bmatrix} \quad (26)$$

Applying this relation to all sets of nodal displacements yields the following equation:

$$\{d_{local}\} = [T] \{d_{global}\} \quad (27)$$

Then, the element stiffness matrix in terms of the global coordinate system is expressed as

$$[K_{global}] = [T]^T [K_{local}] [T] \quad (28)$$

The next section describes how to compute the effective material properties using a multiscale analysis technique.

### 3 Multiscale Analysis of Composite Structures

The schematic diagram in Fig. 3 illustrates the procedure of the developed multiscale analysis technique for composite structures [17–20]. The baseline of the multiscale analysis is the constituent materials for composite structures such as reinforcing fibers and the binding matrix. The mechanical properties of the constituent materials are determined from experimental data or computer simulations such as molecular dynamics. Then, using different semi-analytical models as shown in Fig. 3, the effective material properties are computed. For example, the “Fiber-Strand” model computes the effective material properties for unidirectional composites while the “Strand-Fabric” model calculates the effective material properties for woven fabric composites. Those effective properties are used for the present shell elements of the finite element model of the composite structure. Then, the same models are also used to decompose the macro-scale stresses and strains (i.e. at the composite structure level) into micro-scale stresses and strains (i.e. at the fiber and matrix level). Damage mechanics or failure criteria are applied with the micro-scale stresses and/or

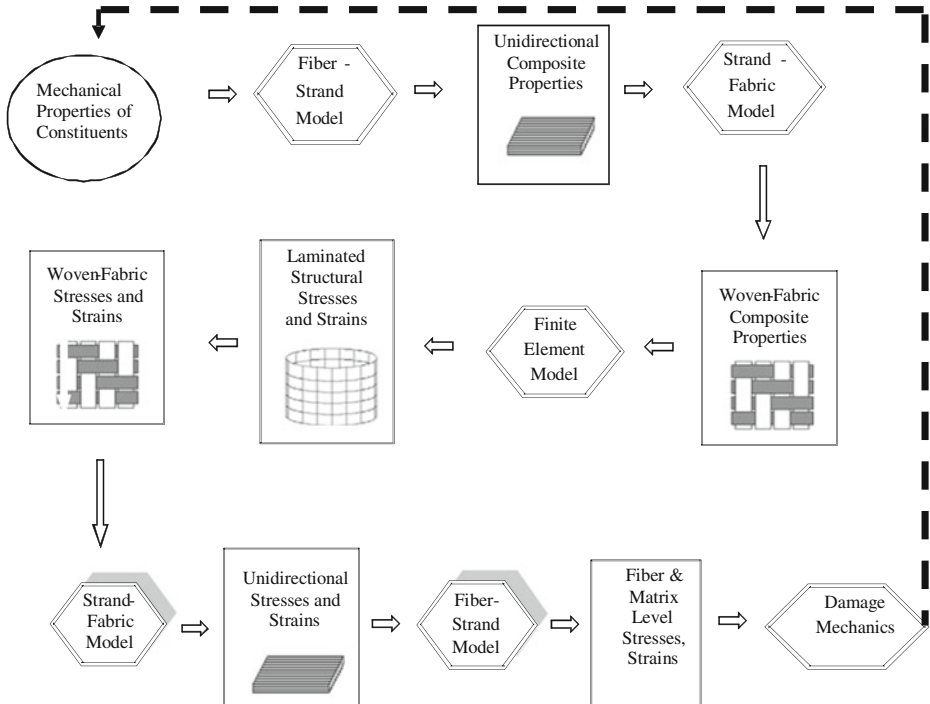


**Fig. 3** Multiscale analysis of composite structures

strains. If there is degradation in the material properties of the fibers and matrix, the reduced properties are determined and used for the next cycle as denoted by the arrow in the broken line. This cycle continues as the damage/failure progresses or if there is a load increase.

The details of the “Fiber-Strand” and “Strand-Fabric” models were provided in Refs. [17–20]. As a result, they are not repeated here to save space. Instead, some important features are described below for completeness of this paper. Each model is based on representative unit cells. Figures 4 and 5 show the unit cells for the “Fiber-Strand” and “Strand-Fabric” models, respectively. Each unit cell is made of sub-cells as shown in the figures. It is assumed that every sub-cell has uniform stresses and strains, and homogeneous material properties, for simplicity. Then, equilibrium at sub-cell interfaces as well as the deformation compatibility among sub-cells are applied. Furthermore, the effective stresses and strains are considered as the volumetric average of the sub-cell stresses and strains, respectively. Algebraic manipulation of all the conditions described above finally yields the two critical expressions used for the multiscale analysis. The first expression is the effective mechanical properties of the unit cell. This is used in the forward process as shown in the hexagonal shapes without shadow effects in Fig. 3. The second expression is to decompose the unit cell stresses and strains into sub-cell stresses and strains to be used in the backward process as shown in the hexagonal shapes with shadow effects.

## 4 Numerical Results

Initially, some examples were solved to check the accuracy of the formulation with known solutions for isotropic materials. Then, laminated sandwich structures were analyzed using the present multiscale shell formulation.

### 4.1 Clamped Square Plate with Center Force

The first example was a static problem with a clamped square plate of length  $L$  made of an isotropic material. The plate was clamped along all edges and a concentrated force was

**Fig. 4** Representative unit cell for Fiber-Strand model. (Subcell ‘a’ represents fiber while other sub-cells are surrounding matrix with symmetric planes of  $l-2$  and  $l-3$ )

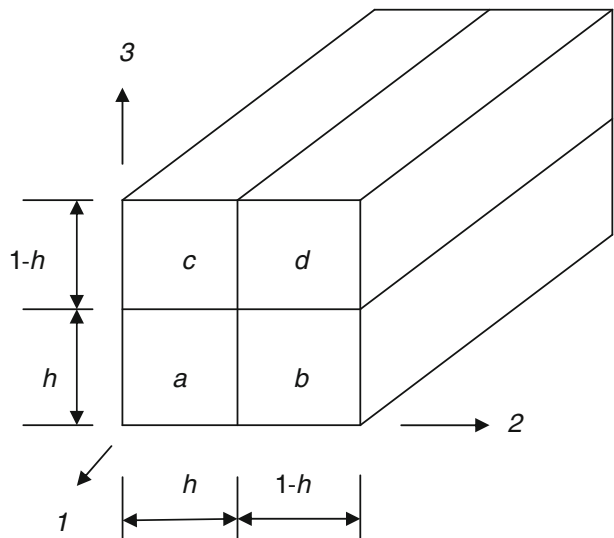
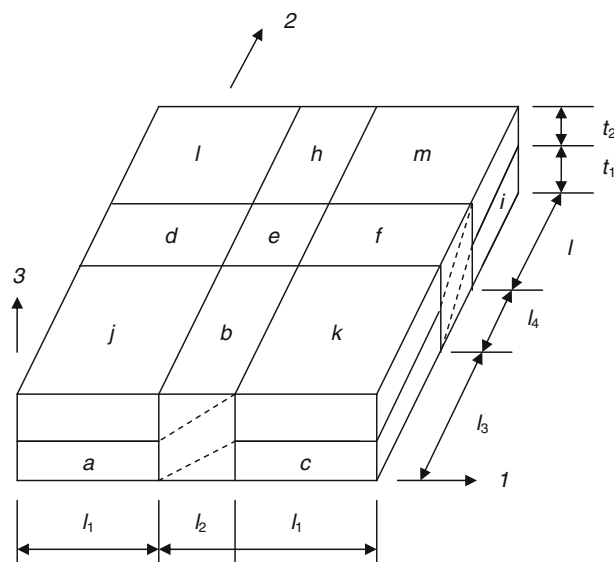


**Fig. 5** Representative unit cell for Strand-Fabric model for plain weave



applied at the plate center where the plate deflection was computed. Because of symmetries, a quarter of the plate was modeled using different numbers of elements. Table 1 shows the finite element solution as a function of the mesh. The deflection was normalized in Table 1, where  $D$  is the plate rigidity and  $P$  is the applied force at the plate center. As shown in the table, the finite element solution approaches the analytical solution [21] as the number of elements increases. Table 2 compares the center deflection with  $2 \times 2$  meshes for the quarter plate while the middle node is displaced from the regular position as sketched in Fig. 6. The result indicates the finite element solution is not sensitive to the mesh distortion.

#### 4.2 Clamped Quarter Ring with End Force

This example was a quarter shape of a cylindrical ring as shown in Fig. 7. The left end was clamped and a vertical static force  $P$  was applied to the right end. The shell has the radius of the midplane  $R$ , thickness  $t$  and width  $h$ . The elastic modulus is  $E$  and Poisson's ratio is zero. The finite element mesh had one element along the width, and the finite element solutions were obtained as the number of elements varied along the radial direction. The vertical and horizontal displacements are  $\delta_v = \frac{3\pi PR^3}{Eht^3}$  and  $\delta_h = \frac{6PR^3}{Eht^3}$ , respectively, at the nodes where the vertical force was applied. Figure 8 shows the convergence of the normalized finite element displacements in both horizontal and vertical directions in terms of the analytical displacements. Both finite element results converged well. Notably, the horizontal displacement was more accurate than the vertical displacement for any given mesh.

**Table 1** Center deflection of a clamped plate with a center force with different mesh sizes

Mesh size	$2 \times 2$	$4 \times 4$	$6 \times 6$	$8 \times 8$	$10 \times 10$	$12 \times 12$	Analytical
$\frac{wD}{PL^2}$	$4.82 \times 10^{-3}$	$5.41 \times 10^{-3}$	$5.53 \times 10^{-3}$	$5.57 \times 10^{-3}$	$5.59 \times 10^{-3}$	$5.60 \times 10^{-3}$	$5.60 \times 10^{-3}$

$w$  = center deflection,  $D$  = plate rigidity,  $P$  = applied force,  $L$  = length of the plate

**Table 2** Center deflection of a clamped plate with a center force with 2×2 mesh with distorted mesh as shown in Fig. 6

Coordinate of middle node ('a')	0.250 L (no distortion)	0.275 L	0.300 L	0.325 L	0.350 L
$\frac{wD}{PL^2}$	$4.82 \times 10^{-3}$	$4.79 \times 10^{-3}$	$4.70 \times 10^{-3}$	$4.52 \times 10^{-3}$	$4.24 \times 10^{-3}$

$w$  = center deflection,  $D$  = plate rigidity,  $P$  = applied force,  $L$  = length of the plate

#### 4.3 Pinched Cylinder with Rigid Diaphragms at Both Ends

A cylinder as shown in Fig. 9 is pinched at the center across the diagonal direction with rigid diaphragms at both ends. The geometric dimensions of the cylinder are  $L=600$ ,  $R=300$ , and  $t=3$ . The material properties consist of an elastic modulus of  $30 \times 10^6$  and Poisson's ratio of 0.3, while the applied force  $P$  is 100. The radial displacement under the load is  $1.8249 \times 10^{-3}$ . Any consistent unit may be used in this computation. Because of multiple symmetries, only one eighth of the cylinder was modeled. The normalized finite element displacements with respect to the analytical solution are shown in Table 3 for different number of elements. The solutions show convergence with the mesh refinement.

The next example is a pinched cylinder with orthotropic material properties. The material properties are shown in Table 4. Fibers were aligned either along the longitudinal (called  $0^\circ$ ) or circumferential (called  $90^\circ$ ) axis of the cylinder. The cylinder was 200mm long and 1mm thick. Its radius was 50mm and it was subjected to a 200N force. The radial displacements along the cylinder were computed and compared in Figs. 10 and 11 for each fiber orientation, respectively. One displacement was along the force direction while the other was normal to the force direction. The present finite element solutions agree well with the approximate analytical solution in Ref. [22].

#### 4.4 Cylindrical Bending of Laminated Composite Plates Under Simple Support

This example considered laminated composite plates under cylindrical bending with simple supports [23]. The plate has the length  $l$  along the  $x$ -axis and infinitely long along the  $y$ -axis.

**Fig. 6** Clamped square plate with mesh distortion. The coordinate of the distorted middle node is  $(a,a)$

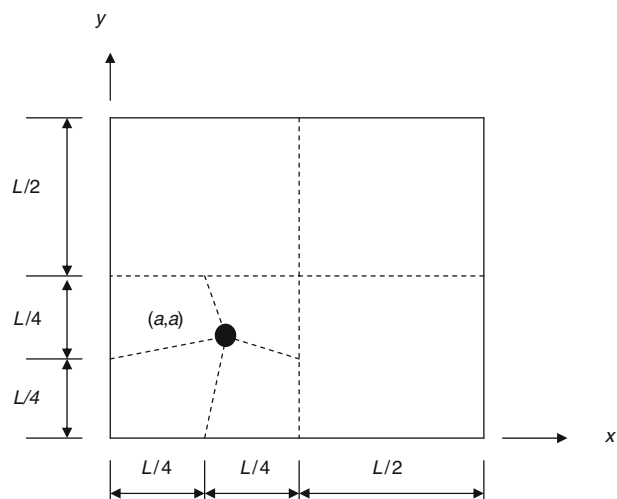
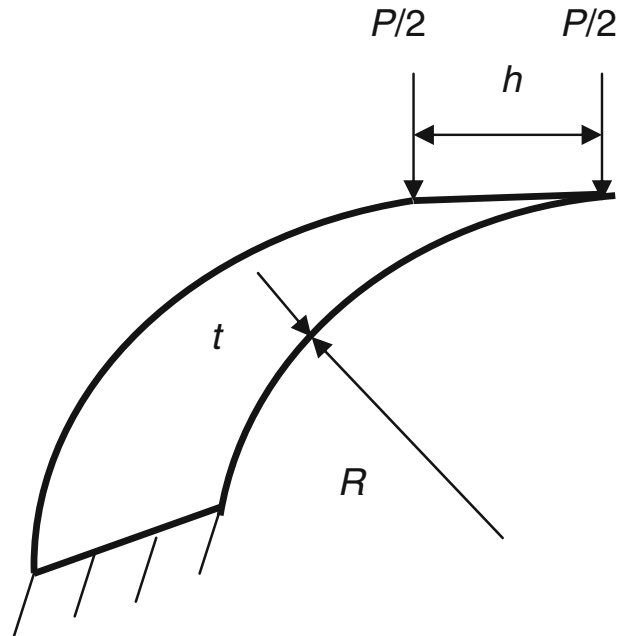


**Fig. 7** Clamped quarter shape of narrow cylinder with concentrated force



The first plate has the layer orientation of  $0^\circ/90^\circ$  with the plate aspect ratio (i.e., side length divided by thickness) of 4. The  $0^\circ$  angle is aligned to the  $x$ -axis. Both layers had the same thickness. The following material properties are used:

$$\begin{aligned} E_L &= 25E_T & G_{LT} &= 0.5E_T \\ G_{TT} &= 0.2E_T & \nu_{LT} &= \nu_{TT} = 0.25 \end{aligned}$$

where subscripts  $L$  and  $T$  denote the longitudinal and transverse directions, respectively. The applied static load is defined by  $q = q_o \sin \frac{\pi x}{l}$ . In all plots associated with this example, the stresses are normalized in terms of  $q_o$  and the  $z$ -axis is normalized with respect to the plate

**Fig. 8** Plot of normalized displacements versus number of elements for quarter ring

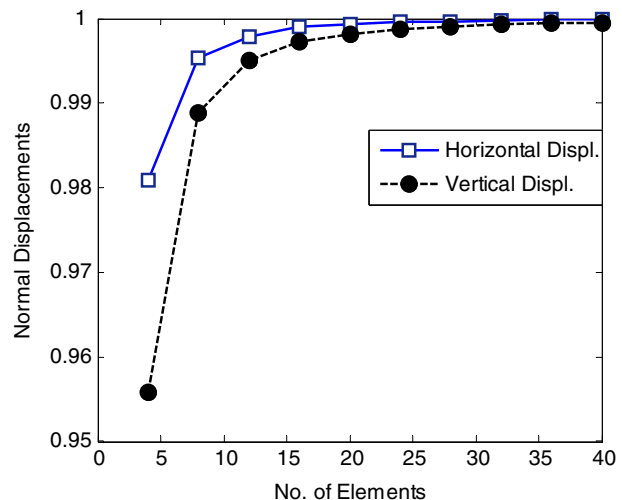
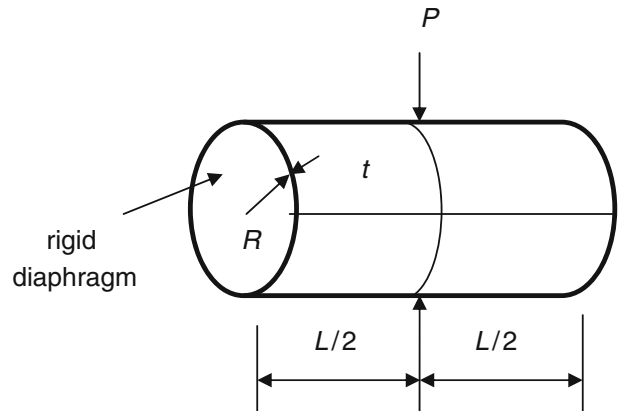




**Fig. 9** Pinched cylinder with rigid diaphragms at both ends



thickness.

The finite element model had 20 elements along the  $x$ -axis and 10 elements through the thickness direction. Figure 12 compares the normalized bending stress  $\sigma_x(x=l/2)$  distribution across the normalized plate thickness between the present finite element solution and the analytical elasticity solution [23]. The solutions agree well. In order to investigate the effect of a resin layer, a resin layer was introduced between the two layers. The resin layer was 1/20th of the plate thickness, and its elastic modulus is  $E_T$  with a Poisson's ratio of 0.25. The difference between the two solutions with or without the resin layer is plotted in Fig. 13 for the normalized stresses  $\sigma_x(x=l/2)$  and  $\tau_{xz}(x=0)$ , respectively. The difference is the solution without the resin layer subtracted from the solution with the resin layer. The effect of the resin layer is quite large for the bending stress distribution.

The second plate had the layer angles of  $0^\circ/90^\circ/0^\circ$  with the plate aspect ratio of 10. Each layer had an equal thickness, the same material properties, and loading conditions as before. The transverse shear stress distribution is compared between the present and the analytical solution [23] in Fig. 14. The effect of the resin layer is also examined for this laminated composite. Each resin layer is introduced between  $0^\circ$  and  $90^\circ$  layers, respectively. The same resin material property was used as before, and each resin layer was assumed to be 1/15th of the plate thickness. The finite element model had 15 elements through the thickness. The effect of the resin layer on the stress distributions is shown in Fig. 15.

#### 4.5 Clamped Sandwich Plate Under Dynamic Loading

The sandwich plate is  $600\text{mm} \times 600\text{mm}$ . Each skin layer is made of a plain weave fabric of 1 mm thick and whose material properties are provided in Table 5. The core layer is 6.4 mm thick and made of an isotropic material with elastic modulus of 0.1 GPa, Poisson's ratio of 0.28 and mass density of  $500\text{kg/m}^3$ . The plate is clamped along all edges and a constant force was applied to the center while the plate was at rest initially.

**Table 3** Normalized deflections of pinched cylinder with diaphragms of different mesh sizes

Mesh size	5×5	10×10	15×15	20×20	25×25
$\frac{w_{\text{fem}}}{w_{\text{analy}}}$	0.514	0.830	0.925	0.963	0.983

**Table 4** Orthotropic material properties used for pinched cylinder

	$E_1$ (GPa)	$E_2$ (GPa)	$G_{12}$ (GPa)	$\nu_{12}$
Fibers along the cylinder longitudinal axis ( $0^\circ$ )	100	10	15	0.3
Fibers along the cylinder circumference ( $90^\circ$ )	10	100	15	0.03

An additional layer was inserted between each skin and core layers resulting two additional layers. These additional layers were  $1 \times 10^{-2} \text{ mm}$  such that it was sufficiently small compared to skin and core layers. For one case, those layers represented the adhesive or resin layer between the skin and core. In that case, the material properties of those layers were assumed to have an elastic modulus of  $2.75 \text{ GPa}$ , Poisson's ratio of 0.28 and density of  $2,000 \text{ kg/m}^3$ . For the other case, the additional layers were assumed to have the same properties as the core layer. In the latter case, the resin or adhesive layers were neglected. The finite element mesh has 10 elements along each length of a quarter plate with symmetry. Because the present shell element is like a 3-D solid element, each layer could be modeled using a shell finite element resulting in five shell elements stacked through the thickness of the sandwich plate.

Figure 16 compares the center displacements between the two cases, i.e. with or without modeling the very thin resin or adhesive layers. Both cases show very comparable displacements without any noticeable difference. Figure 17 shows the comparison of fiber level stresses at the skin layer of the plate center between the same two cases. The results clearly indicate that inclusion of resin layer results in higher stresses in the fibers. This suggests that not including the resin layer, even though it is very thin, will not yield conservative stresses.

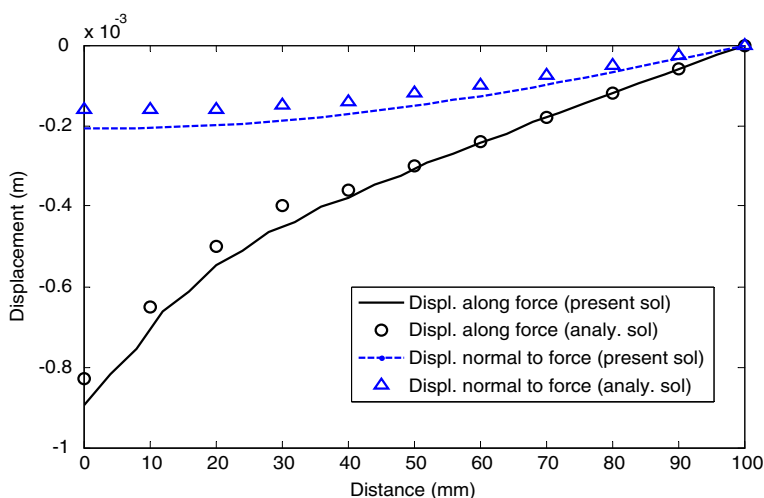


**Fig. 10** Radial displacements along the pinched cylinder with fiber orientation along the cylinder's axis ( $0^\circ$ )

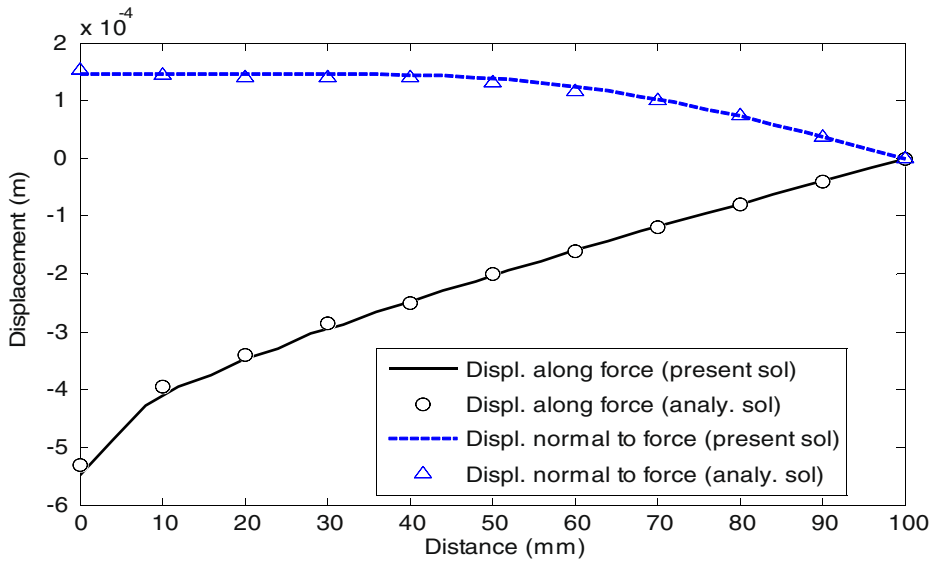


**Fig. 11** Radial displacements along the pinched cylinder with fiber orientation along the cylinder's circumference ( $90^\circ$ )

#### 4.6 Sandwich Composite Cylinder Under Dynamic Loading

This example was a sandwich composite cylinder clamped at both ends and pinched at the center of the cylinder length. The cylinder has an inner radius of  $100\text{ mm}$  and is  $200\text{ mm}$  long.

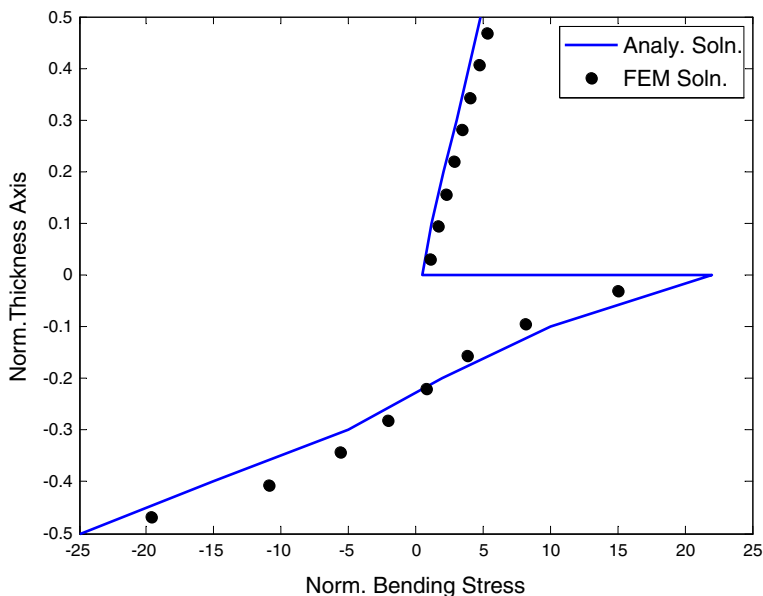


**Fig. 12** Normalized bending stress distribution for laminated composite plate of  $0^\circ/90^\circ$

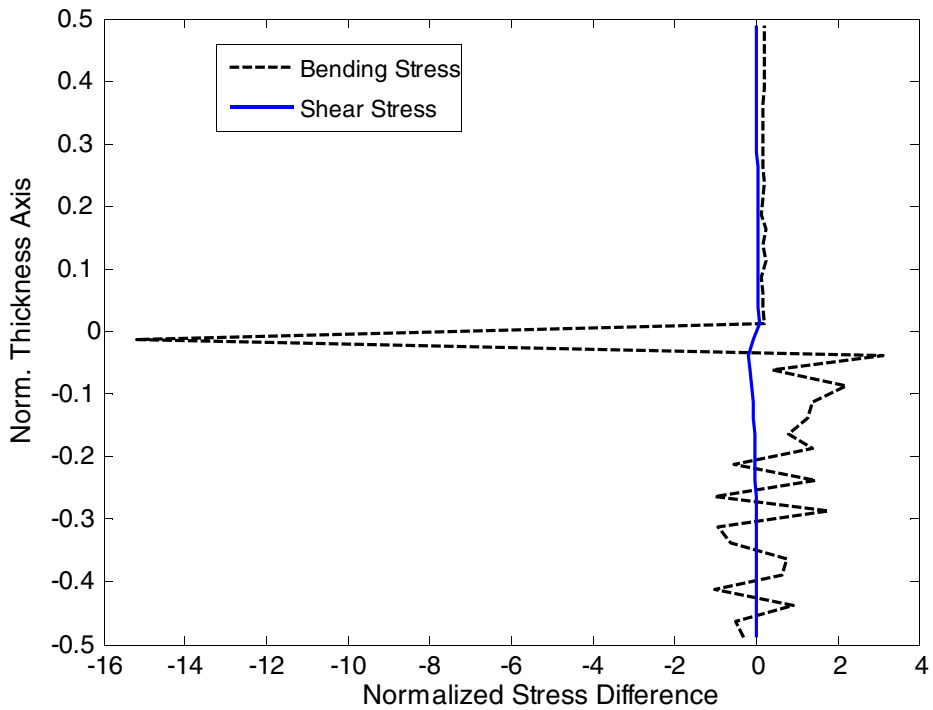


**Fig. 13** Difference of normalized stresses in laminated composite plate of  $0^\circ/90^\circ$  with or without inclusion of a resin layer

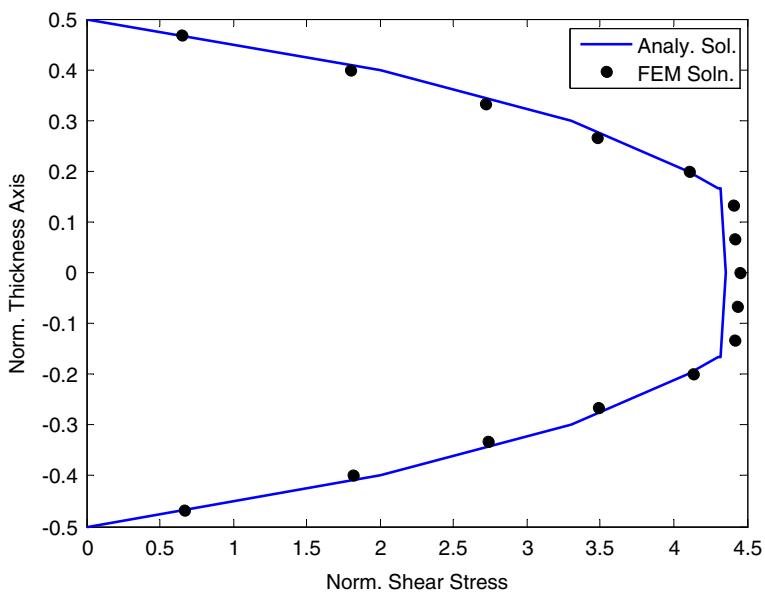
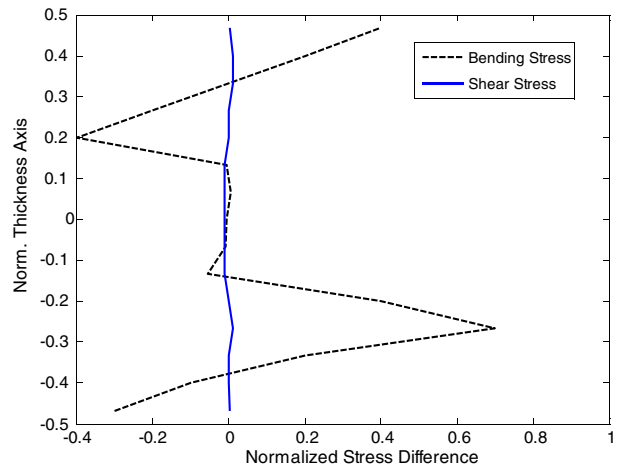


**Fig. 14** Transverse shear stress distribution for laminated composite plate of  $0^\circ/90^\circ/0^\circ$

**Fig. 15** Difference of normalized stresses in laminated composite plate of  $0^\circ/90^\circ/0^\circ$  with or without inclusion of a resin layer



The skin layers were  $1.0\text{ mm}$  thick, the core layer was  $5.0\text{ mm}$  thick, and the additional layers representing resin or adhesive were  $2 \times 10^{-2}\text{ mm}$  thick like the previous sandwich composite plate. The same material properties were used as in the sandwich plate example. The cylinder was at rest initially and subjected to a constant force.

The radial displacements as well as the fiber-level stresses along the longitudinal direction of the cylinder at the skin layer under the applied force were plotted and compared in Figs. 18 and 19; wherein one case neglected the resin layers while the other considering the resin layer. Because of the high frequencies in the response, the plots were only presented for times between  $0.1\text{ s}$  and  $0.15\text{ s}$ . The plots show that both the displacements and fiber-level stresses are different between the two cases. Hence, even though the resin layer is very thin, it should be included for more reliable analyses.

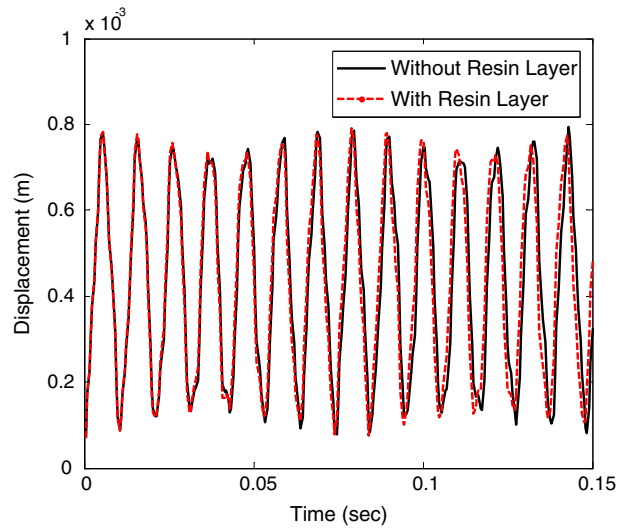
## 5 Conclusions

A new solid-like plate/shell finite element was developed for application in the analysis of laminated and sandwich composite structures. This element can be used to represent each distinctive layer individually so that multiple plate/shell elements can be stacked through the thickness of the structure as is currently the possible with regular 3-D solid elements. By doing so, each layer material property can be applied to the finite element models without using any smeared material property for laminated and sandwich

**Table 5** Material properties used for multiscale analysis with fiber volume fraction 0.3 (density of woven fabric composite =  $1,200\text{ Kg./m}^3$ )

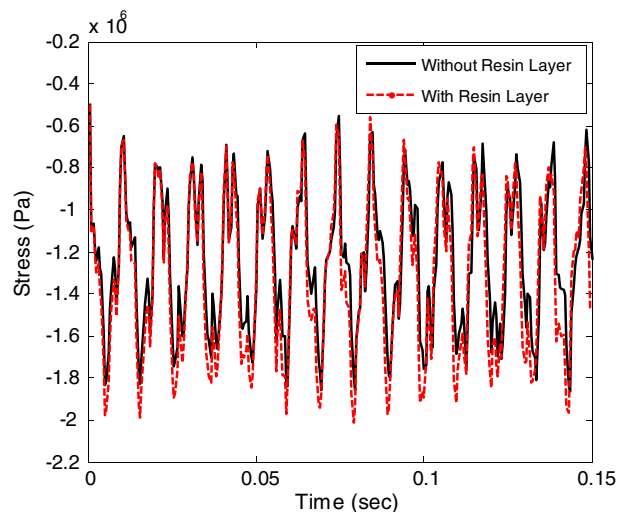
	$E_1$ (GPa)	$E_2$ (GPa)	$G_{12}$ (GPa)	$G_{13}$ (GPa)	$\nu_{12}$
Fibers	72.4	72.4	13.8	5.5	0.2
Matrix	2.75	2.75	1.02	1.02	0.35

**Fig. 16** Comparison of center displacements for clamped sandwich plates with or without modeling the resin layers between skins and the core



structures. Furthermore, the present plate/shell elements were coupled with a previously developed multiscale analysis technique such that microlevel stresses (i.e. stresses at the fiber and matrix levels) could be computed. An initial set of example problems were presented to check the accuracy of the developed plate/shell element. An additional set of examples were analyzed to demonstrate the effectiveness of the present plate/shell elements for laminated and sandwich structures for investigation of the effect of a thin resin or adhesive layer on their structural behavior under static and dynamic loading, respectively.

**Fig. 17** Comparison of fiber-level stresses at skin layer for clamped sandwich plates with or without modeling the resin layers between skins and the core at the plate center



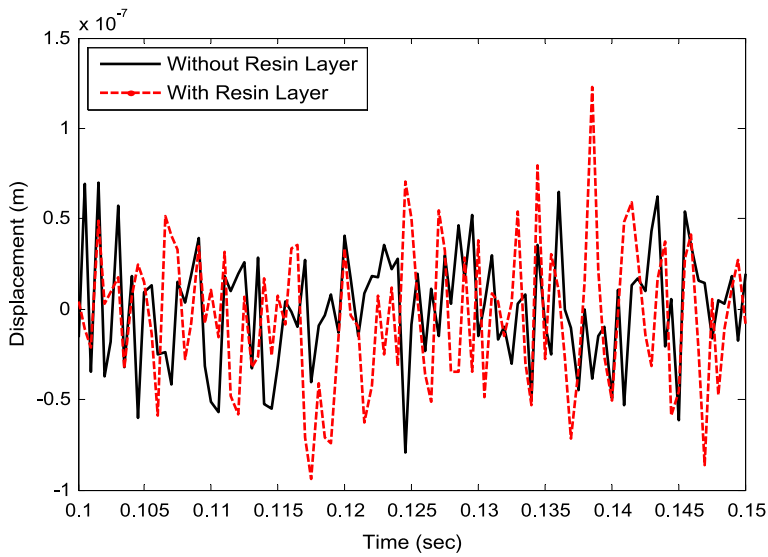


**Fig. 18** Comparison of center displacements for clamped sandwich cylinder with or without modeling the resin layers between skins and the core

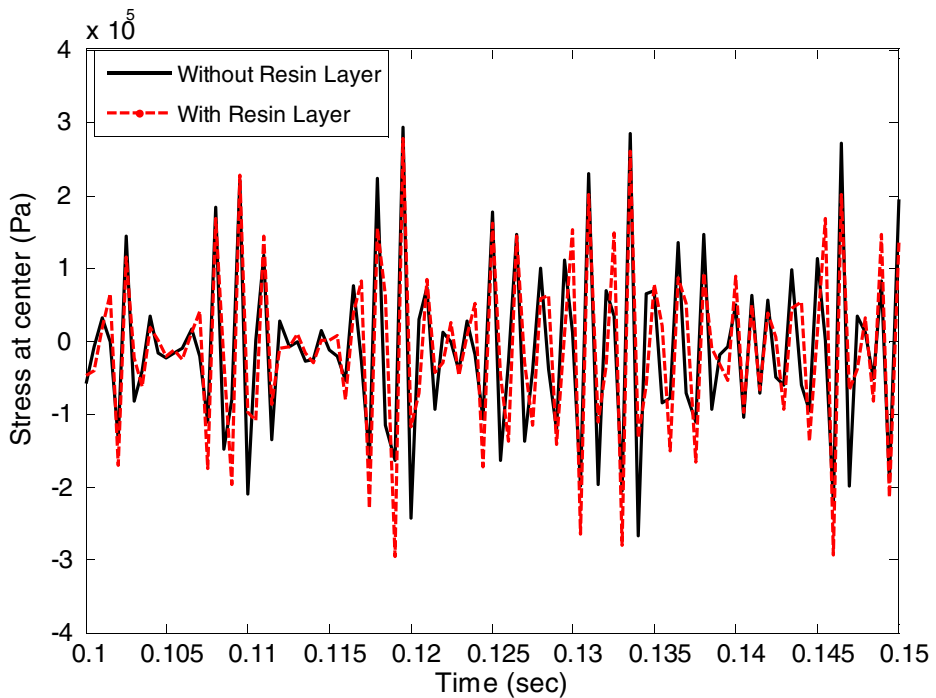


**Fig. 19** Comparison of fiber-level stresses at skin layer for clamped sandwich cylinders with or without modeling the resin layers between skins and the core at the cylinder center

## References

1. Zienkiewicz, O.C., Cheung, Y.K.: The finite element method for analysis of elastic isotropic and orthotropic slabs. *Proc. Inst. Civ. Eng.* **28**, 471–488 (1964)
2. Clough, R.W., Felippa, C.A.: A refined quadrilateral element for analysis of plate bending”, *Proc. 2nd Conf. on Matrix Methods in Structural Mechanics*. Air Force Institute of Technology, Wright-Patterson AF Base, Ohio (1968)
3. Morley, L.S.D.: On the constant moment plate bending element. *J. Strain Anal.* **6**, 20–24 (1971)
4. Reissner, E.: The effect of transverse shear deformation on the bending of elastic plates. *J. Appl. Mech.* **12**, 69–76 (1945)
5. Mindlin, R.D.: Influence of rotator inertia and shear in flexural motions of isotropic elastic plates. *J. Appl. Mech.* **18**, 31–38 (1951)
6. Zienkiewicz, O.C., Too, J., Taylor, R.L.: Reduced integration technique in general analysis of plates and shells. *Int. J. Num. Meth. Eng.* **3**, 275–290 (1971)
7. Hughes, T.J.R., Taylor, R.L., Kanoknukulchai, W.: A simple and efficient finite element for plate bending. *Int. J. Num. Meth. Eng.* **11**, 1529–1543 (1977)
8. Ahmad, S., Irons, B.M., Zienkiewicz, O.C.: Analysis of thick and thin shell structures by curved elements. *Int. J. Num. Meth. Eng.* **2**, 419–451 (1970)
9. Dvorkin, E.N., Bathe, K.J.: A continuum mechanics based four-node shell element for general nonlinear analysis. *Eng. Comput.* **1**, 77–88 (1984)
10. Hughes, T.J.R., Liu, W.K.: Non linear finite element analysis of shells. *Comp. Meth. Appl. Mech. Eng.* **26**, 331–362 (1981)
11. Ibrahimbegovic, A., Wilson, E.L.: A unified formulation for triangular and quadrilateral flat shell finite elements with six nodal degrees of freedom. *Comm. Appl. Num. Meth.* **7**, 1–9 (1991)
12. Owen, D.R.J., Li, Z.H.: A refined analysis of laminated plates by finite element displacement methods – I: Fundamentals and Static Analysis. *Comput. Struct.* **26**, 907–914 (1987)
13. Kwon, Y.W.: Finite element analysis of crack closure in plate bending. *Comput. Struct.* **32**, 1439–1445 (1989)
14. Kulikov, G.M., Plotnikova, S.V.: Finite rotation geometrically exact four-node solid-shell element with seven displacement degrees of freedom. *Comp. Model. Eng. Sci.* **28**, 15–38 (2008)
15. Klinkel, S., Gruttmann, F., Wagner, W.: A continuum based three-dimensional shell element for laminated structures. *Comp. Struct.* **71**, 43–62 (1999)
16. Hauptmann, R., Schweizerhof, K.: A systematic development of ‘solid-shell’ element formulations for linear and non-linear analyses employing only displacement degrees of freedom. *Int. J. Num. Meth. Eng.* **42**, 49–69 (1998)
17. Kwon, Y.W.: “Chapter 4: multiscale and multilevel modeling of composites”, multiscale modeling and simulation of composite materials and structures, by Kwon, Y.W., Allen, D.H., Talreja, R. (eds.), Springer (2007)
18. Kwon, Y.W., Altekin, A.: Multi-level, micro-macro approach for analysis of woven fabric composites. *J. Compos. Mater.* **36**, 1005–1022 (2002)
19. Kwon, Y.W., Roach, K.: Unit-cell model of 2/2-twill woven fabric composites for multi-scale analysis. *Comput. Model. Eng. Sci.* **5**, 63–72 (2004)
20. Kwon, Y.W., Cho, W.M.: Multi-scale thermal stress analysis of woven fabric composite. *J. Therm. Stress.* **27**, 59–73 (2004)
21. Timoshenko, S., Woinowsky-Krieger, S.: *Theory of Plates and Shells*, 2nd edn. McGraw-Hill, New York (1959)
22. Jones, I.A.: Approximate solution to the orthotropic pinched cylinder problem. *Compos. Struct.* **42**, 73–91 (1998)
23. Pagano, N.J.: Exact solutions for composite laminates in cylindrical bending. *J. Compos. Mater.* **3**, 398–411 (1968)





This article appeared in a journal published by Elsevier. The attached copy is furnished to the author for internal non-commercial research and education use, including for instruction at the authors institution and sharing with colleagues.

Other uses, including reproduction and distribution, or selling or licensing copies, or posting to personal, institutional or third party websites are prohibited.

In most cases authors are permitted to post their version of the article (e.g. in Word or Tex form) to their personal website or institutional repository. Authors requiring further information regarding Elsevier's archiving and manuscript policies are encouraged to visit:

<http://www.elsevier.com/authorsrights>



Contents lists available at SciVerse ScienceDirect

## Composite Structures

journal homepage: [www.elsevier.com/locate/compstruct](http://www.elsevier.com/locate/compstruct)

## Coupled finite element and cellular automata methods for analysis of composite structures with fluid–structure interaction

L.E. Craugh<sup>a</sup>, Y.W. Kwon<sup>b,\*</sup><sup>a</sup> Dept. of Mech. Eng., United States Naval Academy, Annapolis, MD 21402, United States<sup>b</sup> Dept. of Mech. & Aero. Eng., Naval Postgraduate School, Monterey, CA 93943, United States

## ARTICLE INFO

## Article history:

Available online 7 March 2013

## Keywords:

Discontinuous Galerkin method

Cellular automata

Composite plates

Fluid–structure interaction

Wave equation

## ABSTRACT

This study examines multiple computational techniques to analyze dynamic responses of composite structures subject to Fluid–Structure Interaction (FSI). A plate bending finite element with displacement degrees of freedom only is developed and implemented using a Discontinuous Galerkin (DG) formulation. Because the plate elements can be stacked on top of one another like 3-D solid elements, delamination or debonding between any two layers can be modeled easily. Multiple approaches to analyzing such failure are presented and evaluated. A hybrid Finite Element–Cellular Automata (FE–CA) approach is also presented to model a fluid domain as an acoustic field using the wave equation. The coupled technique can take advantage of both methods such as computational efficiency, non-reflecting boundary representation and easy coupling with a structure with a complex shape. The FE–CA fluid model is then combined with the DG structural model to simulate fluid–structure interaction. All the computational techniques are assessed for their accuracy by comparing with analytical, experimental and other numerical solutions. Each technique addressed shows promise for flexible and accurate modeling of dynamic behaviors of damaged or undamaged laminated composite structures subject to fluid–structure interaction with moderate computational costs.

Published by Elsevier Ltd.

## 1. Introduction

Composite materials can have very beneficial properties for structural applications. In particular, polymer composites generally have low density but high strength and stiffness, or a very high specific strength and stiffness. Their resistance to corrosion is another tremendous advantage. Consequently, composite materials are used in a number of both civil and military applications. Aerospace structures are among the major applications of polymer composite materials, especially carbon fiber composites. Increasingly, composite materials are used in marine structures. Composite materials have long been used as primary hull materials for sailboats and other small craft, but the nature of larger naval applications of composite materials demands a fuller understanding of the survivability and mission impacts of using such structures in the marine environment.

For marine applications with a polymer composite structure in contact with water, the comparable density of the composite materials to that of water results in a significant hydrodynamic mass effect on the structure. Therefore, the goal of this study is to develop computational techniques to model and simulate transient dy-

namic responses of composite structures with Fluid–Structure Interaction (FSI). To this end, it is necessary to develop computational techniques for composite structures as well as the fluid medium. Eventually, a method to couple both structural and fluid solvers is developed.

The Finite Element Method (FEM) is a well established tool for generating numerical solutions to the partial differential equations that describe a wide range of physical phenomena. The common method of weighted residual used in most finite element codes is the Continuous Galerkin (CG) method in which the same shape functions are used for both test and trial functions. Requiring continuity between neighboring elements makes physical sense and is the norm in CG formulations. However, Discontinuous Galerkin (DG) methods have also become an active area of research.

DG approaches to solving boundary-value problems have their genesis in the work of Nitsche [1] who first proposed weak enforcement of boundary conditions. Douglas and Dupont [2], Arnold [3], Baker [4], and Wheeler [5] expanded the concept to weak enforcement of continuity between elements and applied it to elliptic problems. Easing of the continuity constraints between elements suggests a number of potential advantages to this methodology: element-wise computations lend themselves to parallel computing, the independence of the elements from each other allows different orders of interpolation within elements, and the

\* Corresponding author. Tel.: +1 831 656 3468.

E-mail address: [ywkwon@nps.edu](mailto:ywkwon@nps.edu) (Y.W. Kwon).

potential to model failure without having to re-mesh is intriguing. In recent years discontinuous approaches have been increasingly applied to elliptic partial differential equations such as those that dominate linear elasticity. Arnold and colleagues have produced two excellent overviews of the development and characteristics of various methods in [6,7]. In particular, they gathered the various formulations and cast them all in both flux and primal forms to more clearly see the differences and identifying characteristics. Castillo [8] conducted a cost and performance analysis of three of these methods. Brezzi et al. [9] discuss the stabilization mechanisms necessary for effective DG formulations. Specific work in DG for solid mechanics can be found in Refs. [10–22] among many others.

To accurately model FSI, an appropriate fluid model is also required. In this work no attempt is made to model or solve the full Navier–Stokes equations. Instead, a subset that will allow compatibility between fluid and solid regimes and approximate the hydrodynamic pressure or acoustic field will suffice. Olson and Bathe [23] developed a directly coupled formulation that solves for the velocity potential and hydrostatic pressure in the fluid domain and displacements in the structural; this will be the starting point for development of the fluid model in this work. In order to apply the fluid model to a maritime domain, appropriate boundary conditions must also be included. Two general approaches are to model a vast domain and concern oneself with a small subset relatively far from simple but inaccurate boundaries – a computationally expensive proposition – or to model an appropriately sized domain with non-reflecting boundary conditions – a challenging proposition that remains an active area of research [24]. Application of CA to modeling the acoustic field following from the work of Chopard [25,26], Krutar et al. [27], and Kwon and Hosoglu [28] will be explored.

The balance of this paper is organized as follows: Section 2 presents a development of plate elements using the DG technique. The plate element has only displacement degrees of freedom like a 3-D solid element. Section 3 includes verification of the developed DG structural model for composite structures and discusses multiple modeling techniques for local failure like debonding. Development of the fluid models using FEM, Cellular Automata (CA), and coupled FEM-CA formulations is provided in Section 4. Section 5 contains a demonstration of the developed fluid models and the fluid–structure interaction problems associated with the experimental work [29]. Conclusions are presented in Section 6.

## 2. Discontinuous Galerkin formulation for plate element

This section presents the formulation of a nodal DG, solid-like plate/shell element. The plate/shell element to be developed includes both transverse shear and normal strain energy but all nodal degrees of freedom are displacements without rotations. This element is easily stacked one atop another to represent individual layers of laminated or sandwich composite structures. Additionally, the interaction of this plate/shell element with surrounding acoustic or fluid media is simpler than a traditional plate/shell element containing rotational degrees of freedom. Coupling of structural and fluid elements is easier using the displacement degrees of freedom at the surfaces of the plate/shell element. A detailed development for the DG plate element, as shown in Fig. 1, is provided here. The extension of the plate element to the shell element is given at Ref. [30] so that it is omitted here to save the space.

Liu et al. [21] proposed and implemented a nodal DG formulation that can be easily extended from a nodal CG formulation and can be switched between three different specific methods via the selection of a single scalar parameter,  $\theta_{DG}$ . Their formulation is the starting point for this work and is presented below.

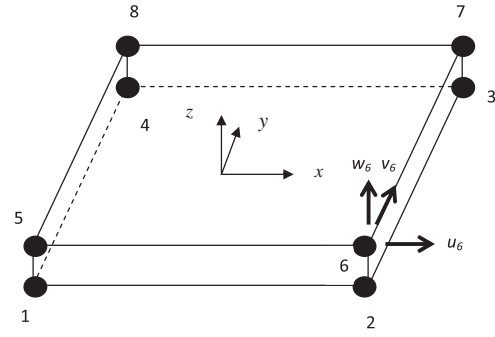


Fig. 1. Plate element in terms of natural coordinate system.

The domain,  $\Omega \subset \mathbb{R}^3$ , has a boundary,  $\partial\Omega$ , comprised of non-intersecting Dirichlet,  $\Gamma_u$ , and Neumann,  $\Gamma_t$ , boundaries upon which displacement,  $\bar{u} \in H^1(\Gamma_u)$ , and surface traction,  $\bar{t} \in L^2(\Gamma_t)$ , are specified.  $\chi = \{E_1, E_2, \dots, E_n\}$  is a non-degenerate discretization of  $\Omega$ ; in this work  $E_j$  are hexahedra.  $S = S_i + \Gamma_u + \Gamma_t$  is the set of faces of  $\chi$  where  $S_i$  are interior faces.

Applying the weighted residual formulation to the theory of elasticity results in

$$\sum_{E \in \chi} \int_E \frac{1}{2} \sigma(u) : \varepsilon(v) dV - \sum_{\partial E \in S} \int_{\partial E} (\sigma n) \cdot v dS = \sum_{E \in \chi} \int_E f \cdot v dV \quad (1)$$

where  $\sigma$  and  $\varepsilon$  are stress and strain tensors,  $n$  and  $f$  are the normal vector to the boundary and body force. Furthermore,  $u$  and  $v$  the trial and test functions, respectively. For the Galerkin formulation, the both functions are selected to be equal. In the CG formulation, the second term of Eq. (1) would disappear on inter-elemental boundaries and only exist on the domain boundary. For DG, however, that is not the case. Define jump and average functions across such an interior boundary, between two elements arbitrarily labeled as “Left” and “Right” as

$$u = u_L - u_R \quad (2)$$

$$\langle u \rangle = \frac{1}{2} (u_L + u_R) \quad (3)$$

Combining those definitions with the identity  $uv = \langle u \rangle v + u \langle v \rangle$  and the assumption that traction across interfaces is continuous, results in

$$\begin{aligned} \sum_{E \in \chi} \int_E \frac{1}{2} \sigma(u) : \varepsilon(v) dV - \sum_{\partial E \in (S_i + \Gamma_u)} \int_{\partial E} \langle \sigma(u) n^s \rangle \cdot v dS \\ = \sum_{E \in \chi} \int_E f \cdot v dV + \sum_{\partial E \in \Gamma_t} \int_{\partial E} \bar{t} \cdot v dS \end{aligned} \quad (4)$$

Liu et al. [21] added face integrals  $\int_{\partial E} \langle \sigma(v) n^s \rangle \cdot u dS$  and  $\frac{\delta_p G}{|S|} \int_{\partial E} u \cdot v dS$ , both of which disappear for an exact solution, to control symmetry and provide stabilization. The following equation results:

$$\begin{aligned} a(u, v) = \sum_{E \in \chi} \int_E \frac{1}{2} \sigma(u) : \varepsilon(v) dV - \sum_{\partial E \in (S_i + \Gamma_u)} \int_{\partial E} \langle \sigma(u) n^s \rangle \cdot v dS \\ + \sum_{\partial E \in (S_i + \Gamma_u)} \theta_{DG} \int_{\partial E} \langle \sigma(v) n^s \rangle \cdot u dS + \sum_{\partial E \in (S_i + \Gamma_u)} \frac{\delta_p G}{|S|} \int_{\partial E} u \cdot v dS \end{aligned} \quad (5)$$

$$\begin{aligned} L(v) = \sum_{E \in \chi} \int_E f \cdot v dV + \sum_{\partial E \in \Gamma_t} \int_{\partial E} \bar{t} \cdot v dS + \sum_{\partial E \in \Gamma_u} \theta_{DG} \int_{\partial E} \langle \sigma(v) n^s \rangle \cdot \bar{u} dS \\ + \sum_{\partial E \in \Gamma_u} \frac{\delta_p G}{|S|} \int_{\partial E} \bar{u} \cdot v dS \end{aligned} \quad (6)$$

where  $G$  is the shear modulus,  $\delta_p$  is a scalar penalty parameter,  $|s|$  is the square root of the area of the element's face, and  $\theta_{DG}$  indicates the DG method in use. For non-zero  $\delta_p$ , if  $\theta_{DG} = -1$ , the method is the Symmetric Interior Penalty Galerkin (SIPG), which also corresponds to the Local Discontinuous Galerkin (LDG) method of Cockburn and Shu with  $\beta = 0$  [31]; if  $\theta_{DG} = +1$ , it is Non-symmetric Interior Penalty Galerkin (NIPG); if  $\theta_{DG} = 0$ , it is Incomplete Interior Penalty Galerkin (IIPG). If  $\theta_{DG} = 0$  and  $\delta_p = 0$ , the method is that of Oden, Babuska, and Baumann (OBB). The problem statement is now: find  $u \in V$  such that

$$a(u, v) = L(v) \quad \forall v \in V \quad (7)$$

$$H^1(\chi) = \{v \in L^2(\Omega) : v|_{E_j} \in H^1(E_j) \forall E_j \in \chi; V = \{v \in H^1(\chi)\} \quad (8)$$

Eqs. (5) and (6) can be converted into matrix–vector form. The first term of Eq. (5) for the present plate element is expressed as:

$$\int_E \frac{1}{2} \sigma(u) : \varepsilon(v) dV = ([K_b] + [K_{ts}] + [K_{tn}])\{U\} \quad (9)$$

where  $[K_b]$ ,  $[K_{ts}]$  and  $[K_{tn}]$  are element stiffness matrices resulting from bending, transverse shear, and transverse normal energy, respectively, and  $\{U\}$  is the nodal displacement vector of the element. Each of the stiffness matrices is shown below:

$$[K_b] = \int_E [B_b]^T [D_b] [B_b] dV \quad (10)$$

$$[K_{ts}] = \int_E [B_{ts}]^T [D_{ts}] [B_{ts}] dV \quad (11)$$

$$[K_{tn}] = \int_E [B_{tn}]^T [D_{tn}] [B_{tn}] dV \quad (12)$$

For the plate element shown in Fig. 1, the details of the matrices in the above expression are given below:

$$[B_b] = [B_{b1} \quad B_{b2}] \quad (13)$$

$$[B_{bi}] = \begin{bmatrix} H_i \frac{\partial N_1}{\partial x} & 0 & 0 & H_i \frac{\partial N_2}{\partial x} & 0 & 0 & H_i \frac{\partial N_3}{\partial x} & 0 & 0 & H_i \frac{\partial N_4}{\partial x} & 0 & 0 \\ 0 & H_i \frac{\partial N_1}{\partial y} & 0 & 0 & H_i \frac{\partial N_2}{\partial y} & 0 & 0 & H_i \frac{\partial N_3}{\partial y} & 0 & 0 & H_i \frac{\partial N_4}{\partial y} & 0 \\ H_i \frac{\partial N_1}{\partial y} & H_i \frac{\partial N_1}{\partial x} & 0 & H_i \frac{\partial N_2}{\partial y} & H_i \frac{\partial N_2}{\partial x} & 0 & H_i \frac{\partial N_3}{\partial y} & H_i \frac{\partial N_3}{\partial x} & 0 & H_i \frac{\partial N_4}{\partial y} & H_i \frac{\partial N_4}{\partial x} & 0 \end{bmatrix} \quad (14)$$

$$[B_{ts}] = [B_{ts1} \quad B_{ts2}] \quad (15)$$

$$[B_{tsi}] = \begin{bmatrix} N_i \frac{\partial H_1}{\partial z} & 0 & H_i \frac{\partial N_1}{\partial z} & N_2 \frac{\partial H_1}{\partial z} & 0 & H_i \frac{\partial N_2}{\partial z} & N_3 \frac{\partial H_1}{\partial z} & 0 & H_i \frac{\partial N_3}{\partial z} & N_4 \frac{\partial H_1}{\partial z} & 0 & H_i \frac{\partial N_4}{\partial z} \\ 0 & N_i \frac{\partial H_1}{\partial z} & H_i \frac{\partial N_1}{\partial y} & 0 & N_2 \frac{\partial H_1}{\partial z} & H_i \frac{\partial N_2}{\partial y} & 0 & N_3 \frac{\partial H_1}{\partial z} & H_i \frac{\partial N_3}{\partial y} & 0 & N_4 \frac{\partial H_1}{\partial z} & H_i \frac{\partial N_4}{\partial y} \end{bmatrix} \quad (16)$$

$$[B_{tn}] = [B_{tn1} \quad B_{tn2}] \quad (17)$$

$$[B_{tni}] = \begin{bmatrix} 0 & 0 & N_i \frac{\partial H_1}{\partial z} & 0 & 0 & N_2 \frac{\partial H_1}{\partial z} & 0 & 0 & N_3 \frac{\partial H_1}{\partial z} & 0 & 0 & N_4 \frac{\partial H_1}{\partial z} \end{bmatrix} \quad (18)$$

in which  $N_i$  ( $i = 1, 2, 3, 4$ ) is the 2-D shape function for inplane interpolation and  $H_i$  ( $i = 1, 2$ ) is the 1-D shape function for the interpolation along the thickness direction. Furthermore,  $[D_b]$ ,  $[D_{ts}]$ ,  $[D_{tn}]$  are the material property matrix for the plane stress, transverse shear, and transverse normal components, respectively.

In a similar fashion, the surface integrals of Eq. (5) can also be expressed as matrix–vector products. Once expanded, the vector components will be comprised of various products of the unknown vector,  $u_L$  or  $u_R$  and the test function,  $v_L$  and  $v_R$ . The interface stiffness matrices will be referred to as  $[K_{MN}^i]$  where the superscript,  $i$ , refers to the integrals in the order they appear in Eq. (5); the subscripts will take the values  $L$  and  $R$ , referring to the left and right

sides of the interface, respectively. The subscript  $M$  will correspond to the  $v$  component and the  $N$  will correspond to the  $u$  component.

For example, the expansion of the first surface integral into the  $K_{MN}^1$  components is

$$\begin{aligned} \int_S \langle \sigma(u) n^s \rangle \cdot v dS &= - \int_S \left( \frac{\sigma(u_L) + \sigma(u_R)}{2} \right) n^s \cdot (v_L - v_R) dS \\ &= - \frac{1}{2} \int_S (\sigma(u_L) n^s) \cdot v_L dS + \frac{1}{2} \int_S (\sigma(u_L) n^s) \cdot v_R dS \\ &\quad - \frac{1}{2} \int_S (\sigma(u_R) n^s) \cdot v_L dS + \frac{1}{2} \int_S (\sigma(u_R) n^s) \cdot v_R dS \end{aligned} \quad (19)$$

The terms of Eq. (19) can be expressed as

$$\int_S (\sigma(u_L) n^s) \cdot v_L dS \int_S [\bar{N}_L]^T [\Lambda^s] [D] [B_L] dS \{U_L\} = [K_{LL}^1] \{U_L\} \quad (20)$$

$$\int_S (\sigma(u_L) n^s) \cdot v_R dS \int_S [\bar{N}_R]^T [\Lambda^s] [D] [B_L] dS \{U_L\} = [K_{RL}^1] \{U_L\} \quad (21)$$

$$\int_S (\sigma(u_R) n^s) \cdot v_L dS \int_S [\bar{N}_L]^T [\Lambda^s] [D] [B_R] dS \{U_L\} = [K_{LR}^1] \{U_R\} \quad (22)$$

$$\int_S (\sigma(u_R) n^s) \cdot v_R dS \int_S [\bar{N}_R]^T [\Lambda^s] [D] [B_R] dS \{U_L\} = [K_{RR}^1] \{U_R\} \quad (23)$$

where  $[\bar{N}]$  is the matrix consisting of 2-D shape functions for each element surface,  $[B]$  is the matrix relating strains to nodal displacements,  $[D]$  is the material property matrix, and  $[\Lambda^s]$  is the matrix consisting of direction cosines as shown below:

$$[\Lambda^s] = \begin{bmatrix} n_x & 0 & 0 & n_y & 0 & n_z \\ 0 & n_y & 0 & n_x & n_z & 0 \\ 0 & 0 & n_z & 0 & n_y & n_x \end{bmatrix} \quad (24)$$

Conveniently the interface stiffness matrices that result from the third term of Eq. (5) are simple rearrangements of those calculated from the second term. That is,  $[K_{LL}^1] = [K_{LL}^2]^T$ ,  $[K_{RR}^1] = [K_{RR}^2]^T$ ,  $[K_{LR}^1] = [K_{RL}^2]^T$ , and  $[K_{RL}^1] = [K_{LR}^2]^T$ . The final term of Eq. (5) is referred to as the interface penalty stiffness,  $[K_{MN}^3]$  and its components are calculated as follows:

$$\begin{aligned} \frac{\delta_p G}{|s|} \int_S u \cdot v dS &= \frac{\delta_p G}{|s|} \int_S (u_L - u_R) (v_L - v_R) dS \\ &= \frac{\delta_p G}{|s|} \int_S (u_L v_L - u_L v_R - u_R v_L + u_R v_R) dS \end{aligned} \quad (25)$$

$$\frac{\delta_p G}{|s|} \int_S u_L v_L dS = \frac{\delta_p G}{|s|} \int_S [N_L]^T [N_L] dS \{U_L\} = [K_{LL}^3] \{U_L\} \quad (26)$$

$$\frac{\delta_p G}{|s|} \int_S u_L v_R dS = \frac{\delta_p G}{|s|} \int_S [N_R]^T [N_L] dS \{U_L\} = [K_{RL}^3] \{U_L\} \quad (27)$$

$$\frac{\delta_p G}{|s|} \int_S u_R v_L dS = \frac{\delta_p G}{|s|} \int_S [N_L]^T [N_R] dS \{U_R\} = [K_{LR}^3] \{U_R\} \quad (28)$$

$$\frac{\delta_p G}{|s|} \int_S u_R v_R dS = \frac{\delta_p G}{|s|} \int_S [N_R]^T [N_R] dS \{U_R\} = [K_{RR}^3] \{U_R\} \quad (29)$$

The terms of  $L(v)$  are vectors resulting from integrating the body forces and given boundary conditions (both displacement and traction) over the volume and surfaces. To ensure each interface integral is calculated once and only once, surface integrals are calculated only for those faces corresponding to the positive canonical directions as the loop through the elements progresses. Eventually, the various  $[K_{MN}^i]$  matrices are assembled into the total system

stiffness matrix; likewise the various force vectors are assembled into the total system force vector, and the system matrix equation is solved simultaneously.

One challenge in using these discontinuous Galerkin elements is selection of an appropriate penalty parameter for the last two terms of Eqs. (5) and (6). As  $\delta_p$  approaches infinity the methods return to their continuous roots, so selection of too large a penalty is a waste of computing resources. The penalty must also be large enough to guarantee existence and uniqueness of the solution [32]. Additionally, the nature of the penalty is often described as a function of the local element order or size with little other clarification. The nature of penalizing the jump as a stabilization mechanism is discussed by Brezzi et al. [9] for elliptic DG formulations in general. Others have computed lower bounds on penalties for various formulations [33–35] among others.

In Liu et al.'s formulation [21], the penalty term is a surface integral multiplied by a parameter to be determined and the material shear modulus divided by the square root of the area over which the integral is calculated. Another intriguing approach is that of Ainsworth and Rankin [36] in which they compute a lower bound on the penalty parameter that is a function of the method selector and the maximum eigenvalue of the elemental stiffness matrix; that value is also divided by a term analogous to the square root of the area of the integral. In view of this approach, the presence of the shear modulus in Liu's penalty term serves as a scaling factor to keep the penalty in the same numerical neighborhood as that of the volume integral or elemental stiffness matrix. Anticipating using this formulation for a composite material with potentially vastly different shear moduli between elements, we will combine these two approaches, replacing  $\delta_p G$  with  $\delta_p \lambda_{\max}$  where  $\lambda_{\max}$  the largest eigenvalue of the elemental stiffness matrix. As long as  $\delta_p > (1 - \theta_p)^2$ , a unique solution will exist [36].

### 3. Structural analysis

#### 3.1. Verification examples

A pair of beam problems was used to validate the formulation: a cantilever subjected to a concentrated force at the free end and a simply supported beam subjected to a concentrated force at mid-span. Both beams are 8 m long and have unit cross-sectional area and the same isotropic material properties. Errors relative to maximum deflections predicted by Euler Beam theory were calculated for various discretizations and plotted in Figs. 2 and 3, both of which demonstrate quadratic convergence rates (the predicted rate for linear elements) for all three methods (NIPG, SIPG, IIPG).

A clamped square plate subject to a concentrated load applied at its center was used to validate the plate element model. The

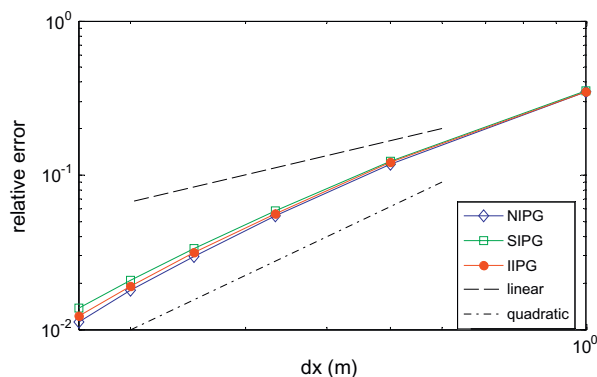


Fig. 2. Convergence of DG formulation for cantilever beam deflection.

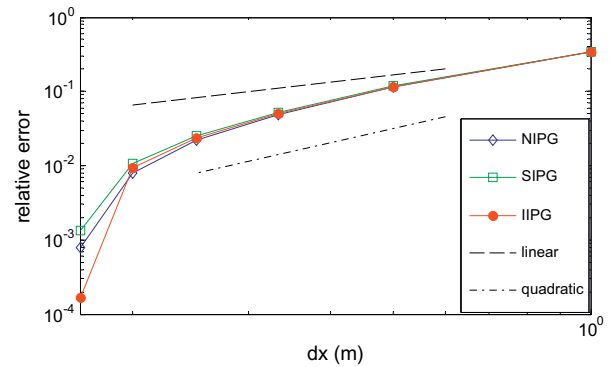


Fig. 3. Convergence of DG formulation for simply supported beam deflection.

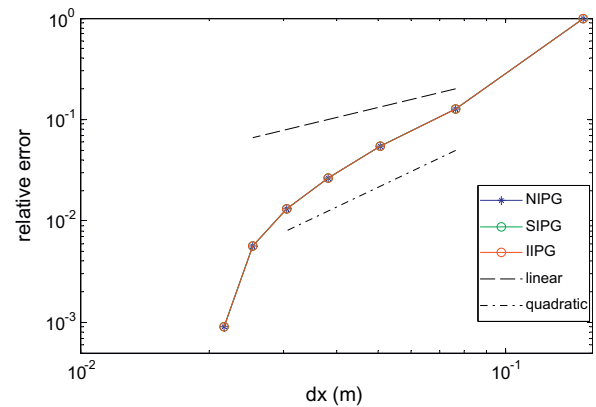


Fig. 4. Convergence of DG formulation for clamped square plate.

plate is  $0.3048 \text{ m} \times 0.3048 \text{ m} \times 0.00635 \text{ m}$  (12 in.  $\times$  12 in.  $\times$  1/4 in.) and isotropic. Theoretical values were calculated according to Timoshenko and Woinowsky-Krieger [37]. All three methods demonstrate quadratic convergence when linear elements are used, as shown in Fig. 4. All three methods produced the same accuracy.

A second validation was conducted by comparing dynamic continuous and discontinuous Galerkin techniques of the same square plate. Both models consist of 144 square elements such that the characteristic length of each element is four times its thickness. Clamped boundary conditions and zero deflection and velocity initial conditions were applied and both models have lumped (diagonal) mass matrices. Figs. 5 and 6 show excellent agreement between the two models for the transverse displacement and velocity of the center of the plate subjected to a constant concentrated force applied at its center.

#### 3.2. Composite structures

This work attempts to model sandwich composite plates. These materials are comprised of low density cores that are relatively stiff transversely and skin layers that provide in-plane strength to the structure. While the core is generally the thickest component in the sandwich, it is still thin relative to its planar cross-section, giving it a sub-optimal aspect ratio for solution with three-dimensional elements. Modeling a sandwich composite structure consists of an assemblage of elements for each layer, that are each homogeneously comprised of the constituent materials, using the plate element described in the previous section. Fig. 7 illustrates



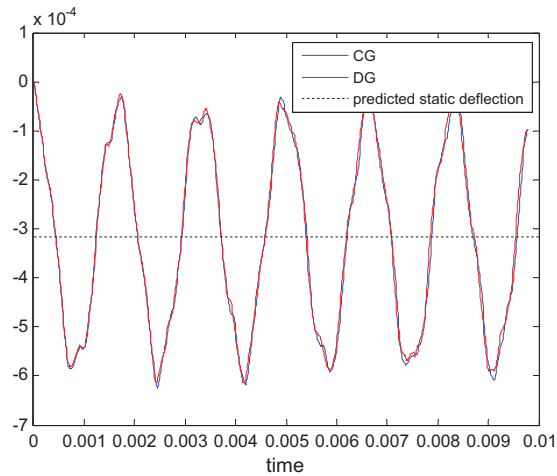


Fig. 5. Comparison of displacement calculated for Continuous Galerkin (CG) and Discontinuous Galerkin (DG) models of a center loaded clamped plate.

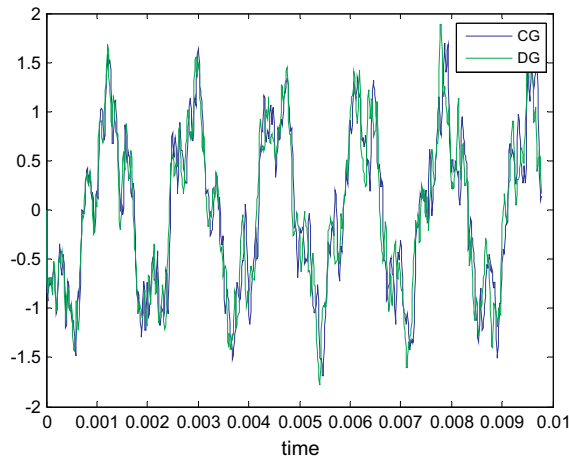


Fig. 6. Comparison of velocity calculated for Continuous Galerkin (CG) and Discontinuous Galerkin (DG) models of a center loaded clamped plate.

the two different transverse lay-ups used to model sandwich plates in this work. The three layer model includes only the core and two skin faces while the five layer or “with resin” model includes a relatively thin layer with material properties similar to common adhesives or resin used in assembling sandwich composites. The two models vary slightly in thickness as well as in overall stiffness due to the inclusion of the extra layers. However, the variation is

very small and negligible because the resin layer is very thin compared to other layers.

Schmit and Monforton [38] developed a discrete element method to predict the static deflection of sandwich plates and shells with laminated faces under a variety of boundary conditions. Kanematsu et al. [39] expanded on that work to examine both bending and vibration of sandwich plates; their work also included experimental validation. The deflection of a 50 in. square clamped plate with a one inch thick core of aluminum honeycomb faced by two 0.015 in. thick aluminum skins under uniform pressure was calculated by both papers and is used here to validate the DG structural model developed in the previous chapter. Using one thickness element for each face and one for the core, maximum static deflection was calculated for a range of square planar discretizations, and they are plotted in Fig. 8. Good agreement was reached with as few as four elements in each direction, and refinement further than twelve elements in each direction was shown to be unnecessary. Both sets of authors neglected in-plane bending of the core material, which the present formulation does not, therefore the current model is stiffer and returns a slightly lesser static deflection. Relative convergence of both maximum deflection and maximum bending stress in a clamped, square, five-layer sandwich plate subject to a concentrated center force was examined by modeling a quarter of the plate, taking advantage of symmetry to achieve finer discretizations without incurring excessive computational cost. For this study, a range of twelve to thirty elements per side of the quarter-plate was modeled. Deflection is the primary variable and bending stresses are post-processed quantities. Both skin and core stresses were calculated, but as there was minimal difference between the two, core stresses are omitted from the plot for clarity. Convergence was calculated relative to the finest discretization calculated, thirty elements per quarter-plate side ( $dx = 0.0075$  m) and is shown in Fig. 9. Both quantities converge at better than quadratic rates, the predicted rate for linear elements.

Failure of sandwich structures is a function of the constituent materials, the geometry of the structure, and the nature of the loading. Common failure modes of such structures include debonding, delamination, core crushing, skin wrinkling, and general buckling. Debonding is the separation of the skin material from the core and delamination usually refers to the separation of layers within the skin material. In this work, debonding will be the primary failure mode examined. No attempt is made here to develop failure criteria. Instead, we will instead attempt to develop an appropriate method to reflect failure within a structural model. Previous work [40] concluded that modeling an independent layer representing the adhesive between laminae of composites was necessary to observe the delamination failure mode. In this work we will examine whether such a layer can be omitted when DG techniques are applied in assembling the structure.

One-quarter of a 24 by 24 element square clamped plate with the same aluminum skins and honeycomb core as was used in the previous section was the basis for this examination. This plate

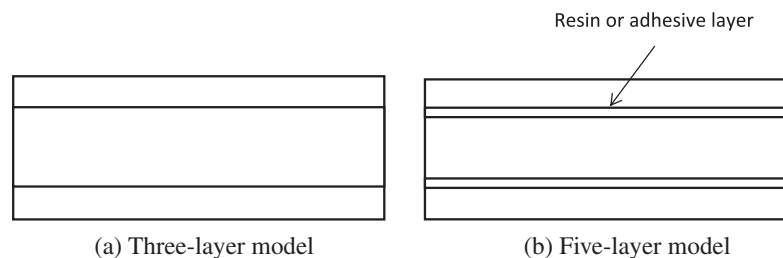


Fig. 7. Three and five layer sandwich plate models.

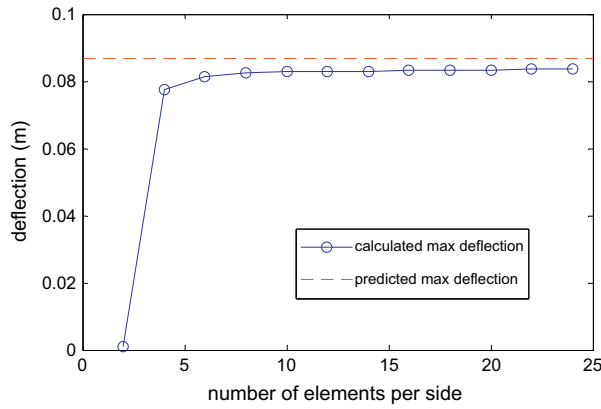


Fig. 8. Convergence of DG Sandwich Plate max deflection (due to uniform load) to predicted, comparison with [41,42].

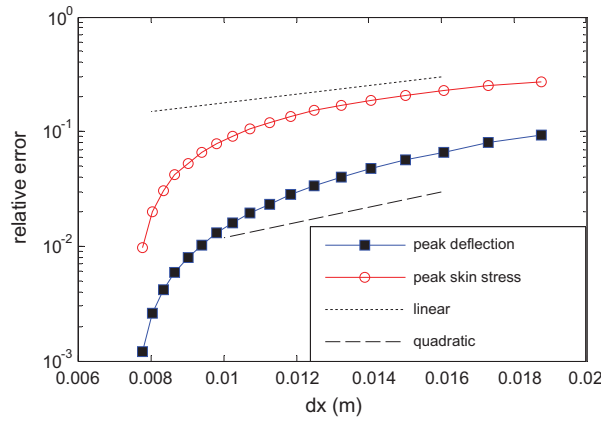


Fig. 9. Relative convergence of DG Sandwich Plate max deflection and skin stress (due to concentrated load).

model is 450 mm × 450 mm, the core is 10 mm thick, each skin is 0.375 mm thick, and the load is a concentrated force of 1000 N applied to the center of the plate. The model was assembled as described in Section 2 and the global displacement vector was calculated. The degrees of freedom of interest, those on the interface between the bottom of the core and the top of the lower skin, were extracted and post-processed to calculate the bending stress vector at each point on that interface.

In order to compare two different models as shown in Fig. 7, the stress  $\sigma_x$  was calculated. The resulting normal stress in the  $x$  direction was computed on the top of the lower skin (the side facing the core) and on the bottom of the core (the side facing the lower skin) for a three layer model. As expected, the peak stress values for both components are located at the center of the plate, and the stiffer skin is taking a significantly larger portion of this inplane load. Table 1 lists the maximum  $\sigma_x$  at the skin and core. This process was repeated for a five-layer model with a lay-up of: skin–resin–core–resin–skin. In this case the resultant stresses were calculated for the top of the lower skin and bottom of the core as before as well as both the top and bottom of the intervening resin layer. The results are shown in Table 1. The stresses on the two faces of the resin layer are close enough in magnitude to treat them as equal. Additionally, the stresses on the skin and core are negligibly affected by the insertion of the resin layer into the model. However, the stresses at the skin and core layers do not suggest the stress at

Table 1

Comparison of maximum normal stress  $\sigma_x$  for clamped sandwich plate with a center load.

	Three layer model		Five layer model	
	Max. value	Location	Max. value (MPa)	Location
Bottom skin layer	97.4 MPa	Center	96.9	Center
Core layer	0.282 MPa	Center	0.280	Center
Resin layer	N/A	N/A	10.8	Center

the resin layer where debonding is mostly initiated. Therefore, the inclusion of an interface layer is needed to accurately model debonding of skin faces from cores of sandwich composites.

### 3.3. Failure modeling

Three proposed methods of modeling debonding failure between the core and the resin layer are compared here. Each of the methods to follow is demonstrated using a five layer plate discretized into a 24 by 24 element mesh. The calculated planar stress values on the bottom of the core, the top and bottom of the lower resin layer and the top of the lower skin layers are discussed. The undamaged model discussed previously is used as a baseline reference case.

The first method is to model the debonding damage via complete disconnection between the skin and core layers. Mergheim et al. [22] introduce a scheme that combines DG methods with existing interface methods for modeling failure. Specifically, they proposed re-defining Eq. (5) as follows:

$$\begin{aligned}
 a(u, v) = & \sum_{E \in \mathcal{E}} \int_E \frac{1}{2} \sigma(u) : \varepsilon(v) dV - \sum_{\partial E \in (S_i + \Gamma_u)} (1 - \alpha) \int_{\partial E} \langle \sigma(u) n^s \rangle \cdot v dS \\
 & + \sum_{\partial E \in (S_i + \Gamma_u)} \theta_{DG} (1 - \alpha) \int_{\partial E} \langle \sigma(v) n^s \rangle \cdot u dS \\
 & + \sum_{\partial E \in (S_i + \Gamma_u)} \int_{\partial E} \left( (1 - \alpha) \frac{\delta_p G}{|S|} u + \alpha t u \right) \cdot v dS \quad (30)
 \end{aligned}$$

where  $\alpha$  is a switching factor and  $t$  is a traction vector governed by a traction–separation law. In the pre-critical or undamaged regime,  $\alpha = 0$  and Eq. (30) is identical to Eq. (5); while in the post-critical or damaged regime,  $\alpha = 1$  and the surface integrals representing connected interfaces are replaced by a traction–separation law that models progressive failure. Adapting this concept and assuming complete failure of the interface between the core and resin, debonding damage was simulated by separating a four by four array of resin elements surrounding the center of the plate from their core element neighbors. In the present formulation, all of the area integrals of Eq. (5) are calculated for both interior and Dirichlet exterior boundaries. If the interface between two elements is deemed to have failed, those faces can then be considered members of  $\Gamma_u$  rather than  $S_i$ , so the  $[K_{LL}^i]$  and  $[K_{RR}^i]$  terms remain and the various left and right components ( $[K_{LR}^i]$  and  $[K_{RL}^i]$ ) are simply deleted from the global stiffness matrix. All other parameters were unchanged from the undamaged case.

The results with this damage model shows that the skin stresses are largely unchanged from the undamaged state. The core, however, bears the brunt of this simulated debonding; its maximum stress value is significantly greater than the stress of its undamaged version. This is because this simulation has effectively removed all constraints to the core in the area of greatest load. In the undamaged model, the static deflection at the center of the plate is consistent through the thickness; that is, the transverse displacement at all center nodes, in both skin layers, both resin layers, and the core, has been the same. In this example, the static

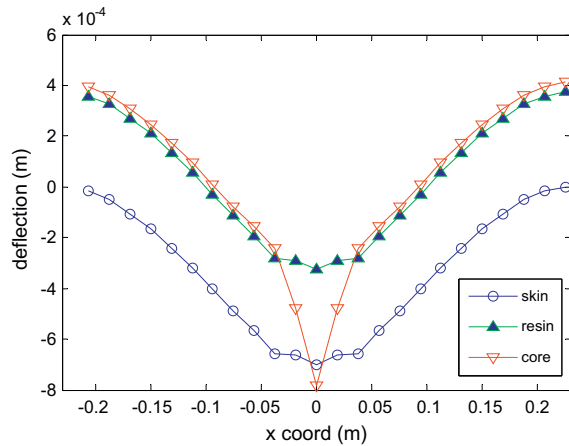


**Fig. 10.** Static deflection along centerline of damaged (via complete disconnection) clamped five-layer sandwich plate subject to concentrated center force. (For simplicity, the slope continuity is not included in the deflection plot.)

deflection is consistent from the top of the structure (point of load application) down to the bottom of the core; the deflection of the lower resin and lower skin layers was consistent within those two layers, but markedly less than that above. Deflection curves along the centerline of the plate for the bottoms of the core, resin, and lower skin layers are shown in Fig. 10. This is because this method of debonding the plate has also eliminated any means of transferring the load between those layers within the damage zone. Complete disconnection of inter-elemental interfaces is not the proper way to model this sort of damage.

A more consistent approach may be to disconnect the planar degrees of freedom between elements, but leave the transverse degrees of freedom connected. In other words, to implement a more physically consistent disconnection between core and resin elements in the debonding zone, only those rows and columns of the interface sub-matrices that correspond to the planar ( $u_i$  and  $v_i$ ) degrees of freedom are removed. That is, the entries in those sub-matrices that correspond to the transverse ( $w_i$ ) degrees of freedom is left in place. Once again, this removal of entries from the global stiffness matrix is executed after its assembly, a step that

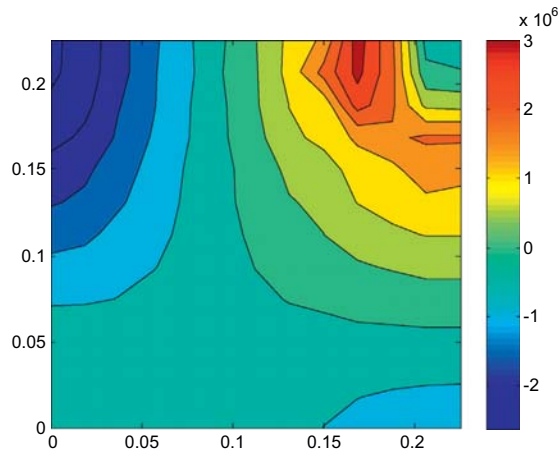


**Fig. 11.** Normal stress  $\sigma_x$  on the bottom of the resin layer of a damaged (by partial disconnection) clamped five-layer sandwich plate subject to concentrated center force.

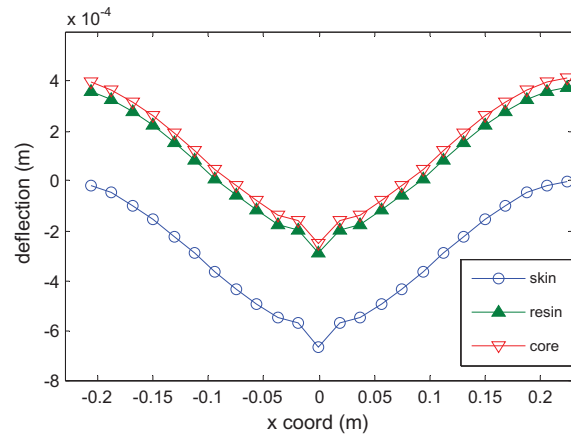


**Fig. 12.** Static deflection along centerline of damaged (via partial disconnection) clamped five-layer sandwich plate subject to concentrated center force. (For simplicity, the slope continuity is not included in the deflection plot.)

can be repeated as necessary for progressive failure with relative simplicity.

With a local debonding represented by the partial disconnection, the maximum stress zone moved to the edge of the debonded zone, as expected. Fig. 11 shows the stress contours for the resin layer between the lower skin and the core. The normal stress  $\sigma_x$  is plotted in the figure. Fig. 12 shows that the static deflection corresponding to this failure model is physically consistent: the core does not deflect beyond or through the resin and skin layers below it.

The next method of imposing damage in this model was to leave all elements connected as in the undamaged state, but to reduce the effectiveness of the resin elements in the damage zone. The same resin elements identified in the previous attempt remained connected to their core counterparts, but their shear and elastic moduli were reduced to 1% of the values used for the rest of the layer – an arbitrarily chosen reduction. In this model, the stress in the core elements is comparable to that of the undamaged plate and the dramatically lower stress values in the center of the resin layer is entirely attributable to the lower modulus. This method would seem to be similar to Mergheim's insertion of a traction–separation law to describe the progression from damage initiation to complete separation [22].

Table 2 contains a summary of the above results by comparing the maximum normal stress zones occurring in all the damage models. Complete elimination of interface terms from the global stiffness matrix does not correctly model physical constraints on the core from remaining layers in the structure below the section deemed to have been delaminated. Disconnection of the planar terms whilst retaining transverse interface terms does appear to correctly model expected physical behavior. Adjusting the physical properties of the resin or interface layer remains a potential tool for faithful modeling of traction–separation laws.

**Table 2**

Comparison of maximum planar stress locations for damaged and undamaged clamped sandwich plates subject to a concentrated center force.

	Undamaged	Complete disconnect	Partial disconnect	Reduced modulus
Lower skin	Center	Center	Debonding edge	Center
Core	Center	Center	Debonding edge	Center
Resin	Center	Center	Debonding edge	Debonding edge



#### 4. Fluid domain analysis

Fluid flow is neglected in the fluid domain considered here, as is viscosity; as a result, the wave equation is used to model the fluid domain. In particular, the velocity potential formulation is selected for the wave equation which is solved using FEM, CA, and the coupled FEM-CA technique. The coupled technique can take advantage of the both techniques as discussed later.

##### 4.1. Finite element formulation

The velocity potential,  $\phi$ , in the acoustic domain is defined as

$$\vec{v} = \nabla \phi \quad (31)$$

where  $\vec{v}$  is the velocity. The wave equation is

$$c^2 \nabla^2 \phi = \frac{\partial^2 \phi}{\partial t^2} = \ddot{\phi} \quad (32)$$

where  $c$  is the acoustic speed of the medium. Coupled with appropriate initial conditions, this well-posed initial value problem has been much studied and discussed [41]. Applying the Galerkin formulation to the wave equation, the following finite element matrix equation is obtained.

$$[M_f] \{\ddot{\phi}\} + c^2 [K_f] \{\phi\} = c^2 \{F_f\} \quad (33)$$

where

$$[M_f] = \int_{\Omega} \{H\}^T \{H\} d\Omega \quad (34)$$

$$[K_f] = \int_{\Omega} \{\nabla H\}^T \{\nabla H\} d\Omega \quad (35)$$

$$\{F_f\} = \int_{\Gamma} \{H\}^T (\vec{v} \cdot \vec{n}) d\Gamma \quad (36)$$

Here,  $\{H\}$  is the vector of nodal interpolation functions. The right-hand side is only defined on the boundary of the domain. At the fluid–structure interface, the velocity and pressure compatibility provides a convenient input to this finite element problem. Specified Dirichlet or Neumann boundary conditions can also be applied with relative simplicity. For the present work, non-reflecting boundary conditions are needed to model an infinite or a semi-infinite fluid domain, but are not easily applied.

##### 4.2. Cellular automata formulation

Cellular automata are discrete, rule-based numerical methods that can model complex physical phenomena with relative simplicity. Generally, both space and time are treated discretely and the value of the quantity in question is limited to a finite set of values. As the space–time domain proceeds or grows the seemingly simple model converges to the complex real-world behavior. The simplicity of the chosen rules and their implementation lowers the computational cost while still achieving required accuracy. CA rules developed for modeling wave propagation are pre-cursors to the lattice Boltzmann method of modeling fluid flow.

Following the work of Chopard [25,26], Kwon and Hosoglu [28] modeled the wave equation in the two-dimension using the following rules:

$$\phi_c(t + \Delta t) = \frac{1}{2} (\phi_w(t) + \phi_E(t) + \phi_S(t) + \phi_N(t) - 2\phi_c(t - \Delta t)) \quad (37)$$

The value of  $\phi$  at each interior grid point in the domain of interest ( $\phi_c$ ) is updated according to the values at its nearest Von Neumann neighbors ( $\phi_N, \phi_S, \phi_E, \phi_S$ ) as shown in Fig. 13. For convenience the set of points is divided into two sets, “black” and “white” (or

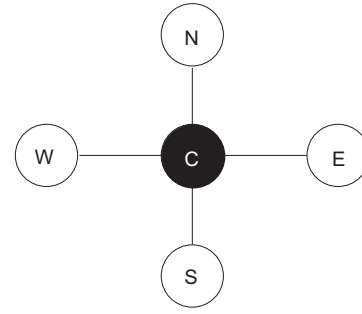


Fig. 13. Center node (black) and its Von Neumann neighbors (white).

“odd” and “even”), such that the neighbors of each white point are all black, and only one “color” is updated during each iteration. The CA technique for the three-dimension is extended from Eq. (37) to the following equation.

$$\phi_c(t + \Delta t) = \frac{1}{3} (\phi_w(t) + \phi_E(t) + \phi_S(t) + \phi_N(t) + \phi_F(t) + \phi_B(t) - 3\phi_c(t - \Delta t)) \quad (38)$$

with the subscripts on the new terms standing for “front” and “back,” respectively.

Fixed boundary conditions are easy to implement, but are of limited utility in modeling a potentially infinite fluid domain. One possible approach is to model a much larger domain than that of interest so that the area of interest is well away from the boundary and, as such, solutions within it are unpolluted by whatever boundary condition is imposed. This requires many computations that will be ignored – a seeming waste. Another approach is to generate a model of a non-reflecting boundary such that the wave in question is unaffected by its proximity. This is an active area of research in the finite element arena. In the CA arena, Chopard and Droz [25] suggested implementing boundary conditions by generating virtual cells adjacent to the boundary cells as shown in Fig. 14. Fixed or specified boundary conditions do not require a virtual neighbor, but are shown for completeness. Non-reflecting (or zero-gradient or adiabatic) boundaries model the behavior in the heart of the domain of interest, well away from the influence of any boundary. The free boundary condition corresponds to that of a constant gradient. In practice, this can be implemented either by generating the virtual neighbor cells or by applying the resulting rule to the actual cells located on the boundary in question.

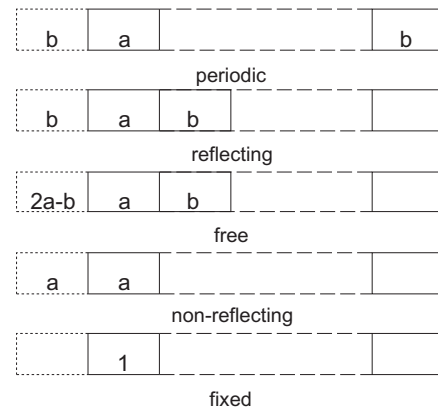


Fig. 14. Virtual cell values for various boundary conditions in one dimension. After [25].

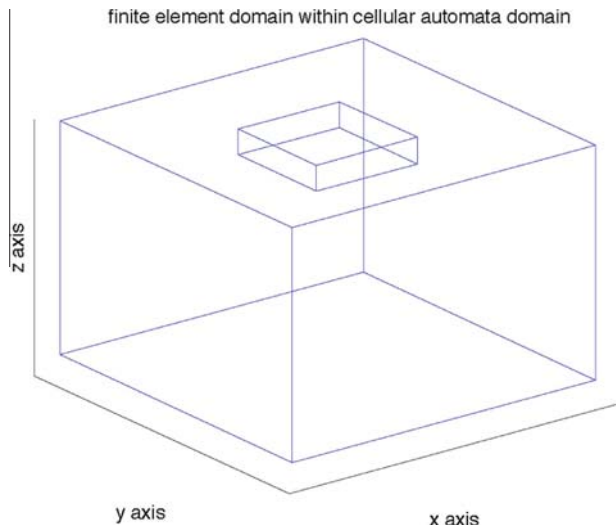


Fig. 15. Finite element fluid domain surrounded by cellular automata fluid domain.

#### 4.3. Coupling of FEM and CA for wave equation

The CA model of the wave equation for velocity potential is simple to implement and can easily be adapted to a variety of non-trivial boundary conditions, but converting velocity potential back into useful quantities like pressure and velocity as time- and spatial derivatives is hampered by the alternating update nature of the model. The finite element model, on the other hand updates the value of every point every time-step, but can be computationally expensive and non-trivial boundary conditions can be difficult to implement. A combination of the two methods would seem to resolve the short-comings of each and enable a faithful model of the fluid portion of our fluid–structure interaction.

The general idea is to have several layers of finite elements in contact with the structure and then to have that fluid volume surrounded with a CA domain upon which the non-reflecting and free boundary conditions can be imposed as shown in Fig. 15. The two fluid domains will overlap such that the outer layer of finite element nodes will be processed as interior CA nodes whose CA-calculated values become FE-specified boundary values. The next set of FE nodes inside the domain are calculated by the FE machin-

ery and then passed to the CA domain to serve as neighbors for application of the CA rule to the outer set. These node sets are illustrated in Fig. 16. The next section presents the numerical examples for verification of the proposed coupled technique.

### 5. Fluid and fluid–structure analyses

#### 5.1. CA for fluid medium

The various waves modeled above by CA rules display a coarseness that results from updating the value of each point in space at alternating time steps. The initial perturbation displayed thus far has been a Gaussian wave of medium width that proved to be smooth enough to demonstrate the desired characteristics. Attempts to model a point source along the lines of  $f(x) = 0, x \neq 0, f(x) = 1, x = 0$  were unsuccessful, begging the question of how smooth a function or discretization are necessary to use CA to model the wave equation. In order to determine a sufficiently fine discretization relative to the sharpness of the initial perturbation,  $f(x) = e^{-x^2/2\sigma^2}$ , a series of progressively narrower Gaussians as shown in Fig. 17. For each initial condition, the CA solution to the wave equation was calculated for the same set of discretizations (progressively smaller  $dx$ ) and error norms relative to the D'Alembert solution were calculated at the same arbitrary time. Non-reflecting boundary conditions were applied in all cases. An error norm of 1% was chosen as the comparison point. The largest  $dx$  value required to achieve that level of convergence was then plotted against the width at half maximum for each initial condition as shown in Fig. 18. A linear estimate of that data is that  $dx_c = \frac{2}{3}\sigma$ . Applying this estimate to the specific  $f(x)$  used, 4.5 elements or nodes are required to represent the descent from peak value of  $f$  to 1% of that peak. Therefore, a discretization that uses eleven or more nodes to represent both sides of a peak should be sufficient.

To examine convergence of the present CA rule for wave propagation with respect to mesh or lattice spacing, comparison to the steady-state plane wave as presented by Junger and Feit [42] was used. Consider a semi-infinite fluid-filled space with a given uniform vibration,  $\dot{w}(t) = We^{-i\omega t}$  at  $z = 0$  boundary and a non-reflecting boundary as  $z \rightarrow \infty$ . The steady state pressure in the wave guide is  $P(z, t) = \rho c W e^{(ikz - i\omega t)}$  where  $k = \frac{\omega}{c}$ . The given function was applied to the  $z = 0$  nodes in a CA domain with the initial values everywhere else uniformly zero. The CA rule was applied for a number of iterations corresponding to over three periods of the steady-state solution, and point-by-point error was calculated

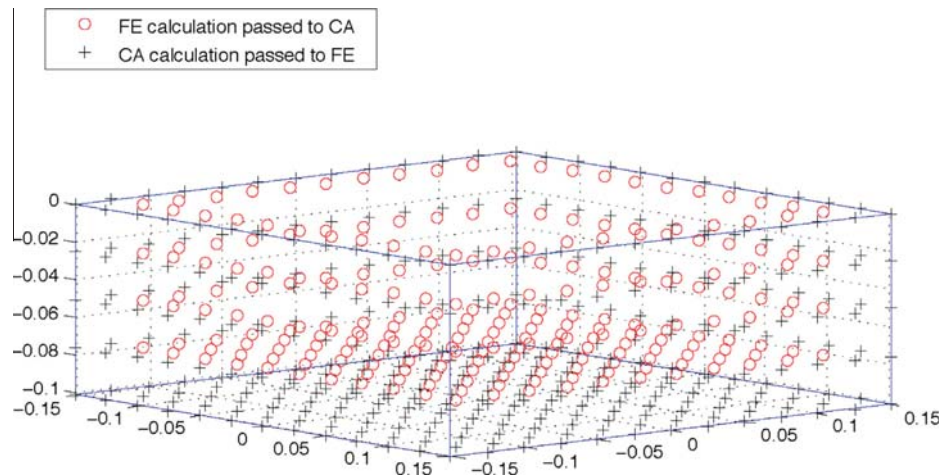


Fig. 16. Node sets for exchange of data between fluid domains.

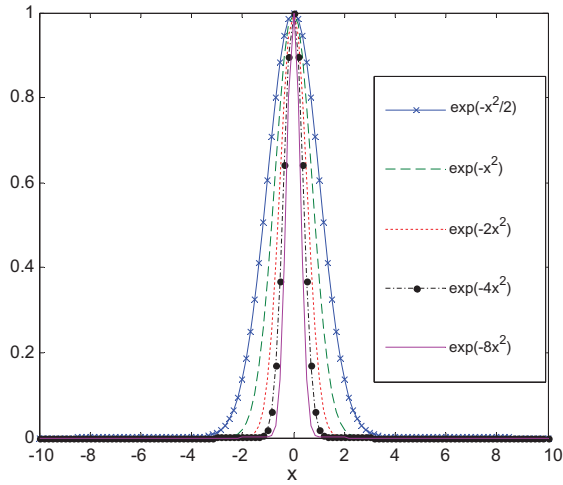


Fig. 17. Initial perturbations of varying width.

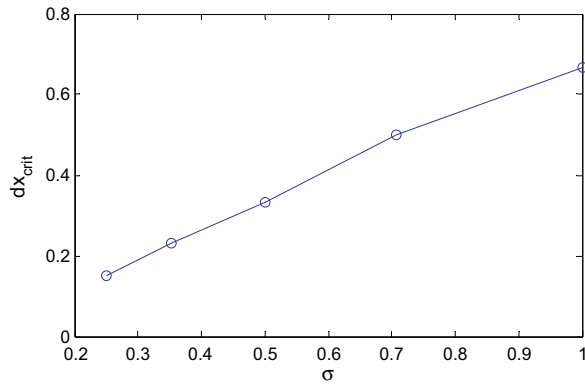


Fig. 18. Critical discretization vs. initial perturbation width.

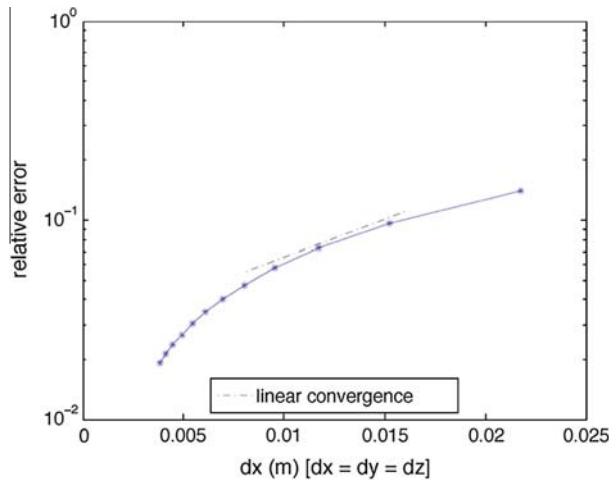


Fig. 19. Convergence of CA wave equation rule to analytic solution as a function of  $dx$ .

relative to the analytic solution over the range  $z \in [0, \frac{2\pi}{k}]$  and plotted in Fig. 19. The rate of convergence is linear, as expected for a first-order method.

To test the CA technique for 3-D, consider a “point” source located in the center of a domain of interest. As was discussed in the previous example, CA is not expected to faithfully model a true point source, so the source under consideration is a smooth radial function that has a maximum value of 1 at the origin of the domain and is zero valued outside a radius of five nodes from the origin. The domain is comprised of 73 equi-spaced nodes in each direction, and non-reflecting boundary conditions were applied on all six sides of the domain. Three points in space are examined: the origin, an arbitrary point inside the initial perturbation ( $r < 5dx$ ), and an arbitrary point outside the initial perturbation ( $r > 5dx$ ).

The analytical solution for the 3-D case is expressed as

$$\phi(x, y, z, t) = t\bar{\psi} + \frac{\partial}{\partial t}(t\bar{\phi}) \quad (39)$$

where  $\bar{\phi}$  and  $\bar{\psi}$  are the averages of their respective initial conditions,  $\phi(x, y, z, 0) = \bar{\phi}(x, y, z)$ , and  $\frac{\partial \phi}{\partial t}(x, y, z, 0) = \bar{\psi}(x, y, z)$ , over the sphere of radius  $ct$  centered at  $(x; y; z)$ ; specifically,

$$\bar{\psi}(x, y, z) = \frac{1}{4\pi c^2 t^2} \int_0^\pi \int_0^{2\pi} \psi(x + ct \sin \vartheta \cos \theta, y + ct \sin \vartheta \sin \theta, z + ct \cos \vartheta)(ct)^2 \sin \vartheta d\theta d\vartheta \quad (40)$$

$$\bar{\phi}(x, y, z) = \frac{1}{4\pi c^2 t^2} \int_0^\pi \int_0^{2\pi} \phi(x + ct \sin \vartheta \cos \theta, y + ct \sin \vartheta \sin \theta, z + ct \cos \vartheta)(ct)^2 \sin \vartheta d\theta d\vartheta \quad (41)$$

For the point source in 3-D, the initial conditions are expressed as

$$\phi(x, y, z) = \begin{cases} 1 - \frac{r}{a} & \text{if } r < a \\ 0 & \text{if } r \geq a \end{cases} \quad (42)$$

$$\psi(x, y, z) = 0 \quad (43)$$

where  $r$  is the Cartesian radius. The analytic solution of the integrals in Eq. (41) is not easily calculated, but application of a composite Simpson's Rule over intervals yields a suitable comparison.

Figs. 20 through 22 show the analytical solutions at the respective points plotted as a function of time directly compared to CA counterparts. The time scaling factor for one iteration in CA is equivalent to

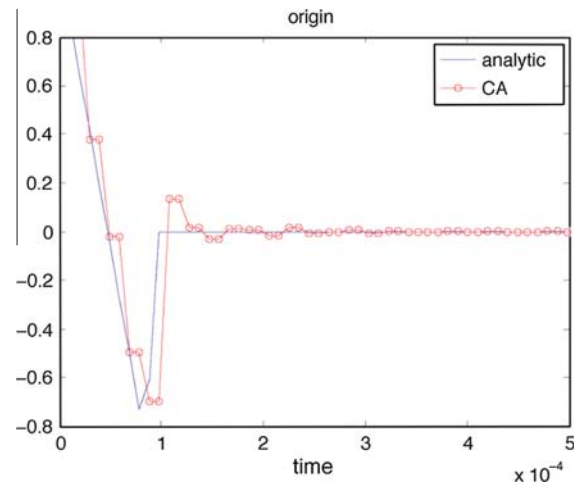


Fig. 20. Three-dimensional wave model at a domain origin.

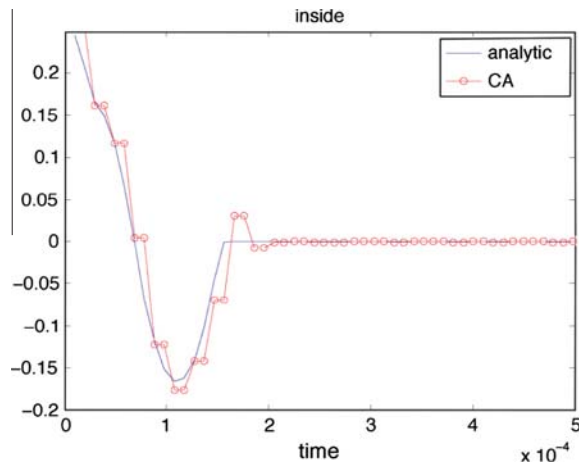


Fig. 21. Three-dimensional wave model at a point inside the initial perturbation.

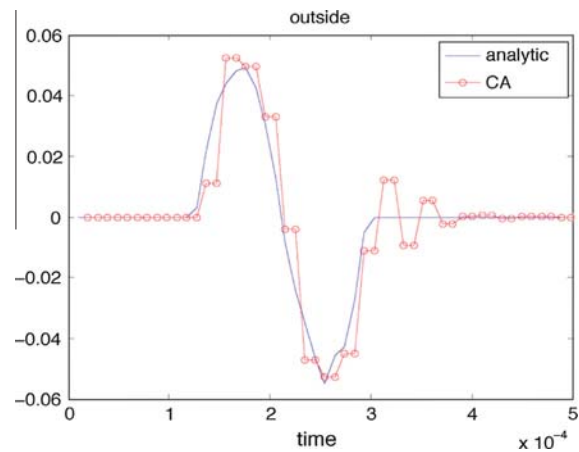


Fig. 22. Three-dimensional wave model at a point outside the initial perturbation.

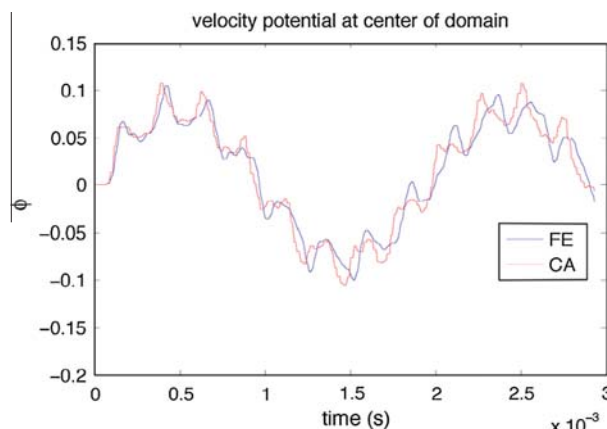


Fig. 23. Comparison of velocity potential propagation between finite element and cellular automata models with common Dirichlet boundary conditions.

$$dt_{CA} = \frac{dx}{c\sqrt{n_{dim}}} \quad (44)$$

in which  $n_{dim}$  is the dimension of the problem, which is 3 for the present example. The comparison is good at all the selected points.

## 5.2. Coupled CA and FEM for fluid medium

First of all, CA and FEM models are solved independently and compared to each other. To compare the solutions, a specified velocity potential field is imposed on one face of the domains (the top), and the other five faces have fixed non-zero values. The specified input is a radially scaled sinusoid. It achieves its maximum value at the center of the face over which it is applied and is zero beyond a radius of one-half the width of the region. The resulting value of the velocity potential at the respective domain centers compares favorably as shown in Fig. 23.

The validation of the coupling scheme was to model a joint domain. The CA domain surrounds the FE domain on five sides and the non-reflecting boundary condition is applied to all six sides of the outer domain with the exception of the top of the FE domain on which a velocity potential is specified. The velocity potential at the mid-point of the overall domain is plotted as a function of time in Fig. 24. The mid-point is inside the CA domain because the FE domain is much smaller than the CA domain. In comparison, the same whole domain is modeled using the CA technique. The CA result is also shown in Fig. 24 for comparison. The two results agree very well suggesting the coupling was implemented properly.

## 5.3. Fluid–structure analysis

Recent experimental work [29,43–45] examined the response of composite plates to low velocity impact with and without fluid–structure interaction. In general, the study found that for a given impact weight dropped from the same height, structures in contact with water experienced higher resultant impact forces and consequently greater strains and damage than the same material in dry conditions. Additionally, they noted that the initial observable damage mode was delamination occurring on the face of the plate opposite the impact site.

In one of the studies, the Vacuum Assisted Resin Transfer Molding technique was used to construct a series of 30.48 cm (12 in.) by 30.48 cm (12 in.) composite plates comprised of sixteen layers of E-glass (approximately 3.5 mm thick in total) and subjected them to low velocity impact forces that resulted from dropping a 10.8 kg weight from various heights to the center of the plate which was clamped along all edges. The plates were instrumented with strain rosettes at four set positions. Data was sampled at a frequency of 10,000 Hz.

Numerical comparison with this experimental data was conducted using a DG structural model comprised of a single layer

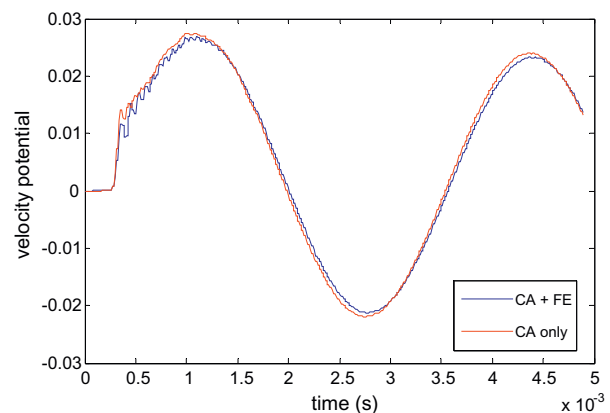


Fig. 24. Comparison of velocity potential at mid-point of the domain resulting from specified velocity potential on one face: FE + CA domain vs. homogeneous CA domain.

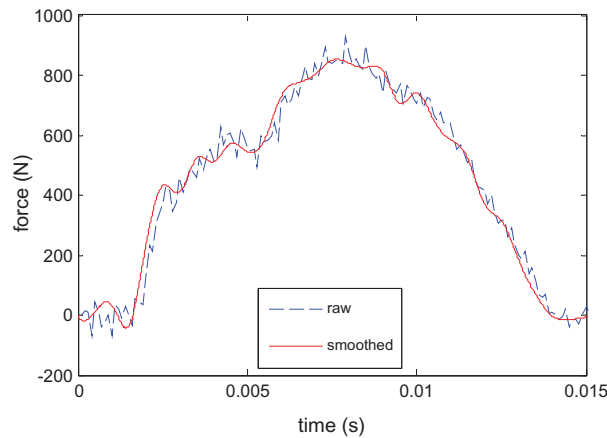


Fig. 25. Raw and smoothed experimental force data for wet plate.

of plate elements with a discretization of twelve elements in each planar direction. The overall structure has a length to thickness ratio of 87:1 and each element has a length to thickness ratio of 7.3:1. In this model, the material properties used are those of E-glass, but treated as an isotropic material because the composite was made of balanced plane weave layers. The lumped mass matrix was used in the model.

The wet, or FSI, response was calculated according to the acoustic field FSI described in the previous section with time step size for the entire model equal to the time scale factor for the CA portion of the fluid model. The force inputs to the numerical plates were smoothed versions of the experimentally measured force data in the time region of interest. Fig. 25 shows the force data used for the FSI case.

In the numerical model, those elements closest to the positions of the strain gages in the experimental work were examined relative to the recorded data and are plotted in Fig. 26 for the gage close to the center for the FSI case. Because the impactor hit the center of the plate, the strain gage was attached near the center. The comparison is acceptable even though there is some difference between the two results. Such differences can be attributed to the smoothing of the input force, ignoring local fluid motion in the experiment, homogeneity of the composite samples. Particularly, the model used non-reflected boundary conditions for the water medium while the anechoic water tank used for the experiment is not fully non-reflective.

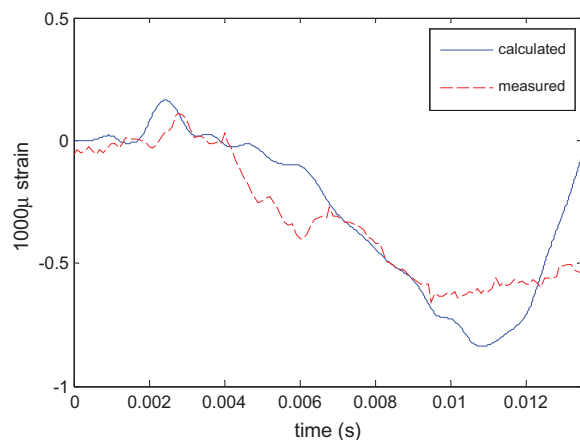


Fig. 26. Measured vs. calculated strain for wet clamped plate near the center.

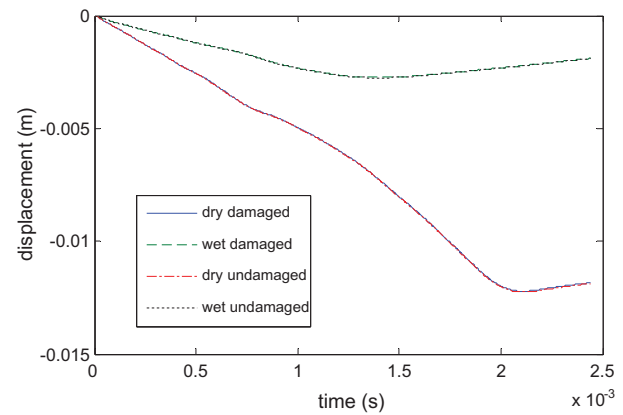


Fig. 27. Displacement of clamped three layer E-glass plate with and without fluid structure interaction and with and without damage.

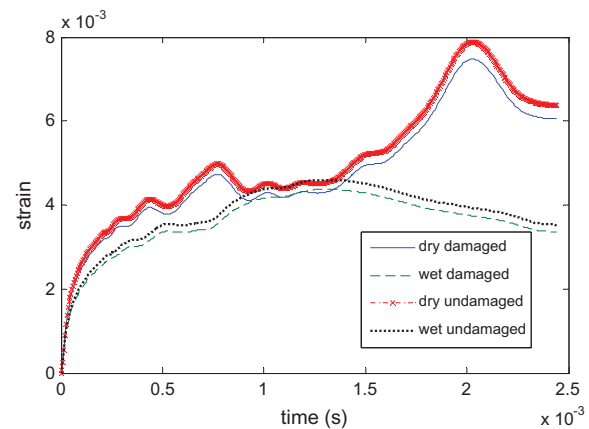


Fig. 28. Strain of clamped three layer E-glass plate with and without fluid-structure interaction and with and without damage at center of lower E-glass layer.

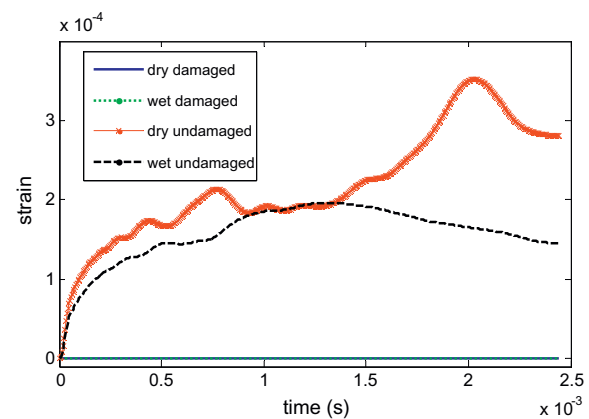


Fig. 29. Strain of clamped three layer E-glass plate with and without fluid-structure interaction and with and without damage at center of interface layer.

The next example considers the E-glass composite plates with local delamination at the center, and subjected to FSI. The composite plate is simulated as a three-layer model. The three-layer model including a thin interface layer with properties approximating a common adhesive inserted between two layers of E-glass is subjected to 1000 N concentrated force at center with clamped edges.



Fig. 27 shows that the displacement response of the center of the plate does not reflect the presence or absence of a delamination zone, but does demonstrate FSI effects. The wet plate has a smaller displacement than the dry plate. Fig. 28 shows that the strain calculated at the center of the E-glass plate reflects presence or absence of damage mildly. Fig. 29, on the other hand, shows clearly that the interface layer is profoundly affected by the presence of a damage zone. To be clear, the strain values at the centers of the interface layers of the damaged plates are not identically zero, but they are four orders of magnitude lower than their undamaged counterparts.

## 6. Conclusions

The goal of this work was to develop computational techniques to accurately model and simulate dynamic responses of composite structures in a fluid medium. A displacement-only plate finite element was formulated and implemented using Discontinuous Galerkin (DG) methodology. Such a displacement-only element allows construction of multi-layered composite structures like sandwich plates and other laminated composites in a manner similar to full three-dimensional solid finite elements. Results generated from this formulation compare favorably with theoretical predictions as well as existing CG numerical models for both static and dynamic responses for both simple and multi-layered plate structures.

Application of the new element to the analysis of sandwich composite structures containing local failure like debonding shows great promise. Static qualitative stress profiles are similar to those found using CG techniques, but the elemental rather than nodal connectivity used in DG formulations suggests a simple means of modeling debonding between material layers by disconnecting their respective elements in the global stiffness matrix. Complete disconnection of neighboring elements in an imposed debonding zone was shown to be incorrect because it allowed the core layer to deflect not only through the disconnected resin layer but also through the still-present skin layer. Partial disconnection – removing connectivity between opposing pairs of degrees of freedom in the planar directions but retaining weak connectivity for transverse pairs of degrees of freedom – resulted in a stress profile that makes good qualitative sense. Maximum stress location in both skin and core layers moved from the center of the plate to the edges of the debonding zone, behaving like a stress concentration. The simplicity of this partial disconnection method can be a tremendous computational savings when modeling the progression of damage without need for re-meshing or recalculation of the global stiffness matrix.

Examination of FSI for the impact problem does not require a full fluid flow model. Instead, the propagation of velocity potential according to the wave equation in the acoustic domain is sufficient for these purposes. As such, an extension of CA from two to three-dimensions in modeling the acoustic field was demonstrated and validated. The cellular automata was chosen for this application not only because of the simplicity of its update rule, but also because of its flexibility in the implementation of non-reflecting boundary conditions. The alternating update nature of CA makes calculation of both spatial and time derivatives, required to convert the velocity of the structure into velocity potential in the fluid domain and to convert velocity potential into a pressure field, difficult. Insertion of a small finite element interface zone between the structure and the CA fluid domain resolved this difficulty for a relatively low computational cost. The combination of a small FE acoustic domain with an enveloping CA domain proved to be an efficient way to implement non-reflecting boundary conditions. Finally, the combined model of a DG structure interacting with a

FE–CA fluid domain was shown to have good agreement between calculated and experimentally measured strain values for plates subject to low-velocity impact in the pre-damage regime. In particular, the added mass effect on structures with low density relative to the fluid medium was apparent in both simulation and experimental comparisons. The methods developed and examined in this study: the displacement-only DG plate finite element, the partial disconnection failure model, and the hybrid FE–CA acoustic field model, show great promise for flexible and accurate modeling of dynamic responses of laminated composite structures, with or without local failure, subjected to FSI.

## References

- [1] Nitsche J. Über ein Variationsprinzip zur Lösung von Dirichlet-Problemen bei Verwendung von Teilräumen, die keinen Randbedingungen unterworfen sind. *Abhandlungen aus dem Mathematischen Seminar der Univ Hamburg* 1971; 36(1):9–15.
- [2] Douglas Jr J, Dupont T. Interior penalty procedures for elliptic and parabolic Galerkin methods. In: *Computing methods in applied sciences and engineering*. New York: Springer-Verlag; 1975. p. 207–16.
- [3] Arnold DN. An interior penalty finite element method with discontinuous elements. *SIAM J Numer Anal* 1982;19(4):742–60.
- [4] Baker GA. Finite element methods for elliptic equations using nonconforming elements. *Math Comput* 1977;31(January):45–59.
- [5] Wheeler MF. An elliptic collocation-finite element method with interior penalties. *SIAM J Numer Anal* 1978;15(1):152–61.
- [6] Arnold DN, Brezzi F, Cockburn B, Marini D. Discontinuous Galerkin methods for elliptic problems. In: *Discontinuous Galerkin methods: theory, computation and applications*. Berlin: Springer; 2000. p. 89–101.
- [7] Arnold DN, Brezzi F, Cockburn B, Marini LD. Unified analysis of discontinuous Galerkin methods for elliptic problems. *SIAM J Numer Anal* 2002;39(5): 1749–79.
- [8] Castillo P. Performance of discontinuous Galerkin methods for elliptic PDEs. *SIAM J Sci Comput* 2003;24(2):524–47.
- [9] Brezzi F, Cockburn B, Marini LD, Suli E. Stabilization mechanisms in discontinuous Galerkin finite element methods. *Comput Methods Appl Mech Eng* 2006;195(25–28):3293–310.
- [10] Riviere B, Shaw S, Wheeler MF, Whiteman JR. Discontinuous Galerkin finite element methods for linear elasticity and quasistatic linear viscoelasticity. *Numer Math* 2003;95(2):347–76.
- [11] Hansbo P, Larson MG. Discontinuous Galerkin methods for incompressible and nearly incompressible elasticity by Nitsche's method. *Comput Methods Appl Mech Eng* 2002;191(17):1895–908. 109.
- [12] Noels L, Radovitzky R. A general discontinuous Galerkin method for finite hyperelasticity: formulation and numerical applications. *Int J Numer Meth Eng* 2006;68(1):64–97.
- [13] Noels L, Radovitzky R. A new discontinuous Galerkin method for non-linear mechanics. In: *47th AIAA/ASME/ASCE/AHS/ASC structures, structural dynamics and materials conference*, May 1, 2006–May 4, vol. 9, Newport, RI, United States, American Institute of Aeronautics and Astronautics Inc; May 2006. p. 6290–7.
- [14] Noels L. Alternative approaches for the derivation of discontinuous Galerkin methods for nonlinear mechanics. *J Appl Mech* 2007;74(5):1031–6.
- [15] Arnold DN, Brezzi F, Marini LD. A family of discontinuous Galerkin finite elements for the Reissner–Mindlin plate. *J Sci Comput* 2005;22–23:25–45.
- [16] Celiker F, Cockburn B, Guzey S, Kanpady R, Soon S-C, Stolarski HK, et al. Discontinuous Galerkin methods for Timoshenko beams. In: *Feistauer M, Dolejsi V, Knoblock P, Najzar K, editors. Numerical mathematics and advanced applications*. ENUMATH 2003, Germany, Springer; August, 2003. p. 221–31.
- [17] Engel G, Garikipati K, Hughes T, Larson M, Mazzei L, Taylor R. Continuous/discontinuous finite element approximations of fourth-order elliptic problems in structural and continuum mechanics with applications to thin beams and plates, and strain gradient elasticity. *Comput Methods Appl Mech Eng* 2002;191(34):3669–750.
- [18] Lew A, Ten Eyck A, Rangarajan R. Some applications of discontinuous Galerkin methods in solid mechanics. In: *Daya Reddy B, editor. Proceedings of the IUTAM symposium on theoretical, computational and modelling aspects of inelastic media*. Springer; 2008.
- [19] Stan F. Discontinuous Galerkin method for interface crack propagation. *Int J Mater Form* 2008;1:1127–30.
- [20] Stan F. Simulation of delamination using discontinuous Galerkin finite element methods and cohesive models. *Key Eng Mater* 2010;417:501–4.
- [21] Liu R, Wheeler MF, Dawson CN. A three-dimensional nodal-based implementation of a family of discontinuous Galerkin methods for elasticity problems. *Comput Struct* 2009;87(February):141–50.
- [22] Mergheim J, Kuhl E, Steinmann P. A hybrid discontinuous Galerkin/interface method for the computational modelling of failure. *Commun Numer Methods Eng* 2004;20(7):511–9.
- [23] Olson LG, Bathe K-J. Analysis of fluid-structure interactions: a direct symmetric coupled formulation based on the fluid velocity potential. *Comput Struct* 1985;21(12):21–32.

- [24] Lindquist J. Unstructured high-order galerkin-temporal-boundary methods for the Klein-Gordon equation with non-reflecting boundary conditions. PhD., Naval Postgraduate School; 2010.
- [25] Chopard B, Droz M. Cellular automata modeling of physical systems. Cambridge: Cambridge University Press; 1998.
- [26] Chopard B. A cellular automata model of large-scale moving objects. *J Phys A: Math Gen* 1990;23(10):1671.
- [27] Krutar RA, Numrich SK, Squier RK, Pearson J, Doolen G. Computation of acoustic field behavior using a lattice gas model. In: *Proceedings of Oceans '91*, October 1, 1991–October 3, vol. 1. Honolulu, HI, USA: Publ by IEEE; 1991. p. 446–52.
- [28] Kwon YW, Hosoglu S. Application of Lattice Boltzmann method, finite element method, and cellular automata and their coupling to wave propagation problems. *Comput Struct* 2008;86(7–8):663–70.
- [29] Kwon YW, Conner RP. Low velocity impact on polymer composite plate in contact with water. *Int J Multiphys* 2012;6(3).
- [30] Kwon YW. Analysis of laminated and sandwich composite structures using solid-like shell elements. *Appl Compos Mater*. doi:10.1007/s10443-012-9273-8.
- [31] Cockburn B, Shu C-W. Local discontinuous Galerkin method for time dependent convection-diffusion systems. *SIAM J Numer Anal* 1998;35(6):2440–63.
- [32] Ainsworth M. A posteriori error estimation for discontinuous Galerkin finite element approximation. *SIAM J Numer Anal* 2007;45(4):1777–98.
- [33] Epshteyn Y, Riviere B. Estimation of penalty parameters for symmetric interior penalty Galerkin methods. *J Comput Appl Math* 2007;206(2):843–72.
- [34] Shahbazi K. An explicit expression for the penalty parameter of the interior penalty method. *J Comput Phys* 2005;205(2):401–7.
- [35] Ainsworth M, Rankin R. Technical note: a note on the selection of the penalty parameter for discontinuous Galerkin finite element schemes. *Numer Methods Partial Differ Eq* 2012;28(3):1099–104.
- [36] Ainsworth M, Rankin R. Fully computable error bounds for discontinuous Galerkin finite element approximations on meshes with an arbitrary number of levels of hanging nodes. *SIAM J Numer Anal* 2010;47(6):4112–41.
- [37] Timoshenko S, Woinowsky-Krieger S. *Theory of plates and shells*. second ed. New York: McGraw-Hill Book Company; 1959.
- [38] Schmit Jr IA, Monforton GR. Finite deflection discrete element analysis of sandwich plates and cylindrical shells with laminated faces. *AIAA J* 1970;8(August):1454–61.
- [39] Kanematsu HH, Hirano Y, Iyama H. Bending and vibration of CFRP-faced rectangular sandwich plates. *Compos Struct* 1988;10(2):145–63.
- [40] Kwon Y, Craugh L. Progressive failure modeling in notched cross-ply fibrous composites. *Appl Compos Mater* 2001;8(1):63–74.
- [41] Farlow SJ. *Partial differential equations for scientists and engineers*. New York: Dover Publications, Inc.; 1993.
- [42] Junger MC, Feit D. *Sound, structures, and their interaction*. Cambridge, MA: The MIT Press; 1986.
- [43] Kwon YW, Owens AC, Kwon AS, Didoszak JM. Experimental study of impact on composite plates with fluid-structure interaction. *Int J Multiphys* 2010;4(3):259–71.
- [44] Kwon Y, Violette M, McCrillis R, Didoszak J. Transient dynamic response and failure of sandwich composite structures under impact loading with fluid structure interaction. *Appl Compos Mater* 2012;19(6):921–40.
- [45] Kwon YW, Violette MA. Damage initiation and growth in laminated polymer composite plates with fluid-structure interaction under impact loading. *Int J Multiphys* March 2012;6:29–42.

# Failure of Ductile Materials Subject to Varying Strain Rates

Y. W. Kwon

K. S. Tan

Department of Mechanical and Astronautical  
Engineering,  
Naval Postgraduate School,  
Monterey, CA 93940

*Strain rate affects the mechanical properties of ductile materials in terms of their stiffness and strength. In particular, yield and failure strengths and strains depend on the strain rate applied to the materials. When a metallic material is subjected to a typical dynamic loading, the material usually undergoes various strain-rate loading conditions. One of the main questions is whether the material is going to fail or not. To the authors' best knowledge, there has been no failure criterion proposed for a varying strain-rate loading condition. This paper presents a failure criterion under nonuniform strain-rate loading conditions. Experiments were conducted to support the proposed failure criterion using aluminum alloy AA3003-H14. This study also investigated the that failure envelopes in terms of strain rates and the normalized failure strengths. Furthermore, the effects of strain rates on strength and stiffness properties were also examined.*

[DOI: 10.1115/1.4002054]

## 1 Introduction

The behavior of materials may vary depending on their loading rates. As the applied strain rate increases, the material strength and stiffness generally vary and the failure mode may also change. Research on the effects of strain rates on the strength and stiffness of materials is important to the design of safe and reliable structures under dynamic loading conditions. For example, structural safety of pressure vessels and pipes under seismic, impact, and/or explosive loading such as steam explosion is of important concern. Since these loadings are not at the constant rates, design of such structures to meet strength requirements derived based on a single strain rate is not realistic.

There has been an extensive research to understand the effects of strain rates on material behaviors. As a result, there is no attempt to review all those previous works. Only some of the relevant studies are reviewed here. Hadianfard et al. [1] investigated the effect of the rate of strain on the mechanical properties and failure mechanisms of the aluminum alloys, AA5754 and AA5182. Conducting quasistatic tensile tests at strain rates less than  $0.1 \text{ s}^{-1}$ , their results indicated negative strain-rate sensitivity in those alloys. Both ultimate and yield strengths were reduced as the strain rate increased. Moreover, the flow stresses and the strains to failure tended to decrease with higher quasistatic strain rates. They [1] attributed the negative strain-rate sensitivity in the quasistatic tensile loading to the dynamic strain aging phenomenon, which was manifested in the serrations. Diffusion process had a large influence on the dynamic aging. As a result, temperature and strain rate had a large impact on the dynamic strain aging. Higher flow stresses at very low strain rates were the consequence of solute atoms interacting with obstacles preventing dislocation movements. With increasing strain rates, this dampening effect was thus reduced and lower flow stresses were resulted.

On the other hand, at dynamic rates of strain greater than  $0.1 \text{ s}^{-1}$ , the studied aluminum alloys exhibited mild positive sensitivity. The elongation to failure increased with the strain rate. Furthermore, different failure mechanisms were also observed between the quasistatic and dynamic tensile tests. Under quasistatic conditions, strain localization and shear band formation were found to be necessary prerequisites for damage and final failure to occur. The thickness of the shear bands, as well as the average size of the damaged particles, was observed to increase with in-

creasing strain rates. The contrary was true under dynamic conditions. The void nucleation, growth, and coalescence process at the second phase particles was the dominant failure mechanism under dynamic conditions. Shear banding was less pronounced.

Similar results were also obtained by Mukai et al. [2] using fine-grained IN905XL aluminum alloys when they examined the dependence of their mechanical properties on the rate of deformation. When dealing with up to a strain rate of  $10 \text{ s}^{-1}$ , all samples showed negative strain-rate sensitivity of flow stress. Positive strain-rate sensitivity of strength was, however, observed above strain rates of  $1000 \text{ s}^{-1}$ . In addition, while yield strength and total elongation were weak functions of the strain rate below a strain rate of  $0.1 \text{ s}^{-1}$ , both increased significantly with higher strain rates when the strain rate exceeded  $1000 \text{ s}^{-1}$ .

In tensile experiments on the aluminum alloy 6061, Srivatsan et al. [3] varied the strain rate from  $10^{-4} \text{ s}^{-1}$  to  $10^{-1} \text{ s}^{-1}$ . Likewise, they observed negative strain-rate sensitivity, with yield and ultimate strengths diminishing as strain rate increased. Concomitantly, both the elongation to failure and the reduction in area increased. During the high strain-rate loading, the deformation time is very short. In such cases, interactions between dislocations and the primary hardening precipitates as well as interactions between dislocations and the coarse constituent particles were limited. This resulted in lower strength and an enhancement in the elongation to failure.

Yu and Jones [4] conducted tensile tests on both aluminum alloy and mild steel specimens. They conducted quasistatic experiments at strain rates less than  $0.02 \text{ s}^{-1}$  and dynamic tests up to a maximum strain rate of  $140 \text{ s}^{-1}$ . Their observations showed that the flow stress of aluminum alloy was insensitive to the rate of deformation. The high strain rates affected only the rupture conditions of aluminum alloy, augmenting the true rupture strains with increasing strain rates.

Results on the mild steel specimens indicated that strain rate had a weaker effect on mild steel at large plastic strains than at small plastic strains. In addition, although the true rupture strain was nearly unaffected by the strain rate, the true rupture stress increased about 20% when the strain rate increased from  $0.001 \text{ s}^{-1}$  to  $100 \text{ s}^{-1}$ . Good agreement was found when the Cowper-Symonds constitutive equation was fitted to the experimental data.

The dynamic uniaxial stress-strain relationship was also studied by Albertini and Montagnani [5] in austenitic stainless steels. Ranging the strain rate between  $0.01 \text{ s}^{-1}$  and  $500 \text{ s}^{-1}$ , they found that higher strain rates led to increasing flow stresses but decreasing uniform and fracture elongations. Not only metallic materials

Contributed by Pressure Vessel and Piping Division of ASME for publication in the JOURNAL OF PRESSURE VESSEL TECHNOLOGY. Manuscript received January 11, 2010; final manuscript received June 1, 2010; published online January 21, 2011. Assoc. Editor: Edward A. Rodriguez.



but also fibrous composite materials [6–14] showed noticeable dependency on the strain-rate loading for the material behaviors.

It is noted that a previous study [12] suggested linear relationships between the logarithm of strain rate  $\dot{\epsilon}$  and various material properties including dynamic elastic modulus  $E$ , yield strength  $\sigma_y$ , and the total strain energy density  $w$  as below:

$$E = a_1 \log \dot{\epsilon} + b_1 \quad (1)$$

$$\sigma_y = a_2 \log \dot{\epsilon} + b_2 \quad (2)$$

$$w = a_3 \log \dot{\epsilon} + b_3 \quad (3)$$

where  $a_i$  and  $b_i$  are constants. Equations (1)–(3) demonstrate the relationships in a general form. More useful forms of the equations are presented in Eqs. (4)–(6).

$$\frac{E}{E_0} - 1 = c_1 \log \left( \frac{\dot{\epsilon}}{\dot{\epsilon}_0} \right) \quad (4)$$

$$\frac{\sigma_y}{\sigma_{y,0}} - 1 = c_2 \log \left( \frac{\dot{\epsilon}}{\dot{\epsilon}_0} \right) \quad (5)$$

$$\frac{w}{w_0} - 1 = c_3 \log \left( \frac{\dot{\epsilon}}{\dot{\epsilon}_0} \right) \quad (6)$$

where  $c_i$  is a constant value. In the above equations, the dynamic elastic modulus, the yield strength, and the expended energy density are normalized against corresponding reference values determined at a reference strain rate, usually at a static loading condition. The reference values and the reference strain rate are denoted by the subscript “0.” Similarly, the Cowper–Symonds constitutive equation may be expressed as follows:

$$\log \left( \frac{\sigma}{\sigma_0} - 1 \right) = \frac{1}{p} \log \left( \frac{\dot{\epsilon}}{D} \right) \quad (7)$$

in which  $p$  and  $D$  are the constants. It may thus be seen that the main difference between Eqs. (5) and (7) is in the left-hand sides of those equations. In Eq. (7), the logarithm of the normalized stress is taken but not in Eq. (5). Furthermore, the strain at yield may be derived from Eqs. (1) and (2) as follows:

$$\epsilon_y = \frac{\sigma_y}{E} = \frac{a_2 \log \dot{\epsilon} + b_2}{a_1 \log \dot{\epsilon} + b_1} = \frac{a_2}{a_1} + \frac{b_2 - b_1 a_2 / a_1}{a_1 \log \dot{\epsilon} + b_1} \quad (8)$$

Thus, the yield strains are not constant with varying strain rates. Even if Eq. (7) is used instead of Eq. (2), the same conclusion is reached.

Because strain rates affect the mechanical properties of materials, one objective of the current study is to further examine the material characteristics of a ductile material when it is subjected to different strain-rate loadings. It has been noted that few studies have reported the variation of the elastic modulus with strain rate in metals. Thus, the current study includes the effects of strain rates on both strength and stiffness. The second objective is to investigate the failure criterion when a material is loaded at a varying strain-rate loading, i.e., at nonuniform strain rates. To the authors’ best knowledge, there has been almost no failure criterion proposed for a varying strain-rate loading condition. A study dealt with combined static and dynamic loading to determine the allowable load limits and proposed an interactive equation for such a combined load [15]. The interactive equation was also evaluated using an experiment [16].

## 2 Experiments

This section describes the experimental setup and procedures employed in this study. Results and discussion are presented in Sec. 3. The material of the specimens tested was aluminum alloy AA3003-H14. The dimensions of the specimens are given in Fig. 1. The thickness of the specimens is 3.175 mm.

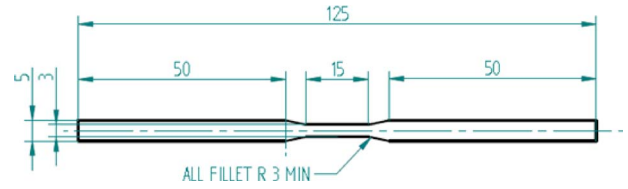


**Fig. 1 Dimensions of test specimens. All dimensions in millimeters.**

The dimensions of the test sections of the specimens were first measured using a pair of vernier calipers. Tensile tests were thereafter performed on an Instron 4507 Universal Materials Testing Machine at room temperature with a 20 kN load cell. The results of the experiments were recorded using a Series IX Instron software. Two important limitations of the current experiments were a maximum crosshead speed of 500 mm/min on the testing machine and a maximum data acquisition rate of 17 Hz. These restricted the maximum strain rate that could be tested in the experiments.

In the first set of experiments, strain rate was varied between  $0.001 \text{ s}^{-1}$  and  $0.5 \text{ s}^{-1}$ . Strain rate was calculated from the crosshead speed of the testing machine using Eq. (9).

$$\dot{\epsilon} = \frac{V}{l_0} \quad (9)$$

where  $l_0$  and  $V$  denote the gauge length of the specimen and the crosshead speed of the testing machine, respectively. Thus, with a gauge length of 15 mm, crosshead speeds of 0.9 mm/min, 9 mm/min, 45 mm/min, 90 mm/min, 270 mm/min, and 450 mm/min were tested. Crosshead speeds and hence strain rates were maintained constant throughout each test. When a specimen is elongated by the test machine, the whole specimen between the two grips will be elongated. However, as long as the gauge section is much longer and narrower than the remaining section of the specimen between the grips, Eq. (9) would represent the strain rate with a reasonable accuracy.

All experiments were repeated and consistency was verified between the two sets of data. In determining the yield strength and strain, the offset method with 0.2% strain was used. Numerical integration was performed to compute the area under the curve so as to evaluate the strain energy density.

In addition to the first set of experiments which were performed with constant strain rates, a second set of experiments were undertaken, in which the strain rate was altered during each test period. More specifically, in these experiments, the test was started with an initial crosshead speed. This was kept constant before it underwent a step change in the crosshead speed to a second speed. The latter was again maintained constant until the specimen failed. Table 1 tabulates the corresponding strain rates and the strains at which the changes in strain rate occurred in these experiments.

## 3 Results and Discussion

Various mechanical material properties are investigated to determine their behaviors under different strain-rate loadings. A fail-

**Table 1 Parameters in varying strain-rate experiments**

Experiment No.	First strain rate (1/s)	Second strain rate (1/s)	Transition strain
1	0.01	0.30	0.00556
2	0.01	0.30	0.00592
3	0.01	0.30	0.01059
4	0.01	0.30	0.01023
5	0.30	0.01	0.01930
6	0.30	0.01	0.02132

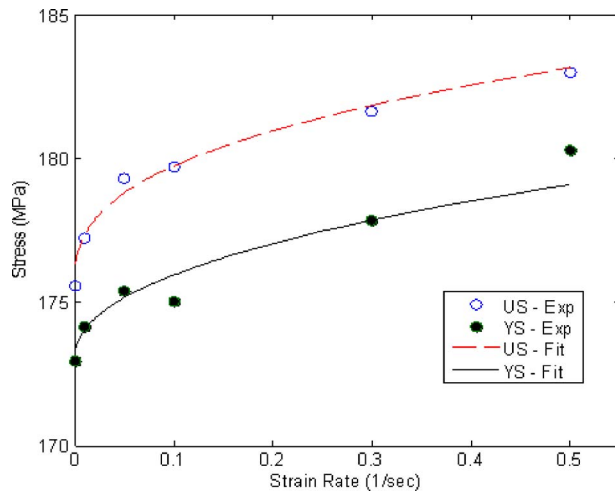


**Fig. 2 Plot of ultimate and yield strengths versus strain rates (U.S. and YS indicate ultimate and yield strength, respectively, and the curve fitting is using the Cowper–Symonds equation)**

ure criterion for a loading with varying strain rates is then proposed followed by an experimental validation. The variations of ultimate and yield strengths with strain rates are shown in Fig. 2. Both ultimate and yield strengths increase nonlinearly as the strain rate increased. The rates of increase are noticeably higher at lower strain rates. Experimental data were fitted using the Cowper–Symonds equation as given below:

$$\frac{\sigma_y}{\sigma_{y,0}} = 1 + \left( \frac{\dot{\epsilon}}{D} \right)^{1/p} \quad (10)$$

where  $\sigma_y$  is the yield or ultimate strength at a given strain rate  $\dot{\epsilon}$ ,  $\sigma_{y,0}$  is the yield or ultimate strength at the static condition, and  $D$  and  $p$  are constants for curve fitting. Two different sets of parameters,  $D$  and  $p$ , were used for yield and ultimate strength, respectively. For the yield strength,  $D=885.2$  and  $p=2.239$  were selected, while for the ultimate strength,  $D=2257.6$  and  $p=2.677$  were chosen. Equation (10) fits the experimental data well.

Yield strength was replotted in Fig. 3 in terms of normalized yield strengths against the inverse of strain rates. The yield strength was normalized in terms of the static yield strength. At low deformation rates, the plot shows relative insensitivity of the normalized yield strength to the strain rate. On the other hand, as the strain rate is increased beyond  $0.1 \text{ s}^{-1}$ , the normalized yield

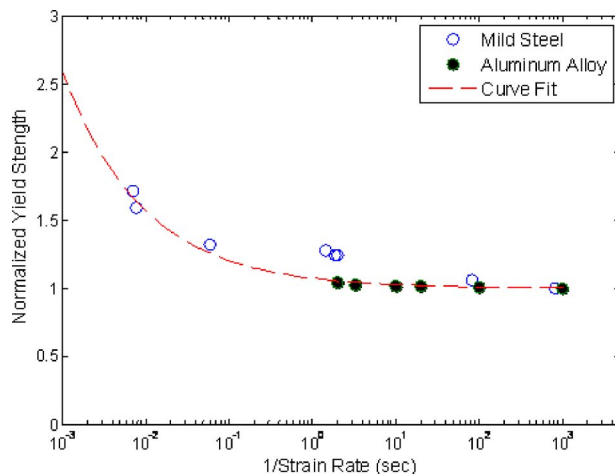


**Fig. 3 Plot of normalized yield strengths versus inverse of strain rates**

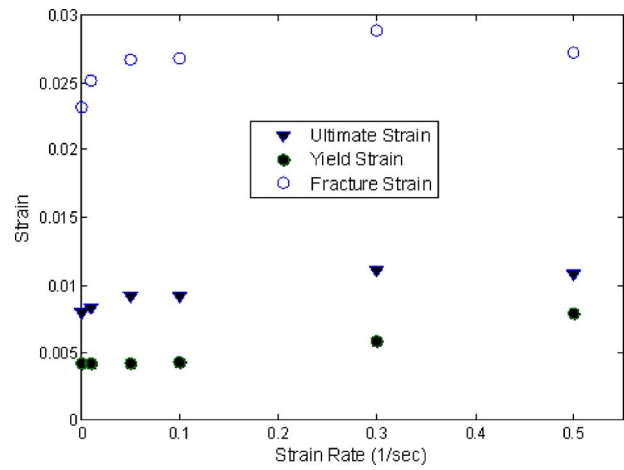


**Fig. 4 Plot of ultimate, yield, and fracture strains versus strain rates**

strength increased noticeably. The inverse of the strain rate, which is plotted on the  $x$ -axis in Fig. 3, gives an indication of the duration of time that the material is allowed to yield. Plastic deformation by loading beyond the yield strength occurs in the material when the stress level lies in the zone above and to the right of the plotted points. The plots show that when deformation is very rapid and the material is not allowed sufficient time to deform, plastic deformation in a material is delayed to a higher stress. This effect, however, may be observed to diminish when the strain rates are less than  $0.1 \text{ s}^{-1}$ . Figure 3 also includes mild steel data [4]. The mild steel yield strength was normalized in terms of its own static yield strength. The plot shows that the same representative curve-fit may be used for different materials for the normalized yield strength plotted against the inverse of the strain rate. These observations were also the same for ultimate strength even though it was not plotted.

The strains at yield, ultimate load, and fracture show increasing trends with strain rate, as seen in Fig. 4. It is observed that an increase in fracture strain is more pronounced at strain rates below approximately  $0.1 \text{ s}^{-1}$ . On the other hand, the yield strain remains relatively constant at strain rates below approximately  $0.1 \text{ s}^{-1}$  and increases thereafter with strain rate. In addition, the ultimate strain changes more uniformly with the strain rate when compared with other strains.

Figure 5 shows the elastic modulus plotted against the strain rate. As shown in the figure, the elastic modulus remains relatively

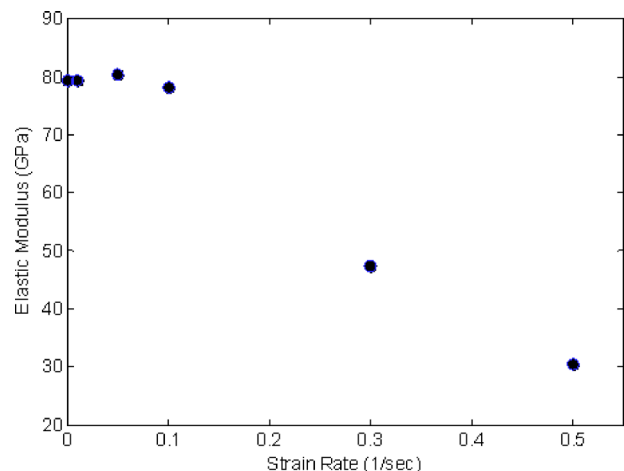


**Fig. 5 Plot of elastic modulus versus strain rates**

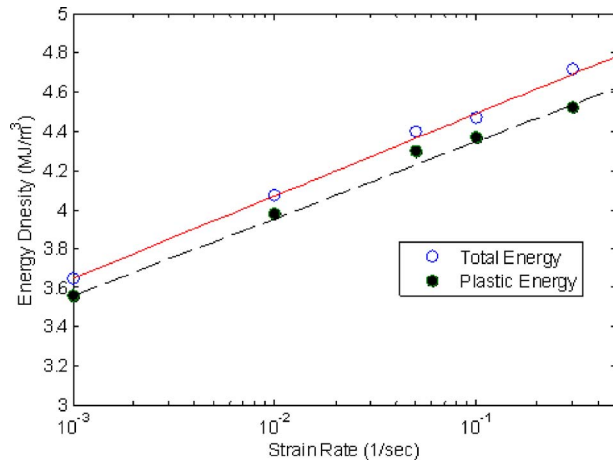


**Fig. 6** Plot of strain energy densities at fracture versus strain rates

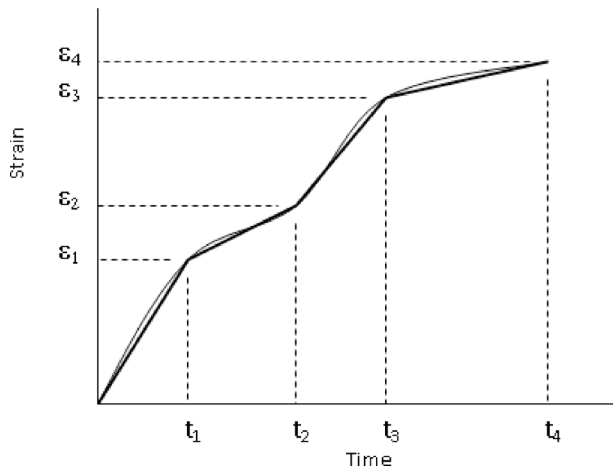
constant at strain rates of below  $0.1 \text{ s}^{-1}$ . Above this strain rate, the elastic modulus follows an approximately linear negative trend with the strain rate. It is not clear what would be the major mechanisms behind this behavior of the elastic modulus. This needs to be further examined to understand proper mechanisms.

Figure 6 shows the plots of the total and plastic strain energy densities absorbed by the material to failure as a function of strain rates. Both energy densities seem to vary linearly with the strain rates when the strain rates are expressed in the logarithmic scale. Those energy densities can be expressed as

$$\frac{w_i}{w_{i,0}} - 1 = \alpha \log\left(\frac{\dot{\epsilon}}{\dot{\epsilon}_0}\right) \quad (11)$$

in which  $w_i$  is either the total or plastic strain energy density at failure,  $\dot{\epsilon}$  is the strain rate, subscript “0” denotes the static loading values, and  $\alpha$  is the proportional constant, which was selected as 0.11. The difference between the total and plastic strain energy densities is the elastic strain energy density at failure. As expected, the elastic strain energy density is much smaller than the other two energy densities.

To propose a failure criterion for varying strain rates, let us consider a loading history, as sketched in Fig. 7, which plots the strain-time history. In the figure, the original strain history curve was represented by multiple piecewise linear lines. The number of breakdowns of a curve into linear segments depends on the complexity of the curve. If the strain history curve has a complex



**Fig. 7** Time-history plot of strain

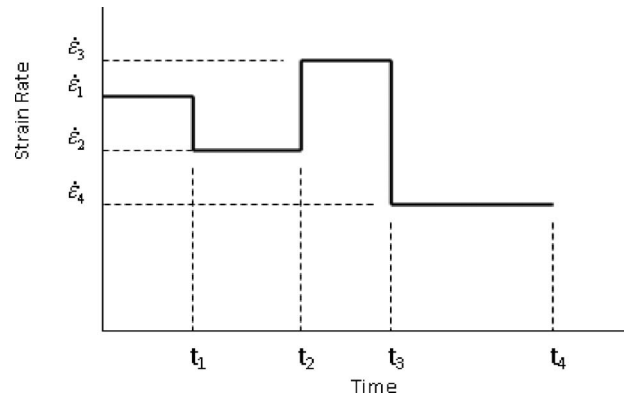


**Fig. 8** Time-history plot of strain rate corresponding to Fig. 7

shape, a large number of linear segments are needed. In Fig. 8, there are four linear segments. For each linear segment, the slope of the line denotes the strain rate. In this figure, there are four different strain rates as expressed below:

$$\dot{\epsilon}_1 = \frac{\epsilon_1}{t_1}, \quad \dot{\epsilon}_2 = \frac{\epsilon_2 - \epsilon_1}{t_2 - t_1}, \quad \dot{\epsilon}_3 = \frac{\epsilon_3 - \epsilon_2}{t_3 - t_2}, \quad \dot{\epsilon}_4 = \frac{\epsilon_4 - \epsilon_3}{t_4 - t_3} \quad (12)$$

The resulting strain-rate history is plotted in Fig. 8. Because stress-strain curves are different depending on strain rates, those curves are shown in Fig. 9 for the four different strain rates as computed above. The bold line in Fig. 9 indicates the section of the stress and strain resulting from the strain history in Fig. 7 as well as the strain-rate history shown in Fig. 8. From the stress-strain curve under the given strain rate, plastic strain energy density is computed between the initial and final strains. Figure 10 illustrates the plastic strain energy density between two strain levels of a stress-strain curve. The gray area is the energy density. Once the plastic strain energy density is computed for each strain and strain-rate histories, a failure criterion is proposed as follows:

$$\sum_i \frac{w_p^i}{(w_p^i)_{\text{crit}}} = \frac{w_p^1}{(w_p^1)_{\text{crit}}} + \frac{w_p^2}{(w_p^2)_{\text{crit}}} + \cdots + \frac{w_p^n}{(w_p^n)_{\text{crit}}} = f \quad (13)$$

where  $w_p^i$  is the plastic strain energy density accumulated during the  $i$ th strain rate, and  $(w_p^i)_{\text{crit}}$  is the maximum plastic strain energy density stored until failure at the same strain rate. The right-

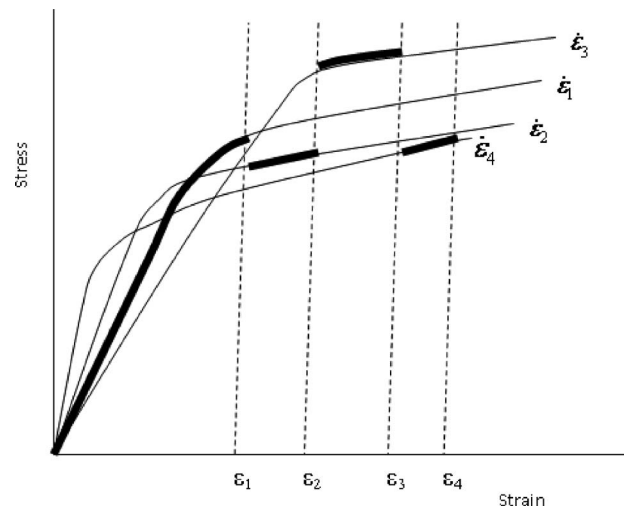


**Fig. 9** Stress-strain curve segments associated with strain and strain-rate histories

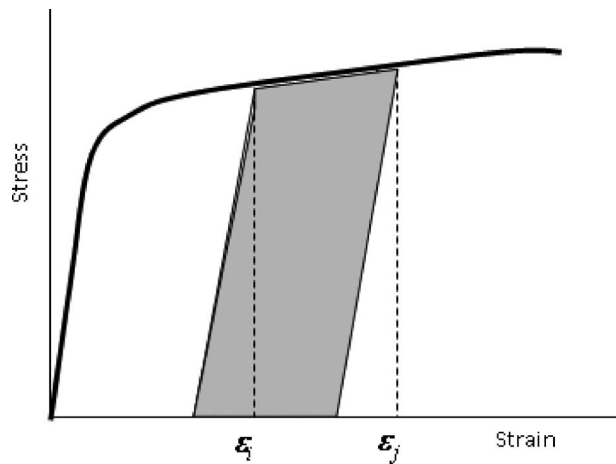


Fig. 10 Plastic strain energy density between two strain levels

hand side value  $f$  is usually set to 1e. However, it may be set less than unity.

The proposed failure criterion given in Eq. (13) is corroborated by results obtained in experiments. In the first set of experiments, the strain rate was increased from  $0.01 \text{ s}^{-1}$  in the first stage of the experiment to  $0.3 \text{ s}^{-1}$  in the second stage until failure. The transition strains between the two strain rates was 0.00556, 0.00592, 0.01023, or 0.01059, respectively. As expected, the stress-strain curve followed that of the  $0.01 \text{ s}^{-1}$  strain rate initially. Upon the step increase in strain rate to  $0.3 \text{ s}^{-1}$ , the stress-strain curve began to deviate from that of the  $0.01 \text{ s}^{-1}$  strain rate to lie in between the two stress-strain curves of constant strain rate. The second set of tests changed the strain rate from  $0.3 \text{ s}^{-1}$  to  $0.01 \text{ s}^{-1}$ . This is the reverse of the first set of tests. The transition occurred at the strain 0.01930 or 0.02132, respectively.

The plastic strain energy densities absorbed by the material during the two stages of the varying strain-rate test, i.e.,  $w_p^1$  and  $w_p^2$ , computed. These were determined from the corresponding stress-strain curves using the numerical integration. Each stored plastic strain energy density was divided by its respective critical plastic strain energy density, and the two ratios were summed. The results are tabulated in Table 2. For the first set of experiments, the maximum difference between the experimental data and the prediction from Eq. (13) with  $f=1$  is 5%. On the other hand, for the second set of tests, the difference is 9%.

In another assessment, the proposed failure criterion was applied to each of the varying strain-rate experiments to predict the fracture strain. These values were estimated based on the transition strain as well as the constant strain-rate stress-strain curves of the first and second strain rates. Table 2 compares the computed failure strains with the experimental data, and this comparison indicates that the former approximates the latter within errors of approximately 4%. To further examine the effect of strain rates on the failure strains, a series of computer predictions based on the

Table 2 Actual and predicted fracture strains in varying strain-rate experiments

Experiment No.	$\sum_i \frac{w_p^i}{(w_p^i)_{\text{crit}}}$	Exp. fracture strain	Predicted fracture strain	Percentage difference (%)
1	0.95	0.0270	0.0279	3.17
2	0.95	0.0268	0.0278	3.78
3	1.01	0.0279	0.0272	-2.60
4	0.97	0.0268	0.0272	1.68
5	0.92	0.0274	0.0268	-2.17
6	0.91	0.0262	0.0269	2.63

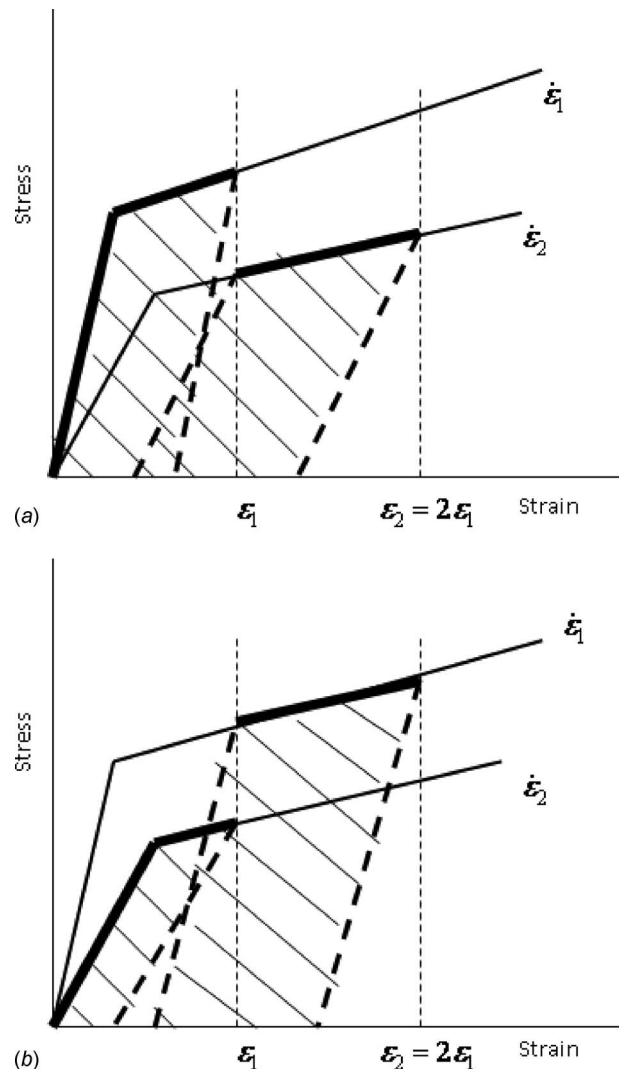
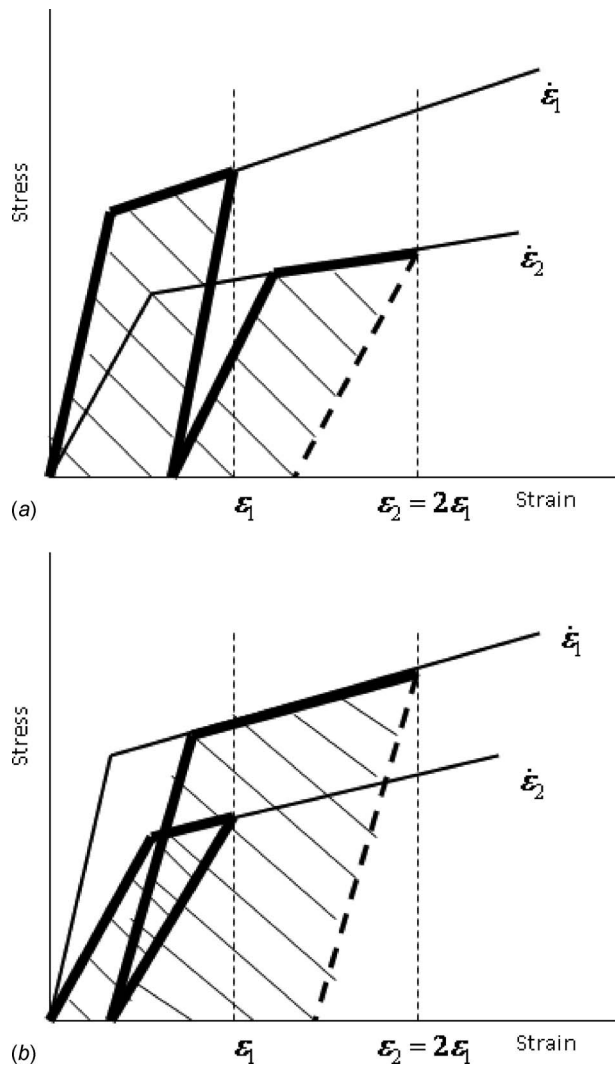


Fig. 11 Comparison of plastic strain energy densities accumulated during two different sequences of loading rates with an equal amount of strain: (a) loading sequence: loading with  $\dot{\epsilon}_1$  followed by loading with  $\dot{\epsilon}_2$  and (b) loading sequence: loading with  $\dot{\epsilon}_2$  followed by loading with  $\dot{\epsilon}_1$

proposed failure criterion and materials data was undertaken. The initial strain rate  $0.001 \text{ s}^{-1}$  was applied to the strain level 0.01, after which the strain rate changed to  $0.01 \text{ s}^{-1}$ ,  $0.05 \text{ s}^{-1}$ , and  $0.1 \text{ s}^{-1}$ , respectively, until fracture. As the second strain rate varied incrementally, the fracture strains increased 4%, 8%, and 10%, respectively, compared with that in one uniform strain rate of  $0.001 \text{ s}^{-1}$ .

The experimental results show an effect of the sequence of strain rates on failure. Figure 11 compares two different loading rates with the same amount of strain during each loading rate. For simplicity, the linear stress-strain curves were used in Fig. 11 for illustration. In Fig. 11(a), the initial strain rate is  $\dot{\epsilon}_1$  up to strain  $\epsilon_1$ , and it is followed by strain rate  $\dot{\epsilon}_2$  until strain  $\epsilon_2=2\epsilon_1$ . Figure 11(b) shows the initial strain rate  $\dot{\epsilon}_2$  until strain  $\epsilon_1$  followed by strain rate  $\dot{\epsilon}_1$  to strain  $\epsilon_2=2\epsilon_1$ . Plastic strain energy density for each loading period is shown by hatched areas in Fig. 11. As these plastic strain energy densities are applied to the failure criterion, Eq. (13), the criterion suggests that the sequence of loading rates affects the failure. A computer simulation was conducted to further elaborate the above statement. In one case, the initial strain rate was  $0.01 \text{ s}^{-1}$  to the strain level 0.01, and the strain rate





**Fig. 12 Comparison of plastic strain energy densities accumulated during two different sequences of loading and unloading: (a) loading sequence: loading with  $\dot{\epsilon}_1 > \text{unloading with } \dot{\epsilon}_1 > \text{loading with } \dot{\epsilon}_2$  and (b) loading sequence: loading with  $\dot{\epsilon}_2 > \text{unloading with } \dot{\epsilon}_2 > \text{loading with } \dot{\epsilon}_1$**

changed to  $0.2 \text{ s}^{-1}$  until the strain level 0.02 after which a strain rate  $0.001 \text{ s}^{-1}$  was maintained up to failure. In the other case, simply the first and second strain rates were exchanged while all other parameters remained the same. When the failure strains were compared between the two cases, the former case had 0.0265, while the latter yielded 0.0270. Thus, the failure seemed to depend on the sequence of the applied strain rates. However, more tests with higher strain rates would be needed to further evaluate this statement.

The failure criterion also suggests that the unloading process during the loading history influences the failure. Figure 12 illustrates the effect of unloading on the plastic strain energy density. Comparison of Fig. 11 to Fig. 12 indicates that the plastic strain energy stored in the material is different if unloading occurs before the next loading. Comparing Fig. 11(a) to Fig. 12(a) shows that the plastic strain energy during strain rate  $\dot{\epsilon}_2$  is smaller with the unloading process. On the other hand, the unloading process produces a greater plastic strain energy density during strain rate  $\dot{\epsilon}_1$  when comparing Fig. 11(b) to Fig. 12(b).

To apply the failure criterion, stress-strain curves should be known for all strain rates experienced by a material in a structure. Practically, it is neither easy nor practical to obtain all those

stress-strain curves experimentally. In that case, the Cowper-Symonds equation as expressed in Eq. (7) may be used to represent the stress-strain curve at different strain rates. The critical plastic strain energy density and the elastic modulus are also estimated at any given strain rate using the curve fitted for the necessary range of strain rates.

## 4 Conclusions

The material property characteristics of aluminum alloy AA3003-H14 were examined under a dynamic uniaxial loading. Both ultimate and yield strengths, as well as the absorbed strain energy density, showed positive sensitivity to strain rate. Moreover, the strains at yield, ultimate load, and fracture increased with the applied strain rate. Under quasistatic strain rates less than  $0.1 \text{ s}^{-1}$ , the low loading rate did not have a significant effect on the elastic modulus, the normalized yield strength, or ultimate strength. When the material was subjected to the loading rates greater than  $0.1 \text{ s}^{-1}$ , the elastic modulus diminished as the strain rate increased, while both normalized yield and ultimate strengths increased noticeably. It was also noted that the amount of plastic strain energy density accumulated in a ductile material in its loading time history was useful as a failure criterion for the prediction of failure. As a result, a failure criterion was proposed for loading with varying strain rates using the concept of accumulated plastic strain energy density. The proposed criterion was validated from experiments consisting of two different strain rates applied one after another subsequently. The test results were limited with the current available testing equipment. As the equipment is updated, more extensive experimental work will be conducted and presented in a subsequent paper.

## References

- [1] Hadianfard, M. J., Smerd, R., Winkler, S., and Worswick, M., 2008, "Effects of Strain Rate on Mechanical Properties and Failure Mechanism of Structural Al-Mg Alloys," *Mater. Sci. Eng., A*, **492**, pp. 283–292.
- [2] Mukai, T., Ishikawa, K., and Higashi, K., 1995, "Influence of Strain Rate on the Mechanical Properties in Fine-Grained Aluminum Alloys," *Mater. Sci. Eng., A*, **204**, pp. 12–18.
- [3] Srivatsan, T. S., Hoff, T., Sriram, S., and Prakash, A., 1990, "The Effect of Strain Rate on Flow Stress, Strength and Ductility of an Al-Li-Mg Alloy," *J. Mater. Sci. Lett.*, **9**, pp. 297–300.
- [4] Yu, J., and Jones, N., 1991, "Further Experimental Investigations on the Failure of Clamped Beams Under Impact Loads," *Int. J. Solids Struct.*, **27**(9), pp. 1113–1137.
- [5] Albertini, C., and Montagnani, M., 1980, "Dynamic Uniaxial and Biaxial Stress-Strain Relationships for Austenitic Stainless Steels," *Nucl. Eng. Des.*, **57**, pp. 107–123.
- [6] Armenakas, A. E., and Sciammarella, C. A., 1973, "Response of Glass-Fiber-Reinforced Epoxy Specimens to high rates of tensile loading," *Exp. Mech.*, **13**(10), pp. 433–440.
- [7] Lifshitz, J. M., 1976, "Impact Strength of Angle Ply Fiber Reinforced Materials," *J. Compos. Mater.*, **10**, pp. 92–101.
- [8] Daniel, I. M., LaBedz, R. H., and Liber, T., 1981, "New Method for Testing Composites at Very High Strain Rates," *Exp. Mech.*, **21**(2), pp. 71–77.
- [9] Harding, J., and Welsh, L. M., 1983, "A Tensile Testing Technique for Fibre-Reinforced Composites at Impact Rates of Strain," *J. Mater. Sci.*, **18**, pp. 1810–1826.
- [10] Melin, L. G., and Asp, L. E., 1999, "Effects of Strain Rate on Transverse Tension Properties of a Carbon/Epoxy Composite: Studied by Moiré Photography," *Composites, Part A*, **30**, pp. 305–316.
- [11] Okoli, O. I., and Smith, G. F., 2000, "The Effect of Strain Rate and Fibre Content on the Poisson's Ratio of Glass/Epoxy Composites," *Compos. Struct.*, **48**, pp. 157–161.
- [12] Okoli, O. I., 2001, "The Effects of Strain Rate and Failure Modes on the Failure Energy of Fibre Reinforced Composites," *Compos. Struct.*, **54**, pp. 299–303.
- [13] Taniguchi, N., Nishiwaki, T., Hirayama, N., Nishida, H., and Kawada, H., 2009, "Dynamic Tensile Properties of Carbon Fiber Composite Based on

Thermoplastic Epoxy Resin Loaded in Matrix-Dominated Directions,” *Compos. Sci. Technol.*, **69**, pp. 207–213.

- [14] Shokrieh, M. M., and Omid, M. J., 2009, “Tension Behaviour of Unidirectional Glass/Epoxy Composites Under Different Strain Rates,” *Compos. Struct.*, **88**, pp. 595–601.
- [15] McLean, J. L., and Bitner, J. J., 1991, “Significance of High Level Test Data in Piping Design,” ASME Pressure Vessels and Piping Conference, San Diego, CA.
- [16] Hampton, E. J., and Bitner, J., 2005, “Stress or Strain Criteria for Combined Static and Dynamic Loading,” *Welding Resource Council Bulletin*, Vol. 500.

# Stress-Strain Behavior of an Aluminum Alloy Under Transient Strain-Rates

Y. W. Kwon<sup>1</sup>

Department of Mechanical & Aerospace Engineering,  
Naval Postgraduate School,  
Monterey, CA 93943

Y. Esmaili

Department of Mechanical & Environmental Engineering,  
University of California-Santa Barbara,  
Santa Barbara, CA 93106

C. M. Park

Department of Mechanical & Aerospace Engineering,  
Naval Postgraduate School,  
Monterey, CA 93943

*Because most structures are subjected to transient strain-rate loading, an experimental study was conducted to investigate the stress-strain behaviors of an aluminum alloy undergoing varying strain-rate loading. To this end, uniaxial tensile loading was applied to coupons of dog-bone shape such that each coupon underwent two or three different strain-rates, i.e., one rate after another. As a basis, a series of single-strain-rate tests was also conducted with strain-rates of 0.1–10.0 s<sup>-1</sup>. When the material experienced multistrain-rate loading, the stress-strain curves were significantly different from any single-strain-rate stress-strain curve. The strain-rate history affected the stress-strain curves under multistrain-rate loading. As a result, some simple averaging of single-strain-rate curves did not predict the actual multistrain-rate stress-strain curve properly. Furthermore, the fracture strain under multistrain-rate loading was significantly different from that under any single-strain-rate case. Depending on the applied strain-rates and their sequences, the former was much greater or less than the latter. A technique was proposed based on the residual plastic strain and plastic energy density in order to predict the fracture strain under multistrain-rate loading. The predicted fracture strains generally agreed well with the experimental data. Another observation that was made was that the unloading stress-strain curve was not affected by the previous strain-rate history. [DOI: 10.1115/1.4003470]*

## 1 Introduction

Most external loads, which include mechanical impact, shock, and seismic loading, are transient in nature. Structures subjected to transient loading experience nonuniform strain-rates. That is, the strain-rates resulting from the loads are not constant but instead vary as a function of time. Material properties such as elastic modulus, yield strength, ultimate strength, and fracture strain generally depend on the applied strain-rates. As a result, it is important to understand and predict the material behaviors under transient strain-rates.

Most previous studies considered the effect of a single-strain-rate (i.e., a constant strain-rate) on material behaviors [1–3]. A

very limited study was conducted for the effect of multiple-strain-rate loading [4–7]. While Bitner and co-workers [4,5] considered two loads combined, i.e., static and dynamic loading, Kwon and Tan [6] discussed a series of different applied strain-rates. However, because of the limitation of the testing machine, the experiment was conducted at relatively low strain-rates up to 0.5 s<sup>-1</sup>.

The objective of the study is to investigate the stress-strain relationship of a metallic material, more specifically an aluminum alloy, undergoing transient strain-rates ranging from 0.1 s<sup>-1</sup> to 10.0 s<sup>-1</sup>. Because the stress-strain curve for transient strain-rate loading is so much different from that for constant strain-rate loading, it is important to investigate the former behavior so as to understand and hopefully predict the transient response and integrity of a structure.

## 2 Mechanical Testing

A series of mechanical tests was conducted to examine the material characteristics of an aluminum alloy 3003 under different strain-rate loading. A hydraulic uniaxial testing machine was utilized so that a relatively high strain-rate could be applied to the test coupons. All testing coupons were made in a dog-bone shape in the same size with the same gauge length. The applied strain-rate was computed from the grip speed of the uniaxial testing machine divided by the gauge length.

The initial set of tests was conducted on coupons using a uniform strain-rate from start to end. However, the strain-rate was varied from coupon to coupon between 0.1 s<sup>-1</sup> and 10.0 s<sup>-1</sup>, inclusively. These sets of test data provided the baseline to investigate the effect of transient strain-rates. Multiple coupons were tested under the same strain-rate condition to make sure of the repeatability of the test data. The test results showed consistency among coupons under the same loading condition. Besides, in order to study the effect of testing machine dynamics at high strain-rates, some coupons were tested using two independent testing machines at the same high strain-rates. One was a hydraulic-driven machine, while the other was a mechanical-driven machine. Both test results were very consistent. This comparison is not a rigorous proof but a good indication of negligible effect of machine dynamics.

The next set of tests considered transient strain-rate loading to test coupons. In other words, the strain-rate was changed from one value to another for the same test coupon. A group of coupons experienced two different strain-rates while another group of coupons underwent three different strain-rates. The sequences of strain-rates were varied from slow to fast or vice versa.

## 3 Test Results and Discussion

Constant strain-rate testing was conducted at the rates of 0.1 s<sup>-1</sup>, 0.2 s<sup>-1</sup>, 0.3 s<sup>-1</sup>, 0.5 s<sup>-1</sup>, 1.0 s<sup>-1</sup>, 2.0 s<sup>-1</sup>, 5.0 s<sup>-1</sup>, and 10.0 s<sup>-1</sup>. Figure 1 shows the stress-strain curves under uniform strain-rates of different values. Because the curves for strain-rates from 0.1 s<sup>-1</sup> to 1.0 s<sup>-1</sup> are very close to one another, the figure does not include the curves for strain-rates of 0.2 s<sup>-1</sup>, 0.3 s<sup>-1</sup>, and 0.5 s<sup>-1</sup> so as not to overcrowd the figure. As shown in the figure and as expected in previous studies [6], the material properties change as a function of the strain-rate. This observation becomes more obvious as the strain-rate becomes 5.0 s<sup>-1</sup> and higher, as seen in Fig. 1.

As shown in Fig. 1, elastic modulus decreases as the strain-rate increases after the rate 1.0 s<sup>-1</sup>. In particular, the reduction in elastic modulus is very significant for strain-rates 5.0 s<sup>-1</sup> and 10.0 s<sup>-1</sup>. On the other hand, the peak stress increases for higher strain-rates. Furthermore, the stress-strain behavior after the peak stress changes for the strain-rates 5.0 s<sup>-1</sup> and 10.0 s<sup>-1</sup>.

The next set of graphs shows the stress-strain curves as the two-strain-rates are applied to test coupons. Figures 2 and 3 are the cases with strain-rates of 0.1 s<sup>-1</sup> and 10.0 s<sup>-1</sup>. The strain-rate of 0.1 s<sup>-1</sup> was initially applied and the rate changed to 10.0 s<sup>-1</sup>

<sup>1</sup>Corresponding author.

Contributed by the Pressure Vessel and Piping Division of ASME for publication in the JOURNAL OF PRESSURE VESSEL TECHNOLOGY. Manuscript received September 10, 2010; final manuscript received November 9, 2010; published online June 3, 2011. Assoc. Editor: Marina Ruggles-Wrenn.

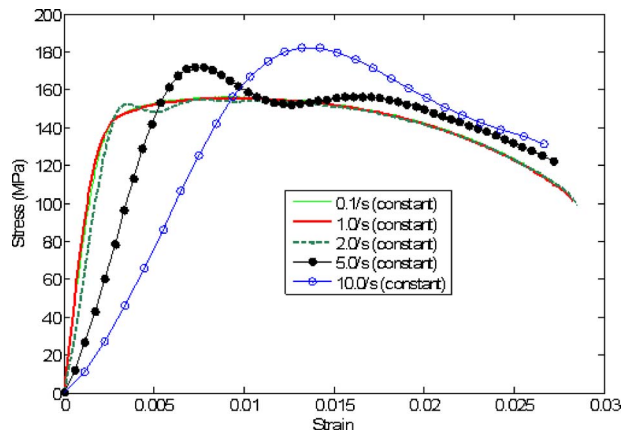


**Fig. 1** Plot of stress-strain curves for different constant strain-rates

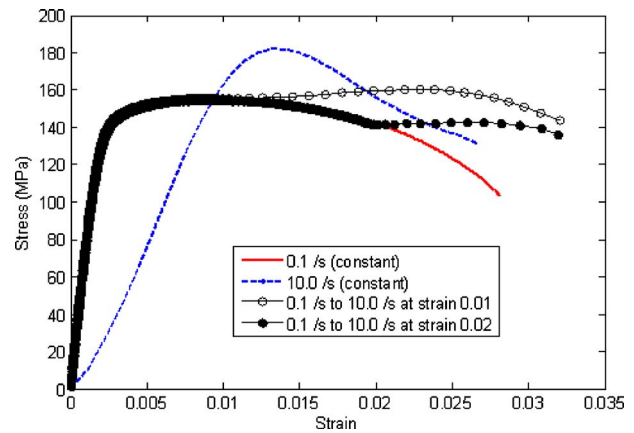


**Fig. 4** Stress-strain curve under two-strain-rate from  $10.0 \text{ s}^{-1}$  to  $0.1 \text{ s}^{-1}$

later, as shown in Fig. 2. The strain-rates were reversed in Fig. 3. In both figures, the two-strain-rate graphs are compared with the relevant single-strain-rate cases. As expected, the two-strain-rate curves overlap the single-strain-rate curves until the strain-rates are varied. Once the rates change, the two-strain-rate curves follow neither the first nor the second single-strain-rate curve. The two-strain-rate curves do not lie even between the two single-strain-rate curves. Thus, using the average of the two single-strain-rate curves does not represent the true two-strain-rate

curves properly. The history of applied strain-rates affects the stress-strain curve of the two-strain-rate case. This is also true for any multistrain-rate loading. Figure 4 compares the stress-strain curves for test coupons, which experience strain-rate loading from  $0.1 \text{ s}^{-1}$  to  $10.0 \text{ s}^{-1}$ , while the changes occur at two different strain levels. Another two-strain-rate test was conducted using  $5.0 \text{ s}^{-1}$  and  $10.0 \text{ s}^{-1}$  and the test results are plotted in Fig. 5. The sequence of the strain-rates was different for two separate tests. The same observation as described above applies to the results. Figure 6 shows the results from three-strain-rate tests using  $0.1 \text{ s}^{-1}$ ,  $5.0 \text{ s}^{-1}$ , and  $10.0 \text{ s}^{-1}$ .

One common thing to be noted from all multistrain-rate test results is that the fracture strain is affected by the combination of strain-rates, as well as their sequences. When the initial strain-rate is greater than the subsequent strain-rate, the fracture strain becomes smaller than that under any individual strain-rate. Comparing Figs. 2 and 3 and observing Fig. 5 show that the opposite is also true. A possible explanation for this is provided below.

Unloading tests were undertaken for two-strain-rate testing. The test coupons were loaded at  $0.1 \text{ s}^{-1}$  initially followed by  $10.0 \text{ s}^{-1}$  later. The applied loading was released at  $0.1 \text{ s}^{-1}$  for one set of coupons and  $10.0 \text{ s}^{-1}$  for the other set of coupons. The two unloading curves are plotted in Fig. 7. As shown in the figure, the slope of the stress-strain curve for unloading after multistrain-rate loading was quite parallel to the slope of the initial stress-strain curve of the single-strain-rate case corresponding to the unloading

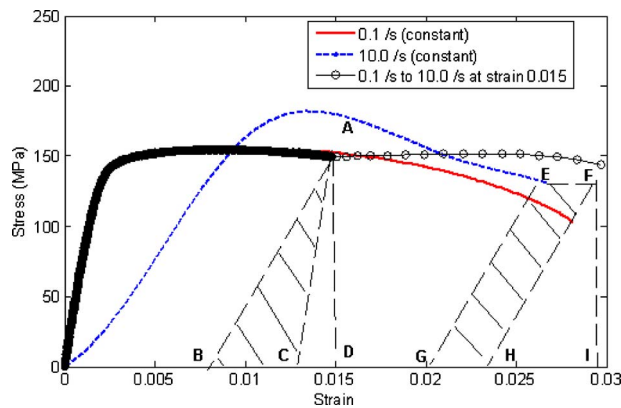


**Fig. 2** Stress-strain curve under two-strain-rate from  $0.1 \text{ s}^{-1}$  to  $10.0 \text{ s}^{-1}$

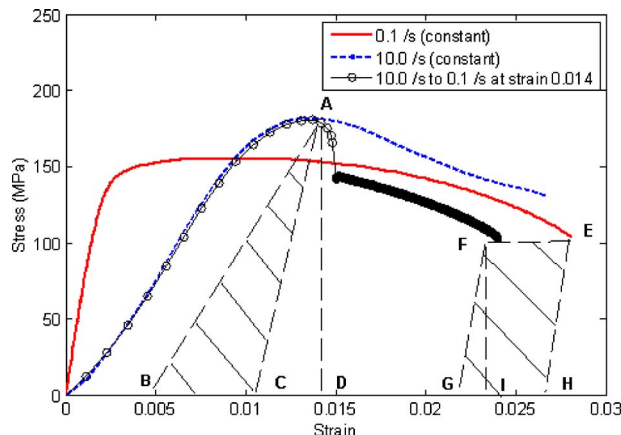


**Fig. 3** Stress-strain curve under two-strain-rate from  $10.0 \text{ s}^{-1}$  to  $0.1 \text{ s}^{-1}$

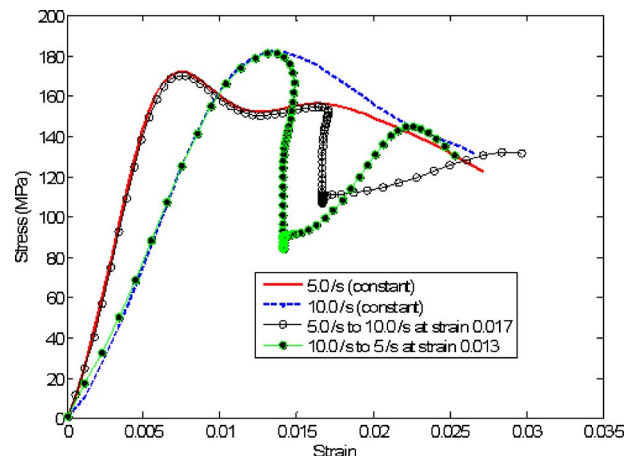


**Fig. 5** Stress-strain curves under two-strain-rates of  $5.0 \text{ s}^{-1}$  and  $10.0 \text{ s}^{-1}$



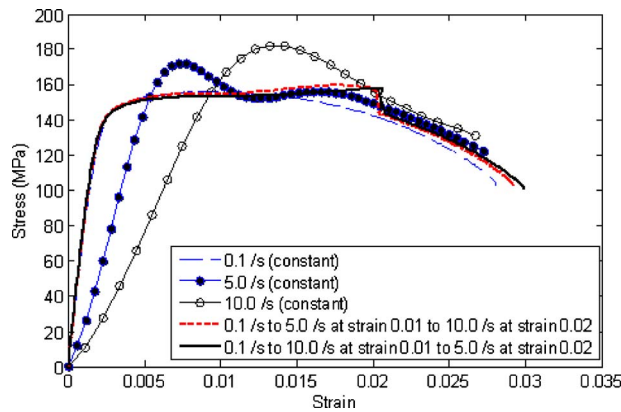


**Fig. 6 Stress-strain curves under three-strain-rates of  $0.1 \text{ s}^{-1}$ ,  $5.0 \text{ s}^{-1}$ , and  $10.0 \text{ s}^{-1}$**

strain-rate. In other words, this fact states that the unloading portion of the stress-strain curve is not affected by the previous strain-rate history. A further test was conducted with the reverse of the strain-rate sequence followed by unloading, i.e.,  $10.0 \text{ s}^{-1}$  initially and  $0.1 \text{ s}^{-1}$  later. The same observation was made.

In order to predict the fracture strain, let us consider point A in Fig. 2 where the change of strain-rate starts to occur. If there were no change of strain-rate, the plastic strain would be at point C. However, the rate change alters the potential unloading slope resulting in plastic strain at point B. As a result, there is a decrease of the plastic strain in the amount of strain value BC with a decrease of plastic strain energy density of area(ABC). It is assumed that such a decrease of the plastic strain energy density would extend the fracture strain. The fracture point at  $10.0 \text{ s}^{-1}$  should be point E if the applied strain-rate is constant all the way. However, because of the change of strain-rate at point A, the fracture strain changes. In order to find the new fracture strain, let point E extend parallel to the horizontal axis to point F such that the area(ABC) is equal to area(EFHG), assuming the saved plastic strain energy density will contribute to the extension of the fracture strain. The predicted fracture strain is point I.

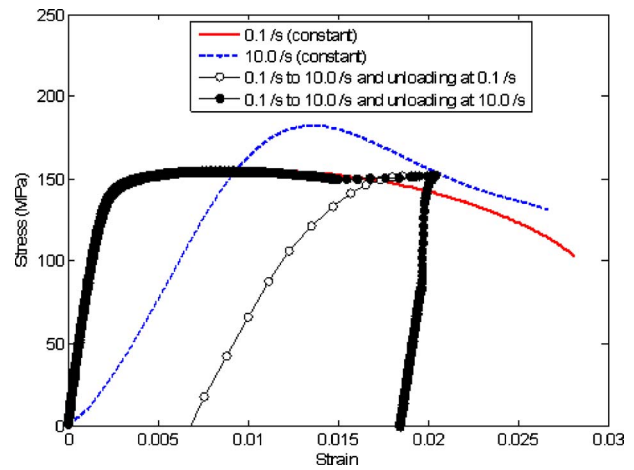


**Fig. 7 Stress-strain curves with unloading after applying two different strain-rates**

For Fig. 3, a similar argument was applied except that there would be an increase of plastic strain energy density for this case by changing the strain-rate from  $10.0 \text{ s}^{-1}$  to  $0.1 \text{ s}^{-1}$  at point A. Therefore, there is a decrease in the fracture strain with the assumption that area(ABC) is equal to area(FEHC). The predicted fracture strain is point I. The same argument can be extended for a multistrain-rate loading. The predicted fracture strains are compared with the experimental fracture strains in Tables 1 and 2. Table 1 is for the two-strain-rate loading, while Fig. 2 is for the three-strain-rate loading. The predicted fracture strains agree well with the experimental values. Fracture strains under single-strain-rate loadings of different values are also included in Table 1 so that they can be compared with the fracture strains under two-strain-rate loading. The fracture strains under single-strain-rate loading from  $0.1 \text{ s}^{-1}$  to  $10.0 \text{ s}^{-1}$  varied from 0.0280 to 0.0267. The difference is around 5%. On the other hand, the two-strain-rate coupons had fracture strains from 0.0235 to 0.0321. The largest fracture strain is more than 35% greater than the smallest fracture strain. The range of the fracture strain can be even greater

**Table 1 Comparisons of experimental and predicted fracture strains with two-strain-rate loading**

Case No.	First strain-rate (/s)	Second strain-rate (1/s)	Strain for rate change	Exp. fracture strain	Predicted fracture strain	Error (%)
A1	0.1	10.0	0.010	0.0321	0.0297	-7.5
A2	0.1	10.0	0.015	0.0297	0.0299	-0.7
A3	0.1	10.0	0.020	0.0319	0.0294	-7.8
A4	10.0	0.1	0.010	0.0235	0.0228	-3.0
A5	10.0	0.1	0.014	0.0238	0.0236	0.9
A6	5.0	10.0	0.017	0.0297	0.0294	-1.0
A7	10.0	5.0	0.014	0.0253	0.0240	-5.1
A8	0.1	—	—	0.0280	—	—
A9	5.0	—	—	0.0272	—	—
A10	10.0	—	—	0.0267	—	—

**Table 2 Comparisons of experimental and predicted fracture strains with three-strain-rate loading**

Case No.	First rate (/s)	Strain for first change	Second rate (/s)	Strain for second change	Third rate (/s)	Exp. fract. strain	Pred. fract. strain	Error (%)
B1	0.1	0.010	10.0	0.021	5.0	0.0300	0.0299	-0.3
B2	0.1	0.01	5.0	0.020	10.0	0.0291	0.0284	-2.4
B3	10	0.014	5	0.019	0.1	0.0247	0.0234	-5.3

depending on the combination of the two-strain-rates, as well as the transition strain levels. The range of fracture strains under three-strain-rate loading is also much greater than that under single-strain-rate loading.

#### 4 Conclusions

Uniaxial testing was conducted to investigate the stress-strain behaviors of an aluminum alloy under transient strain-rate loading. The stress-strain curves strongly depended on the strain-rate history. Therefore, any averaging technique of single-rate stress-strain curves did not represent those of multistrain-rate loading. The fracture strain under multistrain-rate loading was significantly different from that under single-strain-rate loading. Depending on the strain-rate history, the former was much smaller than the latter, which would be more critical for structural failure or vice versa. However, the unloading stress-strain curve was not affected by the strain-rate history. A technique was proposed based on the residual plastic strain and plastic energy density to predict the fracture strain under multistrain-rate loading. The predicted results generally agreed well with the experimental data.

In order to predict the structural behavior under transient loading reliably, it is important to understand the stress-strain behavior under transient strain-rate loading. In that regard, the future study

should be focused to predicting the stress-strain curves under transient strain-rate loading, including all important data for modulus, peak stress, and work-hardening.

#### Acknowledgment

This work was sponsored by the ONR Solid Mechanics Program as well as the NSWC-Carderock Division. The authors greatly appreciate their support.

#### References

- [1] Hadianfard, M. J., Smerd, R., Winkler, S., and Worswick, M., 2008, "Effects of Strain Rate on Mechanical Properties and Failure Mechanism of Structural Al-Mg Alloys," *Mater. Sci. Eng., A*, **492**, pp. 283–292.
- [2] Mukai, T., Ishikawa, K., and Higashi, K., 1995, "Influence of Strain Rate on the Mechanical Properties in Fine-Grained Aluminum Alloys," *Mater. Sci. Eng., A*, **204**, pp. 12–18.
- [3] Srivatsan, T. S., Hoff, T., Sriram, S., and Prakash, A., 1990, "The Effect of Strain Rate on Flow Stress, Strength and Ductility of an Al-Li-Mg Alloy," *J. Mater. Sci. Lett.*, **9**, pp. 297–300.
- [4] McLean, J. L., and Bitner, J. J., 1991, "Significance of High Level Test Data in Piping Design," ASME Pressure Vessels and Piping Conference, San Diego, CA.
- [5] Hampton E. J. and Bitner J., 2005, "Stress or Strain Criteria for Combined Static and Dynamic Loading," *Welding Research Council Bulletin* 500.
- [6] Kwon, Y. W., and Tan, K. S., "Failure of Ductile Materials Subject to Varying Strain Rates," *ASME J. Pressure Vessel Technol.*, in press.
- [7] Ferron, G., Mliha-Touati, M., and Tanti, P., 1983, "Variations in Ductility Produced by Strain Rate Changes in Tensile Testing," *Mater. Sci. Eng.*, **59**(2), pp. 185–196.